Influence of residual stresses on strength and toughness of an alumina/alumina-zirconia laminate

Dissertation zur Erlangung des Grades Doktor
der Montanistischen Wissenschaften an der
Montanuniversität Leoben

eingerichtet von
Dipl. Ing. Javier Pascual Herrero.

Institut für Struktur- und Funktionskeramik der Montanuniversität
Leoben

Leoben, Mai 2007

Declaration

I hereby declare that the presented thesis has been written by myself and that no prohibited aid has been used.
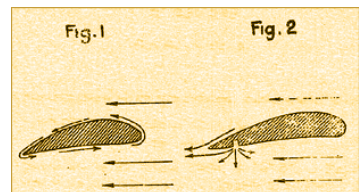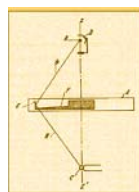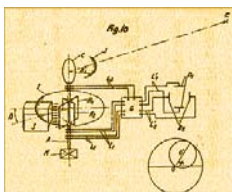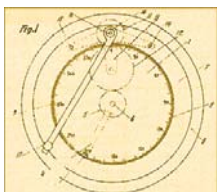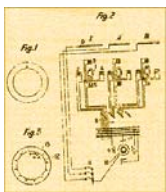
Leoben, May 2007

<div align="right">Javier Pascual Herrero</div>

Que me conseillez-vous d'aller visiter?
La planète Terre. Elle a une bonne réputation.

Saint-Exupéry

(Details of patents from Saint-Exupéry)

Acknowledgements

Danksagung

Agradecimientos

Acknowledgments, Index and Nomenclature

Nomenclature

The following nomenclature has been used through the thesis

A (Al_2O_3)	alumina
AZ (Al_2O_3/ZrO_2)	alumina-zirconia composite

One example is given to clarify the notation of the stacking order. For example, a laminate denominated 2A/AZ/A/AZ/A/AZ/2A. It is a 7-layer laminate (9 tapes), made of 4 layers of alumina A (6 tapes) and 3 layers of the AZ-composite. It is a symmetrical laminate.

Latin symbols

a	crack length, defect size
a_0	crack length arising from an indentation in a non-stressed material
a_1	crack length arising from an indentation in a stressed material
A	parameter in the Paris' Law (subcritical crack growth)
A	constant in the frequency distribution density of defect lengths $g(r)$
A_{kl}	coefficients for the determination of the weight function h
B	width of the specimen
CTE	thermal expansion coefficient
C_{inh}	material inhomogeneity term
d	diagonal of a Vickers indentation, longest diagonal of a Knoop indentation
d_r	interplanar spacing of (h k l) planes of a stressed lattice
d_0	strain-free lattice interplanar spacing
D_{50}	average particle size
E	elastic modulus
$E´$	normalized elastic modulus
E^*	normalized elastic modulus
E_i	elastic modulus of i
E_{oop}	out-of-plane measurement for the elastic modulus
E_{ip}	in-plane measurement for the elastic modulus
E_{long}	longitudinal measurement for the elastic modulus
E_{Reuss}	Reuss elastic modulus
$\overline{E}$	volume-averaged elastic modulus, Voigt elastic modulus
$\dot{E}$	uniaxial viscosity in the Newton's Law
f_i	volumetric fraction of i
f_r	resonant frequency
f_{long}	resonant frequency in the longitudinal response
F	force, probability of failure
F_{fr}	load at fracture
F_0	force for crack opening
$g(r)$	frequency distribution density of defect lengths

G	energy release rate
G_{ED}	edge cracking critical energy release rate
G_{CH}	channel cracking critical energy release rate
$h(z,a)$	weight function
H (or HV)	Vickers hardness
H_K	Knoop hardness
I	moment of inertia
J	crack driving force
J_c	fracture energy or critical crack driving force
J_{tip}	near-tip crack driving force
J_{far}	far-field crack driving force
k	exponential decay
K	stress intensity factor
K_c	fracture toughness
$K_{c,0}$	intrinsic fracture toughness
$K_{c,plateau}$	plateau value toughness for an R-curve
K_{tip}	stress intensity factor at the crack tip
K_{appl}	contribution of the applied stress to K_{tip}
K_{res}	contribution of the residual stress to K_{tip}
K_R	R-curve
$K_{R,effective}$	effective R-curve
L	length of the specimen
L_x	distance necessary to define the integration path Γ
m	Weibull modulus
m^*	Weibull modulus for a 3-parameter distribution
M	bending moment
n	number of layers, exponent of the Paris' Law (subcritical crack growth)
$\underline{n}$	normal unit vector to the path Γ
$\langle N_{c,V}(V) \rangle$	mean number of critical volume defects
P	probability of failure, load
r	exponent in the frequency distribution density of defect lengths $g(r)$
S	surface
S_0	normalizing surface
S_1	span length
S_2	span length
t	thickness, time
t_i	thickness of the layer labeled as i
t_1^*	critical thickness of the layer labeled as 1 (concerning edge cracks)
t_2^*	critical thickness of the layer labeled as 2 (concerning tunnel cracks)
T	temperature
T_{sf}	frozen stress temperature
T_1	correction factor to estimate E with the impulse excitation technique
u_i	displacements in the i-direction
v	velocity of crack propagation
V	volume
V_0	normalizing volume

W	height of the specimen
$x(t)$	vibration during the impulse excitation method to measure the elastic properties
Y	geometrical factor

Greek symbols

α	thermal expansion
α_i	thermal expansion of i
β	indentation parameter
Γ	integration path
Δa	crack extension
Δa^*	critical crack extension
$\Delta\varepsilon$	strain mismatch between two adjacent layers
$\Delta\alpha$	thermal expansion coefficient mismatch
ΔL	length change
ΔT	temperature mismatch
$\Delta\dot{\varepsilon}$	mismatch in strain rate
$\Delta\alpha_{\mathrm{tech}}$	technical thermal expansion mismatch
δ	deflection in a bending test
ε_{τ}	difference in interplanar spacing
ε_i	strain in the layer i
λ	ratio t_2/t_1, ratio $t_{\mathrm{AZ}}/t_{\mathrm{A}}$
μ	shear modulus
ν	Poisson's ration
$\Sigma\Pi_{ii}$	trace of the piezo-spectroscopic matrix
$\Sigma\sigma_{ii}$	trace of the stress tensor.
ρ	density
ρ_i	density of the material i
σ	stress
σ_0	characteristic strength (concerning Weibull distribution)
σ_0^*	characteristic strength (in a 3-parameter Weibull distribution)
$\sigma_x, \sigma_y, \sigma_z$	components of the stress tensor in the direction x, y and z
σ_i	stress in the i-layer
σ_{res}	residual stress
σ_{thr}	threshold stress propitiated by high internal compressive stresses
σ_{th}	threshold stress in the Weibull distribution
$\sigma_{\mathrm{f},0}$	intrinsic strength
σ_{f}	strength, indentation strength
ϕ	Bulk (Helmholtz) free energy per unit area, phase
χ	dimensionless constant
ψ	tilt angle during the measurement of stresses by the X-ray diffraction method

Chapter 1. Introduction

Due to their brittle nature, monolithic ceramics are sensitive to defects that act as stress concentrators. Therefore, structural ceramics are easier to find in parts that are subjected to compressive loading or limited tensile or multiaxial loading. A well-known example is glass and porcelain ware commonly used in our daily lives. Dropping a glass or porcelain cup to the floor is enough to break it. However, structural ceramics are finding applications in the industry mainly due to improvements in the processing routes [1]. Some examples of structural applications for ceramic materials are bearings, seals, armors or cutting tools.

At present, there is still need to improve the response to mechanical solicitations of advanced ceramic applications, especially in those situations in which a ceramic is the best or the only alternative, for example: high temperature environments, aggressive environments (corrosion, oxidation, wear…), or just those fields in which functional properties of ceramics are unquestionable (optical, magnetic, ...).

Apart from processing topics, one of most interesting development was the observation that the mechanical properties of ceramics could be appreciably enhanced by the incorporation of a secondary phase, such a ceramic fibers [2], whiskers [3] or metal particles [4]. New strategies based on the development of materials with controlled microstructures have emerged in the last years by observing natural materials. Natural composites may give us some insights into making better structural materials through biomimetic design [5].

For example; materials such as nacre, shells or teeth, have demonstrated to exhibit excellent mechanical properties because of their composite layered structures. In example, the hierarchical structure of a mollusk shell is formed by aragonite layers about 1 μm thick joined by a kind of mortar of proteins. This particular configuration imparts over one order of magnitude higher bending strength and toughness than those of aragonite single crystals [6]. Therefore, ceramic/ceramic laminar structures provide a great opportunity for tailoring the mechanical properties and meeting apparently contradictory characteristics of structural ceramics.

1

Nowadays, the utilization of ceramic laminates (often called multilayers) is finding a major role in a wide range of technological applications. This is especially so in the area of biomechanical replacements - dental crowns, hip and knee prostheses…- where wear resistance, chemical durability, biocompatibility, and even aesthetics, are critical issues [7]. Not only bio-replacements, ballistic protection [8], or cutting tools [9], but also many functional components such as membranes [10], capacitors [11], fuel-air sensors [12], or high-integrated components in microelectronics [13] are devices in which ceramic laminates are present.
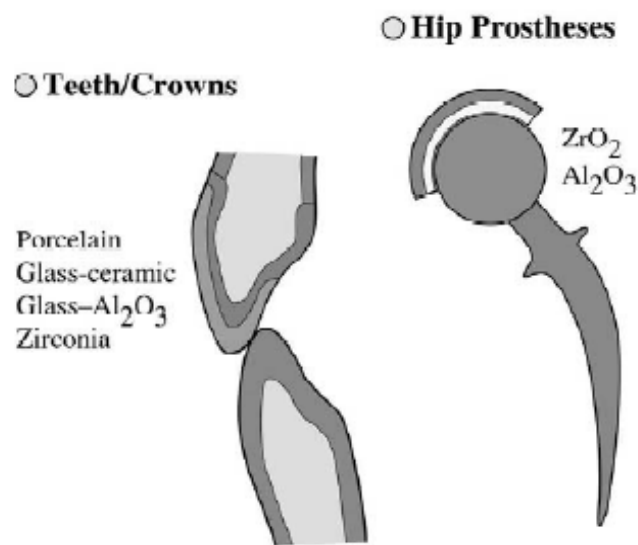
Figure 1.1: Schematic showing biomedical replacements, indicating ceramic components: dental crown and a hip prosthesis [7]

Summarizing, mainly three discoveries/strategies have stimulated the recent research on laminates: the possibility to increase the work of fracture by alternating porous thin layers that induce deflections and bifurcations in the crack path [14], the existence of a threshold strength in strong bond laminates with notably engineering applications [15] and finally, the chance to shield the surface of brittle layers by introducing compressive stresses [16].

This work will focus on the last strategy, to introduce compressive stresses in the material. The idea is simple, by introducing surface compressive residual stresses in a material, we are also reducing the level of tensile stresses in service and therefore protecting the material. Ceramic components that experience near-surface tensile stresses under contact loading, such as balls and rollers in bearings, cam followers, seals and die liners, are the most likely to benefit from surface compression. So far, it is well documented in the literature that through this technique multilayer structures improve in strength, toughness and wear, among others [17].

This work concerns one of the most popular systems in the literature [18]: an alumina/ alumina-zirconia composite laminate, processed by tape casting. Similar laminates were well characterized in the last time [17, 19]. These laminates, when the external/outer layers are made of alumina, as it will be in our case, present compressive stresses in the surface since alumina has a lower thermal expansion coefficient than any alumina-zirconia composite (a more in detail explanation about the origin of residual stresses is given in Chapter 4).

This thesis pretends to introduce the reader on ceramic laminates. Special attention is given onto structural aspects concerning them. An extensive introduction is given in Chapter 2.

Quantifying how much improvement is possible in terms of strength, reliability, and crack resistance are questions that we address through this work, both theoretically and experimentally. After the introductory chapters: "State of the art", "Characterization of the materials" and "Residual stresses", these topics are treated in "Toughness of multilayers" and "Strength of multilayers" separately.

The "Toughness of multilayers" (Chapter 5) is studied since the presence of an R-curve is expected. As it will be explained it is in reality an "apparent R-curve" which can induce some stable crack propagation but only for some range of crack lengths. The main difference to monolithic materials is that in laminates, the toughening is a function of the crack length and not of the crack extension. Two mathematical methods were used to perform calculations on apparent R-curves: the weight function method and the material forces approach.

Lastly, "Strength of multilayers" (Chapter 6) exposes the applicability of Weibull's theory to layered brittle materials. Strength distributions are analytically calculated for materials presenting R-curves and apparent or effective R-curves, its deviation from Weibull's theory is commented.

1.1. Introductory literature

[1]   Evans, A. G., "Structural Reliability: A processing-dependent phenomenon", Journal of the American Ceramic Society, **65**, 127-137, (1982).

[2]   Simon, R., Danzer, R., "Oxide fiber composites with promising properties for high-temperature structural applications", Advanced Engineering Materials, **8**, 1129-1134, (2006).

[3]   Becher, P. F., Hsueh, C. H., Angelini, P., Tiegs, T. N., "Toughening behavior in whisker-reinforced ceramic matrix composites", Journal of the American Ceramic Society, **71**, 1050-1061, (1988).

[4]   Trusty, P. A., Yeomans, J. A., "The toughening of alumina with iron: Effects of iron distribution on fracture toughness", Journal of the European Ceramic Society, **14**, 495-504, (1997).

[5]   Zhou, B. L., "The biomimetic design of worst bonding interface for ceramic matrix composites", Composite Engineering, **5**, 1261-1273, (1995).

[6]   Wang, C., Huang, Y., Zan, Q., Zou, L., Cai, S., "Control of composition and structure in laminated silicon nitride/boron nitride composites", Journal of the American Ceramic Society, **85**, 2457-2461, (2002).

[7]   Lawn, B., "Ceramic-based layer structures for biomechanical applications", Current opinion in Solid State and Materials Science, **6**, 229-235, (2002).

[8]   Orlovskaya, N., Lugovy, M., Subbotin, V., Rachenko, O., Adams, J., Chheda, M., Shih, J., Sankar, J., Yarmolenko, S., "Robust design and manufacturing of ceramic laminates with controlled thermal residual stresses for enhanced toughness", Journal of Materials Science, **40**, 5483-5490, (2005).

[9]   Amateau, M. F., Stutzman, B., Conway, J. C., Halloran, J., "Performance of laminated ceramic composite cutting tools", Ceramics International, **21**, 317-323, (1995).

[10]   Atkinson, A., Selçuk, A., "Residual stress and fracture of laminated ceramic membranes", Acta Materialia, **47**, 867-874, (1999).

[11]   Bruno, S., Swanson, D., Burn, I., "High performance multilayer capacitor dielectrics from chemically prepared powders", Journal of the American Ceramic Society, **76**, 1233-1241, (1993).

[12]   Iwanaga, S., Fujita, T., Iwamura, R., Yokono, H., Ueno, S., Suzuki, S., "Fabrication process of air-fuel ratio sensor by using the green sheet laminating materials" in: Blum, J., Cannon, W. Advances in ceramics. American Ceramic Society, **19**, 49-68, (1987).

[13]   Behrens, G., Heuer, A., "Microstructural characterization of cofired tungsten-metallized high-alumina electronic substrates", Journal of the American Ceramic Society, **75**, 2815-2824, (1992).

[14]   Clegg, W. J., Kendall, K., Alford, N. M., Button, T. W., Birchall, J. D., "A simple way to make tough ceramics", Nature, **347**, 455-457, (1990).

[15]   Rao, M., Sanchez-Herencia, J., Beltz, G., McMeeking, R. M., Lange, F., "Laminar ceramics that exhibit a threshold strength", Science, **286**, 102-105, (1999).

[16]   Sglavo, V. M., Paternoster, M., Bertoldi, M., "Tailored residual stresses in high reliability alumina-mullite ceramic laminates", Journal of the American Ceramic Society, **88**, 2826-2832, (2005).

[17]   Toschi, F., Melandri, C., Pinasco, P., Roncari, E., Guicciardi, S., de Portu, G., "Influence of residual stresses on the wear behavior of alumina/alumina-zirconia laminated composites", Journal of the American Ceramic Society, **86**, 1547-1553, (2003).

[18]   Gee, I., Dobedoe, R., Vann, R., Lewis, M., Blugan, G., Kuebler, J., "Enhanced fracture toughness by ceramic laminate design", Advances in Applied Ceramics, **104**, 103-109, (2005).

[19]   Tarlazzi, A., Roncari, E., Pinasco, P., Guicciardi, S., Melandri, C., de Portu, G., "Tribological behaviour of Al_2O_3/ZrO_2-ZrO_2 laminated composites", Wear, **24**, 29 - 40, (2000).

Chapter 2. State-of-the-Art

This chapter briefly overviews the state of the art in ceramic multilayers. Specifically, outlining the way they are processed, addressing some structural problems that may appear due to the existence of residual stresses and giving criteria how to overcome them. Strategies in designing reliable layered architectures are compiled together. Those situations in which they are more convenient are introduced.

Later, focus is given exclusively on a specific family of multilayers, those that present compressive surface stresses. For these laminates, an overview is given about the influence of compressive residual stresses on mechanical properties.

2.1. Processing routes for laminate structures

Several alternatives exist to produce a laminate. The most suitable procedure to be followed is dependent on the materials, thickness of the layers, number of layers, etc. that will define the laminate. In order to enhance the structural response of laminates, several approaches have been considered. It should be noted that some of the strategies cannot be followed with all the processing routes as it will be shown in this chapter.

The general trend is the utilization of a slurry (casting techniques) for the production of green sheets, subsequently assemblage by thermocompression and later sintering. Components with complex geometries can be produced by lamination of tapes. Simple unstructured tapes are laminated by common thermal compression. However, structured tapes have to be joined by pressureless processes using e.g. gluing agents as lamination aids because deformation of the structures would occur. Additionally, some surface machining is certainly necessary to avoid sharp borders that induce internal stresses.

Thus, lamination of green tapes is the first significant step in the manufacture of layered ceramic structures. First developed for multilayer capacitors, this technique has become the basis for the production of integrated circuits packages. Furthermore, it has become increasingly important for structural applications such as heat exchangers, for functional applications like solid oxide fuel cells and for rapid

prototyping by lamination. Nowadays, efforts turn towards the development of slurries that do not involve environmental unfriendly emissions (water-based slurries) and the development of adhesive films to place between adjacent layers during the lamination process as a way to minimize the pressures and temperatures employed during processing. Dilatometric and sintering kinetics curves are of great interest for the development of adequate slurries [1].

The literature presents a great variety of ways to make green tapes based on ceramic powders. Probably, the most popular being tape casting [2-11]. Other techniques are: rolling that provides a higher green density and a lower amount of solvent and organic additives than tape casting [12-16], slip-casting [17-19], gel-casting [20, 21], centrifugal casting [22-24], or cold extrusion [25]. Also aqueous electrophoretic deposition, a powerful technique for the synthesis of laminar microcomposites with minimum layer thickness as low as 2 µm and interface smoothness in the sub-micrometer scale has been considered [26-29]. Complex shapes can be fabricated by this technique and it is more adequate for a high number of layers. Direct pressing powders can be used when reaction bonded between layers is expected [30], or for three-layer laminates [31].

Table 2.1: Comparative between alternative routes to build-up a multilayer.

process	€	thickness range	number of layers	geometry	green density
direct pressing	€	> 100 µm	3	very simple	***
rolling	€€	> 100 µm	small	simple	***
tape casting	€€€	> 5 µm	small	simple	**
slip casting	€€€	> 50 µm	small	simple	**
electrophoresis	€€€€	> 2 µm	high	complex	-

In the following attention is devoted to tape casting as it is the most frequently used technique, and the procedure followed to process the specimens that concern this doctoral work.

2.1.1. Tape casting

In general, the slurry composition must be defined for each material. It is not an easy task as the slurry is made of several components. In brief, ceramic powders, solvents, surfactants, binders, and plasticizers are necessary [3], but it is also true that occasionally, a substance can support two functions.

A short description is given here about the function of the different components [3]. Being tape casting a "fluid forming process", the mechanical fitting of the powder

into a two-dimensional sheet requires that the powder behave as a fluid. To achieve this degree of formability, a *solvent* is necessary.

The *surfactants* (SURFace ACTive AgeNT) are additives that actively modify the particle surface to impart a desired characteristic, such as lower surface charge, higher surface charge, high/low surface energy, or specific surface chemistry. In particular, the *deflocculants* play an important role. The deflocculants work in the system to keep particles apart, what facilitate that the binder can coat later the particles individually, maintain a moderate viscosity after binder addition and decrease the amount of solvent (cheaper, faster dry and less shrinkage).

The *binder* supplies the network that holds the entire chemical system together for further processing. Essentially, green ceramic tape is a polymer matrix impregnated with a large amount of ceramic material. The binder has the greatest effect on such green tape properties as strength, flexibility, plasticity, laminability, durability, toughness. Finally, *plastizicers* refer to just about anything that makes the tape more bendable, since most of the polymeric binders used for forming tapes form a relatively strong, stiff, and brittle sheet.

Sometimes a *pore forming agent* (a pyrolysable component) is added in the slurry since porous layers may attract cracks and cause serious crack deflection. Normally polymethyl methacrylate [32], polyamides [33] or diverses starches [34] are used. If the pore forming agents particles are sufficiently large, thermodynamically stable pores are formed after burnout that shrink by the same amount as the ceramic material surrounding them.

As an example, components of a typical slurry are listed in Table 2.2.

Table 2.2: Composition of the tape casting slurries.

component	example
ceramic powder	alumina, zirconia, …
solvent	methyl ethyl ketone (MEK), MEK/anhydrous ethanol azeotropic, …
dispersant	stearic acid, glycerol trioleate, …
binder	vinyls (polyvinyl butyral), acrylics, celluloses,…
plasticizer	phthalates, glycols, glycerol, …

A classic flow chart for the production of laminates by tape casting is sketched in Figure 2.1. It gives an orientation about the necessary time during each step. It is clear that the duration of the process is given by the slow burn out of the organic additives.
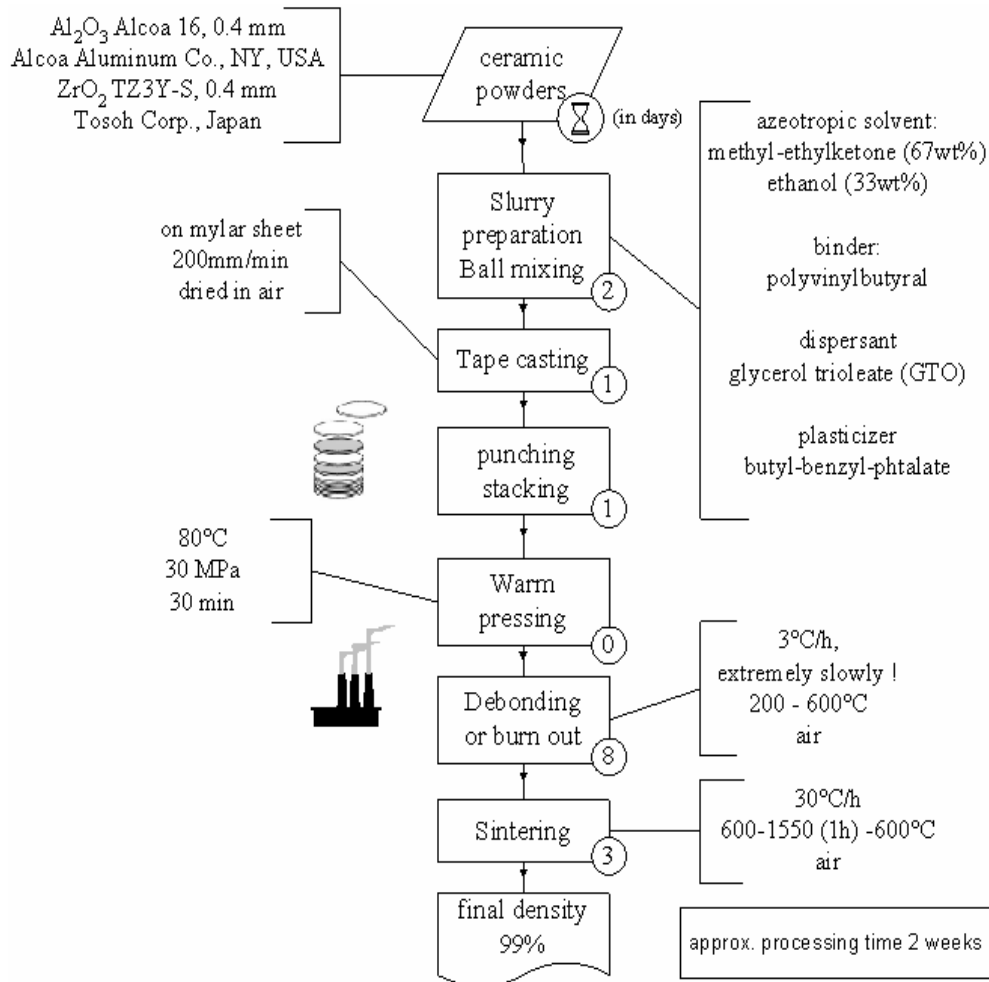
Figure 2.1. Sketch of the process of a layered structure by tape casting.

2.2. Residual stresses

Despite the recent advances on laminates manufacture, cracks are at this point unavoidable in many designs due to the existence of residual stresses. Thus, residual stresses are explained in the following.

When two layers are strongly bonded, residual stresses result from the different properties of the materials in the layers. Their nature and magnitude depend on numerous physical constants including coefficient of thermal expansion (CTE), Young's modulus, Poisson's ratio among others. In addition, the magnitude of the residual stress can be tailored by adjusting the architecture, i.e. the thickness of the different layers [35].

Diverse strategies are recognized to introduce internal stresses in a multilayer. Most of them are based on the existence of a strain mismatch between adjacent layers that

arise during cooling from sintering temperature. For instance, joining materials with a thermal coefficient mismatch [36], or joining layers where one of layers experiences a phase transformation that induce a volumetric change [37], or a multilayer in which an increase in the molar volume appears because of a chemical reaction [38].

One of the more popular ideas is to alternate layers of stabilized zirconia with a zirconia that transforms from the tetragonal to monoclinic phase with a volume expansion [38]. The magnitude of this transformation can be easily controlled by adding small amounts of stabilizers (Y_2O_3 or CaO), among others. It has the advantage of compatibility between layers, but it can be only applied to those materials that undergo a controlled phase transformation and its benefit disappears completely for temperatures above the phase transformation temperature.

The other commonly choice is to alternate layers of one material with a composite of that one. By tailoring the composition of the composite, a desirable degree of thermal expansion misfit can be achieved. It can be applied for a wider variety of ceramics and could be used for applications at relatively high temperatures as the residual stresses disappear gradually with temperature. By this approach different systems have been addressed, Al_2O_3/Al_2O_3-ZrO_2, Si_3N_4/Si_3N_4-SiC [39], Si_3N_4/Si_3N_4-TiN [40], B_4C/B_4C-SiC [16], cordierite/cordierite-$MgSiO_3$ [41], or Cr-Al-Al_2O_3/Fe-Al-Al_2O_3 [42] are some examples. Two different materials could also be used whenever they possess a comparable thermal expansion and are chemically compatible: $Al_2O_3/AlTiO_3$ [19].

An additional cause that originates residual stresses in laminates should be discussed: as in many cases multilayers are produced by joining tapes at high temperature, a stress field may arise from a mismatch in sintering strain rates. The differential densification will place the layers in either biaxial tension or compression, leading to inhibition or enhancement of the densification. These stresses are far from being deeply understood. Basic research has been based on a linear viscous models with data obtained by cyclic loading dilatometry in an Al_2O_3/Al_2O_3-ZrO_2 composite [43]. In order to confirm the biaxial tensile stress values, an experimental approach was also applied to asymmetric composites and was successful in predicting the observed curling behavior. Even though the stress was small (in the order of 10 MPa), they were sufficient to cause a type of linear *cavitation damage*. Cavitation pores were also found to be preferred sites for the cracking that occurs during cooling. Fortunately, this can be controlled by the slurry composition. Thus, the slurries of the different layers can be designed in order to minimize the strain mismatch during densification [1].

2.2.1. Estimation of the residual stresses

Let us now analyze the case of a laminate elaborated by stacking alternatively two materials. Both materials have a different thermal expansion coefficient (CTE) that originates a residual stresses state. Besides, let us assume that the material in the outer layers (named material 1) has a lower CTE than the other material (material 2), then compressive stresses will appear in the layers constituted by the material 1 while tensile stresses are develop in the material 2 (see Figure 2.2). For simplicity, it will be also assumed that all layers of material 1 have the same thickness, and the same applies for the layers made of material 2.
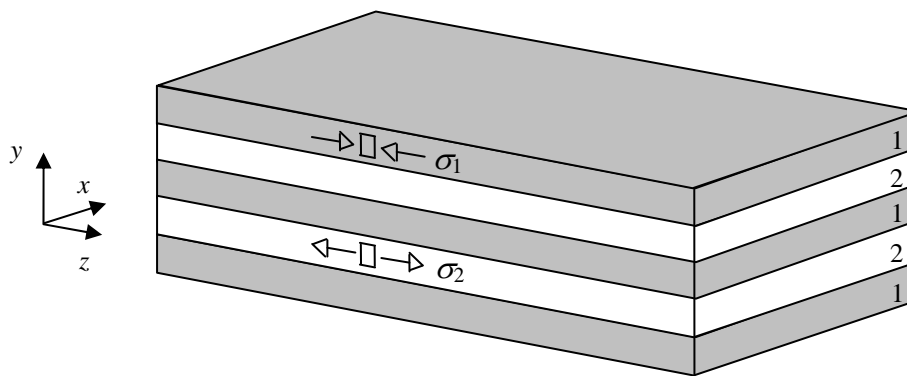
Figure 2.2: Laminate built up by stacking alternatively two materials (called 1 and 2), constituted of a total of *n* layers (in the figure *n* = 5). In this case the coefficient of thermal expansion in the material 1 is smaller than that of material 2. Compressive stresses appear in the layers made of material 1 and tensile stresses in the layers made of material 2.

In practice, the order of magnitude for the CTE mismatch, $\Delta\alpha = \alpha_2 - \alpha_1$, between adjacent layers is normally about $1 \cdot 10^{-6}$ /°C. This value is an experimental recommendation since a higher mismatch could lead to some unwanted relaxation phenomena like delamination (during processing) or cracking (in service).

A rough estimation of the strain, $\Delta\varepsilon$, that this mismatch induces during cooling upon sintering, can be given as follows,

$$\Delta\varepsilon = \Delta\alpha \cdot \Delta T \approx 1 \cdot 10^{-6}\,°\mathrm{C}^{-1} \cdot 10^{3}\,°\mathrm{C} \approx 1 \cdot 10^{-3} \ , \qquad\qquad \textbf{Eq 2.1}$$

where ΔT is the range of temperature in which the stresses develop. It is of the order of thousand Kelvin. The corresponding residual stress is determined from Hooke's law

$$\sigma = E\,\Delta\varepsilon = 1 \cdot 10^{12}\ \ 1 \cdot 10^{-3} \approx 1 \cdot 10^{9}\,\mathrm{Pa} = 1\,\mathrm{GPa} \ , \qquad\qquad \textbf{Eq 2.2}$$

where Young's modulus E has been considered to be about 100 GPa. In the literature realistic values up to 2 GPa ($2 \cdot 10^9$ Pa) have been found without showing problems with the structural integrity [44].

More precise analytical approximations for the residual stress field of the laminate are given by Zhang [45, 46] and earlier by Öel [47]. They are presented in Annex I. Zhang considers the layers as linear elastic and strongly bonded with each other, the residual stress appears due to both a thermal coefficient mismatch and an elastic mismatch and it is obtained through the derivation of the force balance and the momentum balance. Zhang's study presented two solutions, one for a plane strain analysis and the other in plane stress conditions.

The Öel's approximation is a special case of Zhang's solution. It is often found in the literature. It is based on the force balance of a semi-infinite symmetrical laminate. It gives a simplified plane strain solution for a laminate built-up by stacking alternatively two materials.

Öel's solution for the laminate shown in the Figure 2.2 is given in Equation 2.3 and Equation 2.4. It evidences how the architecture (t_1 and t_2) and the elastic constants define the internal stresses.

$$\sigma_1 = -\frac{\Delta\varepsilon\, E_1'}{1 + \dfrac{(n+1)}{(n-1)}\dfrac{t_1}{t_2}\dfrac{E_1'}{E_2'}} \quad \text{and} \qquad\qquad \text{Eq 2.3}$$

$$\sigma_2 = -\sigma_1\frac{(n+1)}{(n-1)}\frac{t_1}{t_2} \quad , \qquad\qquad \text{Eq 2.4}$$

where $E_i' = E_i/(1-v_i)$ is defined by the elastic constants: E, the Young's modulus, and v, the Poisson's ratio, n is the number of layers, and t_1 and t_2 represent the thicknesses of the layers of material 1 and 2 respectively. Equation 2.3 and Equation 2.4 will be referred in the next sections to explain how the structural integrity depends on the internal stresses, and how, in general, they affect the mechanical properties.

The influence of the architecture – for instance the thickness of the layers - on the residual stress state results evident from Equation 2.3 and 2.4, and thus, there is a chance to tailor the stress field with the architecture. It is worth of note that the architecture is present by the thickness ratio (t_1/t_2). It should be noticed that the

residual stress is independent of the overall thickness of the specimen for a given number of layers n.

So far, the practical importance of the tensile residual stress developed in the layers made of the material with a higher coefficient of thermal expansion (material 2) has not been outlined. The magnitude of this tensile stress is given by σ_2. In general, tensile residual stresses have acquired a bad reputation because of their pernicious influence on mechanical properties, but in the case of laminates, they are easier to control as they are confined into a layer and their magnitude is well-defined by Equation 2.3 and 2.4. As it will be shown later, there exist also highly localized tensile stresses at the edges that could affect the structural integrity. These stresses are the origin of edge cracking.

An interesting situation that demonstrates this point is the mathematical limit $t_2 >> t_1$, in which the layers of the material 2 are much thicker than the layers constituted by the material 1. Then, the Equation 2.3 and Equation 2.4 are reduced to $\sigma_2 \longrightarrow 0$ and $\sigma_1 = -\Delta\varepsilon\, E_1'$. It means that the tensile stress σ_2 can be reduced importantly while keeping a high level of compressive stresses in the layers with thickness t_1. On the other hand the limit $t_1 >> t_2$, is not so interesting since it results in a high level of tensile stresses without keeping an interesting level of compressive stresses ($\sigma_1 \longrightarrow 0$ and $\sigma_2 = \Delta\varepsilon\, E_2'$).

The above approximations have a good accuracy for our purposes but realistic stress fields differ from these solutions of Equation 3 and Equation 4 especially at the free surfaces, while in the bulk they are consistent. These solutions do not consider variations of the stress field through the thickness but this variation is of relative importance as demonstrated by finite element calculations [48], or experimentally using a piezospectroscopic technique based on the photostimulated fluorescence from trace Cr^{3+} in alumina [49, 50].

At a first sight, it may appear simple to maximize the compressive stress with the architecture and thus obtaining the best mechanical performance by hindering crack propagation. However, a number of failure mechanisms are associated to very thin compressive layers that may limit the magnitude of the residual stresses which are present in the laminate. These failure mechanisms either will critically damage the laminate or will relax the stresses to an uninteresting level.

2.3. Structural integrity of ceramic multilayers

The expected benefits on mechanical properties derivated from the existence of compressive stresses are not easy to achieve in multilayers, since some problems can appear during processing or in service. At present four types of crack extension mechanisms have been identified. They are relatively well understood and criteria to avoid them have been developed.

The four crack patterns that could affect the integrity of a layered component are sketched in Figure 2.3: tunnel cracks [51-53], edge cracks [23, 54, 55], bifurcations [23, 54, 55], and delamination [29]. Strong deflection is assumed to be part of bifurcation.
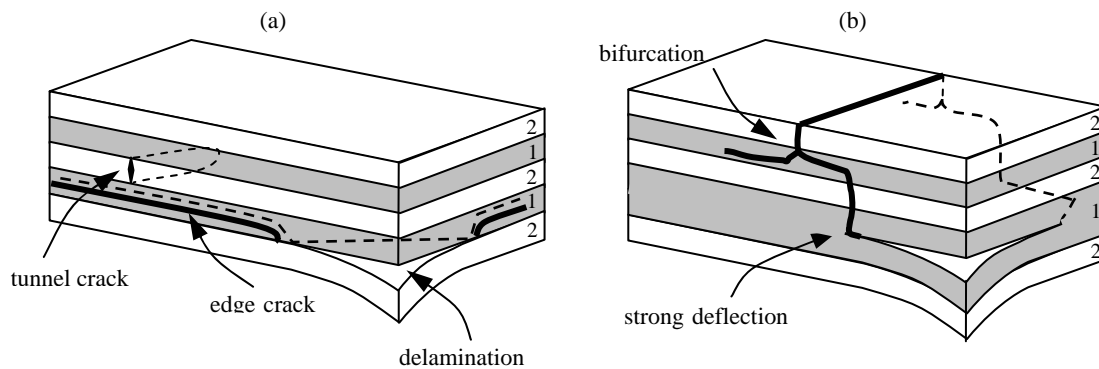
Figure 2.3: Sketch of kinds of cracks in laminates: a) tunnel crack, b) edge crack, c) bifurcation crack and d) delamination. Strong deflection is part of bifurcation.

A brief introduction on them together with design criteria to avoid them is presented in the following.

2.3.1. Tunneling (tensile cracking)

Tunnel cracks are perpendicularly oriented to the interfaces due to the existence of a tensile stress (see Figure 2.3). They do not only come to existence during cooling upon the sintering temperature but also at high temperatures during heating if a significant densification mismatch exists. In the first case the crack opening at room temperature is narrow and the crack borders are not sintered [51]. In the second case the crack opening at room temperature is wider and traces of sintering (rounded grains) can be detected [51]. Tunnel cracks may cross the tensile layer and damage the adjacent compressive layers. Normally an isolated crack is not found but a network of tunnel cracks that could even interact [56]. In general if a tunnel crack exists, the

13

laminate structure may redistribute the stresses internally and survive to high stresses without undergoing catastrophic fracture as shown by De Portu et al. [53] (by means of fluorescence piezo-spectrosocopy). But for some applications, such cracks can evidently either fail the device or degrade the material. For example, tunnel cracks in multilayer capacitors may form easy conducting paths, leading to an electrical leak.

A fracture mechanical analysis can be used to derive the stress necessary to nucleate a tunnel crack from a pre-existing flaw in a tensile layer. Here is shown the solution as derived by Ho and Suo [23, 52]. Tunnel nucleation is a complicated process. The nature of the pre-existing flaws plays a predominant role. Here the pre-existing flaw is taken to be a penny-shaped crack of initial diameter a_0 in the xy-plane. At the beginning the crack grows self-similar until it touches the interfaces. Then it becomes noncircular and propagates in the x-direction.
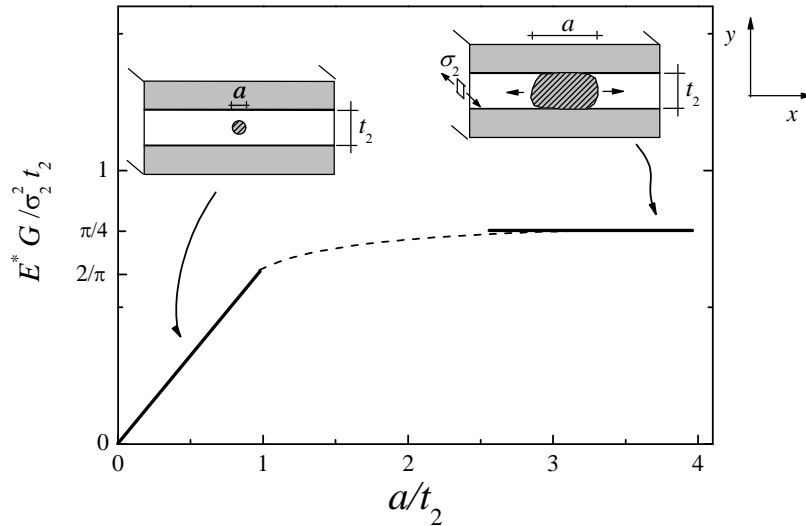
Figure 2.4: Normalized energy release rate for a penny-shaped crack that propagates through the layer thickness (in the xy-plane) until it reaches the adjacent layers. After touching the interfaces, the crack is confined by the adjacent layers. The crack becomes noncircular and propagates in the x-direction [52].

Let a be the current size of the crack (see Figure 2.4). When $a/t_2 < 1$, the growing crack remains penny-shape, since the energy release rate is the same at every point along the front. This energy release rate is given by Tada [57]

$$G = \frac{2}{\pi} \frac{\sigma_2^2 a}{E^*} \ ,$$

Eq 2.5

with $E^* = E/(1-\nu^2)$, E and ν being Young's modulus and Poisson's ratio. The straight line in Figure 2.4 (left side) corresponds to Equation 2.5 up to $a/t_2 \approx 1$. After touching the interfaces, the crack becomes noncircular and Equation 5 does not describe the

crack behavior for $a/t_2 > 1$. The crack will finally become a long tunnel (it grows in the x-direction) and reaches a steady-state that can be described [52] by:

$$G = \frac{\pi}{4} \frac{\sigma_2^2 \, t_2}{E^*}$$

Eq 2.6

This result is indicated in Figure 2.4 as the asymptotic value for $a/t_2 \to \infty$.

Observe in the Figure 2.4 that the solutions for the two limiting cases, $a/t_2 = 1$ and $a/t_2 \to \infty$, differ only by 23%. Consequently, for practical purposes, the tunnel attains the steady-state almost as soon as $a/t_2 \sim 1$. Now consider a brittle layer without subcritical cracking mechanism, but with a well-defined fracture energy J_c, that is the crack will grow if $G \geq J_c$. For a thin bond layer, where the pre-existing flaws are on the order of one layer thickness, one finds that the critical stress to maintain tunnel growth is (where Equation 2.6 has been used with $G = J_c$),

$$\sigma_2^* = \sqrt{\frac{4 J_c E^*}{\pi \, t_2}}$$

Eq 2.7

This critical stress is well defined: no knowledge of flaw geometry or microstructure is needed. It is conservative: a flaw, regardless of its initial size or shape, cannot grow into a long tunnel if the applied stress is below σ_2^*. Observe that the critical stress, σ_2^*, is governed by the layer thickness; the thinner the layer is the higher σ_2^* is. For example, this has motivated the conception of microlaminates, consisting of alternate metal and ceramic, each layer submicron thick, fabricated by a variety of thin film deposition techniques [23].

Consequently, the critical stress derived from G (during tunneling) can serve as a well-defined, conservative design criterion for avoidance of tunnel cracks in brittle thin layers,

$$t_2^* = \frac{4 J_c E^*}{\pi (\sigma_2^*)^2},$$

Eq 2.8

or in terms of fracture toughness

$$t_2^* = \frac{4 K_c^2}{\pi (\sigma_2^*)^2}.$$

Eq 2.9

2.3.2. Edge cracks

It is well known that the residual stresses at the free surface of laminate materials differ from the bulk stress state. In the compressive layer a biaxial compressive stress state exists in the bulk ($\sigma_x = \sigma_z \neq 0$, $\sigma_y = 0$). At the surface a tensile stress component exists $\sigma_y \neq 0$ but the other primary stresses are zero: $\sigma_x = 0$, $\sigma_z \approx 0$ (see Figure 2.5a). Analytical models [51, 58] as well as finite element analyses (see chapter 4) show this fact. This tensile stress component is highly localized, decreasing rapidly away from the surface to become negligible at a distance approximately on the order of the layer thickness.

In the tensile stressed layer, the sign of the stress component in the bulk as well as at the surface is vice verse to that of the compressed layer. This reversal of stresses has also been observed during the analysis of inclusions located either within a body or at the surface [59, 60]. These tensile stresses can naturally cause extension of pre-existing cracks along the center line of the compressive layer (see Figure 2.5b). If pieces are cut out of the layered structure and if the tensile stresses are high enough, edge cracks appear again at the new surfaces.
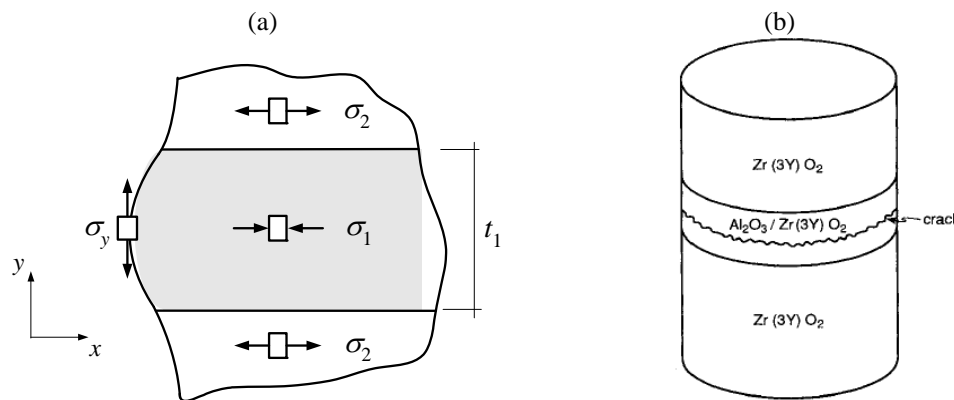
Figure 2.5: (a) Compressive layers (as well as the tensile layers) show a reversal of stress at the free surfaces in a direction perpendicular to the interfaces (σ_y). (b) This can cause extension of pre-existing crack-like flaws at the surface, especially at the center of the compressive layer where this stress reaches its maximum [23].

Ho et al. [23] estimated the tensile surface stresses in the compressive layers considering a thin layer of material 1 (in biaxial compression, thickness t_1) bonded by two identically much thicker layers of material 2 (in tension, thickness t_2). They assumed that the two materials have different thermal expansion coefficients but identical elastic constants and that $t_1/t_2 \to 0$ ($\sigma_2 = 0$ from Equation 2.4).

Consequently at a lower temperature, the area of the less expanding material (material 1) will be larger than that of material 2. Under these hypotheses the stress state can be obtained analytically as the solution of two problems (see Figure 2.6):

1. tearing homogeneously the slab of material 1 to the same size of the rods of material 2 (see Figure 6, center), and
2. add compressive surface stresses of the amplitude of the tensile tearing stresses to get a vanishing total stress component perpendicular to the surface (see Figure 2.6, right)
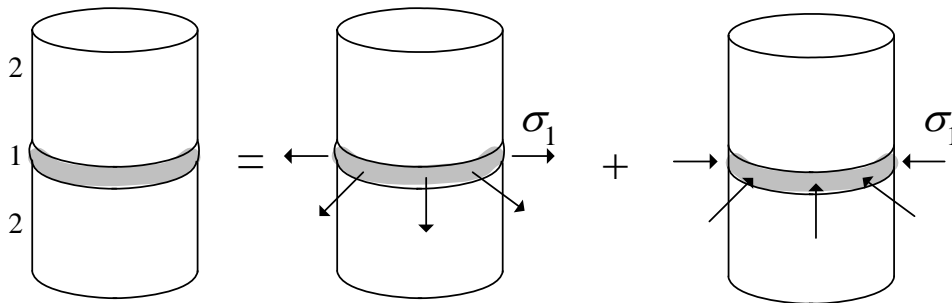
Figure 2.6: The residual stress problem is solved by superposition of two simple stress states. In the first problem the layers are free one of each other and there is a traction of magnitude σ_1 applied at the edge of the thin layer to get the same diameter after cooling in both cases. In the second problem the layers are connected and a tensile traction of magnitude σ_1 is applied to the thin layer [23].

The stress distribution in the first problem is trivial: the two thick layers are stress-free, and the thin layer is under biaxial compression of magnitude σ_1:

$$\sigma_1 = -\Delta\varepsilon\, E_1' \ ,$$

$$\text{Eq 2.10}$$

from the limit $t_1/t_2 \to 0$, in the Equation 2.3.

The second problem is readily solved by integrating the solution for a point force on a free surface over the band where the tractions are applied [61].

By superposition of both solutions σ_y yields,

$$\sigma_y(x)\big|_{y=0} = \frac{2}{\pi}\left[\theta - \frac{1}{2}\sin 2\theta\right]\sigma_1$$

$$\text{Eq 2.11}$$

where $\theta = \tan^{-1}(t_1/2\,x)$.

This stress field is shown in the Figure 2.7.
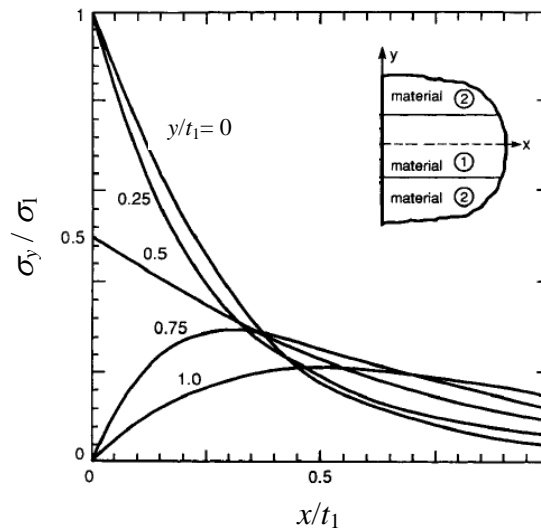
Figure 2.7: Distribution of the normalized stress component $\sigma_y(x,y)$ near the edge. Equation 2.11 is labeled as $y/t_1 = 0$. The elastic mismatch in this solution is assumed to be zero [23].

In the case that an edge crack forms, again two situations must be considered regarding crack extension (see Figure 2.8): one, the extension of a pre-existing crack into the thin layer to a depth a in the x-direction (*edging*), and second, the extension of a crack of depth a along the center line of the thin layer in the $\pm z$-direction (termed *edge channeling* or just *channeling*).
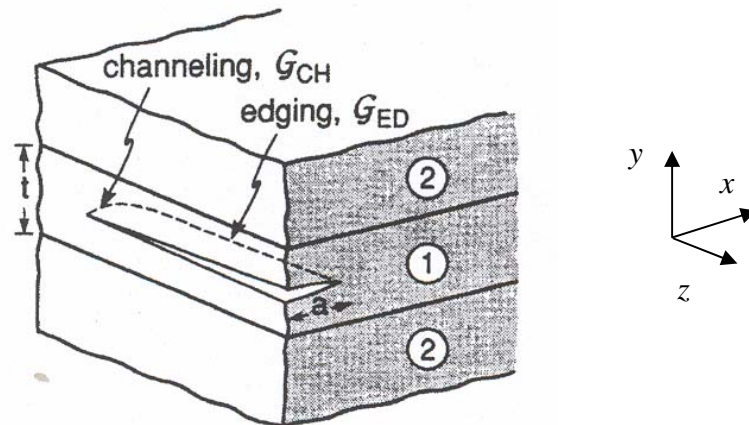
Figure 2.8: Channeling crack (running in $-z$-direction) and edging crack (running in x-direction) in a compressive layer with surface tensile stresses.

The strain energy release rate, G_{ED}, for an edge crack propagating in the x-direction is given by [23]

$$\frac{G_{ED} E^*}{\sigma_1^2 t_1} = \pi \frac{a}{t_1} s^2 \left\{ 1.122 - (1-s) \left[0.296 + 0.25 \, s^{3/4} (0.75-s) \right] \right\}^2 \, , \qquad \textbf{Eq 2.12}$$

where s is defined by

$$s = \frac{2}{\pi} \tan^{-1} \left(\frac{t_1}{2a} \right) \, , \qquad \textbf{Eq 2.13}$$

(see Figure 2.9).

If the critical strain energy release rate of the thin layer material is G_c, then for crack propagation to occur, $G_{ED} \geq J_c$. The strain energy release rate for channeling (crack propagation in the z-direction), G_{CH}, can be computed by integrating G_{ED}, [23]

$$G_{CH} = \frac{1}{a} \int_0^a G_{ED} \, da \, . \qquad \textbf{Eq 2.14}$$

The solution is presented in Figure 2.9.
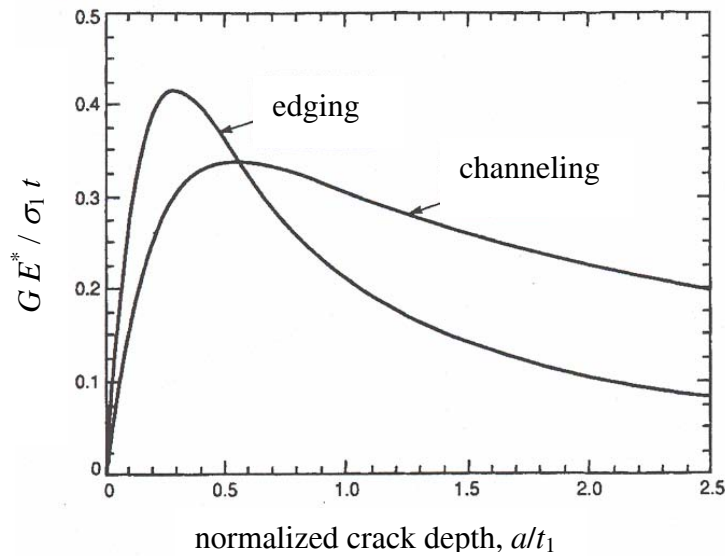
Figure 2.9: The energy release rates of edging G_{ED} and channeling G_{CH} vary with the normalized crack depth a/t_1. Elastic mismatch is assumed to be zero.

At $a = 0.55 \, t_1$, the G_{CH} function reaches its maximum value (see Figure 2.9)

$$\left(G_{CH} \right)_{max} = \frac{0.34 \, \sigma_1^2 t_1}{E^*} \, . \qquad \textbf{Eq 2.15}$$

19

Consequently, for a given layered material cooled to a prescribed temperature, there exists a critical thickness, t_1^*, below which channeling cannot occur:

$$t_1^* \leq \frac{J_c E^*}{0.34\, \sigma_1^2} \quad .$$

Eq 2.16

As the stress increases during cooling and reaches the level determined by Equation 2.16 (using the identity), a single flaw on the surface, of size around $a = 0.55\, t_1$, will be activated to channel into the layer. If the preexisting flaw is much smaller, larger stresses need to develop before the crack spontaneously extends to a greater depth and then channels into the layer. After channeling has occurred once, the crack can extend to greater depths as the temperature drops further. Because G_{ED} diminishes for large depths, the crack can stabilize at a larger depth.

2.3.3. Bifurcation

In laminates bifurcation may occur when a crack runs perpendicular to the interfaces. Bifurcation is associated with strong 90° deflections (see Figure 2.10). In many occasions bifurcation is associated with weak interfaces [34, 62] but it may also happen in the middle of a compressive layer [63]. In the first case an essential point for the mechanism is the matrix/interface strength ratio. Note that in this case the presence or absence of internal stresses is not a necessary condition for the operation of this mechanism. The presence of weak interfaces transverse to a growing crack causes the crack to be deflected with a consequent increase in the crack growth resistance.
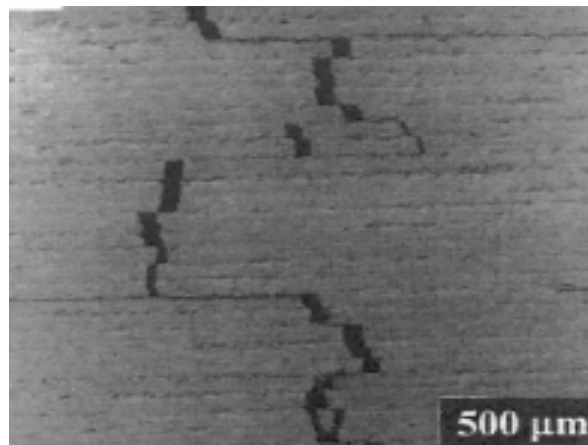
Figure 2.10: Crack propagating path in laminated Si_3N_4/BN composites showing crack bifurcation and deflection through weak BN interlayers [15].

In the second mechanism, cracks are bifurcated along the centerline of layers under high biaxial compressive stresses (see Figure 2.11). This phenomenon appears to be directly related to *edge cracking* (see Section 2.3.2) due to the fact that a crack propagating across a laminate results in the formation of a new free surface. In the vicinity of these free surfaces the residual stress distribution is altered especially at the crack tip. In the compressive layer, the localized stress state near the free surface created by the crack will be opposite in sign to the residual biaxial compressive bulk state. The stress redistribution can result either in small deflection or even bifurcation if the compressive stresses are large enough. On the other hand, if the residual stresses are negligible, of course, a straight fracture path will be observed.
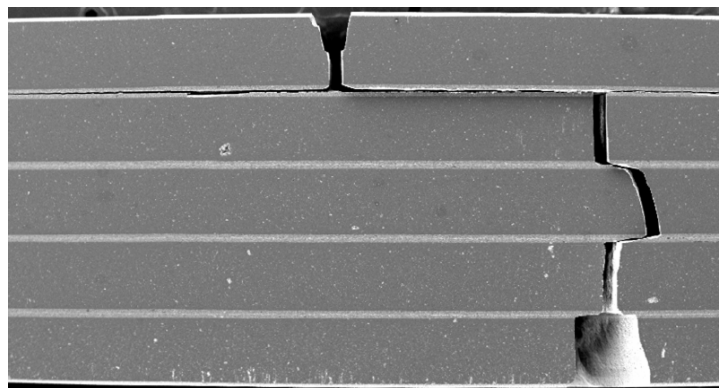
Figure 2.11: Typical bifurcations/deflections observed after the crack meets a layer with high enough compressive stresses. In the micrograph the initial flaw is an artificial notch at the top of the micrograph [64].

This bifurcation causes a toughening of the layered structure. It has been used to design laminates with increased energy-consuming fracture behavior (see Figure 2.12).
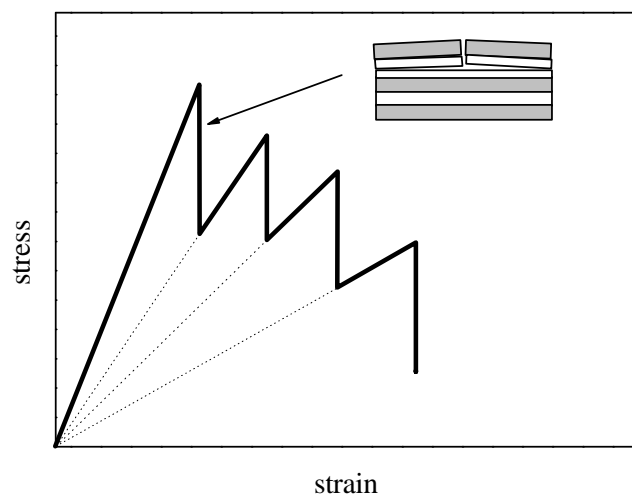
Figure 2.12: Characteristic stress-strain curve in a layered structure that presents bifurcation.

By analogy with the edge cracking phenomenon, Rao and Lange [65] have experimentally observed that bifurcation does not occur for layers thinner than a critical value:

$$t_1^* \leq \frac{J_c E^*}{0.17\,\sigma_1^2}.$$

Eq 2.17

Below t_1^* bifurcation cannot occur. Others, Lugovy et al., [66] prefer to keep the same criterion for bifurcation and for edge cracking (Equation 2.16).

It is important to note that all ceramic laminate materials that are designed to exhibit bifurcation toughening will inevitable demonstrate surface edge cracking and associated problems.

In addition, the potential to use crack bifurcation as a toughening mechanism in laminate ceramics with layers consisting of intrinsically high fracture toughness material is limited as a result of Equation 2.17. The critical compressive layer thickness necessary to produce crack bifurcation increases as the square of the compressive layer material fracture toughness ($J_c \sim K_c^2$) and is inversely proportional to the biaxial compressive stress in the layer. Therefore, for a material of fixed thickness, it is possible to increase the compressive residual stress by reducing the low CTE material layer thickness. However, for high fracture toughness composite materials, this will usually reduce the layer thickness below the critical value for crack bifurcation unless considerable care is taken.

Materials designed to exhibit crack deflection or bifurcation have also shown a propensity to fail by these mechanisms during sample machining, or even earlier during processing (in that case called delamination) [67].

2.3.4. Delamination

Delamination is understood as a spontaneous fracture during processing that is caused by the unstable propagation of edge cracks (see section 2.3.2). Delamination can be traced back to the mechanisms discussed before.

2.3.5. Concluding remark

In summary, especially interesting is the diagram presented by Hatton et al. [29] (Figure 2.13). It shows how the factor $\sigma_1^2 t_1$ is related to the fracture behavior. Three different fracture patterns were observed: brittle fracture (denoted as catastrophic), bifurcation fracture (denoted as multi-stage) and delamination during processing. The factor $\sigma_1^2 t_1$ defines the fracture behavior since the energy release rate that controls all these mechanisms is proportional to it.
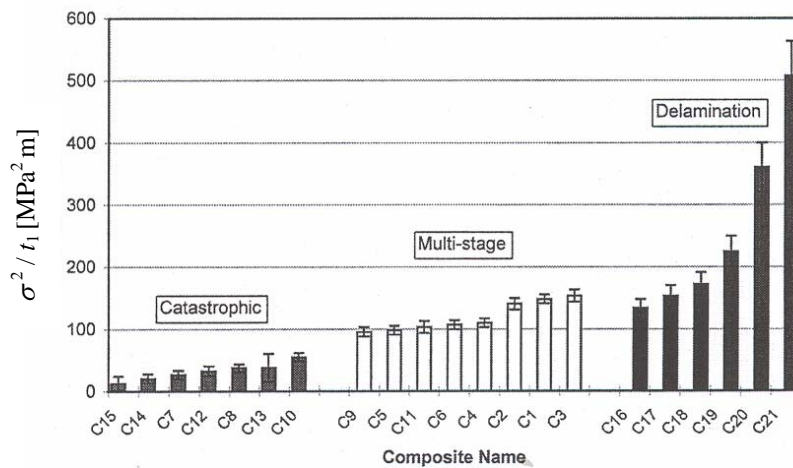
Figure 2.13: The term $\sigma^2 t_1$ is useful to characterize the fracture pattern in laminates. In the figure the calculated values of $\sigma^2 t_1$ for different composites is plotted. The corresponding fracture behavior is also indicated [29].

2.4. Strategies in designing reliable layered architectures

In designing layered damage-resistant structures, it is important to distinguish between two - sometimes mutually exclusive - philosophies: crack containment and crack prevention (this also applies to bulk structures). Virtually all the attention in the mechanics literature has focused on crack containment. The goal is to inhibit the penetration of existing cracks/flaws, either by enhancing crack deflection along weak interfaces [62] or increase artificially the toughness. The increase in toughness can be achieved mainly in two ways: by incorporating compressive stresses in the ceramic layers to inhibit transverse crack growth [36, 63], or by incorporating tough sublayers to arrest any growing crack [68].

Crack prevention is more appropriate for smaller structures where the slightest damage may provoke the end of safe function, and it is normally associated to processing.

Exceptionally, a first approach by Russo et al. [69] tried to optimize both, prevention and containment crack growth in Al_2O_3-Al_2TiO_5 trilaminates. They combined a high-strength Al_2O_3-Al_2TiO_5 fine-microstructure for short cracks (outer layers), and a high crack containment Al_2O_3-Al_2TiO_5 large-microstructure (R-curve microstructure) for large cracks (inner layer). Al_2O_3-Al_2TiO_5 composites present an exceptional flaw tolerance and improved R-curve behavior. This enhancement is obtained at the expense of strength that can be improved by refining the microstructure. This approach - in which one material presents two different microstructures attending to different design criteria - is known in the literature as "duplex microstructures".

Later experiments have demonstrated that introducing compressive stresses or deflecting/bifurcating cracks is more effective than the use of duplex structures, and it may be combined with it. The approaches/mechanisms that have been mentioned to arrest cracks in laminates will be described in the following.

2.4.1. Laminates deflecting cracks along a weak interphase or interface

The crack deflection mechanism was first observed by Clegg's group in the 1990's [34, 62, 70, 71]. Certain multilayer structures are able to deflect cracks through a weak layer or interface, thus increasing the fracture work. The deflection mechanism depends on matrix/interface strength ratio and has had varying degrees of success. Some difficulties arise that should be overcome: controlling the strength of such ceramics is technologically difficult, and furthermore weak interfaces may compromise properties such as corrosion/oxidation resistance [72].

Suitable interfacial materials are difficult to find since in addition to be weak, they must be chemically compatible with the layer materials and must be cofired at the same temperature. Graphite [70], BN [73] and $LaPO_4$ [74] have often been considered.

The most successful laminates are those in which a weak layer is made of the same material as that of the strong layers, but having a certain degree of porosity [34, 71, 75, 76] (see Figure 2.14a). This adds the advantage that any chemically incompatibility or internal stresses are avoided. To make the pore-containing interlayer, an extra pore-forming agent is included in the composition of the slurry to be sintered. This agent must be pyrolysable in such a way that it leaves pores after it is burn-out. If these pores are sufficiently large (larger than the characteristic grain size) they will remain in the microstructure after sintering. Some of the pyrolysable agents

used are: polytetrafluoroethylene [34], starches [33, 71, 77], PMMA [75] or polyamide powders [33].

An interesting alternative to obtained a porous weak layer has been proposed by Shigegaki et al. [78]. They added whiskers in the material matrix to impede densification, therefore obtaining a degree of porosity that can be controlled by the concentration of whiskers. But this approach presents a highly anisotropic shrinkage behaviour during sintering that must be understood and controlled.

Crack deflection along the weak interfaces is thought to be the major mechanism for the improvement in fracture resistance. However, bridging between layer ligaments appeared to contribute also to the fracture energy (see Figure 2.14b) [15].
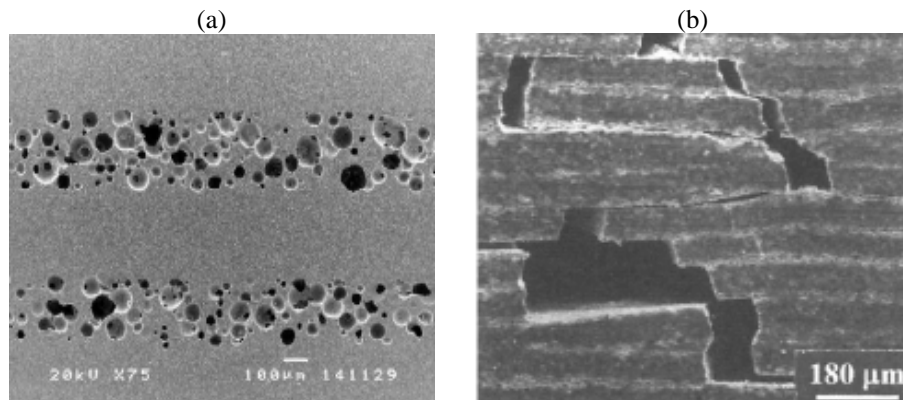
Figure 2.14: (a) Porous layer after burn-out of a polyamide [75] and (b) matrix layer pull-out [15]. Here a BN interlayer acts as weak layer.

Theoretical models proposed in the literature have predicted that if there is no elastic mismatch, the interfacial crack will not kink out of the interface when the ratio of the fracture energy of the interface, $G_{c,int}$, to that of the matrix, $G_{c,m}$ is less than 0.57 [79]. In the literature is possible to find criteria that relate the level of porosity to the existence of deflection in a weak porous layer. For example, assuming spherical pores arranged in a cubic array, a critical porosity higher than 37% would propitiate deflection [34].

Additionally, dynamic fracture properties for these porous multilayers have been measured (in a split Hopkinson bar), they exhibited similar dynamic fracture behavior like that of aluminum alloy foam [32]. Efforts have also been conducted to quantify interesting properties such as frictional sliding resistance and delamination fracture energy [74, 80].

2.4.2. Laminates with internal compressive stresses

For this family of laminates - mainly developed by Lange's group in the 1990's - a thin internal layer is capable of arresting a large crack due to a high compressive stress state. The arresting has several interesting outcomes: the first is that the laminates present a threshold strength. That means below a certain stress level the multilayer cannot fail. This threshold strength is independent of the initial flaw size that could initiate the failure at the surface [37, 44, 65, 68, 81-85] (see Figure 2.15a). Therefore, a second outcome is that laminates incorporating a inner compressive layer are more surface damage tolerant than monolithic materials. Since this phenomenon increases the damage tolerance and may allow engineers to design reliable ceramic components, they are receiving serious consideration for structural applications. The threshold strength phenomenon therefore truncates the statistical strength distribution, yielding a stress range for save operations (see Figure 2.15b).
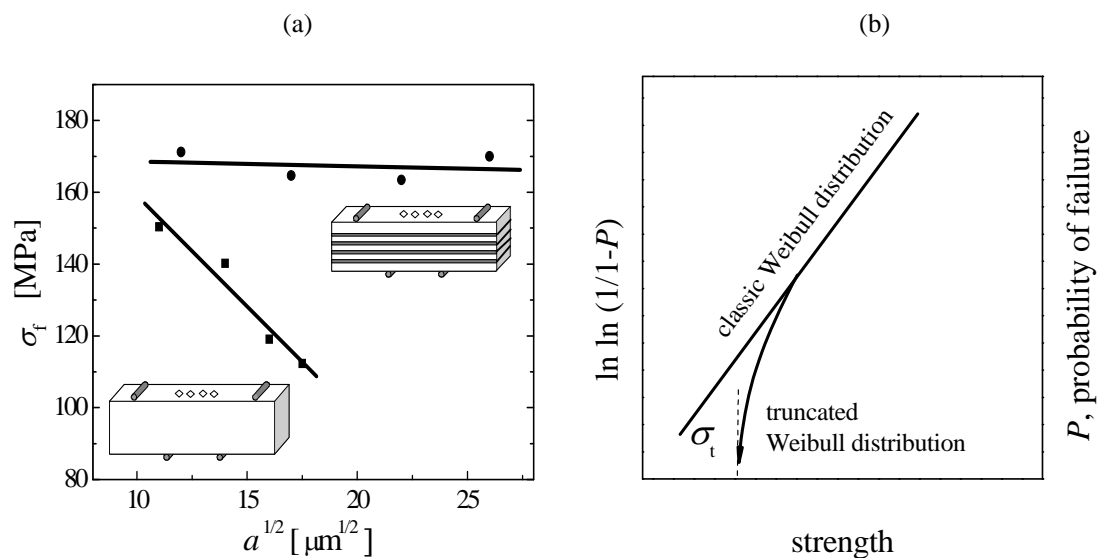
Figure 2.15: (a) Bending strength of specimens containing cracks made by indents: Monoliths are strongly influenced by the defect size but the laminates show no crack size sensitivity [86]. (b) The threshold strength σ_t truncates the typical Weibull distribution of brittle materials.

It should be remembered that the outer layers are under tension, what could also have some negative engineer implications (i.e, concerning wear resistance). The laminates are not recommended for applications in which some surface damage causes the breakdown of the component.

It can be assumed that a crack does not propagate through the composite if it bifurcates (at a weak interlayer or through the center of a compressive layer). This gives the possibility to determine the stress necessary for bifurcation. This stress is a threshold stress for strength which will be determined in the following.

The stress intensity factor, K, of the crack in the laminate shown in Figure 2.16 is determined by superimposing two stress fields. The first is a tensile stress of magnitude ($\sigma - \sigma_1$) applied to a cracked specimen that does not contain residual stresses. The second is a tensile stress of magnitude ($\sigma_1 + \sigma_2$), which is only applied across the thick layer (the portion of crack defined by t_2)
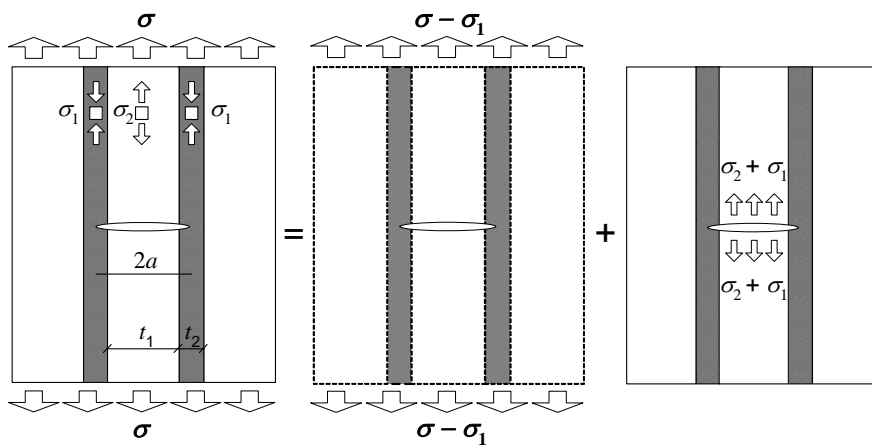
Figure 2.16: The stress intensity factor K is determined by superimposing the two stress fields.

The stress intensity factor is thus given by [68]

$$K = (\sigma - \sigma_1)\sqrt{\pi a} + (\sigma_1 + \sigma_2)\sqrt{\pi a}\left(\frac{2}{\pi}\sin^{-1}\left(\frac{t_2}{2a}\right)\right).$$ **Eq 2.18**

Assuming that failure occurs for $K \geq K_c$, K_c being the fracture toughness, Equation 18 can be rearranged in order to have an expression for the threshold strength below which the laminar body cannot fail when the tensile stress is applied parallel to the layers:

$$\sigma_t = \frac{K_c}{\sqrt{\pi\frac{t_2}{2}\left(1+\frac{2t_1}{t_2}\right)}} + \sigma_1\left[1-\left(1+\frac{t_1}{t_2}\right)\frac{2}{\pi}\sin^{-1}\left(\frac{1}{1+\frac{2t_1}{t_2}}\right)\right].$$ **Eq 2.19**

Equation 2.19 shows that the threshold strength, σ_t, scales with the fracture toughness of the thin-layer material $K_{c,1}$, the magnitude of the compressive stress σ_1, and the thickness of the compressive layer t_1.

This threshold strength calculation is only valid for cracks that propagate straight through the compressive layer without bifurcation or significant deflection. In such cases, where bifurcation is exhibited by the crack as it propagates through the compressive layer (see Figure 2.11), a greater threshold strength may be observed than predicted by the model [65]. Quantitative prediction of threshold strength in such cases is extremely complicated.

An inconvenience is that such laminates "work" in only two dimensions. Cylindrical [87, 88] and spherical laminar architectures are thus potentially more interesting than plates. At present, different authors are devising ways of forming compressive layers in the third dimension with layers that curve around one another. Two innovative alternatives have been recently explored, a three dimensional composites formed by spherical laminates [89, 90] (see Figure 17a) and a simpler technique that covers the tensile layers with a compressive layer through the thickness (see Figure 17b) [55] (interesting to avoid edge cracks). So far, the 3-dimensional structures require a complicated processing and are far from really developing successfully a threshold strength.

(a)   (b)
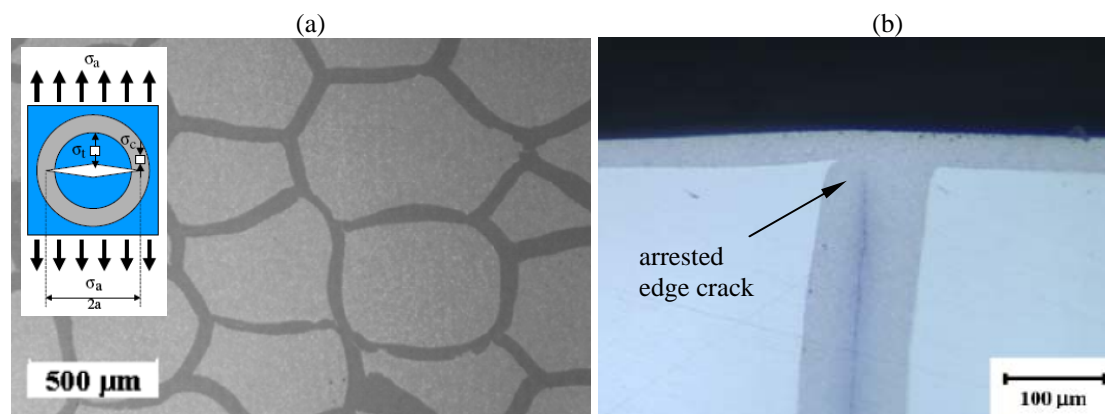
Figure 2.17: Three dimensional architectures designed to produce a threshold strength. (a) 3-dimensional spherical multilayers after [89] and (b) surface layer through the thickness after [55] (the edge crack just appeared after sectioning).

2.4.3. Laminates with surface compressive stresses

The last group of laminates includes those that possess compressive stresses in the surface layers. Then, the compressive stress shields the material against surface damage and thus is receiving attention for structural applications. Ceramic

components that experience near-surface tensile stresses under contact loading, such as balls and rollers in bearings, cam followers, seals and die liners, are the most likely to benefit from surface compression.

In principle, an engineer is cautioned not to maximize the strain mismatch in order to get a high level of shielding (compressive stress) due to the appearance of structural cracks that can damage the integrity of the laminate. These relaxation phenomena (the cracks) can be avoided by respecting several rules of design that were earlier introduced (see section 2.3). Besides, a high level of shielding means, in general, a thin outer layer, so it could happen that this architecture does not sustain the improved strength under severe damage conditions because the flaw is larger than the compressive stress zone.

In the following, only this group of laminates with a well-bond interface and compressive stresses at the surface are considered since they are the core of this doctoral work. Thus, in the following the influence of surface compression on different mechanical properties is outlined. In general, improvements in strength [91], toughness [92, 93], wear [36, 94] have been observed.

Strength and damage resistance

If a priori, one can imagine that the failure will initiate at the surface, then the improvement in strength by adding a compressive stress at the surface is obvious. Realistic situations such as thermal load, contact load or wear exposes the surface and subsurface ($\sim$100 mm) to highly-localized tensile stresses. In other load configurations such as simple bending or tension, the enhancement is also expected.

An early approach that demonstrated the enhancement of strength and damage resistance in laminates was presented by Virkar's group [95]. In these experiments, Virkar fabricated bar-shaped specimens consisting of three layers with different layer thickness ratio. The outer layers always contained Al_2O_3-15 vol.% ZrO_2 (without stabilizing additive) while the central layer was made of Al_2O_3-15 vol.% ZrO_2 (with 2% mol Y_2O_3 additive). When cooled from the sintering temperature, the zirconia in the outer layers transformed to the monoclinic phase while zirconia in the central layer retained the tetragonal phase. The transformation of zirconia in the outer layers led to the establishment of compressive stresses and balancing tensile stresses in the bulk.

The damage resistance was evaluated by quasi-static indentation using a Vickers indenter. The surface radial crack size were assessed for the three-layer composites and compared with that of monolithic Al_2O_3. The surface radial cracks produced by indentation were significantly smaller in the three-layer composites as compared with the monolithics (in agreement with the predictions of fracture mechanics theory).

The strength on indented specimens - known as *indentation strength* [95] - was assessed in four-point bending tests (40 and 20 mm). The indented surface was the tensile side during the test. The tests were performed in bars 4.5 mm×5 mm×50 mm. The bars were symmetrical laminates with different outer layer thickness thus the thicker the outer layers are the thinner the inner layer is (see sketch in Figure 2.18). From Equation 2.3, it can be seen that the thinner the outer layers are the higher the compressive stress level is.
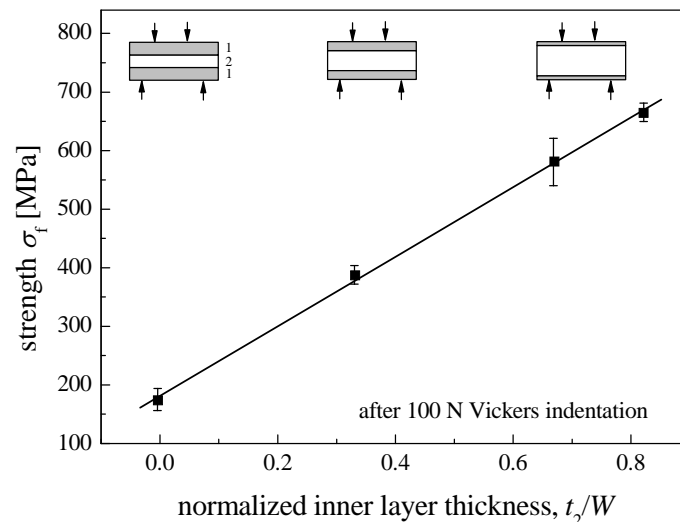
Figure 2.18: Fracture stress (σ_f) of three-layer laminates. The higher the compressive stress at the surface is (the thinner the surface layer is) the higher the measured strength is. Specimens were indented with 100 N at the surface [95].

Indentation strength results for laminates are shown in Figure 2.18. The strength increases as long as the outer layer thickness in tension, t_1, decreases (the inner layer; t_2; increases). It means, the strength is higher for the architecture with the highest compression at the surface. The scatter of the measurement reveals that the increase of strength can only be attributed to the residual stress. This small scatter is characteristic of indented specimens that fail from a controlled-size flaw (the indentation).

The effect of residual stress on *indentation strength* has been addressed by Green et al. [43]. The indentation strength of a laminate, σ_f, can be calculated in a straightforward manner if it is assumed that the stress in the outer layer is uniform and

if the indentation crack sizes are smaller than the layer thickness. Since the critical crack size at instability is identical for multilayer composites and the monolithic ceramic, the multilayer does exhibit an enhanced fracture stress due to the superposition of the compressive residual stress. This approach gives [96],

$$\sigma_f = \left(\frac{\beta \, K_c^{4/3}}{P^{1/3}} \right) - \sigma_1 , \qquad \qquad \textbf{Eq 2.20}$$

where β is an indentation parameter, K_c is the fracture toughness, P is the indentation load and σ_1 is given by Equation 2.3.

From the studies by Green et al. [43], it is possible to conclude that the compressive stresses not only increase the indentation strength but also change the slope of the strength-load behavior in the log-log plot (see Figure 2.19). Therefore, compressive stresses induce a *damage tolerance* to the material. The higher the shielding is (by the compressive stress), the higher the damage tolerance is.
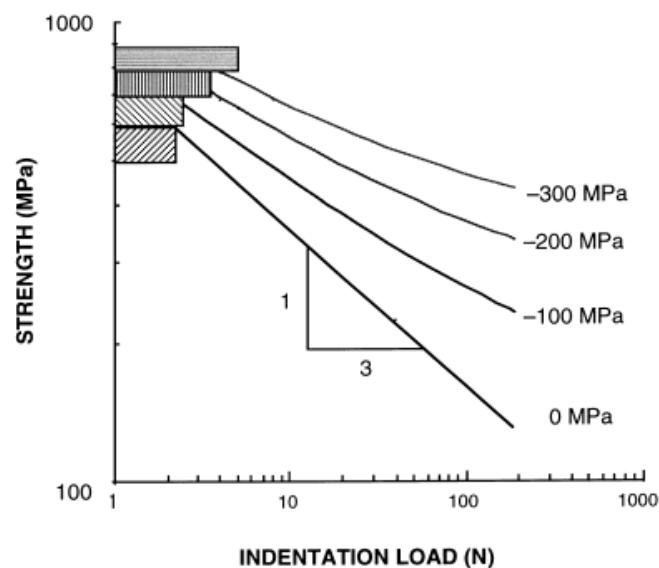
Figure 2.19: Schematic showing the effect of a compressive residual surface stresses on indentation strength. The higher the compressive stress is the smaller is the slope, and therefore the material resistance is less dependent on the flaw size. The bars on the left represent the non-indented strength, which increases with the compressive shielding.

Toughness

Improvements in *toughness* have also been observed. In fact, this is a topic that attracted a lot of interest in the last years. If a crack propagates perpendicular to the layers in a layered component, if they contain residual stresses, an apparent R-curve is provoked by the residual stresses. A first work by Blattner et al. [92] showed how the

surface compressive stresses reduce the stress intensity factor at the crack tip, hence a higher external stress level must be applied to make the laminate fail, and therefore a higher fracture toughness is observed.

Figure 2.20 shows results from the a pioneering work by Lakshminarayanan [48]. A notable increase in toughness from 7 to about 30 MPa·m$^{1/2}$ is observable while the crack propagates through the first layer. In this case a residual compression of about 400 MPa was developed in the outer layer by the constrained transformation of unstabilized zirconia from the tetragonal to the monoclinic phase. As said, the toughening derived from macroscopic surface compression is, in effect, a crack-shielding phenomenon and the fracture toughness is equivalent to a crack growth resistance curve. It is also of interest to realize how the toughening effect decreases as long as the crack propagates through the layer under tension.
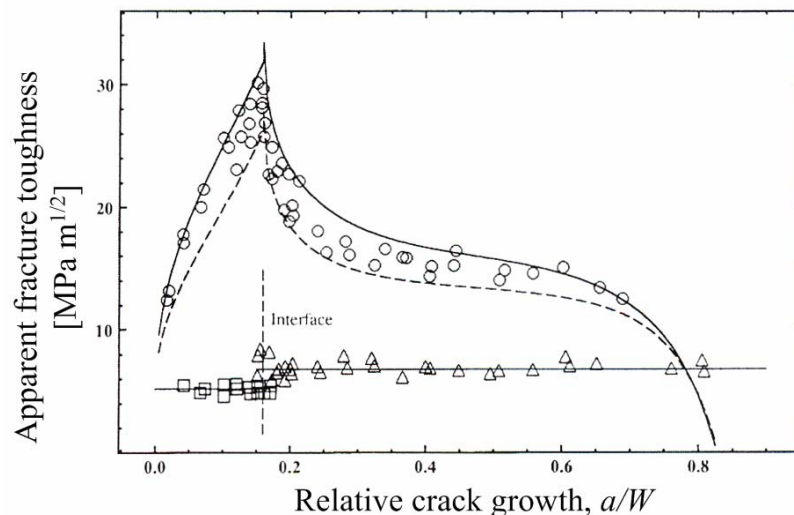
Figure 2.20: Toughness measured in a three-layer laminate for different crack lengths (open circles). An increase in toughness is observed in the first layer due to the existence of a shielding compressive stress (similar to a crack growth resistance curve) [48]. After crossing the interface the toughness decreases due to the existence of tensile stresses. The experimental values fit well with finite element simulations (continuous line). As a comparison toughness is measured on the material of the layers but without residual stresses (□ and Δ). The influence of the residual stress on the toughness measurements is evident from the comparison.

Wear, time and temperature dependent failure

The production of laminated structures with compressive residual stresses at the surface makes it possible to obtain materials whose tribological behavior is slightly superior to that of stress-free materials. For example, Toschi et al. [36] fabricated symmetric structures by superimposing alternating layers of Al_2O_3 and an Al_2O_3/ZrO_2 composite prepared by tape casting. This configuration caused residual compressive stresses in the surface due to the different thermal expansion coefficients of the

various layers ($9 \cdot 10^{-6}$ to $10 \cdot 10^{-6}$ °C^{-1} from 25 to 1400 °C, respectively). The amount of residual stress was determined to be about 140 MPa at the surface by an indentation technique. The tribological behavior of the laminated structures was evaluated using the pin-on-disk method for different loads and sliding speeds. Comparison with the results obtained from stress-free alumina showed that, within the range of the experimental conditions, the improvement in surface toughness leads to a reduced friction coefficient and increased wear resistance of the composites (Figure 2.21).

The presence of a biaxial compressive stress plays an important role in improving the wear resistance when the applied loads and sliding speeds induce a wear mechanism that is mainly ascribable to micro- and macrocracking. Micro- and macrocracking followed by limited removal of material, and limited abrasion by a third body were identified as wear mechanisms for mild wear. Under the severest conditions, the consistent removal of a plastically deformed surface layer and, consequently, a more consistent abrasion mechanism triggered a transition to severe wear (see Figure 2.21).
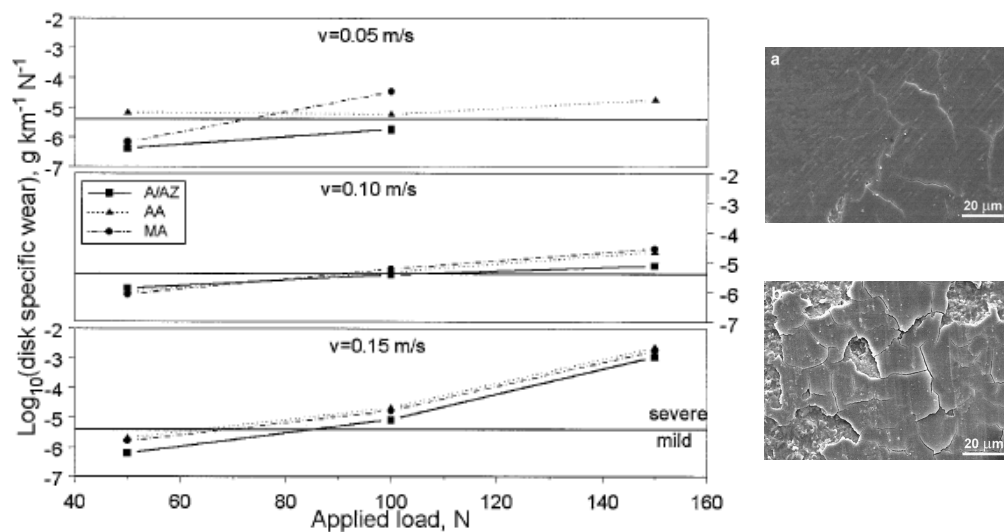
Figure 2.21: Comparative semilog plot of the specific wear of a A/AZ multilayer, a "layered" alumina (A/A/A/A or AA in the plot) and a monolithic alumina (MA). The wear is presented for different applied loads and sliding speeds, v. The best wear resistance corresponds to the multilayer. The micrographs show the surface cracking under the same experimental condition (100 N and 0.05 m/s) for a multilayer A/AZ (a) and monolithic alumina (b) [36].

Other mechanical properties in laminates have been deeply investigated. It has been observed that certain layered composites can exhibit better *creep* properties at low strain rates than either of the constituent materials [97, 98]. For instance, Jiménez-Melendo et al. [98] investigated laminates of Al_2O_3 and a composite 85 vol.% Al_2O_3 + 15 vol.% ZrO_2 doped with 3 mol% Y_2O_3 (also known as ZTA, zirconia

toughened alumina) produced by sequential slip casting under compression at 1400 °C. The composites were stressed both parallel and perpendicular to the layer planes. After testing, the layer interfaces maintain their structural integrity. The comparison with monolithic Al_2O_3 and ZTA produced by the same processing technique shows that the laminated composites exhibit enhanced ductility (characteristic of monolithic zirconia toughened alumina) and creep resistance (characteristic of alumina) simultaneously (see Figure 2.22). This behavior cannot be explained by a composite creep model based on the individual properties of the two constituent materials. The improvement in mechanical properties is essentially related to the presence of strong interfaces in the laminated composites.
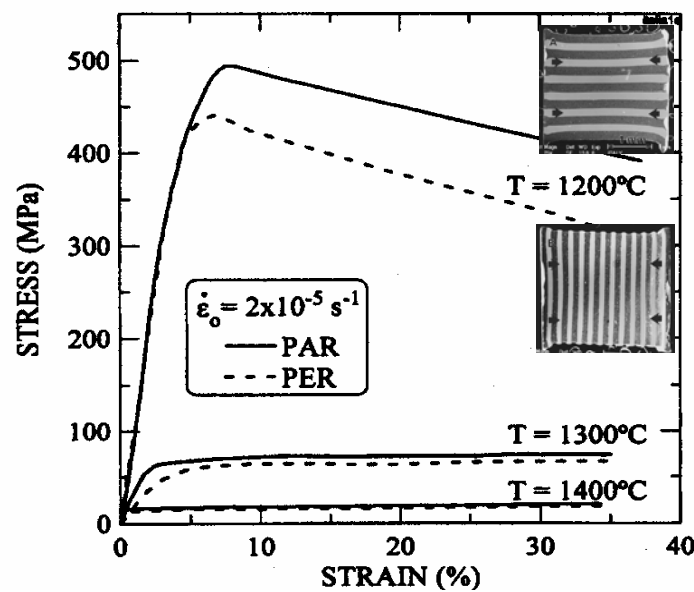
Figure 2.22: Stress-strain behavior at several temperatures of an A/AZ/A/AZ/A/AZ… laminate. If the load is applied parallel to the interfaces (LPAR) the multilayer presents an enhanced ductility and creep resistance compared to that of the constituents [97]. The micrographs show the structures after deformation, LPAR and LPER respectively.

Lastly, it is worth of note that in the tensile layers *subcritical crack growth* may take place. Since a residual stress state exists delayed failure could happen without applying an external stress. Usually for ceramics, the relation between the stress intensity factor *K* and the subcritical crack growth rate d*a*/d*t* has been expressed by a power law [99, 100]

$$v = \frac{\mathrm{d}a}{\mathrm{d}t} = AK^n \qquad , \qquad\qquad\qquad \textbf{Eq 2.21}$$

where A and n are parameters which depend on the material, the temperature and the surrounding atmosphere. K is given by $K = Y\sigma\sqrt{a}$, where σ is the nominal stress, a the crack length and Y a geometric factor. From the crack growth rate, the lifetime of a component can be derived. A numerical example is presented for layers in tension of an alumina-zirconia composite in Figure 2.23. An alumina-zirconia tensile layer with about 210 MPa will fail after 1 year even if the static strength of that composite is about 770 MPa measured in a 3-point bending test.
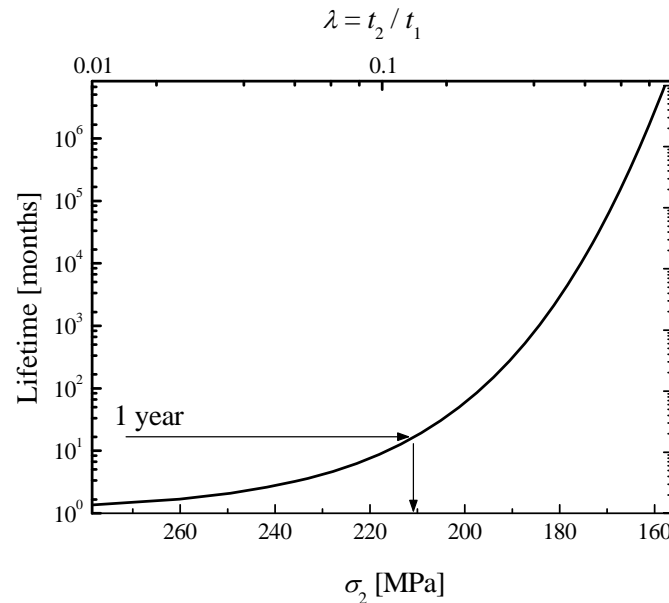
Figure 2.23: Lifetime predictions can be done by integration of the subcritical crack growth. ($A = 1.8 \cdot 10^{-6}$ and $n = 32$) [101].

It should also not be forgotten that the magnitude of the residual stresses is related to the temperature, especially when the internal stresses are due to a thermal expansion misfit. This means that *fatigue* could happen in components that work under a cyclic temperature environment.

2.5. *Literature*

[1]   Gurauskis, J., Sánchez-Herencia, A. J., Baudín, C., "Alumina-zirconia layered ceramics fabricated by stacking water processed green ceramic tapes", UPC, (2006).
[2]   Tarlazzi, A., Roncari, E., Pinasco, P., Guicciardi, S., Melandri, C., de Portu, G., "Tribological behaviour of Al_2O_3/ZrO_2-ZrO_2 laminated composites", Wear, **24**, 29 - 40, (2000).
[3]   Mistler, R. E., Twiname, E. R., "Tape casting: Theory and practice", American Ceramic Society, (2000).
[4]   Chartier, T., Rouxel, T., "Tape-Cast Alumina-Zirconia Laminates: Processing and Mechanical Properties", Journal of the European Ceramic Society, **17**, 299-308, (1997).
[5]   Bitterlich, B., Heinrich, J. G., "Processing, microstructure, and properties of laminated silicon nitride stacks", Journal of the American Ceramic Society, **88**, 2713-2721, (2005).
[6]   Gurauskis, J., Sánchez-Herencia, A. J., Baudín, C., "Joining green ceramic tapes made from water-based slurries by applying low pressures at ambient temperature", Journal of the European Ceramic Society, **25**, 3403-3411, (2005).

[7]   Doreau, F., Tari, F., Guedes, M., Chartier, T., Pagnoux, C., Ferreira, J. M. F., "Mechanical and Lamination Properties of Alumina Green Tapes Obtained by Aqueous Tape-casting", Journal of the European Ceramic Society, **19**, 2867-2873, (1999).

[8]   Tariolle, S., Reynaud, C., Thévenot, F., Chartier, T., Besson, J. L., "Preparation, microstructure and mechanical properties of SiC-SiC and B$_4$C-B$_4$C laminates", Journal of Solid State Chemistry, **177**, 487-492, (2004).

[9]   Piwonski, M. A., Roosen, A., "Low pressure lamination of ceramic green tapes by gluing at room temperature", Journal of the European Ceramic Society, **19**, 263-270, (1999).

[10]   Ham-Su, R., Wilkinson, D. S., "Strength of tape cast and laminated ceramics", Journal of the American Ceramic Society, **78**, 1580-1584, (1995).

[11]   Boch, P., Chartier, T., Huttepain, M., "Tape casting of Al$_2$O$_3$/ZrO$_2$ laminated composites", Journal of the American Ceramic Society, **69**, C191-C192, (1986).

[12]   Zan, Q., Wang, C.-a., Huang, Y., Zhao, S., Li, C., "The interface-layer and interface in the Al$_2$O$_3$/Ti$_3$SiC$_2$ multilayer composites prepared by in situ synthesis", Materials Letters, **57**, 3826-3832, (2003).

[13]   Shin, D.-W., Guo, H., "Fabrication and mechanical properties of silicon nitride laminate composites", Journal of Ceramic Processing Research, **6**, 263-265, (2005).

[14]   Orlovskaya, N., Adams, J., Chheda, M., Shih, J., Yarmolenko, S., Sankar, J., Lugovy, M., Subbotin, V., "Boron carbide-silicon carbide laminate ceramics for ballistic protection". In: ASME International Mechanical Engineering Congress & Exposition. (Washington, (2003).

[15]   Wang, C., Huang, Y., Zan, Q., Zou, L., Cai, S., "Control of composition and structure in laminated silicon nitride/boron nitride composites", Journal of the American Ceramic Society, **85**, 2457-2461, (2002).

[16]   Orlovskaya, N., Lugovy, M., Subbotin, V., Rachenko, O., Adams, J., Chheda, M., Shih, J., Sankar, J., Yarmolenko, S., "Robust design and manufacturing of ceramic laminates with controlled thermal residual stresses for enhanced toughness", Journal of Materials Science, **40**, 5483-5490, (2005).

[17]   Requena, J., Moreno, R., Moya, J., "Alumina and alumina/zirconia multilayer composites obtained by slip casting", Journal of the American Ceramic Society, **72**, 1511, (1989).

[18]   Sanchez-Herencia, J., Moya, J., Tomsia, A., "Microstructural design in alumina-alumina/zirconia layered composites", Scripta Materialia, **38**, 1-5, (1998).

[19]   Bueno, S., Moreno, R., Baudín, C., "Design and processing of Al$_2$O$_3$-Al$_2$TiO$_5$ layered structures", Journal of the European Ceramic Society, **25**, 847-856, (2005).

[20]   Montgomery, J. K., Botha, A. S., Drzal, P. L., Shull, K. R., Faber, K. T., "A thermoreversible gelcasting technique for ceramic laminates", Scripta Materialia, **48**, 785-789, (2003).

[21]   Montgomery, J. K., Faber, K. T., "Processing and surface flaw tolerance of alumina bilayers", Journal of the American Ceramic Society, **88**, 287-292, (2005).

[22]   Drewry. E. N, J, M. R., J, B. K., P, T. K., "Fracture Behavior of Centrifugally cast Multilayer Alumina/Alumina composites", Scripta Materialia, **41**, 749-754, (1999).

[23]   Ho, S., Hillman, C., Lange, F. F., Suo, Z., "Surface cracking in layers under biaxial, residual compressive stress", Journal of the American Ceramic Society, **78**, 2353-2359, (1995).

[24]   Marshall, D. B., Ratto, J. J., Lange, F., "Enhanced fracture toughness in layered microcomposites of Ce-ZrO$_2$ and Al$_2$O$_3$", Journal of the American Ceramic Society, **74**, 2979-2987, (1991).

[25]   She, J., Inoue, T., Ueno, K., "Fabrication and characterization of multilayer alumina-based composites with improved fracture behavior", Materials Letters, **42**, 155-161, (2000).

[26]   Ferrari, B., Sánchez-Herencia, A. J., Moreno, R., "Aqueous electrophoretic deposition of Al$_2$O$_3$/ZrO$_2$ layered ceramics", Materials Letters, **35**, 370-374, (1998).

[27]   Ferrari, B., Sánchez-Herencia, A. J., Moreno, R., "Electrophoretic forming of Al$_2$O$_3$/Y-TZP layered ceramics from aqueous suspensions", Materials Research Bulletin, **33**, 487-499, (1998).

[28]   Sarkar, P., Haung, X., Nicholson, P. S., "Structural ceramic microlaminates by electrophoretic deposition", Journal of the American Ceramic Society, **75**, 2907-2909, (1992).

[29]   Hatton, B., Nicholson, P. S., "Design and fracture of layered Al$_2$O$_3$/TZ3Y composites produced by electrophoretic deposition", Journal of the American Ceramic Society, **84**, 571-576, (2001).

[30]   She, J., Scheppokat, S., Janssen, R., Claussen, N., "Reaction-bonded three-layer alumina-based composites with improved damage resistance", Journal of the American Ceramic Society, **81**, 1374-1376, (1998).

[31]   Sharma, M. S., Amateau, M. F., "Processing of laminated hybrid ceramic composites", Composites Part B: engineering, 189-194, (1998).

[32]   He, Z., Ma, J., Wang, H., Shu, D., Zheng, J., "Dynamic fracture behavior of layered alumina ceramics characterized by a split Hopkinson bar", Materials Letters, **59**, 901-904, (2005).

[33]   Reynaud, C., Thevenot, F., Chartier, T., "Processing and microstructure of SiC laminar composites", International Journal of Refractory Metals & Hard Materials, **19**, 425-435, (2001).

[34]   Blanks, K. S., Kristoffersson, A., Carlström, E., Clegg, W. J., "Crack deflection in ceramic laminates using porous interlayers", Journal of the European Ceramic Society, **18**, 1945-1951, (1998).

[35]   Zhang, X. C., Xu, B. S., Wang, H. D., Y.X, W., "An analytical model for predicting thermal residual stresses in multilayer coating systems", Thin Solid Films, **488**, 274-282, (2005).

[36]   Toschi, F., Melandri, C., Pinasco, P., Roncari, E., Guicciardi, S., de Portu, G., "Influence of residual stresses on the wear behavior of alumina/alumina-zirconia laminated composites", Journal of the American Ceramic Society, **86**, 1547-1553, (2003).

[37]   Pontin, M. G., Rao, M., Sanchez-Herencia, J., Lange, F., "Laminar ceramics utilizing the zirconia tetragonal-to-monoclinic phase transformation to obtain a threshold strength", Journal of the American Ceramic Society, **85**, 3041-3048, (2002).

[38]   Bermejo, R., Torres Hernández, Y., Sánchez-Herencia, A. J., Baudín, C., Anglada, M., Llanes, L., "Residual stresses, strength and toughness of laminates with different layer thickness ratios", Acta Materialia, **54**, 4745-4757, (2006).

[39]   Choi, B. J., Koh, Y.-H., Kim, H.-E., "Mechanical properties of Si_3N_4-SiC three-layer composite materials", Journal of the American Ceramic Society, **81**, 2725-2728, (1998).

[40]   Orlovskaya, N., Kübler, J., Subbotin, V., Lugovy, M., "High toughness ceramic laminates by design of residual stress", Mat. Res. Soc. Symp. Proc, **702**, (2002).

[41]   Cook, R. F., "Toughening of a cordierite glass-ceramic by compressive surface layers", Journal of the American Ceramic Society, **88**, 2768-2808, (2005).

[42]   Arslan, G., Janssen, R., Claussen, N., "Processing and characterisation of three-layer alumina-based composites with enhanced damage tolerance", Journal of the European Ceramic Society, **25**, 3553-3561, (2005).

[43]   Green, D. J., Cai, P., Messing, G. L., "Residual stresses in alumina-zirconia laminates", Journal of the European Ceramic Society, **19**, 2511-1517, (1999).

[44]   Oechsner, M., Hillman, C., Lange, F., "Crack bifurcation in laminar ceramic composites", Journal of the American Ceramic Society, **79**, 1834-1838, (1996).

[45]   Zhang, X. C., Xu, B. S., Wang, H. D., Wu, Y. X., "An analytical model for predicting thermal residual stresses in multilayer coating systems", Thin Solid Films, **488**, 274-282, (2005).

[46]   Zhang, X. C., Xu, B. S., Wang, H. D., Jiang, Y., Wu, Y. X., "Modeling of thermal residual stressses in multilayer coatings with graded properties and compositions", Thin Solid Films, **497**, 223-231, (2006).

[47]   Oël, H. J., Fréchette, V. D., "Stress distribution in multiphase systems: I, composites with planar interfaces", Journal of the American Ceramic Society, **50**, 542-549, (1967).

[48]   Lakshminarayanan, R., Shetty, D. K., Cutler, R. A., "Toughening of layered ceramic composites with residual surface compression", Journal of the American Ceramic Society, **79**, 79-87, (1996).

[49]   De Portu, G., Micele, L., Sekiguchi, Y., Pezzotti, G., "Measurement of residual stress distributions in Al_2O_3/3Y-TZP multilayered composites by fluorescence and Raman microprobe piezo-spectroscopy", Acta Materialia, **53**, 1511-1520, (2005).

[50]   Tomaszewski, H., Strzeszewski, J., Gebicki, W., "The role of residual stresses in layered composites of $Y-ZrO_2$ and Al_2O_3", Journal of the European Ceramic Society, **19**, 255-262, (1999).

[51]   Hillman, C., Suo, Z., Lange, F., "Cracking of laminates subjected to biaxial tensile stresses", Journal of the American Ceramic Society, **79**, 2127-2133, (1996).

[52]   Ho, S., Suo, Z., "Tunneling cracks in constrained layers", Journal of Applied Mechanics, **60**, 890-894, (1993).

[53]   De Portu, G., Micele, L., Pezzotti, G., "Characterization of tunneling cracks in Al_2O_3/Al_2O_3+3Y-TZP multilayered composites by Raman and fluorescence piezo-spectroscopy", Journal of Materials Science Letters, **40**, 1505-1508, (2005).

[54]   He, M. Y., Evans, A. G., Yehle, A., "Criterion for the avoidance of edge cracking in layered systems", Journal of the American Ceramic Society, **87**, 1418-1423, (2004).

[55] Kiefer, T., Moon, H., Lange, F. F., "Compressive surface layer to avoid edge cracking in laminar ceramic composite", Journal of the American Ceramic Society, **88**, 2855-2858, (2005).

[56] Lube, T., "Mechanical properties of ceramic laminates", Key Engineering Materials, **333**, 239-242, (2007).

[57] Tada, H., Paris, P. C., Irwin, G. R., "The stress analysis of cracks handbook", Del Research Corporation, (1986).

[58] Sergo, V., Lipkin, D. M., de Portu, G., Clarke, D. R., "Edge stresses in alumina/zirconia laminates", Journal of the American Ceramic Society, **80**, 1633-1638, (1997).

[59] Lange, F., Metcalf, M., "Processing-related fracture origins: II, agglomerate motion and cracklike internal surfaces caused by differential sintering", Journal of the American Ceramic Society, **66**, 398-406, (1983).

[60] Cox, B. N., "Surface displacements and stress gradients and stress generated by a semi-ellipsoidal surface inclusion", Journal of Applied Mechanics, **56**, 564-570, (1989).

[61] Timoshenko, S., Goodier, J., "Theory of elasticity", Mc Graw-Hill, (1970).

[62] Clegg, W. J., Kendall, K., Alford, N. M., Button, T. W., Birchall, J. D., "A simple way to make tough ceramics", Nature, **347**, 455-457, (1990).

[63] Sanchez-Herencia, J., Pascual, C., He, J., Lange, F., "ZrO_2/ZrO_2 Layered Composites for Crack Bifurcation", Journal of the American Ceramic Society, **82**, 1512-1518, (1999).

[64] Bermejo, R., "Structural integrity of alumina-zirconia multilayered ceramics", (Universitat Politècnica de Catalunya, Barcelona 2005).

[65] Rao, M., Lange, F., "Factors affecting threshold strength in laminar ceramics containing thin compressive layers", Journal of the American Ceramic Society, **85**, 1222-1228, (2002).

[66] Lugovy, M., Orlovskaya, N., Slyunyayev, V., Gogotsi, G., Kübler, J., Sanchez-Herencia, J., "Crack bifurcation features in laminar specimens with fixed total thickness", Composites Science and Technology, **62**, 819-830, (2002).

[67] Gee, I., Dobedoe, R., Vann, R., Lewis, M., Blugan, G., Kuebler, J., "Enhanced fracture toughness by ceramic laminate design", Advances in Applied Ceramics, **104**, 103-109, (2005).

[68] Rao, M., Sanchez-Herencia, J., Beltz, G., McMeeking, R. M., Lange, F., "Laminar ceramics that exhibit a threshold strength", Science, **286**, 102-105, (1999).

[69] Russo, C. J., Harmer, M. P., Chan, H. M., Miller, G. A., "Design of a laminated Ceramic Composite for Improved Strength and toughness", Journal of the American Ceramic Society, **75**, 3396-4000, (1992).

[70] Clegg, W. J., "The fabrication and failure of laminar ceramic composites", Acta Metallurgica et Materialia, **40**, 3085-3093, (1992).

[71] Davis, J. B., Kristoffersson, A., Carlström, E., Clegg, W. J., "Fabrication and crack deflection in ceramic laminates with porous interlayers", Journal of the American Ceramic Society, **83**, 2369-2374, (2000).

[72] Badini, C., Fino, P., Ortona, A., Amelio, C., "High temperature oxidation of multilayered SiC processed by tape casting and sintering", Journal of the European Ceramic Society, **22**, 2071-2079, (2002).

[73] Liu, H., Hsu, S., "Fracture behavior of multilayer silicon nitride/boron nitride ceramics", Journal of the American Ceramic Society, **79**, 2452-2457, (1996).

[74] Mawdsley, J. R., Kovar, D., Halloran, J. W., "Fracture behaviour of alumina/monazite multilayer Laminates", Journal of the American Ceramic Society, **83**, 802-808, (2000).

[75] Ma, J., Wang, H., Weng, L., Tan, E. B., "Effect of porous interlayers on crack deflection in ceramic laminates", Journal of the European Ceramic Society, **24**, 825-831, (2004).

[76] Winn, E. J., Chen, I.-W., "Crack deflection in composites with very thin interlayers", Journal of the American Ceramic Society, **83**, 3222-3224, (2000).

[77] Tariolle, S., Thévenot, F., Chartier, T., Besson, J. L., "Properties of reinforced boron carbide laminar composites", Journal of the European Ceramic Society, **25**, 3639-3647, (2005).

[78] Shigegaki, Y., Brito, M., Hirao, K., Toriyama, M., Kanzaki, S., "Processing of a novel multilayered silicon nitride", Journal of the American Ceramic Society, **79**, 2197-2200, (1996).

[79] He, M. Y., "Kinking of a crack out of an interface", Journal of Applied Mechanics, **56**, 270-278, (1989).

[80] Kovar, D., Thouless, M., "Simple method for determining frictional sliding resistance and frictional energy dissipation in layered ceramics", Journal of the American Ceramic Society, **80**, 673-679, (1997).

[81]   Rao, M., Rödel, J., Lange, F., "Residual stress induced R-curves in laminar ceramics that exhibit a threshold strength", Journal of the American Ceramic Society, **84**, 2722-2724, (2001).

[82]   McMeeking, R. M., Hbaieb, K., "Optimal threshold strength of laminar ceramics", Zeitschrift metallkunde, **90**, 1031-1036, (1999).

[83]   Hbaieb, K., McMeeking, R. M., "Threshold strength predictions for laminar ceramics with cracks that grow straight", Mechanics of Materials, **34**, 755-772, (2002).

[84]   Pontin, M. G., Lange, F. F., "Effects of porosity on the threshold strength of laminar ceramics", Journal of the American Ceramic Society, **88**, 376-382, (2005).

[85]   Moon, H., Pontin, M. G., Lange, F., "Crack Interactions in Laminar Ceramics That Exhibit a Threshold Strength", Journal of the American Ceramic Society, **87**, 1694-1700, (2004).

[86]   Bermejo, R., Torres Hernández, Y., Sánchez-Herencia, A. J., Baudín, C., Anglada, M., Llanes, L., "Fracture behaviour of an Al_2O_3-ZrO_2 multi-layered ceramic with residual stresses due to phase transformations", Fatigue and Fracture of Engineering Matererial Structures, **29**, 71-78, (2006).

[87]   Vandeperre, L. J., Kristoffersson, A., Carlström, E., Clegg, J. W., "Thermal shock of layered ceramic structures with crack-deflecting interfaces", Journal of the American Ceramic Society, **84**, 104-110, (2001).

[88]   Vandeperre, L. J., Van der Biest, O., "Graceful failure of laminated ceramic tubes produced by electrophoretic deposition", Journal of the European Ceramic Society, **18**, 1915-1921, (1998).

[89]   Fair, G. E., He, M. Y., McMeeking, R. M., Lange, F., "Ceramic composites with three dimensional architectures designed to produce a threshold strength - II. Mechanical Observations", Journal of the American Ceramic Society, **88**, 1879-1885, (2005).

[90]   Fair, G. E., Lange, F., "Ceramic composites with three-dimensional architectures designed to produce a threshold strength-I. Processing", Journal of the American Ceramic Society, **88**, 1158-1164, (2005).

[91]   Pascual, J., Chalvet, F., Lube, T., de Portu, G., "Strength distributions in ceramic laminates", Materials Science Forum, **492-493**, 581-586, (2005).

[92]   Blattner, A., Lakshminarayanan, R., Shetty, D. K., "Toughening of layered ceramic composites with residual surface compression: effects of layer thickness", Engineering Fracture Mechanics, **68**, 1-7, (2001).

[93]   Moon, R. J., Hoffman, M., Hilden, J., Bowman, K. J., Trumble, K. P., Rödel, J., "Weight function analysis on the R-curve behavior of multilayered alumina-zirconia composites", Journal of the American Ceramic Society, **85**, 1505-1511, (2002).

[94]   De Portu, G., Micele, L., Prandstraller, D., Palombarini, G., Pezzotti, G., "Abrasive wear in ceramic laminated composites", Wear, (2005).

[95]   Hansen, J. J., Cutler, R. A., Shetty, D. K., Virkar, A. V., "Indentation fracture response and damage resistance of Al_2O_3-ZrO_2 composites strengtened by transformation-induced residual stresses", Journal of the American Ceramic Society, **71**, C501-C505, (1988).

[96]   Cai, P., Green, D. J., Messing, G. L., "Mechanical characterization of Al_2O_3/ZrO_2 hybrid laminates", Journal of the European Ceramic Society, **5**, 2025-2034, (1998).

[97]   Jimenez-Melendo, M., Clauss, C., Dominguez-Rodriguez, A., de Portu, G., Roncari, E., Pinasco, P., "High temperature plastic deformation of multilayered YTZP/ZTA composites obtained by tape casting", Acta Materialia, **46**, 3995-4004, (1998).

[98]   Jimenez-Melendo, M., F, G.-M., Dominguez-Rodriguez, A., "Effect of layer interfaces on the high-temperature mechanical properties of alumina/zirconia laminate composites", Acta Materialia, **48**, 4715-4720, (2000).

[99]   Munz, D., Fett, T., "Ceramics. Mechanical properties, failure behaviour, materials selection", Springer, (1999).

[100]   Nejma, R., Lang, K. H., Löhe, D., "Influence of the temperature on the strength and the subcritical crack growth rate of alumina", Materials Science and Engineering A, **387-389**, 832-836, (2004).

[101]   Chevalier, J., Olagnon, C., Fantozzi, G., Cales, B., "Subcritical crack growth and thresholds in a 3Y-TZP ceramic under static and cyclic loading conditions", Ceramics International, **23**, 263-266, (1997).

Chapter 3. Introduction to A/AZ Laminates

This work deals with one of the layered systems more popular in the literature [1, 2]. It is a system constituted by layers of alumina (A) and an alumina-zirconia composite (AZ). Different architectures have been studied, parameters such as the stacking order, the number of layers and the thickness of the layers have been varied to investigate the influence of the residual stress on the mechanical performance. There is a common characteristic to all the laminates studied here; the outer layers are made of alumina. This propitiates the most representative characteristic of this family of laminates: they all contain surface compressive stresses. The internal stress state is due to the thermal expansion mismatch between the layers.

In this thesis a nomenclature is used to describe the architecture of a laminate. For example, for a laminate which is called "3A/2AZ/3A", we are talking about a laminate that consists of a layer made of three tapes of alumina, later a layer made of two AZ-tapes and finally a layer made of three tapes of A. That is a symmetrical laminate, which is the normal case through this work.

The internal stresses in the laminate have a strong influence on the mechanical properties (strength or toughness). Therefore, interpretation of the measurements needs a carefully analysis. Thus, in order to understand results on strength or toughness the residual stresses shall be quantified first. Chapter 2 already presented the dependence of the residual stresses on the architecture, on the thermal expansion mismatch and on the elastic properties of the layers. In this chapter the thermal expansion coefficient (or CTE) and elastic properties are measured for the layers constituyents of the laminates. To measure them, "laminates" made of exclusively alumina (A/A/A/A…) or the composite AZ (AZ/AZ/AZ…) were also produced in an identical manner as the A/AZ-laminates. Additionally, some other "independent properties" of the architecture are presented: hardness, density, microstructure.

This chapter briefly introduces some basic knowledge on alumina and zirconia and shows the processing route (which is common to all the laminates presented here). The review of the materials pretends to be a short background that gives some understanding on potential applications for this laminates. The processing description may serve to understand how the residual stresses develop during cooling from the sintering temperature and the complexity of the process. The specimens were

provided by the "Istituto di Scienza e Tecnologia dei Materiali - ISTEC" in Faenza, Italy (www.istec.cnr.it). Later, the physical constants necessary for the estimation of the residual stress state are presented. This chapter concludes with a study of the interface, as the mechanical properties of the interface will influence the mechanical properties of the laminate.

3.1. Introduction to Structural Ceramics

Due to their brittle nature, monolithic ceramics are sensitive to defects that act as stress concentrators [3]. Therefore, structural applications of monolithic ceramics are focused to parts that are subjected to compressive loading or limited tensile or multiaxial loading. A well-known example is glass and porcelain ware commonly used in our daily lives. However, structural ceramics are finding applications in the industry mainly due to improvements in the processing routes. Some examples of structural applications of ceramic materials are bearings, seals, armors, cutting tools and others.

The particular properties of structural ceramics are the result from their particular atomic structure (mainly directional covalent bonds and ionic bonds) that distinguish them from other materials, polymers or metals. Some properties of commercial ceramics are listed in Table 3.1.

Table 3.1. Properties of hot-pressed structural ceramics at room temperature. (Source: www.ceradyne.com)

material	SiC	Si_3N_4	AlN	B_4C	Al_2O_3	ZrO_2[*]
factor cost	€€€	€€	-	€€€€	€	€€
density (g/cm^3)	3.15	3.30	3.26	2.50	3.99	6.02
HV0.3 (GPa)	23	18	11	32	14[*]	1300
E (GPa)	400	320	320	460	395	210
Poisson's ratio ν	0.17	0.28	0.22	0.17	0.22	0.23
Fract. Toughness $(MPam^{1/2})$	2.5	6	2.5	2.5	4-5[*]	13
Flexural strength (MPa)	380	930	330	410	200-450	900
Weibull Modulus	12	15-20	10	12	10	10
Applications	wear components	wear components	thick film heaters	ballistic armor	orthodontic, …	

[*] extracted from www.coorstek.com for an Y_2O_3 partially stabilized zirconia (YTZP).

41

3.1.1. Alumina (Al_2O_3)

Alumina has been very well documented, compilations of Gitzen [4] or Morrell [5] are excellent references and the basis of this section. Alumina is one of the most versatile of refractory ceramic oxides and consequently finds the widest range of applications. Alumina based products currently have more than 50% of the total world market for technical ceramics [5]. Alumina is chemically inert and stable to its melting point of 2050 °C. The alumina crystals (known as *corundum* in mineralogical terms, or *sapphire* in single-crystal form) are relatively hard, stiff and refractory compared with silicate ceramics or glasses. In its pure form, it has a high Young´s modulus (~ 400 GPa) and strong polycrystalline materials can be made of it. Alumina ceramics are more expensive than silicate ceramics made from minerals, such as porcelains, but are generally the cheapest of all oxide ceramics, the raw material being a by-product of the aluminium industry [4, 5].

Aluminium oxide, both as single crystal and in polycrystalline sintered form, has remarkable mechanical properties in comparison with conventional porcelains and other single oxide ceramics. None other refractory oxide has a higher bending or tensile strength at room temperature as pure sintered alumina, and only ZrO_2 and ThO_2, have a similar compressive strength. At about 1000°C, alumina has the highest tensile strength, and is exceeded only by ZrO_2 in compressive strength. A summary of typical properties for alumina at room temperature is given in Table 3.1.

Many alumina ceramics have been developed not only for structural applications but also specifically for obtaining certain electrical properties, particularly low levels of dielectric loss. This property is controlled mainly by the amount of secondary phase present, and by the levels of alkali-metal impurities. The choice of purity of the starting raw powder batch is usually dictated by the end requirements. Thus, a material designed to have good wear and chemical corrosion resistance will not necessarily also have good electrical properties comparable with materials of the same alumina content but developed specifically for electrical or electronic engineering. Conversely, some materials with good electrical properties have a relatively coarse grain size in order to resist distortion during high-temperature metallizing processes which enable the component to be joined subsequently to metal parts. This leads to lower strength than might be desirable for a component used mechanically. In summary, care must be taken to ensure that the correct type of material is chosen.

Additionally, tests have shown that the best resistance to corrosion by acids is shown by aluminas in which the amounts of secondary phase and residual closed porosity are reduced to a minimum. This occurs in high purity alumina provided the deliberate additions of MgO which controls grain growth in firing are not excessive [5].

3.1.2. Zirconia (ZrO_2)

Zirconia occurs as a natural mineral in igneous rocks. The commercial grades of zirconia powders are produced by a number of routes, usually involving zircon as a precursor ($ZrSiO_4$) [6]. Zircon is broken down into its constituents, ZrO_2 and SiO_2, either chemically, by the addition of an aggressive alkali, or by heating to a high temperature. In the bulk form, zirconia exhibits some desirable properties, notably high elastic modulus and hardness, a high melting point, and outstanding corrosion resistance [6]. The microstructure can also be engineered such that very high fracture toughness can be generated. Some typical properties for a commercial zirconia are listed in Table 3.1.

The monoclinic form is thermodynamically stable at room temperature but transforms reversibly to the tetragonal crystallographic system on heating above 1173 °C, the transformation being accompanied by a decrease in volume of approximately 4% [7]. Conversely, the transformation from tetragonal to monoclinic on cooling shows a volume increase. When it occurs at high speed (martensitic transformation) it is used to develop zirconia-based engineering ceramics. The relationships of the crystallographic phases are shown in Figure 3.1, where it can be seen that the symmetry increases with temperature.
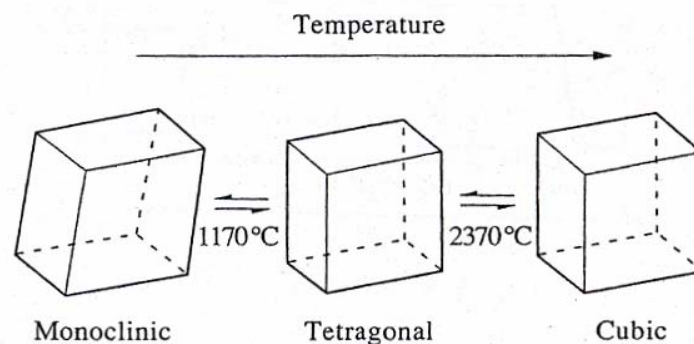
Figure 3.1: The crystal structures of zirconia showing the effect of temperature on their stability.

The higher temperature phases may be stabilized by the alloying solid solution with specific cubic oxides that form a solid solution with ZrO_2. Additives such as CaO,

MgO, Y_2O_3, and CeO_2, which have cations with a similar ionic radius (and therefore sufficient solid solubility), will, when incorporated into the monoclinic phase, first stabilize the tetragonal form and with further addition, the cubic phase.

Y_2O_3 is currently used to stabilize tetragonal zirconia [8], although Y_2O_3 and ZrO_2 crystallize in different space groups, the arrangement of the ions is similar to a cubic phase with only a small shift in the atomic positions. Thus, the solubility limit of Y_2O_3 in both the monoclinic and tetragonal phase is relatively high, giving extensive tetragonal and cubic solid solution phase fields in the phase diagram. The addition of yttria to zirconia has two significant effects: it does not only extend the range of the tetragonal phase field but also has the effect of lowering the temperature at which the tetragonal-monoclinic transformation takes place. This enables the fabrication of a dense zirconia polycrystalline ceramic consisting of nearly 100% tetragonal phase. At 2-3 mol.% Y_2O_3 the material produced is metastable at room temperature provided it has a sufficiently small grain size.
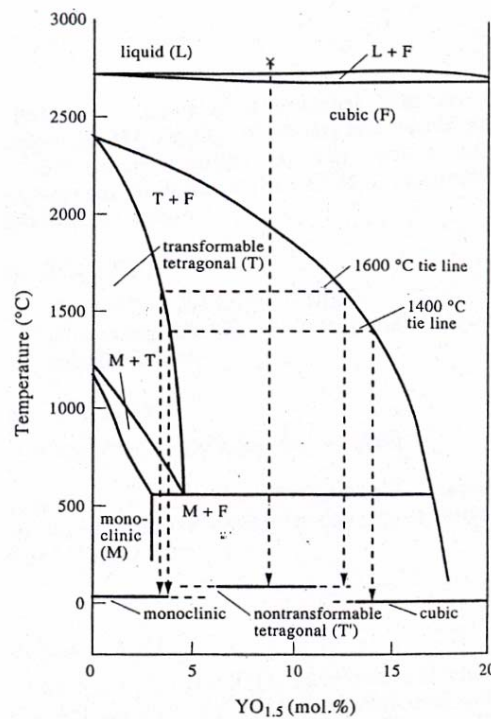
Figure 3.2: Phase diagram $ZrO_2 - Y_2O_3$ [6].

Materials based on these compositions are fabricated commercially and have found widespread use in niche markets involving cutting and wear applications, where the materials have proved superior to any available alternative metal or ceramic. Use of pure zirconia as a bulk refractory is not feasible due to the large volume change of the tetragonal to monoclinic phase transformation.

In zirconia, *ageing* occurs by a slow surface transformation to the stable monoclinic phase in the presence of water or water vapor [9]. Transformation starts first in isolated grains on the surface by a *stress corrosion* type mechanism. This nucleation of the transformation leads then to a cascade of events occurring neighbor to neighbor. The transformation of one grain leads to a volume increase stressing up the neighboring grains and to microcracking. This offers a path for the water to penetrate down into the specimen. The consequences of ageing process on the long term performance of zirconia components are roughening and microcracking [9].

3.1.3. Alumina-zirconia composite (AZ): a stress-induced transformation toughened composite.

The development of alumina-zirconia composites (AZ) and especially zirconia-toughened alumina (ZTA or an AZ-composite in which the zirconia content is about 15 vol. %) was aimed to substitute alumina ceramics in applications where a higher fracture resistance was required, i.e. orthopedic implants. Besides, zirconia-toughened aluminas are recently successful in improving ageing problems appearing in zirconia femoral head prostheses [9]. Both phases are mutually insoluble, with no intermediate phases, and are thermally and chemically stable up to the eutectic temperature (~1700 °C) [10]. The industrial success of these composites is based on stress-induced phase transformation that enhances the crack resistance of the material.

With the publication of the article "Ceramic Steel?" by Garvie et at. [11], it was shown that the fracture toughness of partially stabilized zirconia materials (PSZ) could be increased by *stress-induced martensitic transformation* of tetragonal zirconia particles (t-ZrO_2) to the monoclinic form (m-ZrO_2) [7]. The incorporation of zirconia inclusions into oxide ceramics, especially into alumina matrixes was undertaken shortly thereafter [12].

The stress-induced phase transformation is explained in the following: when heated above 1173°C zirconia forms the tetragonal phase. On cooling, the tetragonal to monoclinic transformation should take place with a significant volume increase. However, if the ZrO_2 is in the form of finely divided particles, or has a constraining pressure exerted on it by the matrix, then the tetragonal particle can be kept as a metastable tetragonal crystal. If a crack is made to extend under stress, then tensile stresses are generated around and ahead of the crack tip (see Figure 3.3). When the stresses are large enough, a release of constraint on the metastable tetragonal zirconia particles takes place. As a result the particles transform to the monoclinic phase with

an accompanying volume increase, typically 4%. The volume expansion generates large compressive stresses in the constrained region of the crack tip, opposing further growth. Thus, for the crack to grow, extra work is required to move the crack through the ceramic and this reflected in the higher toughness of the material. The zirconia particles must have a size distribution ranging between a "critical" size for spontaneous transformation during cooling to room temperature and a "critical" size for stress-induced transformation [3]. One of the problems with ZTA may be caused by overstabilization of the tetragonal zirconia phase.

○ Original metastable zirconia particle (tetragonal)

◎ Martensitically transformed zirconia particle (monoclinic)

▨ Stress field around crack tip
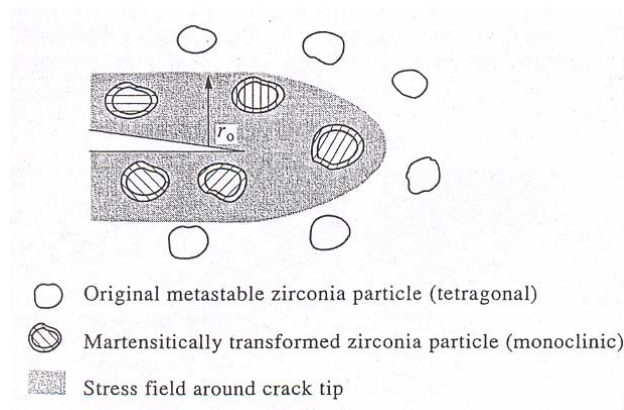
Figure 3.3: Toughening mechanism with small zirconia particles around a crack tip.

Processing is thus critical to obtain ZTA ceramics composites with maximum fracture toughness. The amount of stabilizer (Y, Ca, Ce, Mg) must be optimized experimentally, and it is dependent on the volume fraction of zirconia in the composite, the grain size of the zirconia, and the stress state on the zirconia. Today, there is a trend to develop more complex fabrication techniques which may allow the obtaining of a narrow size distribution of zirconia particles homogeneously dispersed in the alumina matrix.

The mechanisms by which zirconia acts to toughen the composites are complementary: not only *transformation toughening*, but also *microcracking* and crack deflection. In the case of ZTA, the creation of microcracks in the tip field of a growing crack was observed by means of electron microscopy [13].

An important aspect of the mechanical behavior of transformation-toughened ZrO_2-containing ceramics is their R-curve behavior, i.e., the phenomenon wherein the crack resistance increases with increasing crack propagation. R-curve behavior due to crack tip transformation was first analyzed in detail by McMeeking and Evans [14], who showed that a fully developed transformation "wake" on the flanks of the crack is necessary for a propagating crack to experience the full crack resistance due to transformation toughening. Recent models present that the plateau toughness is

achieved after crack propagation for a distance about 5 times the dimension of the transformation zone [15].

3.2. From the powders to the laminate (Processing)

Laminates used in this study were tape-casted in the Istituto di Scienza e Tecnologia dei Materiali (ISTEC), Faenza (I). Dr. de Portu and Francis Chalvet are acknowledged for this.

Two different powders were necessary for the built-up of the laminates. The alumina layers were fabricated with an A16 grade from Alcoa Aluminium Co, NY (USA). Alcoa powders are produced by the classical Bayer process with bauxite as raw material (www.alcoa.com). The layers made of the alumina-zirconia composite were fabricated with the same alumina grade and tetragonal TZ3Y-S zirconia powders, from Tosoh Corp, Japan (www.tosoh.com). Their properties are listed in Table 3.2.

Table 3.2: Powder properties provided by supplier.

Powder	Provider	Purity	Specific surface area (m^2/g)	Average particle size (μm)	Others
A 16 SG (Al_2O_3)	ALCOA	99.7	9.5	0.5 (D_{50})	spherical in shape
TZ3Y-S (ZrO_2)	TOSOH	-	7 ± 2	0.3 (D_{50})	Y_2O_3 3mol%

The AZ-composite was always produced with the same composition, 60 vol.% of alumina and 40 vol.% of zirconia. In weight, this is equivalent to a 50 wt. % of alumina and 50 wt.% of zirconia composition. This composition presents an adequate thermal stress mismatch in relation with the alumina layers as it will be shown later. It increases the low toughness of pure alumina while it reduces the aging of pure zirconia. This composition differs from classical zirconia-toughened alumina which contain about 15 vol.% of zirconia and is optimized with respect to *microcrack toughening* [16, 17].

Creating a proper slurry is not easy. Fortunately tapes of alumina are well developed as they are the main constituent of every integrated circuit of microelectronics. The additives of the slurry were the same for the alumina layers and for the AZ layers. Poly-vinylbutyral was used as binder and glycerol trioleate (GTO) as dispersant for all the slips prepared for the tape casting. To complete the tape casting slurries, butylbenzyl-phtalate (BBP) as plasticizer and an azeotropic mixture of MEK /EtOH

(67/33 wt.%) as solvent were used [1, 18]. The composition of the slurry is reported in Table 3.3. In all slurry compositions the dispersant/powder ratio was fixed at 1.6 wt.% and the binder was present in the same percentage as the plasticizer.

Table 3.3: Composition of the tape casting slurries.

	ceramic powder	solvent	dispersant	binder	plasticizer
component	A or A/AZ	azeotropic MEK[*]/ethanol (67/33 wt. %)	glycerol trioleate (GTO)	poly-vinylbutiral	butyl-benzyl-phalate (BBP)
wt. %	58.96	29.48	0.94	5.31	5.31

[*] MEK is methyl-ethyl-ketone. Dispersant/ceramic weight ratio = 1.6 wt.%

The tape casting was carried out on the basis of previous experiences [1, 18, 19]. The powders were ball-milled for 1 h in the solvent with the dispersant and a small amount of binder in a teflon jar, using either alumina or zirconia balls as milling media depending on the ceramic powder used. The remaining part of the binder was added and the mixing proceeded for another 16 h. Finally, the plasticizer was added to the suspension and the homogenisation was continued for 4 h. Tape casting was performed using a laboratory tape casting bench with a stationary double blade system. Slurries were tape casted onto a mylar sheet moved at a constant speed of 200 mm/min. The position of the blades was regulated to the desired tape/sheet height. The drying of the tapes was carried out in air for 24 h. The types of powders and the experimental procedures used in this work did not lead to an evident green density gradient through the thickness of the tapes.

Plates with geometry about 41 x 27 mm were cut from the different ceramic sheets. The plates were stacked and thermocompressed without any gluing agent at a temperature of 80 °C for 30 min with an external pressure of 30 MPa (in order to homogenize the temperature, the pressure was only applied after 30 min).

Most of the research was done on a non-homogeneous laminate with the following staking order: 2A/AZ/A/AZ/A/AZ/2A. That is a 7-layer laminate, 4 layers made of alumina (A) and 3 layers made of the AZ composite. In order to stimulate compressive stresses at the surface, the structure was so designed that it has surface layers of alumina. A double external A-layer was used on each side to allow for machining after sintering if necessary. In this case one layer could be removed from each side by grinding, leaving a perfectly symmetrical structure.

All the laminates were sintered at 1550 °C for 1 h. Because two materials (A and AZ) must be sintered simultaneously, a compromise temperature is chosen. Monolithic

"layered" alumina and monolithic "layered" AZ as well, were sintered at 1550 °C for comparative purposes. It was necessary to limit the sintering temperature to 1550 °C in order to avoid an exaggerated tetragonal to monoclinic spontaneous phase transformation of the 3Y-TZP although 1550 °C is relatively low for the alumina grade that we used. Figure 3.4 compiles recent literature about sintering temperatures for AZ composites.
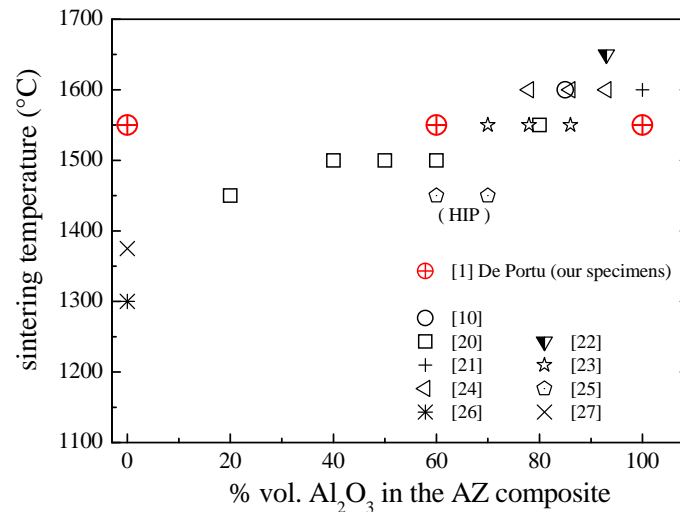
Figure 3.4: Literature review on sintering temperatures for different A/AZ composites. All the composites are made of 3Y-ZrO$_2$ from Tosoh and submicron powders of high-purity alumina [1, 10, 20-27].

Because the heating and cooling rates are parameters determining the residual stresses in the alumina/zirconia composite [28], the sintering cycle was carefully controlled. To allow the burn out of the organic components, a very slow debonding cycle is necessary: 3 °C/h up to 600 °C and fast cooling (50 °C/h). Later, the heating rate was increased to 30 °C/h up to the maximum temperature, 1550°C. After the holding period (1 hour), the samples were cooled down to 600 °C at a controlled cooling rate of 30 °C/h, and then brought down to room temperature by natural furnace cooling. The slower the cooling rate the less the number of tunneling cracks that appear in the laminate. The decrease in the extent of cracking, when a slower heating rate is used, can be explained by the viscous nature of the sintering laminate. The reduced cracking under the slow cooling rate is due to the relaxation of residual stresses during the initial period of cooling [29].

Under these conditions the layers of alumina/zirconia composite exhibited a certain amount of porosity (but the final relative density was always superior to 97.5%). The shrinkage, measured on all the plates (A/A/A.., AZ/AZ/AZ.. and A/AZ/A/..) was about 15 – 17 %.

3.2.1. Microstructure

Two techniques have been used to reveal the microstructure. Both involve a diamond polishing procedure down to a 1 µm in a fully automatic Struers RotoPol-25 device. The procedure is depicted in Table 3.4. Later, either an oxide polishing suspension (OPS) or a thermal etching was used.

Table 3.4: Reference polishing sequence

	grit size			
	9 µm	6 µm	3 µm	1 µm
polishing time [min]	~ 2 - 5	~ 5 - 10	~ 5 - 10	~ 5 - 10
polishing revolution [rpm]	150	150	150	150
polishing force [N]	40	40	50	50

The OPS method is relatively successful for the alumina since it presents a larger grain size. The microstructure of the AZ composite was not possible to be developed/etched by OPS.
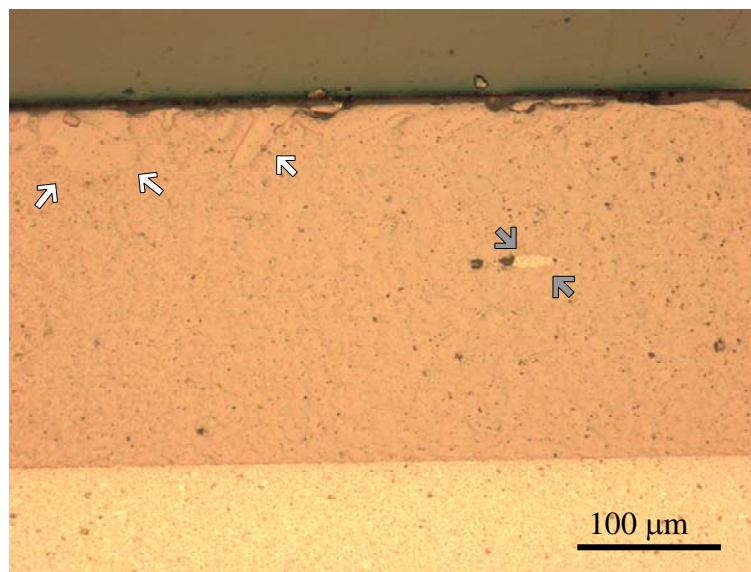
Figure 3.5: OPS polished cross-section of an A/AZ-laminate. The upper layer (A) contains abnormal large grains at the edge, the surface of the specimen (white arrows). An inclusion of the AZ composite is also observable in the A-layer (gray arrows). The grain size is not observable in the AZ-layer while in the A-layer it can be guessed.

Then, in order to obtain better results, a classic alternative for alumina was performed: thermal etching. The technique involves heating a polished sample in a furnace for 10 - 30 min at a temperature 100 – 200°C below the sintering temperature, and subsequent SEM observation. Surface diffusion redistributes the material on the

surface during heating to compensate the thermodynamically-instable flatness, thus revealing the locations of grain boundaries in the surface. Furthermore, any scratch produced during grinding and polishing is partly filled during thermal etching. Along with surface diffusion, a mass flow across grain boundaries under the surface also takes place during thermal etching, therefore the temperature should be as low as possible to minimize grain growth.

In this work cross sections of the sintered laminates were polished down to a 1 μm finish for optical microscopy, thermal etching was carried out for 20 min in air at 1375 °C for A and 1410 °C for AZ (thermal etching at 1375 °C demonstrated not to be high enough for revealing the AZ microstructure). Before the SEM observation some preparation is necessary to provide them some electrical conductivity. The samples were gold-coated for 12 seconds at 35 mA in a commercial Agar sputter coater. Approximately 15 mm were kept between the specimen and the gold surface. SEM and light microscopy revealed the microstructure (see Figure 3.6). Some scanning electron micrographs were taken in backscatter mode which gives a strong atomic number contrast between the zirconia (bright phase) and alumina (dark phase).
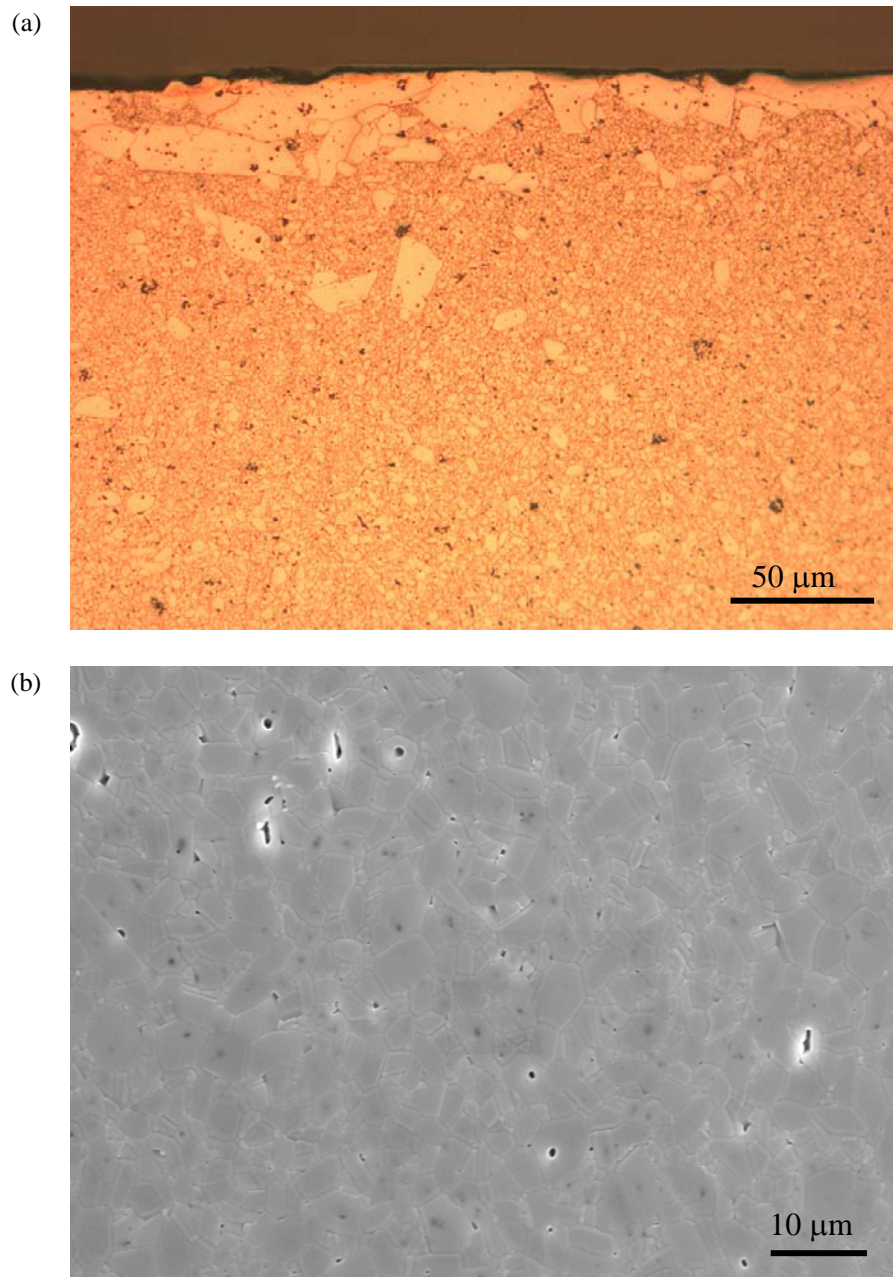
Figure 3.6: Microstructure of alumina after thermal etching at 1375 °C as observed by (a) light microscopy and (b) SEM. In (a) abnormal grain growth of alumina is observable at the surface.

(a)

(b)
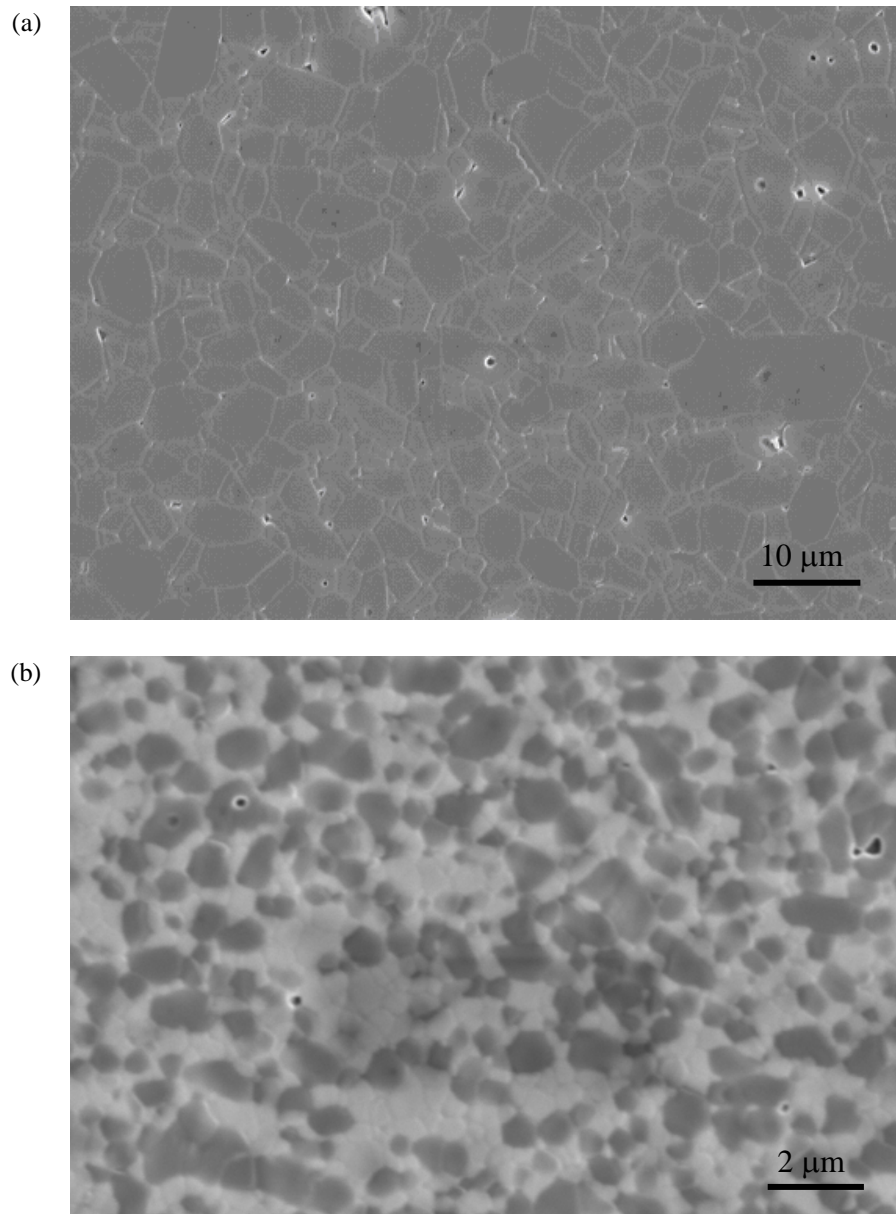
Figure 3.7: Microstructure of A (a) and AZ (b) after thermal etching at 1410 °C as observed by SEM.

The microstructures obtained in the AZ composite, as compared with those observed in alumina, evidence that addition of zirconia particles effectively hinders alumina matrix grain growth. This is according to the literature which states that the larger the zirconia content is the smaller the alumina grain size is [10]. The low grain-growth rates in such duplex composites have been attributed to the limited mutual solid solubility and the extended diffusion path length that are associated with the interconnection of the Al_2O_3 and ZrO_2 phases [30].

For the AZ composite, it can be noted that the alumina and zirconia are well dispersed. There were no large agglomerates rich in zirconia or alumina, just small agglomerates with a typical size around 5 µm. No agglomerates larger than 10 µm were found. These agglomerates must be controlled since they are the predominant cause of failure in AZ composites. They are the origins for cracks that could occur during sintering due to a differential shrinkage. In this work cracks starting from agglomerates were not observed. Porosity was kept to a reduced level for the material in both layers ($< 2\%$). Some intracrystalline pores were observed in the alumina grains. Table 3.5 summarizes the microstructure.

Table 3.5: Microstructure

	grain size [µm]	morphology	notes
A	~ 2 - 5	equiaxed (small grains) planar facets (large grains)	internal grain porosity
AZ	0.5	equiaxed	agglomerates < 7 µm

3.2.2. Abnormal grain growth in alumina

On sintering, grain growth and densification occur simultaneously as intergranular pores are removed through grain-boundary diffusion until, without any exceptions, a few grains start to grow extremely fast (abnormal grain growth) and become excessively large by consuming small matrix grains [31]. Then, further densification is practically impossible, because the majority of the pores are trapped within or between the abnormally grown large grains. It is interesting to outline that the exaggerated grain growth may have deleterious effects on fracture strength, because the large edges of abnormal grains may provide preferred sites for fracture initiation. Thus, from a mechanical viewpoint, the absence of exaggerated grains is required [32].

Abnormal grain growth (AGG) is not one of the intrinsic properties of alumina but rather is an extrinsic property that is controlled by certain impurities that are

introduced during powder synthesis, processing, or sintering. It must be understood that impurities in lab-tape casting facilities are difficult to avoid, while clean rooms are used for industrial purposes. The purity of the alumina powders is 99.7% (see Table 3.2).

When small amounts of glass-forming impurities are introduced, some portion beyond their solubility limit will accumulate at grain boundaries at the final stage of densification, form thin intergranular glass films of thermodynamically stable thickness, and induce the sudden appearance of abnormal grains by increasing the rate of grain-boundary migration abruptly [32]. Some impurities such as MgO pin the grain boundaries and prevent abnormal grain growth as they lowers grain boundary mobility by solid solution-drag. However, proper explanations have not been given to answer why commercially pure Al_2O_3 with purity as high as 99.99% always encounters AGG, if sintered at sufficiently high temperature (1600 °C-1850 °C), regardless of its particle size, size distribution, packing, or sintering conditions.

A commonly used method for determining whether or not such phenomenon takes place is calculating the ratio between the maximum and mean value of grain size, (D_{max}/D_{mean}). When this ratio is larger than 2.72, it is accepted that exaggerated grain growth occurs [10, 33]. A rough observation analysis of the micrograph in Figure 3.8 results in values of $D_{max}/D_{mean} > 10$.

As shown in Figure 3.8 abnormal large grains were present at the surfaces of some laminates. The boundaries of these grains are frequently planar or large grain faceted. In the inner AZ layers no large grains were identified, for the AZ composite, the ZrO_2 particles are effective in pinning the Al_2O_3 grain boundaries, so that abnormal or exaggerated grain growth occurs difficultly. Lange et al. [34] reported that abnormal growth of Al_2O_3 was prevented by the ZrO_2 inclusions at volume fractions > 5%.
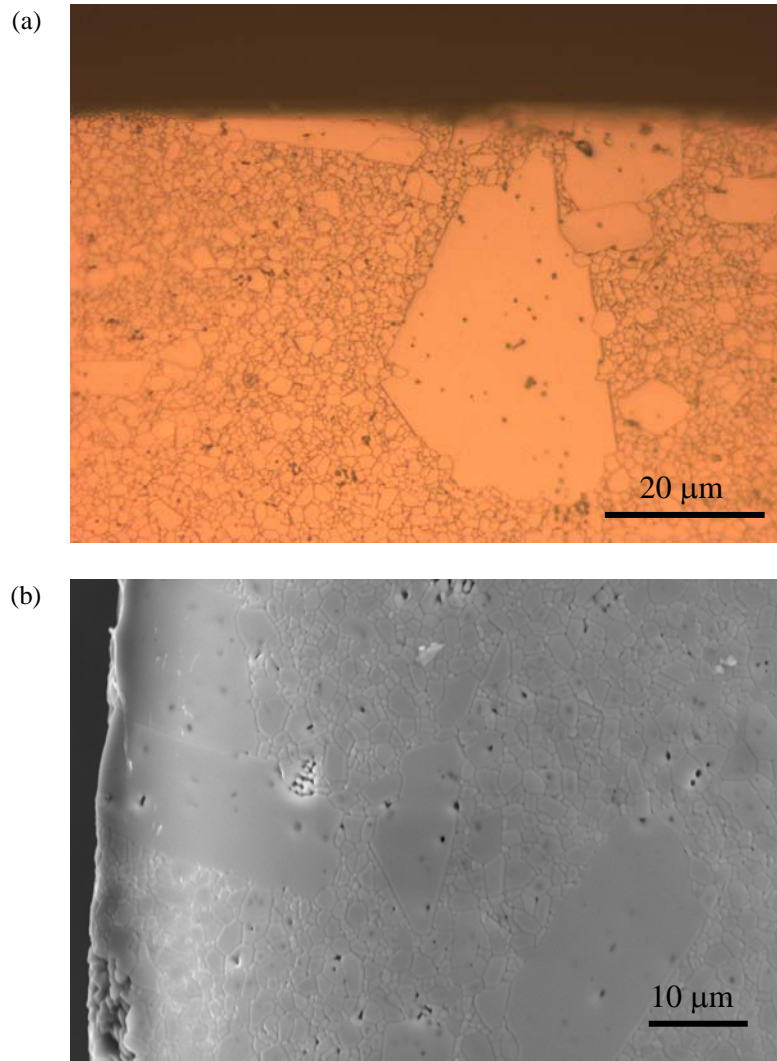
Figure 3.8: Abnormal large grains of alumina after thermal etching at 1375 °C as observed (a) by light microscopy and (b) by SEM. These grains are not due to thermal etching as they were also observed prior to thermal etching.

3.3. Physical properties of the constituents

In this section some basic properties of the constituents: alumina (A) and the alumina/zirconia composite (AZ) are studied.

3.3.1. Density

The density is important in structural ceramics. The higher the porosity is the less the mechanical performance is. Pores are also defects in which environmental effects (corrosion, oxidation,…) can easily take place. However, in laminates thin porous interlayers are occasionally desired since they may act as crack-deflectors [35].

56

To sinter a multilayer made of several materials a compromise has to be adopted since most probably both materials will not sinter at the same temperature. The chosen temperature was 1550 °C which propitiates a high density together with an adequate grain size as shown in Figure 3.6 and Figure 3.7 (if we do not consider the fact that we encounter abnormal large grain of alumina at the surface).

The theoretical densities corresponding to Al_2O_3 and ZrO_2 are $\rho_A = 3.98$ g/cm^3 and $\rho_{ZrO2} = 6.08$ g/cm^3 respectively. The theoretical density of the AZ-composite can be derived from the *rule of mixtures* (let us remember its composition: 60 vol.% Al_2O_3 and 40 vol.% ZrO_2).

$$\rho = \sum_i f_i \, \rho_i \, . \qquad\qquad\qquad \textbf{Eq 3.1}$$

In the rule of mixtures, the density of a composite material ρ can be calculated as the sum, for every phase i, of its volumetric fraction f_i times its density ρ_i. The theoretical density yields $\rho_{AZ} = 4.81$ g/cm^3.

The density of the samples was measured by the Archimedes method at ISTEC Faenza. Alumina laminates (A/A/A/…) present a high relative density between 99.0% - 99.1%. Alumina/zirconia laminates (AZ/AZ/AZ/…) present an almost fully dense microstructure, with a relative density ranging from 99.3% to 99.6%. This high degree of densification is beneficial to retain tetragonal ZrO_2 at room temperature. On the other hand, laminates with alternating materials (A/AZ/A/AZ/…) present a slightly lower density than the constituents, even if they were processed in similar way. The density was found to be between 97.6% and 98.6% for different architectures. It is believed that the densification process is slightly hindered due to a misfit in the densification rate between the A and AZ layers. The densification rate mismatch causes small tensile stresses at high temperature that could even lead to a cavitation damage [36]. Another hypothesis is that the interfaces could hinder in some degree the densification, and therefore the more interfaces are present the lower the density is. Following this idea a polishing procedure was conducted looking for porosity gradients close to the interfaces. No evidence of its existence was concluded.

3.3.2. Elastic Properties

Structural ceramics present a high Young's modulus (*E*), ranging from 300 GPa for Si_3N_4 to 650 GPa for WC, apart from diamond (1000 GPa). The elastic modulus *E*

and the Poisson's ratio ν define the relation between the stress field and the strain field. This section presents the elastic properties as measured by an excitation technique for the monolithic "laminates" (A/A/A... and AZ/AZ/AZ…). Later, and based on those results, the elastic modulus for A/AZ/A/AZ… laminates is commented.

The *impulse excitation technique (IET)* is a resonant-based, non-destructive, standard test method for the determination of the elastic properties of materials at ambient temperatures and also high temperatures [37]. With this technique, a beam-shaped test sample is excited by a mechanical impulse, its vibration is captured, and the digitized vibration signal is processed with a software (IMCE; Diepenbeek, Belgium). This software assigns a vibration of the form,

$$x(t) = x_0 \cdot \mathrm{e}^{-kt} \cdot \sin(2\pi f_\mathrm{r}\, t + \phi)\ ,$$

Eq 3.2

to a predefined number of resonant frequencies, where x and t mean displacement and time respectively. An algorithm simulates the measured signal as a sum of these transient sinusoidal signal components, optimizing iteratively the initial amplitude (x_0), the exponential decay (k), the resonant frequency (f_r) and the phase (ϕ) of every signal component. Having reached a predefined convergence criterion, the software provides the resonant frequencies and associated k values of all the measured vibration modes. An internal friction (Q^{-1}) value is calculated from each k, based on the relation $Q^{-1} = k\,/(\pi\, f)$. Finally, the elastic material properties can be derived from the resonant frequencies of the fundamental flexural and torsional vibration modes, using the formulas of the ASTM standard E 1876-99 [37].

$$E = 0.9465\, \rho\, f_r^{\,2}\, \frac{L^4}{W^2} T_1,$$

Eq 3.3

where ρ is the material density, L the length of the specimen, W the thickness and T_1 is a correction factor which depends on the ratio L/W and the Poisson's ratio. Its value is found in the standard [37].

The elastic modulus is also possible to be measured from the longitudinal response according to [37]

$$E = 4\, \rho\, f_{\mathrm{long}}^{\,2}\, L^2\ .$$

Eq 3.4

The A and AZ monolithic "laminates" were excited in three different vibration modes at room temperature: out-of-plane flexion (*oop*), in-plane flexion (*ip*) and torsional vibration. From each vibration mode it is possible to extract a measurement for the elastic modulus E, the shear modulus μ and the Poisson's ratio ν. The measured elastic properties are exposed in Table 3.6. This values are similar to those previously measured by other authors [38]. The isotropy of the A and AZ "laminates" explains the similar values for E_{oop}, E_{ip} and E_{long}.

Table 3.6: Elastic properties of the monolithic "laminates" as measured by IET.

	E [GPa]			ν	μ [GPa]
excitation	in-plane flexion	out-of-plane flex.	longitudinal		torsional
A/A/A/…	387 ± 9	392 ± 9	392 ± 5	0.24 ± 0.04	158 ± 2
AZ/AZ/AZ/…	305.6 ± 4	306 ± 4	308 ± 2	0.26 ± 0.03	122 ± 1

The elastic modulus *E* was also measured at high temperatures. There is an interest in predicting the residual stresses at medium and high temperatures and therefore *E* and α (CTE) are necessary to be measured as function of temperature. Thus, the laminates were excited in out-of-plane flexural vibration at high temperatures in nitrogen (N$_2$). The employed heating cycle - the aim of which was to simulate as close as experimentally possible the laminate sintering cycle - was the following: heat at 5 °C/min to 1100 °C, later 1 °C/min to 1550 °C, a dwell for 5 min at 1550 °C and cooling at 5 °C/min to room temperature. The results during the heating cycle are presented in Figure 3.9.
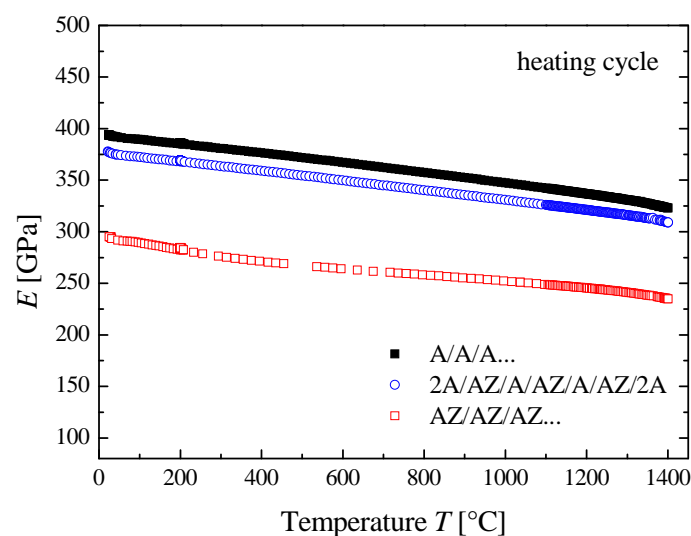
Figure 3.9: Elastic modulus for an A/A/A laminate, an AZ/AZ/AZ laminate and a 2A/AZ/A/AZ/AZ/2A multilayer as a function of the temperature. Measurements were performed by IET test.

As expected, Figure 3.9 reveals that the elastic modulus decays with the temperature. For both materials, it could be approximated by a linear relation, with a slope around 5 GPa every 100 °C.

Elastic properties of laminates

The elastic response of a non-isotropic material depends on the load configuration. This is clearly the case for laminates. Diverse models exist in the literature to estimate E in a composite. The simplest theoretical treatment of the elastic behavior is based on the premise that no interfacial sliding occurs while a stress is applied in a direction contained in the interface plane (Voigt model).
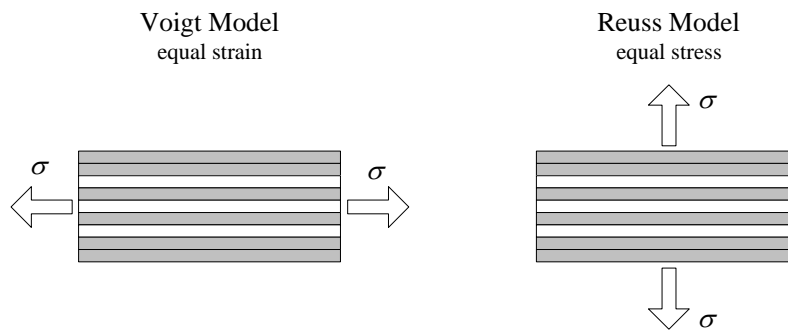
Figure 3.10: Elastic properties depend on the load configuration for composites.

If sliding is not taking place then all layers exhibit the same strain, and the Young's modulus can be written [39]:

$$\overline{E} = (f_A) E_A + (1 - f_A) E_{AZ} , \qquad\qquad \textbf{Eq 3.5}$$

where f_A is the volumetric fraction of A-layers in the laminate.

This well known "Rule of Mixtures" indicates that the composite stiffness is simply a weighted mean between the moduli of the two components, depending only on the volume fraction of the constituents. This equal strain treatment is often called "Voigt Model". A prediction of the transverse stiffness is also possible, assuming the all the layers are constrained with an equal stress in a direction perpendicular to the interface plane (often known as the "Reuss model"). The transversal elastic modulus yields

$$E_{Reuss} = \left[\frac{f_A}{E_A} + \frac{(1-f_A)}{E_{AZ}} \right]^{-1} . \qquad\qquad \textbf{Eq 3.6}$$

An analytical example is given for a laminate with the following stacking order: 2A/AZ/A/AZ/A/AZ/2A. That is, a 7-layer laminate with double-thickness external layers. The thicknesses of the layers were approximately 190 and 220 μm for A and AZ, respectively. The volumetric fraction can be calculated for the A-layers as,

$$f_A = V_A/V = n_A\, t_A\, / \,(n_{AZ}\, t_{AZ} + n_{AZ}\, t_{AZ})\ , \qquad\qquad \text{Eq 3.7}$$

with n being the number of layers and t, the thickness of the layers. For this laminate the volumetric fraction of A is, $f_A = 0.63$ (and consequently $f_{AZ} = 0.37$).The Reuss and Voigt solution is presented in Table 3.7. They are based on the elastic moduli measured for the "layered" monolithics (A/A/A.. and AZ/AZ/AZ..) by longitudinal IET. Additionally, for comparative purposes, experimental results as measured by IET are included for the 2A/AZ/A/AZ/A/AZ/2A laminate are listed.

Table 3.7: Elastic modulus for a 2A/AZ/A/AZ/A/AZ/2A laminate.

model	E_{Reuss} [GPa]	$\overline{E}$ [GPa]	E_{oop} [GPa]	E_{ip} [GPa]	E_{long} [GPa]
A/AZ/A/..	355±15	360±10	377 ± 7	350 ± 6	358 ± 3

Table 3.7 clearly reflects the anisotropic response of the laminate. The experimental measurements E_{long} and E_{ip} are in between E_{Reuss} and $\overline{E}$. In fact, E_{Reuss} and E_{Voigt} represent theoretical bounds (lower and upper) for the elastic modulus. The elastic modulus of a composite for a given load configuration must be between these two limits. It is revealed that the measurent E_{oop} falls out of the theoretical bounds if the uncertainty of the measurement is not considered for E_{Reuss}.

Other elastic properties as the shear modulus G and the Poisson's ratio ν of composites can be predicted in a similar way like the axial and transverse stiffness, using the slab model [39]. This is done by evaluating the net shear strain induced when a shear stress is applied to the composite, in terms of the individual displacement contributions from the constituents

$$\mu_{A/AZ} = f\, \mu_A + (\, 1\text{-}f\,)\, \mu_{AZ}\ , \text{and} \qquad\qquad \text{Eq 3.8}$$

$$\nu_{A/AZ} = f\, \nu_A + (\, 1\text{-}f\,)\, \nu_{AZ} \qquad\qquad\qquad \text{Eq 3.9}$$

which is again the "rule of mixtures".

Table 3.8: Shear modulus and Poisson ratio for a 2A/AZ/A/AZ/A/AZ/2A laminate (rule of mixtures).

	$\mu_{A/AZ}$ [GPa]	$\nu_{A/AZ}$
2A/AZ/A/..	143.13 – 146.17	0.211 – 0.283

Additionally, Young's Modulus measurements in laminates have been conducted by means of an alternative method: a three-point bending test. The elastic modulus can be determined for a thin beam from the slope of the load P-deflection δ curve as [40]

$$E = \frac{a(3S_1 x - 3x^2 - a^2)}{12\,I} \frac{\Delta P}{\Delta\delta} \; , \qquad\qquad \textbf{Eq 3.10}$$

where I is the moment of inertia, S_1 is the span length and x is the position, $a \le x \le S_1/2$ at which the deflection δ is measured. Most commonly, δ is measured either at the centre, $x = S_1/2$ or at the position of load application, $x = a$. For a rectangular beam, I is $I = BW^3/12$ where B is the width of the specimen and W is its thickness.

In this case measurements were conducted in a 3-layer laminate: 3A/6AZ/3A. The thickness of the layers were 350 µm (A), 970 µm (AZ) and 350 µm (A) respectively. Figure 3.11 shows the load-deflection curve from whose slope the elastic modulus can be extracted. The results are compared with the predictions from Reuss and Voigt in Table 3.9. The results fit well.
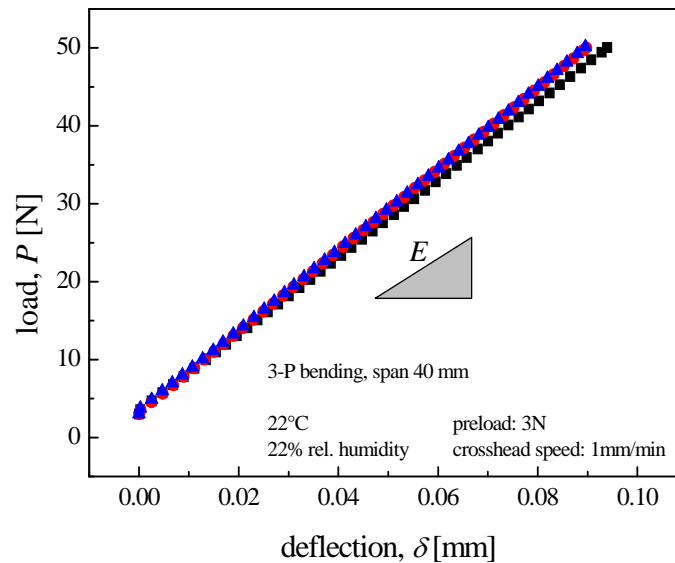
Figure 3.11: Measurements of the elastic modulus on 3A/6AZ/3A samples by means of a 3-point bending test (three tests). The slope is related to the elastic modulus.

Table 3.9: Elastic modulus of a 3A/6AZ/3A laminate calculated analytically by the rules of mixtures and measured experimentally by bending tests.

analytical models		$E_{\text{3-P bending}}$ [GPa]	
E_{Reuss} [GPa]	$\overline{E}$ [GPa]	*sample # 11*	*sample # 12*
337	342	338	342

3.3.3. Thermal expansion: α or CTE

The thermal expansion characterization of the layers has a vital importance. The thermal expansion mismatch, $(\alpha_A - \alpha_{AZ})$, will define the strain mismatch that origins the residual stress state. The technical thermal expansion was measured in both, "laminated" alumina and the AZ-composite by dilatometry. The coefficients of thermal expansion were measured between room temperature and different temperatures in two ways: a quasi-static measurement and a dynamic measurement (2 °C/min). The equipment used was a dilatometer Netzsch 402-E/7.
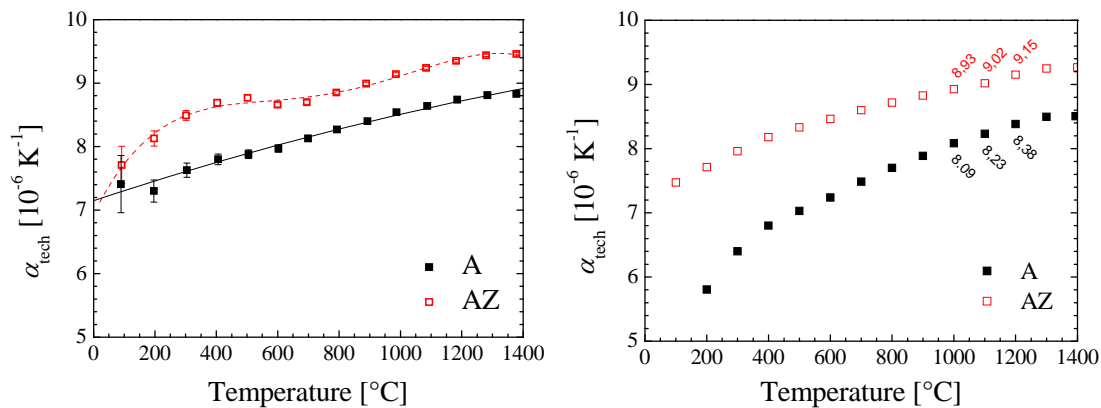
Figure 3.12: Coefficient of thermal expansion as measured: (a) quasi-statically and (b) dynamically (2°C/min). In order to calculate α_{tech} the lower temperature is the room temperature.

The values obtained in the quasi-static mode are considered more realistic and they will be used in the subsequent calculations. The technical thermal expansion mismatch calculated as the difference $(\alpha_A - \alpha_{AZ})$ is presented in Table 3.10. In order to calculate the technical thermal expansion, the room temperature was considered the reference temperature.

Table 3.11: Technical thermal expansion mismatch

		Temperature [°C]		
		1000	**1100**	**1200**
$\Delta\alpha_{\text{tech}} = (\alpha_A - \alpha_{AZ})$ [10^{-6}/K] (measured from T_{room} to the corresponding temperature)	static measurement	0.60	0.60	0.61
	dynamic measurement	0.84	0.79	0.77

Even more interesting, the strain mismatch that occurs upon cooling could be directly measured from the dilatometry. First, it is necessary to define a reference temperature, often known as "frozen stresses temperature" which defines the temperature where the stresses arise since they can not be relaxed anymore at high temperature. This temperature was determined to be 1160 °C by measuring the strength of different unsymmetrical architectures (see description in Chapter 4).

Once the reference temperature is chosen, considering bars of the layer's materials with a same length at the "frozen stress temperature" and cooling them, the strain mismatch can be measured at room temperature as presented in Figure 3.13. In this case, the strain mismatch yields $\Delta\varepsilon = \varepsilon_A - \varepsilon_{AZ} = -8.0 \cdot 10^{-4}$ (measured from 1160 °C to 50 °C).
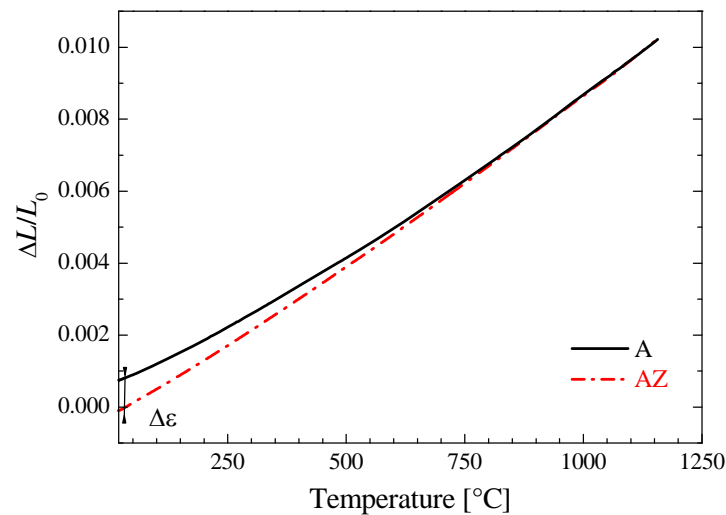
Figure 3.13: Strain mismatch $\Delta\varepsilon$ as measured by dilatometry.

3.3.4. Hardness

Hardness is recognized as one of the "properties" that make ceramics attractive for certain applications; i.e. applications involving wear. Hardness in our laminates has been measured by means of an indentation tester Zwick 3212B. Tests were performed using a Vickers indenter and loads ranging from 0.5 kg to 15 kg. The hardness was calculated through the following relation

$$\text{HV}[\text{MPa}] = 1.8544 \, \frac{P}{d^2} \,, \qquad \qquad \textbf{Eq 3.11}$$

where HV is the Vickers hardness in MPa, P is the applied load in N and d is the diagonal average in mm^2.

Alumina hardness has been measured in the outer layers, while AZ-hardness after indenting in a cross-section. The results are presented in Table 3.12 together with the corresponding standard deviation (after a minimum of five measurements, except for 100 and 150 N after three measurements). Table 3.12 evidences how AZ is clearly softer than A.

Table 3.12: Vickers hardness of alumina (A) and toughened-zirconia alumina (AZ) for different loads P.

		P [N]				
		10	30	50	100	150
A	HV [GPa]	19.33 ± 0.46	17.37 ± 1.11	17.28 ± 0.93	17.76 ± 0.40	16.82 ± 0.75
AZ	HV [GPa]	17.29 ± 0.19	15.98 ± 0.29	15.79 ± 0.14	-	-

Additionally, these results were part of a round robin on hardness. Four partners (ISFK Leoben, Polytechnic University of Barcelona (Mr. Jimenez), ISTEC Faenza (Mr. De Portu) and Slovak Academy of Sciences in Kosice (Mr. Dusza)), measured the hardness on identical specimens that were machined in a similar way. The results are presented in Figure 3.14.
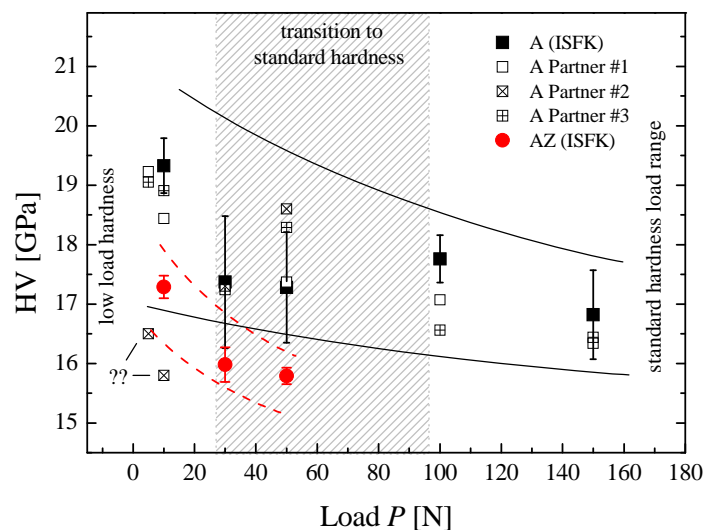
Figure 3.14: Hardness of A and AZ. Results of a round robin.

Figure 3.14 shows what is called the "indentation size effect" or the volume/load dependence of hardness. It occurs when this property is determined by an indenter. Hardness increases as the applied load decreases, because the volume of material used to yield is smaller and the mechanism for yielding is dependent on a volume term

which becomes more significant as the indent size decreases. The most obvious development of this idea is that the shallow near-surface volume of the deformation zone can become a significant fraction of the total affected volume when a very small load is used to make the indent. Thus, work hardened layers, surface compressed layers, ion-implanted layers, and the possibility of chemical reactions between the atmosphere and the surface can dominate the yielding mechanism to produce nonstandard hardness values [41].

In this study, differences in hardness were investigated between alumina free of stresses and a compressive stressed alumina (about -140 MPa) by means of a Vickers indenter. The theoretical influence of the residual stress on hardness was not observable due to the scatter in the measurements. Jiménez-Pique [42] also could not observe any hardness difference for the two layers after evaluation of nano-indentations.

The hardness has also been evaluated with a Knoop indenter for alumina

$$H_K [MPa] = 14.229 \frac{P}{d^2}$$ **Eq 3.12**

where H_K is the Knoop hardness in MPa, P is the load in N and d is the long diagonal in mm. The measurement resulted in 16.52 ± 0.33 MPa.
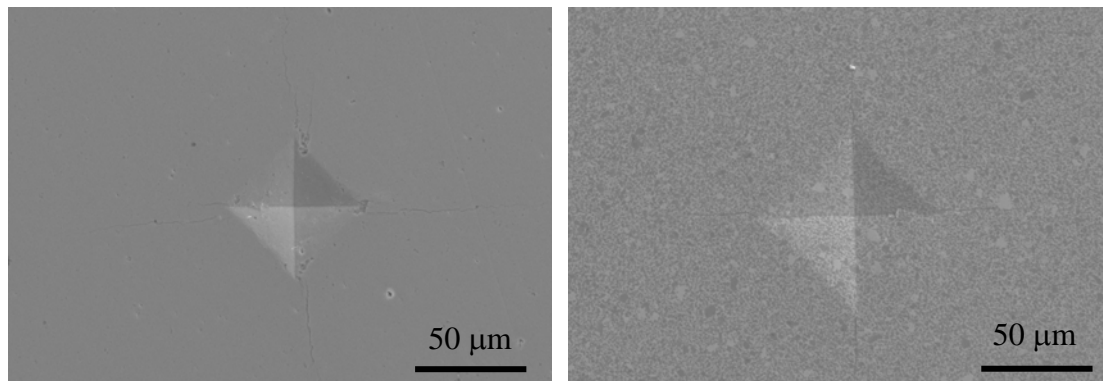
Figure 3.15: SEM micrographs of indentation in (a) alumina and (b) the AZ composite (both 3 kg load).

3.4. The third constituent: The interface

Strength or toughness for a layered structured may be defined by the properties at the interface if they are weaker than in the matrix. Gutierrez et al. [20, 43] have previously characterized the interface between alumina and AZ. Their experience

showed that interfaces or joints between alumina and zirconia-toughened alumina are strongly bond. It has been demonstrated that A and AZ can be joined by *superplasticity* at temperatures as low as 1350 °C [20]. The mechanism responsible for superplasticity in AZ is grain-boundary sliding. Grains of two different polycrystalline samples put together and deformed under superplastic conditions will slide and rotate, interpenetrating to form a high-strength bond, which is indistinguishable when identical materials are joined (superplastic joining of structural ceramics has proved to be a successful technique for fabrication of complex shaped components starting from simpler previously sintered geometries).

A SEM analysis was conducted on the interface (see Figure 3.16). The micrographs do not show poor joining or an increased porosity close to the interface. It is easy to observe the difference in grain size between the alumina and the AZ-composite. The interfaces are straight with a "roughness" in the order of the grain size (a few microns).

(a)

10 μm

(b)

5 μm
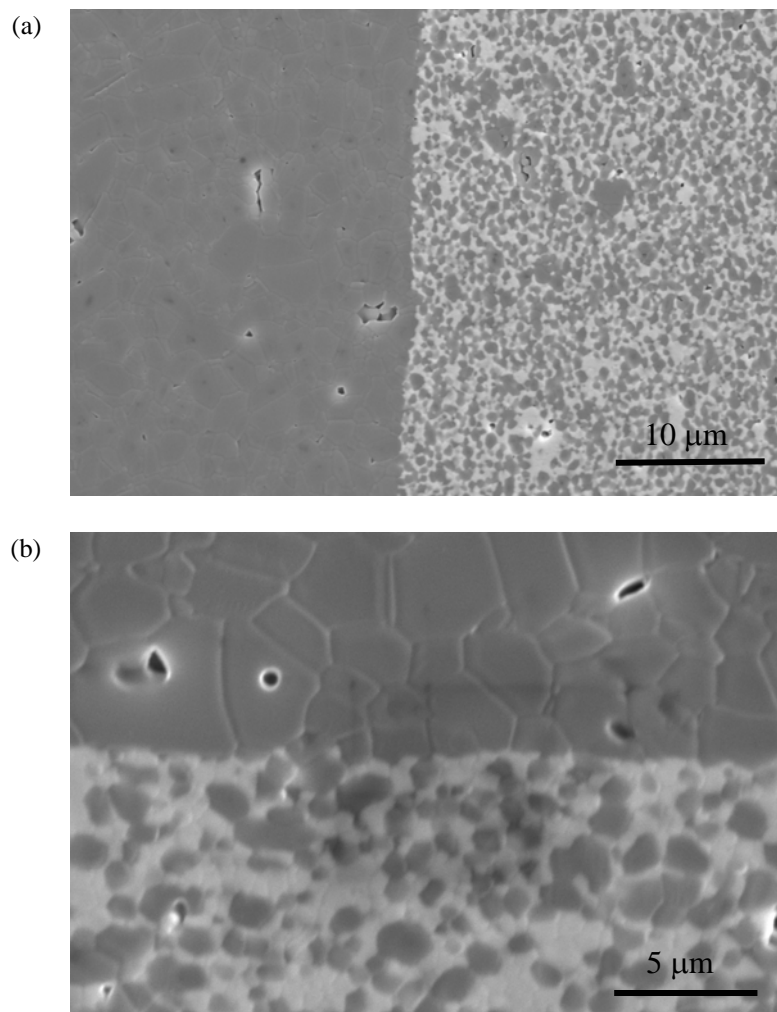
Figure 3.16: SEM-micrographs of an A/AZ interface. No relevant defects were observable at the interface.

Even tough a clean room was not used for the processing of the laminates no impurities were found at the interfaces (probably, one of the main drawbacks concerning tape casting is that clean rooms are convenient). Exceptionally, a very small specimen (cross-section about 1 mm x 0.5 mm) broke during ultrasounds cleaning at the interface. A SEM-micrograph of it is shown in Figure 3.17. Something like an impurity or probably an agglomerate of alumina was evidence.

Some experimental work was conducted to understand the mechanical response of the A/AZ interface. Based on the experience of prior works, it was expected to find a strong interface as it was observed.
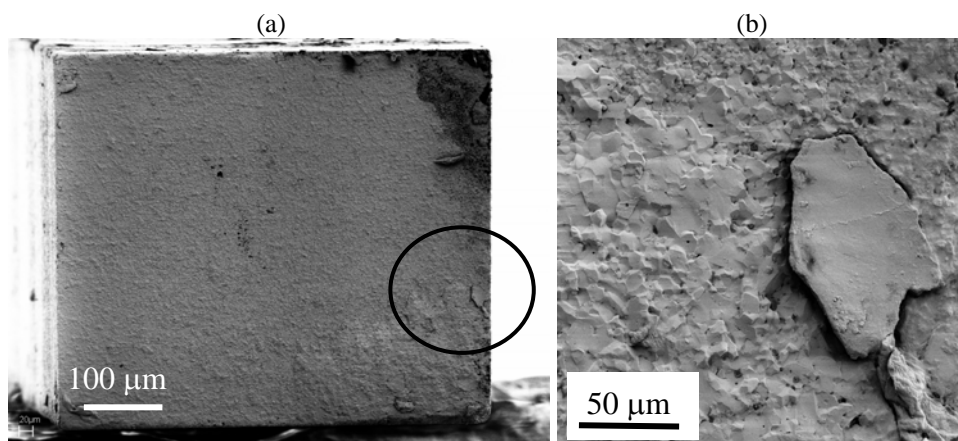
Figure 3.17: 95% interface failure due to an agglomerate or impurity (a) x300, (b) x1500.

Vickers indentations were imprinted as close as possible to the interface (see Figure 3.18). The interaction between the cracks arising from the indentation corners and the interface was analyzed. Cracks propagating through the interface were not observed. Figure 3.18a shows one of the cases in which the cracks propagated closer to the interface, but anyway after a short distance the crack popped out of the interface. It is noticeable that sometimes the indentation cracks did not appear at the corner but at the intersection between the indentation and the interface.

(a)

(b)
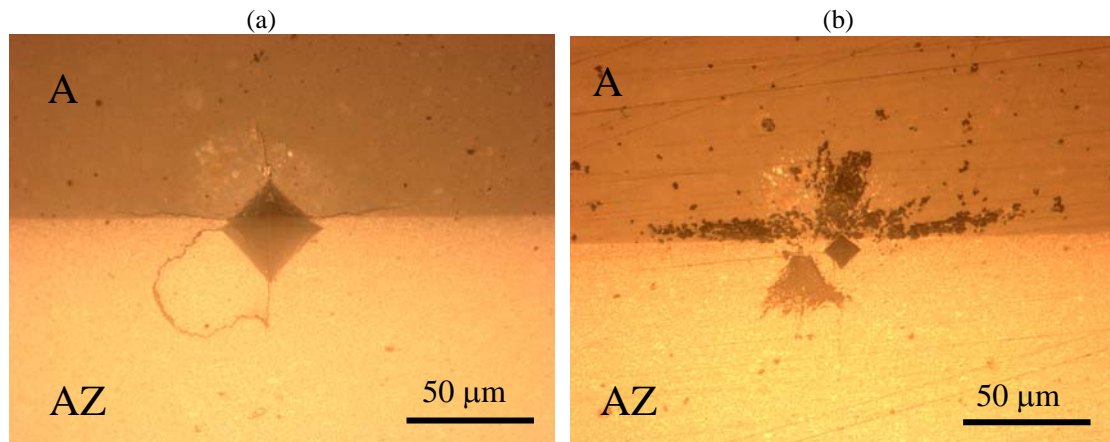
Figure 3.18: Vickers indentation close to the interface: (a) cracks originating from the indentation do not interact with the interface (also a chip due to a sub-surface lateral crack is present). (b) Damage is mainly observed in the A-layer after polishing the indented surface.

An investigation of the sub-surface under the indentation was carried out by polishing carefully the surface of the indented surface (see Figure 3.18b). It can be clearly observed how the magnitude of the damage caused in the A-phase is much higher than in the AZ-phase (some damage is observed in the AZ layer but is due to a lateral crack). The radial cracks do not seem to interact with the interface in the sub-surface and they seem to affect exclusively the A-layer.

Imprints were also produced by means of a Knoop indenter showing the same behavior: the cracks do not run through the interface. Exceptionally, a somehow anomalous behavior of the cracks close to the interface was observed. In a three-layer laminate indentations placed close to the interface in the central AZ-layer cross through the interface and grow extremely.

A polishing procedure parallel to the indented surface resulted in even longer cracks, probably artificially due to the material removing process. It could also be observed how the damage was transferred to the external alumina layer.

A polishing procedure perpendicular to the indented surface clearly shows how the median crack bends and propagates to the adjacent layer without interacting with the interface, similar to an edge-chipped crack. Same loads were applied at a shorter distance from the edge - therefore in the alumina layer - and chipping-like cracks were not evidenced.
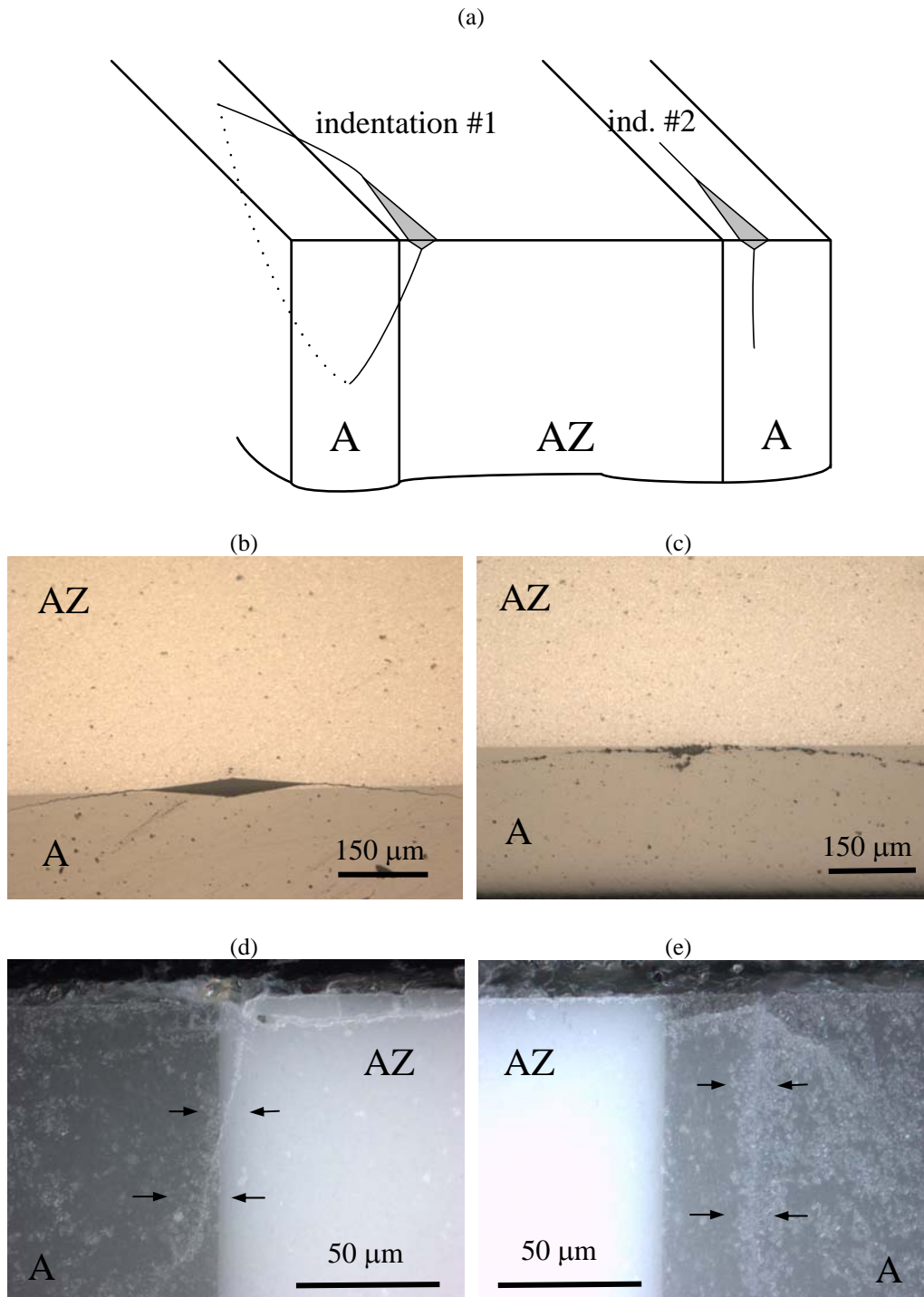
Figure 3.19: (a) Sketch of Knoop indentations performed in a trilayer. (b) Indentations applied in the central layer deflect to the surface layer. This effect is shown in (c) by polishing the indented plane and in (d) by polishing perpendicularly to the indented plane (in a different indentation). (e) shows the conventional behavior of an indentation placed in the outer A-layer.

Additionally, 3-point bending tests were performed in a mini-device applying a load parallel to the interfaces. Notches were produced as close as possible to the interface with a first idea to measure interfacial toughness. This was not possible since the specimens did not fail at the interface. Indeed they always failed in the alumina layer which has a lower strength than the AZ-composite. Two characteristic fracture paths are presented in Figure 3.20. It shows the notch from which the fracture originates and how the crack propagated through the A-layer. For the specimen in the right, (c), the crack seems to run along the interface but it failed through the A-layer as could be demonstrated by scanning electron microscopy.
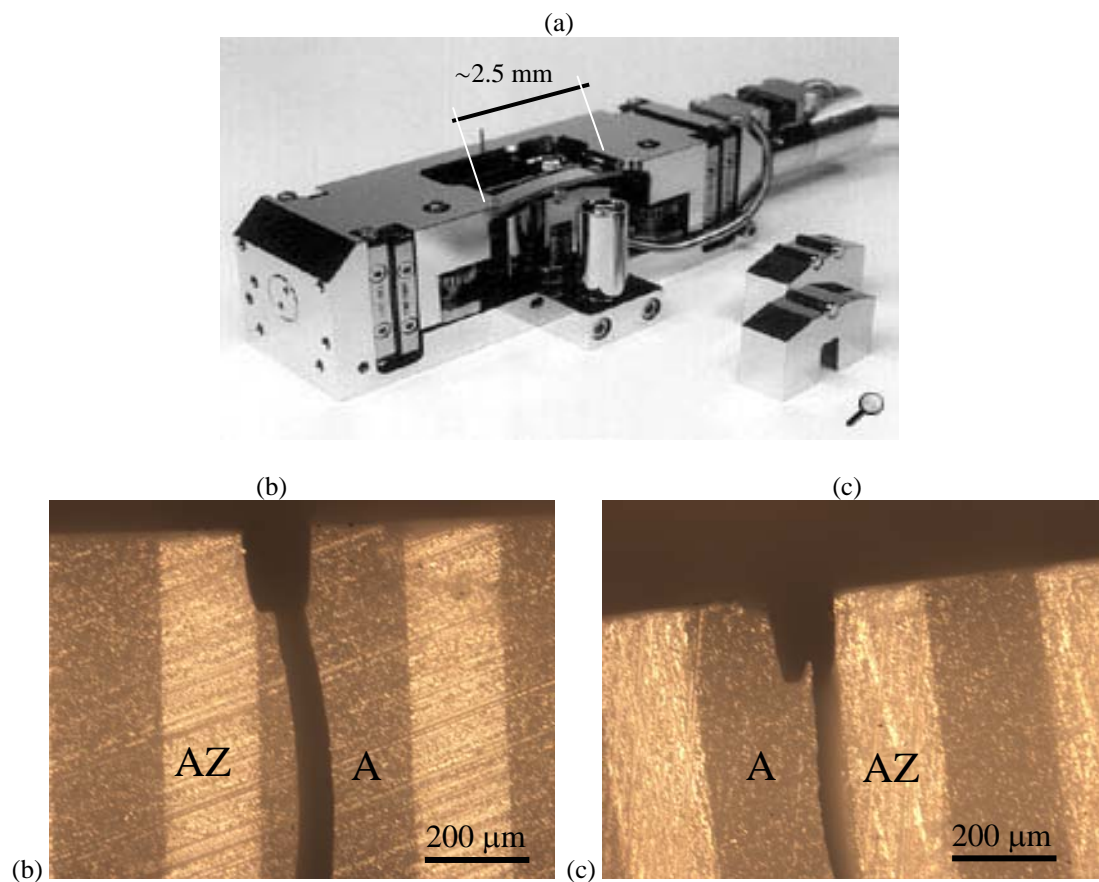
Figure 3.20: (a) Mini bending module used for conducting the 3-point bending tests which has a span length 2.5 mm. (b) and (c) Characteristic path fracture. Note that (c) is NOT an interfacial fracture.

3.5. Literature

[1]   Tarlazzi, A., Roncari, E., Pinasco, P., Guicciardi, S., Melandri, C., de Portu, G., "Tribological behaviour of Al_2O_3/ZrO_2-ZrO_2 laminated composites", Wear, **24**, 29 - 40, (2000).
[2]   Toschi, F., Melandri, C., Pinasco, P., Roncari, E., Guicciardi, S., de Portu, G., "Influence of residual stresses on the wear behavior of alumina/alumina-zirconia laminated composites", Journal of the American Ceramic Society, **86**, 1547-1553, (2003).
[3]   Munz, D., Fett, T., "Ceramics. Mechanical properties, failure behaviour, materials selection", Springer, (1999).

[4]   Gitzen, W. H., "Alumina as a Ceramic Material", (1970).

[5]   Morrell, R., "Section 1 High-alumina ceramics" in: Handbook of properties of technical & engineering ceramics. HMSO, **Part 2 Data Reviews**, (1987).

[6]   Stevens, R., "Zirconium oxide" in: Cahn, R.W., Brook, R.J. Encyclopedia of materials science and engineering. Pergamon press, 2965-2971, (1993).

[7]   Hannink, R., Kelly, P. M., Muddle, B. C., "Transformation toughening in zirconia-containing ceramics", Journal of the American Ceramic Society, **83**, 461-487, (2000).

[8]   Lange, F., "Transformation toughening: part 5, Effect of temperature and alloy on fracture toughness", Journal of Materials Science, **17**, 225-262, (1982).

[9]   Chevalier, J., "What future for zirconia as a biomaterial?" Biomaterials, **27**, 535-543, (2006).

[10]   Casellas, D., Nagl, M. M., Llanes, L., Anglada, M., "Fracture toughness of alumina and ZTA ceramics: microstructural coarsening effects", Journal of Materials Processing Technology, **143-144**, 148-152, (2003).

[11]   Garvie, R. C., Hannink, R., Pascoe, R. T., "Ceramic steel?" Nature, **258**, 703-704, (1975).

[12]   Claussen, N., "Fracture toughness of Al_2O_3 with an unstabilized ZrO_2 dispersed phase", Journal of the American Ceramic Society, **59**, 49-51, (1976).

[13]   Charalambides, P. G., McMeeking, R. M., "Near-tip mechanics of stress-induced microcracking in brittle materials", Journal of the American Ceramic Society, **71**, 465-472, (1988).

[14]   McMeeking, R. M., Evans, A. G., "Mechanics of transformation-toughening in brittle materials", Journal of the American Ceramic Society, **65**, 242-246, (1982).

[15]   Heuer, A., "Transformation toughening in ZrO_2-containing ceramics", Journal of the American Ceramic Society, **70**, 689-698, (1987).

[16]   Han, L. X., Warren, R., Suresh, S., "An experimental study of toughening and degradation due to microcracking in a ceramic composite", Acta mett mater, **40**, 259-274, (1992).

[17]   Rühle, M., Claussen, N., Heuer, A., "Transformation and microcrack toughening as complementary processes in ZrO_2-toughened Al_2O_3", Journal of the American Ceramic Society, **69**, 195-197, (1986).

[18]   Conoci, S., Melandri, C., De Portu, G., "Tape casting: A technique for preparing and studying new materials". In: Novel ceramic fabrication processes and applications. (Shelton, Stoke-on-Trent. UK., British Ceramic Proceedings) (1986).

[19]   Fiori, C., De Portu, G., "Fabrication, microstructure and properties of ZrO_2-toughened Al_2O_3 substrates, advances in ceramics". In: Science and Technology of Zirconia III. (Columbus OH, USA, The Am. Ceram. Soc. Inc.,) (1988).

[20]   Gutierrez-Mora, F., Goretta, K. C., Majumdar, S. H., Routbort, J. L., Grimdisch, M., Dominguez-Rodriguez, A., "Influence of internal stresses in superplastic joining of zirconia toughened alumina", Acta Materialia, **50**, 3475-3486, (2002).

[21]   Sone, T.-W., Han, J.-H., Hong, S.-H., Kim, D.-Y., "Effect of surface impurities on the microstructure development during singtering of alumina", Journal of the American Ceramic Society, **84**, 1386-1388, (2001).

[22]   Szutkowska, M., Boniecki, M., "Subcritical crack growth in zirconia-toughened alumina (ZTA) ceramics", Journal of Materials Processing Technology, **175**, 416-420, (2006).

[23]   Novak, S., Kalin, M., Lukas, P., Anne, G., Vleugels, J., Van der Biest, O., "The effect of residual stresses in functionally graded alumina-ZTA composites on their wear and friction behaviour", Journal of the European Ceramic Society, **27**, 151-156, (2006).

[24]   Bartolome, J. F., Pecharromán, C., Moya, J., Martín, A., Pastor, J. Y., Llorca, J., "Percolative mechanism of sliding wear in alumina/zirconia composites", Journal of the European Ceramic Society, **26**, 2619-2625, (2006).

[25]   Magnani, G., Brillante, A., "Effect of the composition and sintering process on mechanical properties and residual stresses in zirconia-alumina composites", Journal of the European Ceramic Society, **25**, 3383-3392, (2005).

[26]   Tekeli, S., "Effect of Y_2O_3 content on cavity formation in ZrO_2-based ceramics", Materials Letters, **57**, 715-719, (2002).

[27]   Li, J., Zhang, L., Shen, Q., Hashida, T., "Degradation of yttria stabilized zirconia at 370 K under a low applied stress", Material Science and Engineering A, **297**, 26-30, (2001).

[28]   Merlani, E., Schmid, C., Sergo, V., "Residual stresses in alumina/zirconia composites: Effect of cooling rate and grain size", Journal of the American Ceramic Society, **84**, 2962-2968, (2001).

[29]   Cai, P., Green, D. J., Messing, G. L., "Constrained densification of alumina/zirconia hybrid laminates, I: Experimental observations of processing defects." Journal of the American Ceramic Society, **80**, 1929-1939, (1997).

[30]   Jimenez-Melendo, M., Clauss, C., Dominguez-Rodriguez, A., Sánchez-Herencia, A. J., Moya, J., "Microstructure and high-temperature mechanical behavior of alumina/alumina-yttria stabilized tetragonal zirconia multilayer composites", Journal of the American Ceramic Society, **80**, 2126-2130, (1997).

[31]   Chiang, Y. M., Birnie, D. P., Kingery, W. D., "Physical ceramics", John Wiley & Sons, (1997).

[32]   Bae, I. J., Baik, S., "Abnormal grain growth of alumina", Journal of the American Ceramic Society, **80**, 1149-1156, (1997).

[33]   Kurtz, S. Z., Carpay, F. M. A., "Microstructure and normal grain growth in metals and ceramics. Part I: theory", Journal of Applied Physics, **51**, 5725-5744, (1980).

[34]   Lange, F., Hirlinger, M. M., "Hindrance of grain growth in Al_2O_3 by ZrO_2 inclusions", Journal of the American Ceramic Society, **67**, 164-168, (1984).

[35]   Blanks, K. S., Kristoffersson, A., Carlström, E., Clegg, W. J., "Crack deflection in ceramic laminates using porous interlayers", Journal of the European Ceramic Society, **18**, 1945-1951, (1998).

[36]   Green, D. J., Cai, P., Messing, G. L., "Residual stresses in alumina-zirconia laminates", Journal of the European Ceramic Society, **19**, 2511-1517, (1999).

[37]   "Standard test method for dynamic Young's modulus, shear modulus, and Poisson's ratio by impulse excitation of vibration", ASTM Standard, **E**, (1999).

[38]   Radovic, M., Lara-Curzio, E., Riester, L., "Comparison of different experimental techniques for determination of elastic properties of solids", Materials Science and Engineering A, **368**, 56-70, (2004).

[39]   Hull, D., Clyne, T. W., "An introduction to composite materials", Cambridge university press, (1996).

[40]   843-2, E., "Advanced technical ceramics - Monolithic ceramics. Mechanical properties at room temperature - Part 2: Determination of Young's modulus, shear modulus and Poisson's ratio", European Standard, .

[41]   Malzbender, J., "Comment on hardness definitions", Journal of the European Ceramic Society, **23**, 1355-1359, (2003).

[42]   Jimenez-Piqué, E., "Personal Communication" personal communication, (2006).

[43]   Gutierrez-Mora, F., Singh, D., Chen, N., Goretta, K. C., Routbort, J. L., Majumdar, S. H., Dominguez-Rodriguez, A., "Fracture of composite alumina/yttria-stabilized zirconia joints", Journal of the European Ceramic Society, **26**, 961-965, (2006).

Chapter 4. Residual Stresses in A/AZ Laminates

4.1. Introduction

As presented in Chapter 2, residual stresses, if compressive at the surface, can importantly improve the mechanical properties. Not only classic applications like ion-exchange glasses [1] or flame hardened steels [2] (for nuclear steam turbine blades) but also novel complex structures like thermal barrier coatings [3] or multilayer structures can benefit from surface residual stresses. Examples of ceramic multilayer structures can be solid oxide fuel cells (SOFC) [4], capacitors [5] or piezo-stacks [6]. The understanding of the residual stress state, especially for complex structures, is one of the pillars of their design. Residual stresses have a vital influence during processing stage - they could even prevent its manufacturing (delamination) - and later in service.

One example of a functional device in which the residual stresses must be considered during the structural design are briefly presented. Firstly, the case of solid oxide fuel cells (SOFCs) which are electrochemical devices for high efficiency energy conversion. Besides the electrochemical criteria, e.g. power density and degradation, the mechanical integrity of the electrolyte under service conditions and during thermal cycling is crucial for the successful operation of the cell. To ensure a failure free electrolyte layer during manufacturing and operation, critical tensile stresses which
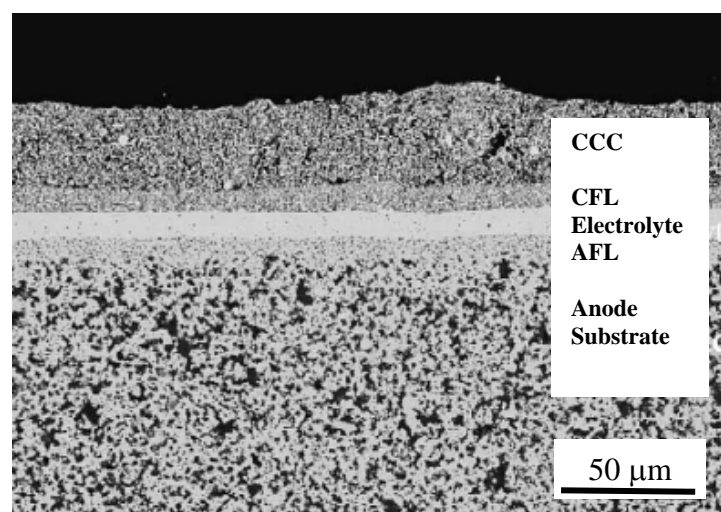
Figure 4.1: Cross-section of a SOFC cell, a multilayer device for energy conversion. CCC is the cathode current collector and CFL is the cathode functional layer (both made of lanthanum strontium manganite with different densities). AFL is the anode functional layer (made of ZrO_2/NiO as well as the substrate but more densified). The electrolyte is made of yttria-stabilized zirconia [4].

exceed the fracture stress have to be avoided. In this respect, a thermal mismatch stress which keeps the electrolyte layer under compression appears to be advantageous [4].

Chapter 4 will introduce the reader on residual stresses appearing in ceramic multilayers. It explains how they appear, introduces the most usual techniques to measure them, and presents analytical and experimental results on the A/AZ laminates concerning this doctoral work.

4.1.1. Nature of the residual stresses

4.1.1.1 Densification mismatch stresses

The literature offers few information about densification mismatch stresses at high temperature [7-10] but they can be relevant. In fact, Green et al. [7] measured stresses around 1-2 MPa that were sufficient to cause some cavitation damage.

Because at high temperature the layers do not behave elastically, residual stresses cannot be directly evaluated according to Equation 2.3 presented in Chapter 2. Nevertheless, a simple linear viscous constitutive relationship is sufficient to model the mechanical response of a sintering compact (this is consistent with models for diffusional creep which yield a linear correlation between stress and strain rate).

The stresses in viscous layers can be calculated from the Equation 2.3 introduced in Chapter 2 using the analogy between Hooke's law (linear elasticity) and Newton's law (linear viscosity). It is only necessary to replace the elastic modulus E', by the uniaxial viscosity $\dot{E}'$, and the strain mismatch $\Delta\varepsilon$, by the mismatch in strain rate, $\Delta\dot{\varepsilon}$.

A calculation by Cai and Green [7] is shown in Figure 4.2. The data primarily reflects the mismatch in strain rate for the unconstrained layers. Interestingly, it was predicted that residual stresses may also occur at the maximum sintering temperature but the bodies will be more coherent in this final densification stage. The densification stresses are low but are close enough to the stress that produces de-sintering or other mechanisms. Microstructural observations after laminate processing identified linear arrays of voids in the tensile layer and these voids appeared to be nucleation sites for tunnel cracks that formed for some of the laminates during cooling. These pores are similar to the creep cavitation damage observed in ceramics.
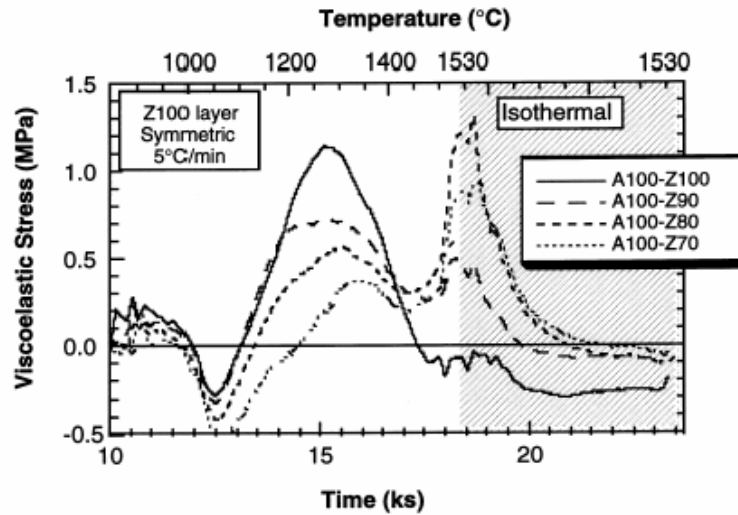
Figure 4.2: Viscoelastic stresses during a sintering cycle for A/AZ multilayers [7] (different lines correspond to different A/AZ laminates). Initially a constant heating rate is applied: 5 °C/min, later the temperature is kept at the sintering temperature. At the highest temperature, 1530 °C; stresses of about 1.5 MPa appear for the A100-Z80 laminate, which contains 20 wt.% Al_2O_3 in the AZ composite. The stresses relaxed after some time at high temperature due to viscous flow.

Green [7] formed alumina tapes into uniaxial tensile specimens. These specimens were then subjected to stresses up to 2 MPa, while being subjected to the standard firing cycle. Damage was observed with almost identical morphology to that seen in the laminates, confirming that damage can arise in laminates during densification even at tensile stresses of ~ 1 MPa.

Gurauskis et al. [11] have experimentally confirmed that the green densities of the tapes can be adjusted to minimize the strain mismatch at high temperatures while keeping an adequate strain rate mismatch. They adjusted the compositions of the slurry by interpreting dilatometer and sintering kinetics curves for monolithic samples (see Figure 4.3).
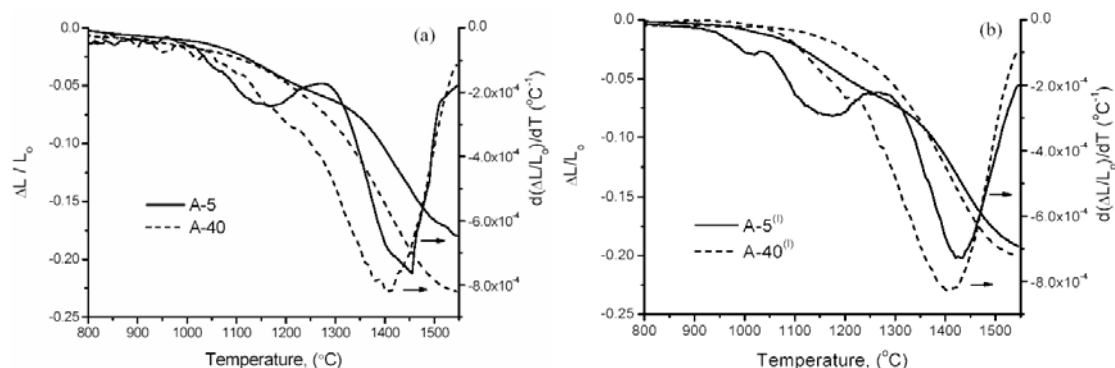
Figure 4.3: Dilatometer and sintering kinetics curves for monolithic samples: (a) samples with non-adjusted green densities. (b) Samples with adjusted green densities: observe the similar $\Delta L/L_0$ between A-5$^{(I)}$ and A40$^{(I)}$ at high temperature. Interesting to note is that the large strain rate mismatch happens at high temperature (~1300°C).

4.1.1.2. Macroscopical stresses

The existing bibliography reveals that different concepts have been used in order to create an internal stress state. In the most popular cases, the strain mismatch is mainly introduced during processing by a phase transformation [12] or a thermal coefficient mismatch [13]. Figure 4.4 plots dilatometric curves where the strain mismatch that happens during cooling upon the sintering temperature is observable at room temperature. Figure 4.4 represents, firstly, a mismatch strain due to a thermal expansion mismatch and secondly, a strain mismatch due to a phase transformation.
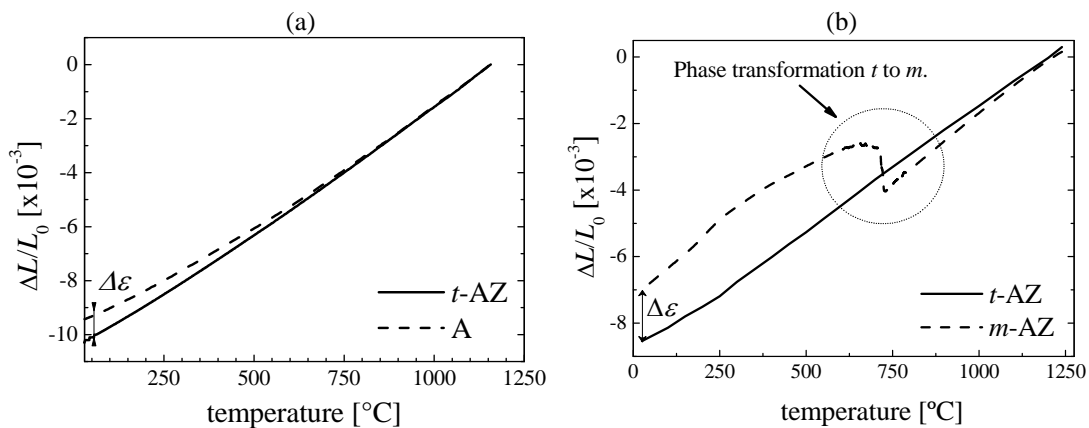
Figure 4.4: During cooling upon the sintering temperature a strain mismatch appears. Two examples are plotted: (a) A couple of tapes made of *t*-AZ and A which present a thermal expansion coefficient mismatch. (b) The tetragonal to monoclinic phase transformation of ZrO_2 is responsible of the mismatch strain in a layer in which the zirconia is stabilized [14].

Figure 4.4a presents the strain mismatch for the family of laminates that concerns to this study, alternate layers of alumina (A) and zirconia-toughened alumina (AZ). Two layers - with the same length at the temperature when the residual stresses cannot be relaxed anymore and therefore appear - will contract in a different way resulting in a strain mismatch at room temperature. In this case, the strain mismatch is just an approximation since the frozen stress temperature - the temperature at which the residual stresses appears - is unknown.

The second case, Figure 4.4b, presents a dilatometric curve corresponding to a laminate that alternates different layers of zirconia-toughened alumina. Some of the layers contain unstabilized zirconia that will transform during cooling, while the other layers contain an Y_2O_3-stabilized zirconia and thus a strain mismatch occurs during cooling. The zirconia is the most popular material to benefit of a phase transformation. The magnitude of this transformation can be controlled by adding small amounts of stabilizer like Y_2O_3 or CaO, among others. If the addition is not sufficient to completely stabilize the high temperature phase, the transformation strain

will decrease as dopant amount increases [15]. Residual stresses due to this technique are "independent" of the temperature, at least below the transformation temperature.

4.1.2. Measuring residual stresses

Residual stresses may be assessed by means of different experimental techniques. For this purpose, several destructive or nondestructive methods based on different physical principles have been developed [16]. Some of the techniques, especially those based on different diffraction methods are commented in the following. Others, just referred, for example, the instrumented indentation method [17-19], the Hertzian indentation method [20, 21] or the hole drilling method [22, 23]

Diffraction based techniques are potential non-destructive probes for residual strains and stresses. However, for non-destructive investigations the techniques are restricted in terms of the radiation's penetration power, which is typically 5-10 μm in typical structural ceramics. Hence, non-destructive investigations are limited to measurements of surface stresses. Advanced techniques such as synchrotron radiation allow a larger penetration depth.

The *classic X-ray diffraction method* ($\sin^2 \psi$ *method*) [24, 25] as all diffraction techniques is based on the difference in interplanar spacing for unstressed and stressed lattices. Assuming that a layer - or film - is isotropic and the stress state is biaxial, residual stress in the film can be calculated according to Hooke's law as [25]

$$\varepsilon_\mathrm{r} = \frac{d_r - d_0}{d_0} = \frac{1+\nu}{E}\sigma_\mathrm{res}\sin^2\psi - \frac{\nu}{E}(\sigma_x + \sigma_y) \ , \qquad \textbf{Eq 4.1}$$

where d_r is the interplanar spacing of (*h k l*) planes of stressed lattice tilted by ψ and rotated by ϕ. d_0 is the strain-free lattice interplanar spacing. The terms E and ν represent Young's modulus and Poisson's ratio, respectively. σ_x and σ_y are the stresses in the principle directions. In the classical XRD method, which is also known as the "rocking" method, the residual stress (σ_res) can be obtained from the slope of the ε_r or d_r vs. $\sin^2\psi$ plot. It can happen that is not possible to collect spectra at higher tilt angles because the diffracted intensity is too low. [25]. This technique that was develop in the 60's has its evolution in high-energy X-ray diffraction methods (80.72 keV synchrotron radiation [26] or diffraction methods with 2D detector that allow to evaluate the residual stress with a very high spatial resolution [27]).

Specially, the synchrotron radiation is of outstanding interest due to its large penetration depth.

The technique of piezospectroscopy applied both to the *chromophoric fluorescence of Al₂O₃* and to a selected *Raman band of 3Y-TZP* has been presented by De Portu et al. [28-30]. The piezo-spectroscopic technique was first applied by Grabner [31] to the measurement of residual stresses in Al_2O_3. This technique is also valid for Raman assessments and it has been applied to some selected Raman bands of ZrO_2. In a polycrystalline sample (having no significant texture and a fine grained microstructure), the spectral shift, $\Delta\nu$, of the Cr^{3+} fluorescence lines (**R**₁ and **R**₂ lines) in Al_2O_3 and of the Raman bands of 3Y-TZP under uniaxial stress can be expressed, to a linear approximation, as:

$$\Delta\nu = \frac{1}{3}\sum_i \Pi_{ii} \sum_j \sigma_{jj} \; , \qquad\qquad \textbf{Eq 4.2}$$

where $\Sigma\Pi_{ii}$ is the trace of the piezo-spectroscopic matrix and $\Sigma\sigma_{jj}$ is the first invariant (or trace) of the stress tensor. $\Sigma\sigma_{jj}/3$ is being commonly referred to as the mean normal stress. If Π_{ii} is known, the spectral shift $\Delta\nu$ can be considered to be a direct measure of the normal stress within the volume probed by the laser beam for each spectra acquisition. In laminate structures, the residual stress field can be considered to be biaxial; accordingly, it should be computed as $2/3\ \sigma_{res}$. On the other hand, nearby the edges the residual stress field is typically three-dimensional. Thus, it requires the use of a mean normal stress $\Sigma\sigma_{jj}$. Of course, a calibration of spectral shift vs. externally applied stress is necessary. This can be done by means of a miniature four-point bending jig connected with a load-cell to measure in situ the applied load [30].

Figure 4.5 plots measurements conducted with this technique. The results concern the same material that is investigated through this doctoral work. Residual stresses field are measured on a lateral face close to the surface. As expected, the A-layers are under compression while the AZ-layers are in tension. It is interesting to note the parabolic profile within each layer. This effect cannot be accounted with analytical models which assume that the stress in each layer is homogeneous. It is possible to observe some relaxation of the stresses at the free surface that again cannot be described with analytical models.
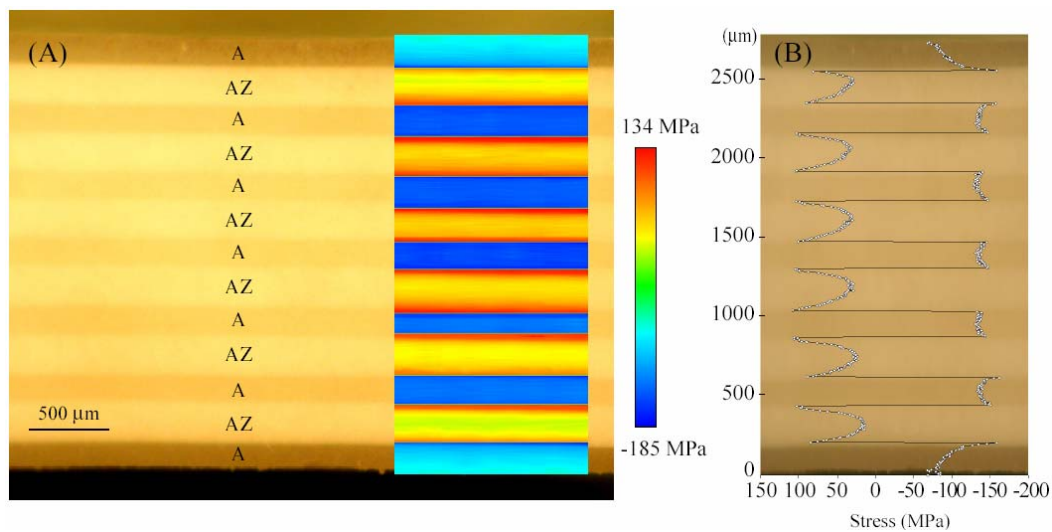
Figure 4.5: Two-dimensional (a) and linear (b) residual stress maps as recorded with a laser beam-diameter of 5 μm (spacing 2 μm) in a 13-layer composite specimen [30]. These maps are computed by using the R_1 band of chromophore Al_2O_3 as a stress tensor. Tensile stresses are represented by red colours, while compressive stresses are negative numbers represented by blue colours.

Neutron diffraction [32, 33] is a complementary technique –also based on traditional Bragg scattering experiments-, with the power to probe bulk regions non-destructively and for many structural materials it is possible to investigate residual strains and stresses in regions up to a few centimeters inside a component.

The *curvature measurement techniques* are generally considered to give relatively accurate results. An example problem is the prediction of stress in a coating applied to a thick, non-deforming substrate from the curvature measured on a coating applied to a thin substrate. For instance in ceramic multilayers, Virkar [34] determined residual stresses using a strain gage technique in which a strain gage was mounted on one face while the opposing face was incrementally ground off. Measurement of the strain as a function of thickness permitted the evaluation of residual stresses using pertinent equations from simple beam theory.

The reader can find many others what in the literature but most probably they will be related to one of the physical principles introduced here. It is worth of note that most of these methods, if not destructive, only give results on surface residual stresses, the stresses in the bulk are recommended to be measured by syncrothron radiation or otherwise, an analytical estimation or finite element simulations are necessary.

4.2. Residual stresses in A/AZ multilayers

The residual stress state in our A/AZ systems has been investigated. Firstly analytically as well as by finite element simulations, additionally the surface residual stress was measured experimentally.

4.2.1. Analytical results

The modeling of thermal residual stress has been well developed and some closed-form solutions have been found (see Chapter 2). The general model by Zhang et al. [35] in which every layer is free to have whatever properties (thickness, elastic properties and thermal expansion) and which is valid under plane strain/stress conditions has been used (the derivation of Zhang's solution is presented in the Annex I).

The residual stress in the *ith*-layer of a symmetrical laminate (see Figure 4.6) under plane stress condition is given by:

$$\sigma_{res}^{i} = \varepsilon_i E_i = \frac{\sum_{k=1}^{n} E_k t_k (\alpha_k - \alpha_i)\Delta T}{\sum_{k=1}^{n} E_k t_k} E_i \; , \qquad \textbf{Eq 4.3}$$

where the index k indicates the layer's number, E is the elastic modulus, α is the thermal expansion coefficient, t is the thickness layer and ΔT is the temperature interval in which the stresses develop. If the system has a planar geometry rather than a strip, i.e. plane strain state, the elastic modulus E should be replaced by $E/(1-\nu)$, where ν is the Poisson's ratio. An extension of this solution to asymmetrical laminates in which a moment appears can be found in the literature [35]. If applied to an infinite plate (plane strain condition), containing alternative layers of just two materials (A and AZ), Zhang's solution becomes the well-known Öel's solution presented in Chapter 1. This analytical estimation has a drawback, it is not able to represent some important local effects that appear in multilayers, i.e. edge stresses in the center of the compressive layers.
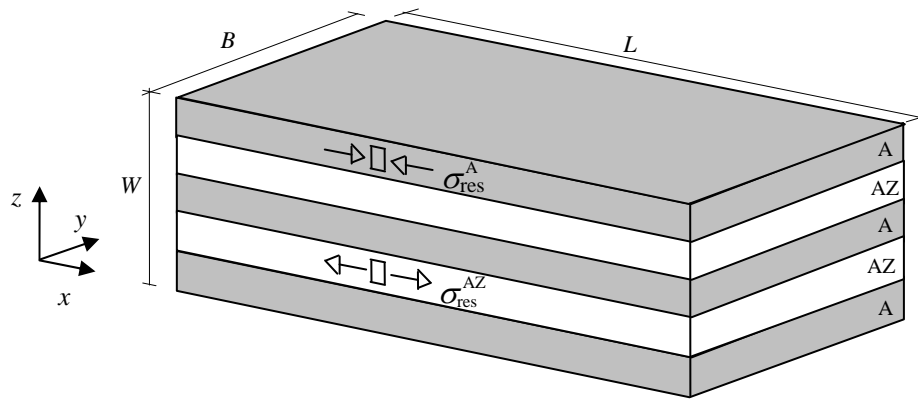
Figure 4.6: Sketch of the laminate being investigated.

Concerning the laminates in our study, in the Figure 4.7 the stress in the A-layers and in the AZ-layers is plotted as a function of $\lambda = t_{AZ}/t_A$ (the ratio between the sum of the overall thickness of material AZ to the sum of all layer thicknesses of material A). The values used in the calculation are summarized in Table 4.1 as extracted from the previous chapter. The coefficients of thermal expansion, α, are considered those that were measured between room temperature and 1150°C quasi-statically.
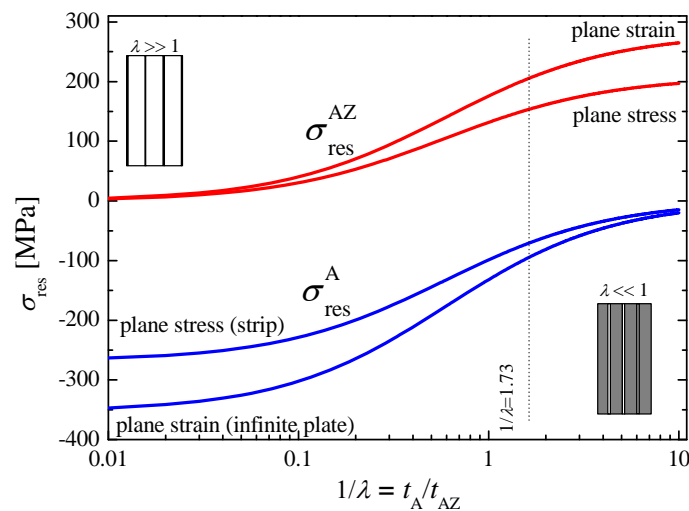
Figure 4.7: Dependence of the residual stress on the architecture.

Table 4.1: Basic properties necessary to evaluate the residual stresses.

	α [10^{-6} °C^{-1}]	E [GPa]	ν	T_{sf} [°C]
A	8.64	391.7	0.241	1160
AZ	9.24	306.5	0.257	

82

The analytical solution for one architecture is given. Let us consider a laminate with the following architecture: 2A/AZ/A/AZ/A/AZ/A/AZ/2A ($1/\lambda = 1.73$): under plane strain conditions, the residual stresses are -107 MPa (A-layers) and +211 MPa (AZ-layers). It is interesting to note that this model gives the same stress to all the layers made of a same material, independently of their thickness. As it will be presented later, finite element simulations agree with this model.

It is noticeable that it is not possible to increment infinitely the compressive stresses at the surface by building very thin compressive layers. In the limit $t_A/t_{AZ} \rightarrow 0$, the stresses are found to be $\sigma_A = -\Delta\varepsilon\, E'_A = -\Delta\alpha\,\Delta T\, E'_A \approx -350\,\text{MPa}$ and $\sigma_{AZ} = 0$. Another example, a compressive stress about 1 GPa in the alumina layer would require about $\Delta\alpha = 2.2\ 10^{-6}\ ^\circ\text{C}^{-1}$. This $\Delta\alpha$ is possible but it is not recommendable as it could bear practical problems during processing as it has been discussed with possible connection to cracking (see Chapter 2).

An interesting dependence to note is that the stresses are a function of the temperature since $\Delta\varepsilon = \Delta\alpha\,\Delta T = \Delta\alpha\,(T_{sf} - T)$. It means that all those advantages/disadvantages that a multilayer could offer will gradually disappear by increasing the temperature. Figure 4.8 plots this dependence; a confidence interval is given since uncertainity exists for the frozen stress temperature at which the residual stresses appear, T_{sf}.
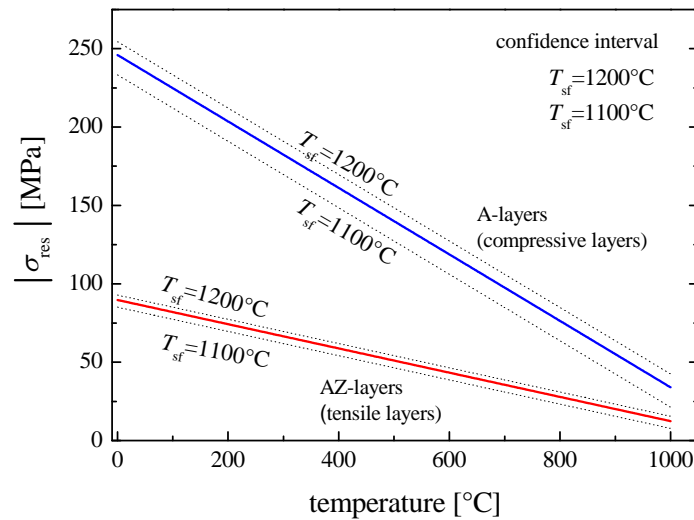
Figure 4.8: Dependence of residual stresses on temperature.

So, again, to estimate the residual stresses in the bulk it is necessary to know the exact strain mismatch. For laminates presenting a thermal strain mismatch this is equivalent to measuring the "frozen stress temperature", T_{sf}. As shown in Table 4.1, it was experimentally found to be $T_{sf} = 1160\ ^\circ\text{C}$ but other authors consider it to be $T_{sf} = 1200\ ^\circ\text{C}$ for similar laminates [7]. The reason why the residual stresses appear at

a lower temperature than the sintering temperature, 1550 °C, is that plastic deformation relaxes stresses in zirconia-toughened alumina at high temperature [36, 37].

The problem how to estimate the "frozen stress temperature" has been addressed recently by Blugan et al. [38] for a Si_3N_4/Si_3N_4-TiN laminate. To determine ΔT, Blugan performed experimental high temperature fracture toughness tests until the increase in apparent toughness due to the residual stresses disappeared.

4.2.2. Finite element results

Residual stress analyses by the finite elements method are especially interesting in cases where the stresses in the bulk are of interest and cannot be measured experimentally. Finite element calculations not only confirm those estimations obtained by simple analytical calculations but demonstrate the existence of interesting localized effects.

This section presents a FE-solution for a well-defined geometry but the conclusions can be extrapolated to any other geometry. It is a laminate with the following architecture or stacking order: 2A/AZ/A/AZ/A/AZ/A/AZ/2A.

Figure 4.9 represents a sketch of the simulated laminate. We use a three-dimensional (3D) model of the specimen, consisting of an eighth part of the laminate since the planes defined by $x = 0$, $y = 0$ and $z = 0$ are symmetry planes. The origin of the space coordinates is in the bulk of the laminate. The necessary physical properties are those listed in Table 4.1. The dimensions of the laminate are presented in Table 4.2 for clarity of the sketch.
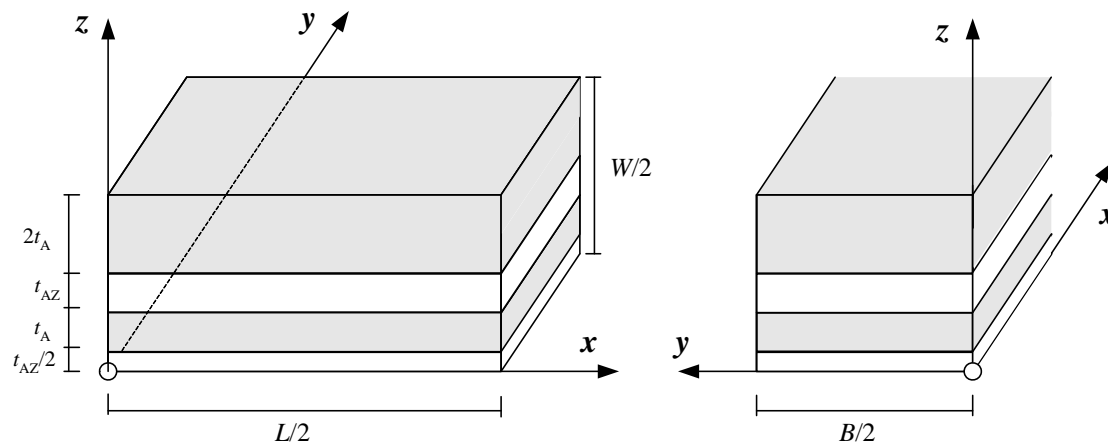
Figure 4.9: Sketch of one eighth of the laminate studied by finite elements. The origin of the spatial coordinates represents the center of the laminate (or the bulk).

Table 4.2: Geometry of the laminate

t_A [mm]	t_{AZ} [mm]	B [mm]	L [mm]	W [mm]
0.190	0.220	2.5	28	1.8

In this work simulations were conducted with the help of ANSYS 10.0. The materials of the A- and AZ-layers are modeled as linear-elastic. The corresponding material properties are taken from Table 4.1. The room temperature was considered to be 20 °C, and therefore $\Delta T = 1140$ °C.

The mesh is built-up of solid element Solid95. This element is a higher order version of the 3-D 8-node solid element Solid45. It can tolerate irregular shapes without as much loss of accuracy. Solid95 elements have compatible displacement shapes and are well suited to model curved boundaries. The element is defined by 20 nodes having three degrees of freedom per node. The element may have any spatial orientation [39]. The mesh was optimized to present more elements in the vicinity of the interfaces where larger gradients were observed in the eigenstress field.

Boundary conditions were defined as follows: At the center point displacements are not allowed in any direction ($u_x = u_y = u_z = 0$), for the plane defined as $x = 0$ displacements are not allowed in the x-direction ($u_x = 0$), for the plane defined as $y = 0$ displacements are not allowed in the y-direction ($u_y = 0$), and finally for the plane defined as $z = 0$ displacements are not allowed in the z-direction ($u_z = 0$).

The solution is presented along different paths. Firstly σ_x was investigated across the layers in the bulk and in the surface (see Figure 4.10). For clarity, the two paths are not only mathematically defined but also sketched in Figure 4.10. The paths correspond to $x = 0$, $y = 0$ and $0 < z < W/2$ in the bulk and $x = 0$, $y = B/2$ and $0 < z < W/2$ in the surface.
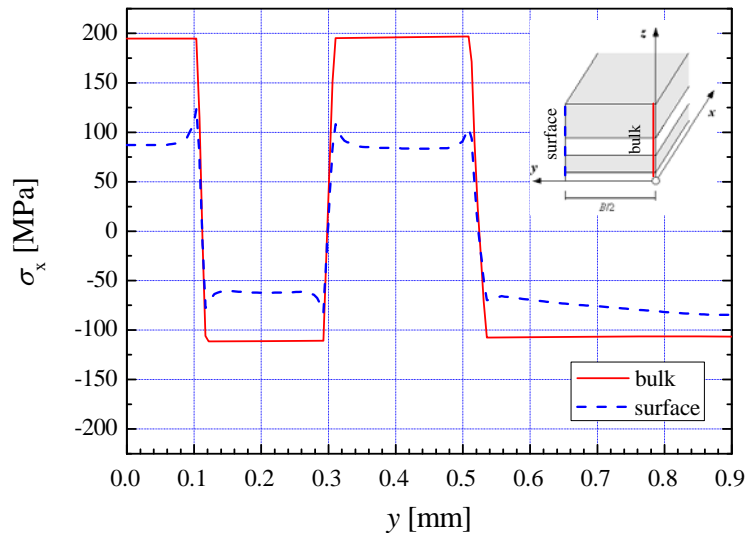
Figure 4.10: Thermal residual stresses $\sigma_{x,\text{res}}$ along the z-direction in the bulk ($x = 0$, $y = 0$, solid line) and in the surface ($x = 0$, $y = B/2$, dashed line). The solution corresponding to a 3-D model is presented.

As expected, tensile stresses are present in the AZ-layers while compressive stresses prevail in the A-layers. In the bulk the magnitude of the stresses is always higher than at the surface. The solution in the bulk is the same that the analytically one calculated in plane strain. In the bulk, the magnitude of the stresses is the same for the layer A and for the layer 2A, therefore only the ratio of overall thickness seems to affect the magnitude of the stresses. Close to the surface stress gradients appear at the interfaces. By reducing the element size these gradients were found to be very localized. The FE analysis shows that the stresses are constant with exception to a small region near the interfaces. Chen et al. [40] have shown a similar profile in a similar laminate. This solution differs from the profile experimentally measured by De Portu [30], who observed a much more parabolic profile (see Figure 4.5). It is believed that the experimental measurements from de Portu [30] may contain some uncertainty; in fact, it can be observed (Figure 4.5) that the residual stress profile is not balanced. At the surface, a priori, $\sigma_{x,\text{res}}$ was expected to decrease continuously to the edge since the origin of the stresses is given by the thermal mismatch at the interface. The FE-simulation reflects how it starts decreasing but at a certain distance from the interface grows slightly. The simulation is believed to be correct and can be explained by the Poisson's ratio (or what is the same, the magnitude $\sigma_{z,\text{res}}$ that appears at the free surface). This is supported in Figure 4.11.

Figure 4.11 represents $\sigma_{z,\text{res}}$ for the same paths that were described previously. In the bulk $\sigma_{z,\text{res}}$ is very low (< 25 MPa). Since the origin of the residual stresses is a strain mismatch in the xy-plane stresses are expected to be small in the z-direction. Most probably the stresses in the z-direction that appear in the bulk are due to the effect of the Poisson's ratio. Interestingly, at the surface $\sigma_{z,\text{res}}$ is quite different from zero. This

surface effect is known to be responsible of edge cracks. The sign of this stress is different to that in the bulk, it means, layers in biaxial compression ($\sigma_{x,res}$ and $\sigma_{y,res}$) contain tension $\sigma_{z,res}$ in the z-direction and vice versa. As a conclusion the tensile stress in z-direction influences $\sigma_{x,res}$ via the Poisson's ratio.
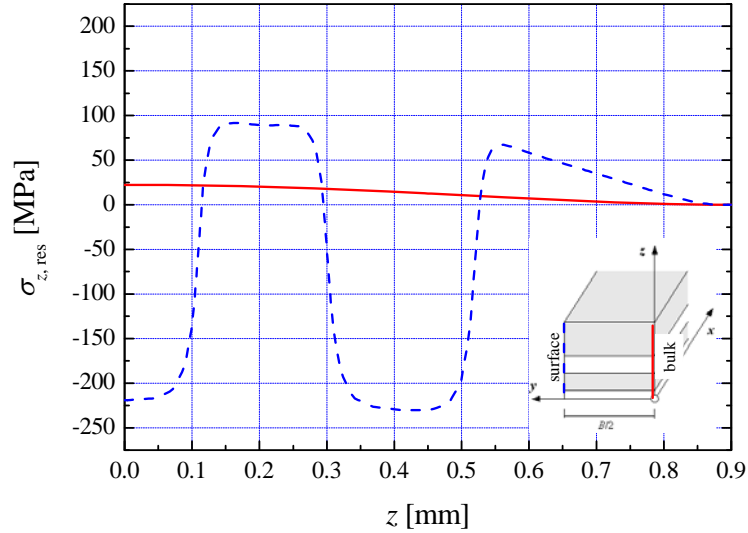

Figure 4.11: Thermal residual stresses σ_z along the z-direction in the bulk ($x = 0$, $y = 0$, solid line) and in the surface ($x = 0$, $y = B/2$, dashed line). The solution corresponding to a 3-D model is presented.

Lastly, the last component $\sigma_{y,res}$ is presented for both paths of interest in Figure 4.12. As expected, $\sigma_{y,res}$ is similar to $\sigma_{x,res}$ in the bulk, so the stress state is biaxial, and $\sigma_{y,res}$ at the surface is close to zero as no forces are applied at the surface.
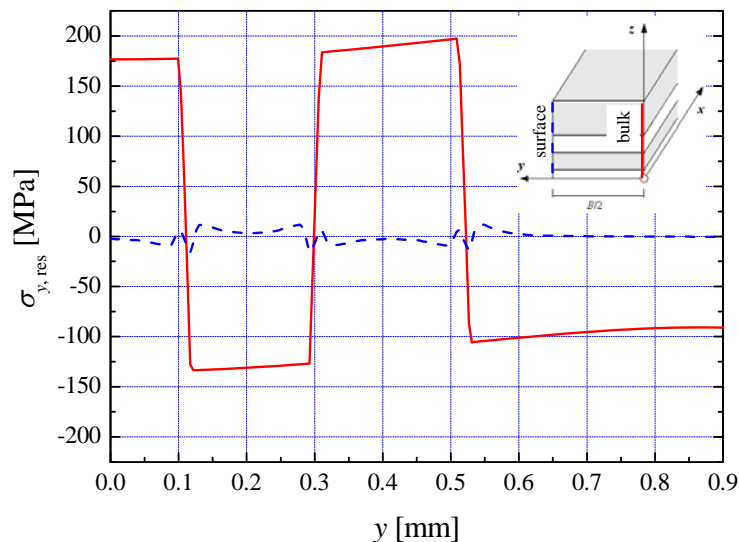
Figure 4.12: Thermal residual stresses $\sigma_{y,res}$ along the z-direction in the bulk ($x = 0$, $y = 0$, solid line) and in the surface ($x = 0$, $y = B/2$, dashed line). The solution corresponding to a 3-D model is presented.

It is also interesting to investigate $\sigma_{x,\text{res}}$ in the *y*-direction. This is done in the Figure 4.13. Several paths were taken along the centerline of different layers. For all the paths applies $x = 0$ and $0 < y < B/2$. The *z* coordinate depends on each path. Four paths were chosen, two in compressive layers and other two in tensile layers.
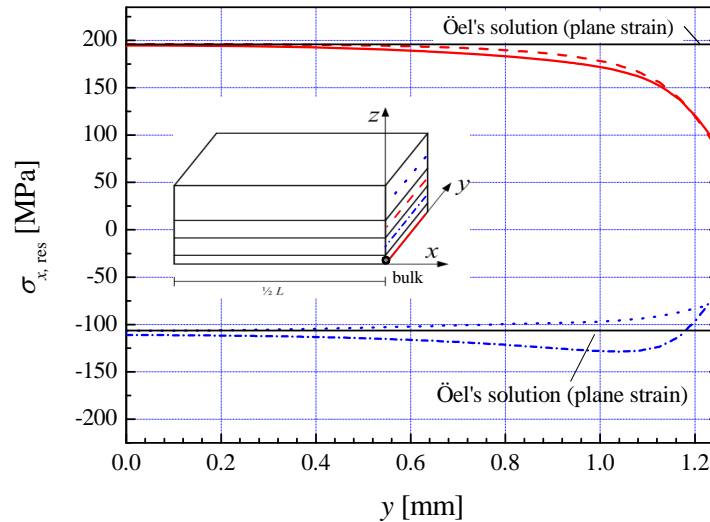
Figure 4.13: Thermal residual stresses $\sigma_{x,\text{res}}$ along the *y*-direction for various layers. The *z*-coordinates correspond to the centerline of each layer.

The 2-dimensional plane strain solution seems to fit in about the 80% of the width *B*. This is important for further calculations. In future chapters the plane strain solution will be considered for solving the apparent toughness problem in two dimensions. The magnitude of the stress is similar for the layers 2A and A. The stress relaxes when approaching the free surface.

4.2.3. Experimental results

An indentation technique is used to experimentally determine the residual stresses. It has not been previously described in this work and thus, some short introduction is given. It consists in comparing the crack length arising from Vickers indentations. This method is only valid to measure surface stresses in brittle materials (materials brittle enough to present cracks in the corners of the indentation). It has been used by some authors [41, 42] to estimate stresses in alumina and zirconia.

The Vickers indentations are imprinted in two laminates of alumina: one residual stresses-containing (a 2A/AZ/A/AZ/A/AZ/A/AZ/2A laminate) and the other without residual stresses (an A/A/A/A.. laminate). The 2A/AZ/A/AZ/A/AZ/A/AZ/2A laminate is the laminate that has also been studied by finite elements.

For the non-stressed material it holds

$$P = \chi \left(\frac{a_0^{3/2}}{K_c} \right) , \qquad \qquad \textbf{Eq 4.4}$$

where a_0 is the crack length in the unstressed material. K_c was independently measured, $K_c = 3.8$ MPa$\sqrt{m}$ (see chapter 5). By indenting with different loads and measuring the corresponding crack lengths, the parameter χ can be calibrated (see close symbols in Figure 4.14). If no independent value for K_c is known, it can be calculated as $\chi = 0.016 \cdot (E/H)^{1/2}$ with a standard deviation of 25% [43].

However, in a stressed material it is well known that the fracture toughness is related to the indentation load P, and the residual stress σ_{res} by the following relation [44]:

$$K_c = \chi \left(\frac{P}{a_1^{3/2}} \right) + Y \sigma_{res} \sqrt{a_1} , \qquad \qquad \textbf{Eq 4.5}$$

where K_c is the toughness of the stress-free material, c_1 is the crack length in the stressed material and $Y = 1.26$ is a geometric factor for semicircular surface cracks [41]. χ is the same dimensionless constant as above.
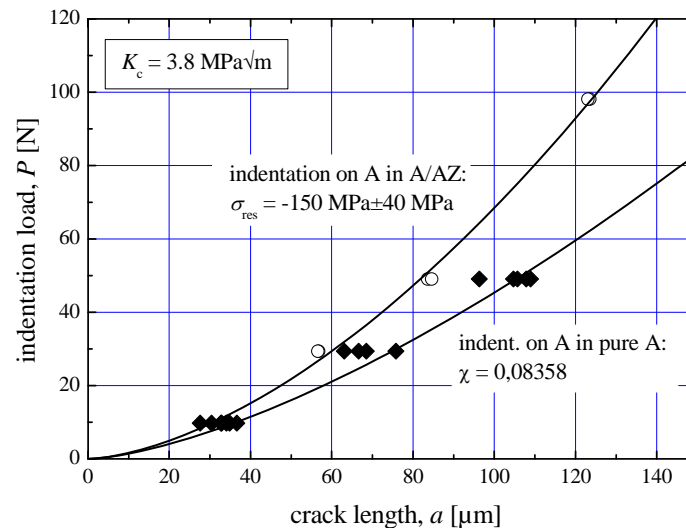
Figure 4.14: Implicit applied load - crack length relationship used to calculate the surface residual stress.

Once the parameter χ has been calibrated, the regression of the experimental data of P and a_1 using Equation 4.5 allows us to estimate σ_{res}. The value obtained from the fitting, $\sigma_{res} \approx -150$ MPa (after fitting the open symbols in Figure 4.14), is a somewhat

higher than the surface residual stress estimated analytically or simulated by FE (-105 MPa). Let's remember that both solutions consider a thermal mismatch; $\Delta\alpha = 0.6\times10^{-6}°C^{-1}$; that corresponds to quasi-static measurements. If the dynamic measurement would have been considered ($\Delta\alpha = 0.8\times10^{-6}$ °C^{-1}) the analytical solution and the FE-solution would be around -105 MPa $\times$ 0.8 / 0.6 = -140 MPa that fits well with the experimental results.

Another reason for the difference can be the polishing procedure. It is necessary prior to indenting and removed around 50 μm of material, which is enough to increase the stress at the surface about 15 MPa (see Figure 4.13). The uncertainty of the measurement could be reduced by performing indentations at higher load but the limited size of the specimen prevents this.

4.2.4. Determination of ΔT

As commented earlier, residual stresses do not develop at the sintering temperature but at a lower one as they relax at high temperatures. Several models have been reported that could explain the relaxation of stresses in materials at high temperatures. They differ depending on the assumed atomistic mechanism of deformation: (a) *relocation of atoms through the bulk* (Nabarro-Herring creep) [45] shows a strain-rate dependence on grain size and (b) *relocation of matter through the grain boundary* (Coble creep) [46] shows a strain-rate dependence on grain size to the power of three. Because, usually, diffusion through grain boundaries is faster than through the bulk (at a given temperature), modeling the stress relaxation according to Coble is more usual. They are in fact not the only mechanisms that can relax stresses, for the case of zirconia and zirconia-toughened alumina *superplasticity* has been observed [47, 48]. An important topological feature of superplastic flow is that the grains rotate with respect to each other with almost no change in the grain shape, even after very large macroscopic strains and without activity of dislocations within the grains. This indicates that the deformation is achieved primarily by *grain boundary sliding*.

An alternative to estimate the stress frozen temperature is the analysis of the strength of asymmetrical laminates. For asymmetrical 3-layer laminates (see Figure 4.15) the residual stresses have to be redistributed in such a way that the residual compression is higher in the thinner outer layer than in the thicker one to maintain mechanical equilibrium.
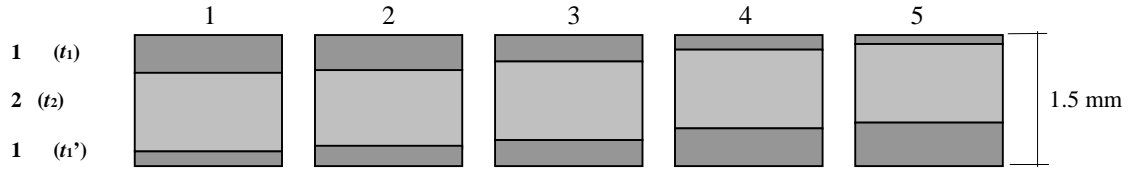
Figure 4.15: Cross-section sketch of asymmetrical 3-layers with a same inner layer and overall thickness. t_1' is placed under tension during the bending tests.

A series of asymmetrical specimens –like those sketched in Figure 4.15- were tested in bending test. The thickness t_1' was always in tension during the bending test. It can be expected that the strength of such specimens -with a constant overall thickness- is a function of the thickness of the outer layer t_1', since the thinner t_1' is, the higher the compressive residual stress will be and therefore, the higher the strength will be.

For asymmetrical laminates, the residual stress field is modified due to a bending moment M that appears to maintain mechanical equilibrium. The analytical solution presented in Equation 4.3 for the residual stress field has to be slightly modified to incorporate this moment [34, 35]. The bending moment M has been calculated in the literature [34]. The total residual stress in layer 1' at any depth y measured from the neutral axis can be expressed by (see Figure 4.16)

$$\sigma_{res,\,total}^{A}(y) = \sigma_{res,\,symm}^{A} + \frac{M\,y}{I}\ ,$$
                                                                                    Eq 4.6

where I is the moment of inertia.
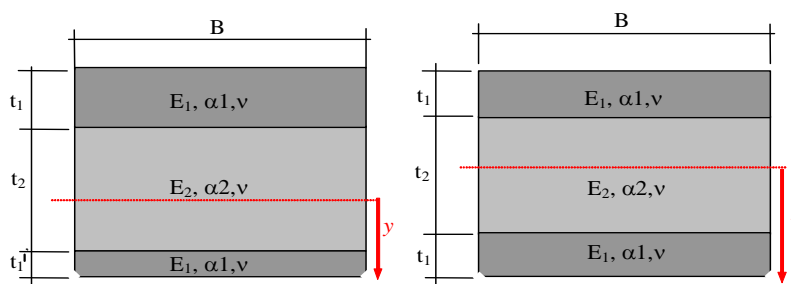
Figure 4.16: Cross sections of (a) an asymmetrical and (b) a symmetrical tri-layer. The dashed line indicates the position of the neutral axis.

Now, let us consider our laminates of study. The architecture of the as received trilayers was 3 layers distributed in a symmetrical way 2A/4AZ/2A. Later, this laminates were ground off asymmetrically. The 4-point bending tests were carried out with a Zwick Z010 device. The tests were performed on $1.5\ mm \times 2\ mm \times 16\ mm$ chamfered specimens (13/3 mm and 13 mm span lengths). The chosen test speed was

1.5 mm/min (temperature and relative humidity were recorded during tests as 23ºC and 36% respectively).

If the laminate fails due to surface flaws during the bending test it could be assumed that the strength in bending is given by the addition of two contributions: the residual stress at the surface ($y = \bar{y}$) plus the bending strength of the same material free of stresses, $\sigma_{f,0}$,

$$\sigma_f = \sigma_{\text{res, total}}^{A}(\bar{y}) + \sigma_{f,0} \ , \qquad\qquad \textbf{Eq 4.7}$$

This surface failure hypothesis seems to be valid as, in general, there are large grains of alumina at the surface (see Figure 4.18).

Values of σ_f can be measured for specimens with different t_1' and plotted as strength versus t_1' (see Figure 4.17). Equation 4.7 can be fitted to this data. As a result, an estimation for $\Delta\varepsilon$ and $\sigma_{f,0}$ can be obtained. Figure 4.17 shows a plot of the strength depending on the outer layer thickness t_1' for asymmetrical tri-layers made from two different batches (batches are referred to as #11 and #12) Microscopy investigations on the tensile surfaces revealed that with the exception of two specimens, all specimens of batch #11 failed due to large grains of alumina located at the tensile surface. The two specimens for which this was not the case (presumably because the material that originally contained the large grains was ground off completely) are indicated in Figure 4.17 with small open squares.

Figure 4.17: Plot of strength as a function of the outer layer thickness t_1' for batches #11 and #12. Specimens of #11 that did not fail due to large grains and were excluded from the fitting are marked with small square symbols. The lines correspond to a simultaneous fit of Equation 4.7 on both data sets with common $\Delta\varepsilon$.
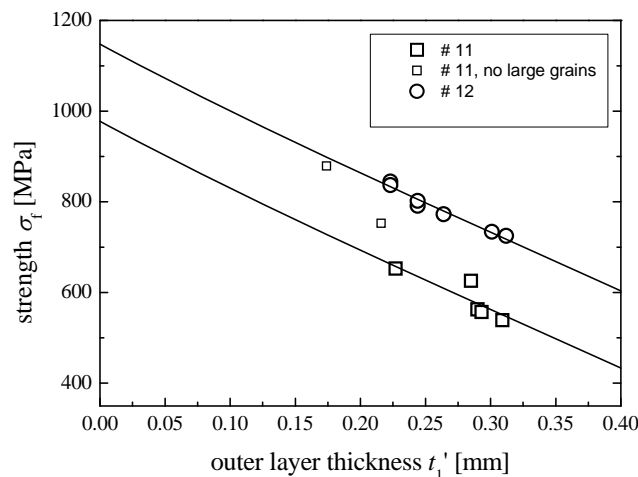
The strength values plotted in Figure 4.17 were fitted to the Equation 4.7 by means of Origin 7.5 where $\Delta\varepsilon$ and $\sigma_{f,0}$ were the parameters to fit. The specimens from the batch #11 that did not fail from large grains were excluded from the fit. The results for the fitting are presented in Table 4.3. Since the value for $\Delta\varepsilon$ is supposed to be the same for both data sets, a simultaneous fit is performed on both data-sets where the value for $\Delta\varepsilon$ is forced to be the same for both #11 and #12 while $\sigma_{f,0}$ is allowed to be different for both sets.

Table 4.3: Results for σ and $\Delta\varepsilon$ from the fitting procedure.

specimen	fracture origins	$\sigma_{f,0}$ [MPa]	$\Delta\varepsilon$ [-]	T_{sf} [ºC]
11	surface large grain	247	0.00114 ± 0.00015	1160
12	machining defects	417		

The results for $\sigma_{f,0}$ can be interpreted as the strength of two microstructurally different aluminas. The value of $\sigma_{f,0} = 417$ MPa for #12 is a reasonable value for the strength of alumina. A similar value was determined on bend bars made from pure A-alumina [49]. The typical fracture surface for specimens from the plate #11 is shown in Figure 4.18. Large grains about 50 µm size were found in that sample. Fracture origins for specimens of batch #12 were also surface defects although no abnormal large grains were found in this material. The value for #11 is rather low, but it can be explained by the existence of the large surface defects. With the fracture toughness $K_c = 3.8$ MPa√m, measured by SEVNB, the size of a semicircular surface flaw that leads to failure at this stress can be estimated to be approx. $a = 47$ µm. This size corresponds satisfactory with the observations on fracture surfaces, see Figure 4.18.

The results for $\Delta\varepsilon$ leads to a $T_{sf} = 1160°C$ ($\Delta\varepsilon = \Delta\alpha$ (T_{sf} - T_{room})) that is slightly lower than the value $T_{sf} = 1200°C$ which has been reported for similar materials [7]. From Equation 4.3 the crucial influence of this temperature on the magnitude of the residual stresses is obvious.
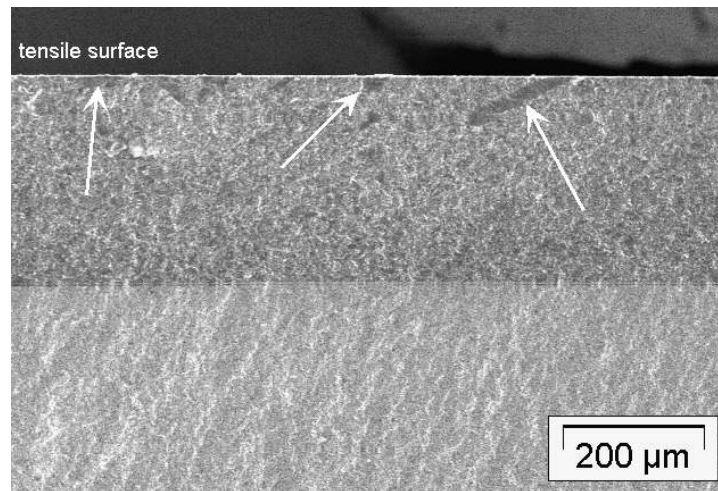
Figure 4.18: Fracture surface of a specimen showing abnormal large alumina grains.

4.3. Bibliography

[1]   Sglavo, V. M., Larentis, L., Green, D. J., "Flaw-insensitive ion-exchanged glass: I, Theoretical aspects", Journal of the American Ceramic Society, **84**, 1827-1831, (2001).

[2]   Lee, M. K., Kim, G. H., Kim, K. H., Kim, W. W., "Effects of the surface temperature and cooling rate on the residual stresses in a flame hardening of 12Cr steel", Journal of Materials Processing Technology, **176**, 140-145, (2006).

[3]   Lima, C. R. C., Nin, J., Guilemany, J. M., "Evaluation of residual stresses of thermal barrier coatings with HVOF thermally sprayed bond coats using the modified layer removal method", Surface and coatings technology, **200**, 5963-5972, (2006).

[4]   Fischer, W., Malzbender, J., Blass, G., Steinbrech, R. W., "Residual stresses in planar solid oxide fuel cells", Journal of power sources, **150**, 73-77, (2005).

[5]   Hsueh, C.-H., Ferber, M. K., "Apparent coefficient of thermal expansion and residual stresses in multilayer capacitors", Composites, **33**, 1115-1121, (2002).

[6]   Supancic, P., Wang, Z., Harrer, W., Danzer, R., "Strength and Fractography of Piezoceramic Multilayer Stacks" in: Key Engineering Materials. Trans-Tech Publications Ltd, **290**, 46-53, (2005).

[7]   Green, D. J., Cai, P., Messing, G. L., "Residual stresses in alumina-zirconia laminates", Journal of the European Ceramic Society, **19**, 2511-1517, (1999).

[8]   Cai, P., Green, D. J., Messing, G. L., "Constrained densification of alumina/zirconia hybrid laminates, I: Experimental observations of processing defects." Journal of the American Ceramic Society, **80**, 1929-1939, (1997).

[9]   Cai, P., Green, D. J., Messing, G. L., "Constrained densification of alumina/zirconia hybrid laminates, II: Viscoelastic stress computation", Journal of the American Ceramic Society, **80**, 1940-1948, (1997).

[10]   Gurauskis, J., Sánchez-Herencia, A. J., Baudín, C., "Joining green ceramic tapes made from water-based slurries by applying low pressures at ambient temperature", Journal of the European Ceramic Society, **25**, 3403-3411, (2005).

[11]   Gurauskis, J., Sánchez-Herencia, A. J., Baudín, C., "Alumina-zirconia layered ceramics fabricated by stacking water processed green ceramic tapes", UPC, (2005).

[12]   Bermejo, R., Torres Hernández, Y., Sánchez-Herencia, A. J., Baudín, C., Anglada, M., Llanes, L., "Fracture behaviour of an Al_2O_3-ZrO_2 multi-layered ceramic with residual stresses due to phase transformations", Fatigue and Fracture of Engineering Matererial Structures, **29**, 71-78, (2006).

[13]   Tomaszewski, H., Strzeszewski, J., Gebicki, W., "The role of residual stresses in layered composites of Y-ZrO_2 and Al_2O_3", Journal of the European Ceramic Society, **19**, 255-262, (1999).

[14]   Bermejo, R., "Structural integrity of alumina-zirconia multilayered ceramics", (Universitat Politècnica de Catalunya, Barcelona 2005).

[15]   Pontin, M. G., Rao, M., Sanchez-Herencia, J., Lange, F., "Laminar ceramics utilizing the zirconia tetragonal-to-monoclinic phase transformation to obtain a threshold strength", Journal of the American Ceramic Society, **85**, 3041-3048, (2002).

[16]   Withers, P. J., Bhadeshia, H. K. D. H., "Overview - Residual stress. Part 1 Measurement techniques", Material Science and Technology, **17**, 355-365, (2001).

[17]   Suresh, S., Giannakopoulos, A. E., "A New Method For Estimating Residual Stresses By Instrumented Sharp Indentation", Acta Materialia, **46**, 5755-5767, (1998).

[18]   Carlsson, S., Larsson, P. L., "On the determination of residual stress and strain fields by sharp indentation testing. Part I: Theoretical and numerical analysis." Acta Materialia, **49**, 2179-2191, (2001).

[19]   Carlsson, S., Larsson, P. L., "On the determination of residual stress and strain fields by sharp indentation testing. Part II: Experimental investigation." Acta Materialia, **49**, 2193-2203, (2001).

[20]   Roberts, S. G., Lawrence, C. W., Bisrat, Y., Warren, P. D., Hills, D. A., "Determination of surface residual stresses in brittle materials by hertzian indentation: theory and experiment", Journal of the American Ceramic Society, **82**, 1809-1816, (1999).

[21]   Bisrat, Y., Robert, S. G., "Residual stress measurement by Hertzian indentation", Material Science and Engineering A, **288**, 148-153, (2000).

[22]   Schajer, G. S., "Measurement of non-uniform residual-stresses using the hole-drilling method. Stress calculation procedures", Journal of engineering materials and technology. Transactions of the ASME, **10**, 338-343, (1988).

[23]   Santana, Y. Y., La Barbera-Sosa, J. G., Staia, M. H., Lesage, J., Puchi-Cabrera, E. S., Chicot, D., Bemporad, E., "Measurement of residual stress in thermal spray coatings by the incremental hole drilling method", Surface & coatings technology, **201**, 2092-2098, (2006).

[24]   Adachi, T., Sekino, T., Nakayama, T., Kusunose, T., Niihara, K., "Measurement of microscopic stress distribution of multilayered composite by X-ray stress analysis", Materials Letters, **57**, 3057-3062, (2003).

[25]   Atar, E., Sarioglu, C., Demirler, U., Sabri Kayali, E., Cimenoglu, H., "Residual stress estimation of ceramic thin films by X-ray diffraction and indentation techniques", Scripta Materialia, **48**, 1331-1336, (2003).

[26]   Thornton, J., Slater, S., Almer, J., "The measurement of residual strains within thermal barrier coatings using high-energy X-ray diffraction", Journal of the American Ceramic Society, (2005).

[27]   Gelfi, M., Bontempi, E., Roberti, R., Depero, L. E., "X-ray diffraction Debye Ring Analysis for STress measurement (DRAST): a new method to evaluate residual stresses", Acta Materialia, **52**, 583-589, (2004).

[28]   De Portu, G., Bueno, S., Micele, L., Baudín, C., Pezzotti, G., "Piezo-spectroscopic characterization of alumina-aluminium titanate laminates", Journal of the European Ceramic Society, **26**, 2699-2705, (2005).

[29]   De Portu, G., Micele, L., Pezzotti, G., "Characterization of tunneling cracks in Al_2O_3/Al_2O_3+3Y-TZP multilayered composites by Raman and fluorescence piezo-spectroscopy", Journal of Materials Science Letters, **40**, 1505-1508, (2005).

[30]   De Portu, G., Micele, L., Sekiguchi, Y., Pezzotti, G., "Measurement of residual stress distributions in Al_2O_3/3Y-TZP multilayered composites by fluorescence and Raman microprobe piezo-spectroscopy", Acta Materialia, **53**, 1511-1520, (2005).

[31]   Grabner, L., "Spectroscopic technique for the measurement of residual stress in sintered Al_2O_3", Journal of Applied Physics, **49**, 580, (1978).

[32]   Stacy, A., MacGillivary, H. J., Webster, G. A., Webster, P. J., Ziebeck, K. R. A., "Measurement of residual stresses by neutron diffraction", J. Strain Anal., **20**, 93-100, (1985).

[33]   Ruiz Hervias, J., Bruno, G., Gurauskis, J., Sánchez-Herencia, A. J., Baudín, C., "Neutron diffraction investigation for possible anisotropy with monolithic Al2O3/Y-TZP composites fabricated by stacking together cast tapes", Scripta Materialia, **54**, 1133-1137, (2006).

[34]   Virkar, A. V., Jue, J. F., Hansen, J. J., Cutler, R. A., "Measurement of residual stresses in oxide-ZrO_2 three-layer composites", Journal of the American Ceramic Society, **71**, C148-C151, (1988).

[35]   Zhang, X. C., Xu, B. S., Wang, H. D., Wu, Y. X., "An analytical model for predicting thermal residual stresses in multilayer coating systems", Thin Solid Films, **488**, 274-282, (2005).

[36]   Jimenez-Melendo, M., Clauss, C., Dominguez-Rodriguez, A., de Portu, G., Roncari, E., Pinasco, P., "High temperature plastic deformation of multilayered YTZP/ZTA composites obtained by tape casting", Acta Materialia, **46**, 3995-4004, (1998).

[37]   French, J., Chan, H. M., Harmer, M. P., Miller, G. A., "High-Temperature fracture toughness of duplex microstructures", Journal of the American Ceramic Society, **79**, 58-64, (1996).

[38]   Blugan, G., Dobedoe, R., Gee, I., Orlovskaya, N., Kübler, J., "Failure behaviour of high toughness multi-layer Si_3N_4 and Si_3N_4-TiN based laminates" in: Dusza, J., Danzer, R., Morrell, R. Fractography of advanced ceramics II. Trans Tech Publications, 175-182, (2005).

[39]   "ANSYS Theory reference", .

[40]   Chen, C. R., Fischer, F. D., Kolednik, O., Pascual, J., Danzer, R., "A fracture mechanics study of a ceramic laminate specimen: experiments and modelling", in preparation, (2005).

[41]   Tarlazzi, A., Roncari, E., Pinasco, P., Guicciardi, S., Melandri, C., de Portu, G., "Tribological behaviour of Al_2O_3/ZrO_2-ZrO_2 laminated composites", Wear, **24**, 29 - 40, (2000).

[42]   Bermejo, R., Llanes, L., Anglada, M., Supancic, P., Lube, T., "Thermal shock behavior of an Al_2O_3/ZrO_2 multilayered ceramic with residual stresses due to phase transformations" in: Dusza, J., Danzer, R., Morrell, R. Key Engineering Materials. Trans Tech Publikations Ltd., **290**, 191-198, (2005).

[43]   Anstis, G. R., Chantikul, P., Lawn, B., Marschall, D. B., "A critical evaluation of indentation techniques for measuring fracture toughness: I, Direct crack measurements", Journal of the American Ceramic Society, **64**, 533-538, (1981).

[44]   Lawn, B., "Fracture of Brittle Solids- Second Edition", Cambridge University Press, (1993).

[45]   Nabarro, F. R. N., "Steady-state diffusional creep", Philosophical magazine, **16**, 231, (1967).

[46]   Coble, R. L., "A model for boundary diffusion controlled creep in polycrystalline materials", Journal of Applied Physics, **34**, 1679, (1963).

[47]   Dominguez-Rodriguez, A., Gutierrez-Mora, F., Jimenez-Melendo, M., Routbort, J. L., R, C., "Current understanding of superplastic deformation of Y-TZP and its application to joining", Material Science and Engineering A, **302**, 154-161, (2001).

[48]   Jimenez-Melendo, M., Clauss, C., Dominguez-Rodriguez, A., Sánchez-Herencia, A. J., Moya, J., "Microstructure and high-temperature mechanical behavior of alumina/alumina-yttria stabilized tetragonal zirconia multilayer composites", Journal of the American Ceramic Society, **80**, 2126-2130, (1997).

[49]   Pascual, J., Chalvet, F., Lube, T., de Portu, G., "Strength distributions in ceramic laminates", Materials Science Forum, **492-493**, 581-586, (2005).

Chapter 5. Fracture Toughness and R-curve in A/AZ Laminates

5.1. Introduction

A prerequisite for the application of multilayer ceramics is the understanding of their resistance against crack propagation. Although fracture toughness of a layered composite can be experimentally measured, it is only an apparent or effective value because of the superposition of an internal stress. Besides, different shielding effects or intrinsic mechanisms of the structure, such as bridging associated to grain size, make the interpretation of toughness measurements difficult.

So far, different authors have modeled the toughening effect of internal stresses by means of the weight function method [1-4]. They use the classical weight function concept to calculate the stress intensity factor, considering an inhomogeneous distribution of the residual stresses in a homogeneous body. According to Fett et al. [5, 6], the weight function method can also be applied to heterogeneous, graded or laminated materials with a variable Young's modulus.

The immanent inhomogeneity of the material, however, causes implications which are not taken into account by the current weight function solutions: Spatially varying material properties induce an additional crack driving force term. The propagation of a crack in a direction orthogonal to the laminate planes can be promoted (anti-shielding) or retarded (shielding) by the different elastic properties (elastic mismatch) of the laminate [1]. The spatially varying residual stress state can have a similar effect [7].

One goal of this chapter is, therefore, to present an alternative procedure which takes these spatial inhomogeneities into account − the method of configurational (or material) forces − to predict the fracture toughness of a ceramic multilayer composite. The numerical predictions will be compared to experimental fracture toughness data and the solution obtained the weight function method. Besides, the weight function method – due to its low computing time - will be used to discuss the influence of different parameters on the effective toughness of the laminate.

5.2. Experimental results

Laminates were studied with the structure A/AZ/A/AZ/A/AZ/A (7 layers), in which the thicknesses of the individual A- and AZ-layers are 190 µm and 220 µm, respectively. More details about processing can be found in Chapter 3.

A complete characterization of the material layers was performed according to methods introduced in Chapter 3, and the results are can be schematically listed in Annex 2. The elastic constants, Young's modulus E and Poisson's ratio ν, are measured at room temperature. The coefficients of thermal expansion, α, are measured between room temperature and 1150 °C.

The fracture toughness of the laminates was measured on single edge V-notched beams, following the VAMAS-ESIS procedure [8]. Bar-shaped specimens with length $L = 28$ mm, width $W = 1.42$ mm, and thickness $B \approx 2.6$ mm were cut from the original plates using a diamond saw (compare Figure 5.1). The interfaces were perpendicular to the width W.

According to VAMAS, a starter notch should be cut with a diamond saw to a depth of about 500 µm. In this case, the step was skipped as we wanted to characterize specific crack lengths. The notches were machined in a custom-made automatic device which uses a razor blade sprinkled with diamond paste (see Figure 5.1). The procedure yields a notch with a tip radius of about 10 µm (measured at the lateral surfaces before fracture). This should assure reliable fracture toughness measurements [9].

Figure 5.1: Custom-made device to produce V-notches by means of a razor blade.

Four-point-bending tests were conducted in a commercial Zwick Z010 machine under room conditions (34% relative humidity and a temperature of 20 °C). The side in tension is the notch-containing face. According to the VAMAS procedure a testing machine capable of keeping a uniform crosshead speed should be used (in this work the tests were performed at 1 mm/min). Further, the machine should be capable of measuring the true load at rupture of the specimen to better than 1%.
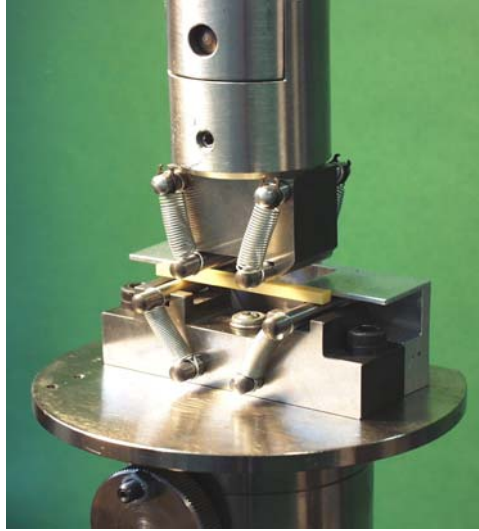
Figure 5.2: 4-point bending test set-up.

To compute the fracture toughness K_c the following expression is given for the 4-point bending test case:

$$K_c = \frac{F}{B\sqrt{W}} \frac{S_1 - S_2}{W} \frac{3\sqrt{a/W}}{2(1-a/W)^{1.5}} Y \ ,$$
Eq 5.1

with

$$Y = 1.9887 - 1.326\frac{a}{W} - \frac{(3.49 - 0.68\frac{a}{W} + 1.35\left(\frac{a}{W}\right)^2)}{(1+\frac{a}{W})^2} \frac{a}{W}(1-\frac{a}{W})$$
Eq 5.2

where F is the fracture load, S_1 and S_2 the support spans ($S_1 > S_2$) and a/W is the relative V-notch depth. The initial crack length a, was measured after the tests, taken as an average of three measurements on the fracture surface (well-distributed along the thickness B). According to the VAMAS procedure the depth of the V-notches shall be measured by observing the fracture surface using a calibrated microscope with a magnification ≥ 50 X. The limitation, $(a_{max} - a_{min}) / a \leq 0.1 \ a$, shall be fulfilled, being a the average of all three measurements.

The intrinsic fracture toughness $K_{c,0}$ of the A and AZ material was determined by testing multilayered homogeneous specimens consisting only of A- and AZ-layers (A/A/A… and AZ/AZ/AZ..), respectively. For that, VAMAS experiments were performed. For the A-layers the VAMAS-ESIS procedure gave $K_{c,0} = 3.8 \pm 0.3$ MPa√m. For the AZ-layers, however, it was not possible to perform a notch with a radius tip sharp enough (thinner than two times the characteristic grain size). Therefore, experimental measurements by the indentation fracture method [10] were necessary in the AZ composite. A value of $K_{c,0} = 4.3 \pm 0.6$ MPa√m was obtained. It is believed to be reliable and it is a value comparable with other measurements from the literature [11] which has been performed in exactly the same material and measured by a chevron notch-technique (the experimental results by the VAMAS procedure showed a big scatter and lie higher: $K_{c,0} = 5.4 \pm 1.0$ MPa√m).

The K_c-values and the corresponding J_c-values are also listed in Table 5.1. It is seen that the fracture toughness (and energy toughness) values of the A/AZ laminates are significantly larger than the corresponding intrinsic values of the A- and AZ-materials. It should be noted here that the J_c-values characterize the fracture initiation toughness of the materials; in the ceramic community the term fracture energy is often used.

Three specimens of the multilayer composite with various initial crack lengths were tested. In the first specimen the crack tip was located in the middle of the first layer, in the second specimen shortly before and in the third shortly behind the interface to the second layer (interface 1). The initial geometries and the results of the experiments are listed in Table 5.1. Besides the K_c-values, also the loads at fracture F_{fr} are given. Additionally, approximate J_c-values are listed which are calculated from the relation $J = \left(1 - \bar{v}^2\right) K^2 / \bar{E}$, using volume-averaged values of the Poisson's ratio, $\bar{v} = 0.25$, and the Young's modulus, $\bar{E} = 375$ GPa.

Table 5.1: Results of the fracture toughness tests on the multilayer composites.

Specimen	B [mm]	W [mm]	a [mm]	tip location	F_{fr} [N]	K_c [MPa.m$^{1/2}$]	J_c^{appr} [J/m^2]
1	2.72	1.42	0.10	in A	117	6.1	98
2	2.64	1.42	0.18	in A	103	7.3	142
3	2.64	1.42	0.21	in AZ	110	8.4	188

5.3. Numerical Modeling of apparent R-curves

The study of stress intensity factors as well as of their relevance for crack growth has been one of the topics of fracture mechanics research in composite materials, see e.g.

recent works [1, 12-14]. Once the stress intensity factor is known, it is possible to use a failure criterion that predicts failure.

For the solution of many problems stress intensity factors can be found in the comprehensive handbooks of Murakami [15], Tada [16], etc. However, the relevant stress intensity factor cannot be found for every specific problem. By application of the principle of linear superposition stress intensity factors for complicated load cases can be combined from solutions of simple load cases found in handbooks. A great number of methods have been developed for the determination of stress intensity factors: method of complex stress function, method of conform mapping, weight function method, finite element method, boundary element method, boundary collocation method, J-integral and many others. A brief overview on them is given in [17].

Most of the methods mentioned in the introduction require separate calculation of the stress intensity factor for each stress distribution and each crack length. The weight function method developed by Bueckner [18] simplifies the determination of stress intensity factors considerably. It can be demonstrated that a weight function exists for any crack problem specified by the geometry of the component and a crack type. If this function is known, the stress intensity factor can be obtained by simply multiplying this function by the stress distribution and integrating it along the crack length.

In the current investigation, a second method is used, the concept of configurational forces approach. Here we refer to previous works by Simha, Kolednik et al. [7, 19-21]. References to the open literature with respect to this concept and also some related formulations can be taken from these rather extensive papers. Specifically, the reference [21] provides the corresponding equations which are reshaped below in the specific form for composites with constant material properties within each lamina. This method will be used for comparative purpose, the comparison will be established with the solution given by the weight function method.

The results presented in the section 5.3.2 ("Modelling the crack driving force by the configurational forces approach") are the result of a enjoyable collaboration with the Institute of Mechanics, Montanuniversität Leoben and the Erich Schmid Institute of Materials Science in Leoben. The FE-simulations were performed by Dr. C.R. Chen (crchen64@yahoo.com.cn). This section is similar to the publication [22]. The axes nomenclature and some figures are changed to be consistent with the rest of this work.

5.3.1. Analytical model by the weight function method

5.3.1.1 Description of the model

The apparent R-curve of a laminate can be calculated considering the equilibrium condition at the crack tip, i.e. crack propagation is possible if the stress intensity at the crack tip, K_{tip}, equals or exceeds the intrinsic material toughness $K_{c,0}$ ($K_{\text{tip}}(a) \geq K_{c,0}$). K_{tip} is the contribution of two terms

$$K_{\text{tip}}(a) = K_{\text{appl}}(a) + K_{\text{res}}(a) \quad , \qquad\qquad \textbf{Eq 5.3}$$

where $K_{\text{appl}}(a)$ is the applied stress intensity and $K_{\text{res}}(a)$ the stress intensity contribution from the residual stress. Solving for $K_{\text{appl}}(a)$ holds

$$K_{\text{appl}}(a) \geq K_{c,0} - K_{\text{res}}(a) = K_{R,\text{effective}} \ , \qquad\qquad \textbf{Eq 5.4}$$

where $K_{\text{appl}}(a)$ equals the desired effective R-curve, $K_{R,\text{effective}}(a)$.

It is important to note that the so called effective R-curve differs in nature from classic R-curves. A classic R-curve follows a mathematical relation of the kind $K_c = K_c(\Delta a)$ where Δa is the crack extension. On the other hand, effective R-curves follow a relation $K_c = K_c(a)$ where the fracture toughness depends on the crack length. Of course, it can happen that the residual stresses-containing material presents a natural R-curve, then Equation 5.4 would read $K_{R,\text{effective}}(\Delta a, a) = K_{c,0}(\Delta a) - K_{\text{res}}(a)$ and $K_{R,\text{effective}}(\Delta a, a)$ is therefore dependent on a and Δa.

In fracture mechanics, both residual and applied stresses are usually included in the crack driving force. However, it is useful to consider the residual stresses as part of the crack resistance. Thus, in laminates with compressive stress at the surface, the higher resistance to failure results from a reduction of the crack driving force rather than from an increase in the intrinsic material resistance to crack extension.

So far the only unknown term is the contribution of the residual stresses. The term $K_{\text{res}}(a)$ can be approximately assessed by means of the weight function approach [17], that allows us to calculate the stress intensity factor $K(a)$, for an edge crack of length a for an arbitrary stress distribution acting normal to the prospective fracture path (see Figure 5.3). The weight function procedure developed by Bueckner [18] simplifies the determination of $K(a)$ since most of the numerical methods require separate

calculations for each given stress distribution and each crack length. This method is of particular interest when the material is submitted to a "complicated" stress profile such as creep [23], residual stresses in tempered glasses [24], or residual stresses in multilayers [12]. Applying this concept to our residual stress profile σ_{res} results,

$$K_{res}(a) = \int_0^a h(x,a)\,\sigma_{res}(z)\,dz \quad , \qquad\qquad \textbf{Eq 5.5}$$

where $h(z,a)$ is the suitable weight function, a is the crack length, and z is the distance from the surface (see Figure 5.3).
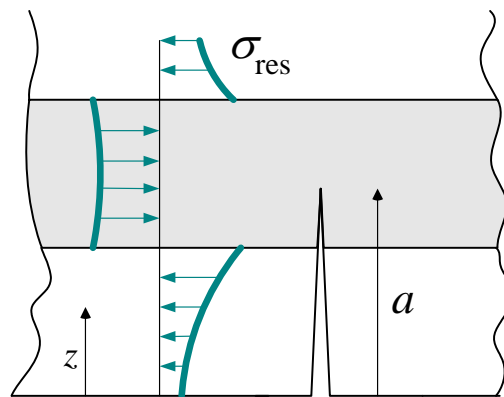
Figure 5.3: Sketch of the weight function analysis in a laminate.

Previous works by Fett et al. [5, 6] validate the applicability of this methodology to inhomogeneous materials. The weight function presented in Equation 5.6 was developed using the boundary collocation method [25]. It models materials with an homogeneous Young's modulus. It will be used as a first approximation. For inhomogeneous materials a suitable weight function will depend on the local variations of the elastic modulus, $E(z)$. The consequences of using this simplified weight function for a laminate will be discussed later.

The weight function is

$$h(z,a) = \sqrt{\frac{2}{\pi a}}\,\frac{1}{\sqrt{1-\frac{z}{a}\left(1-\frac{a}{W}\right)^{1.5}}}\left[\left(1-\frac{a}{W}\right)^{1.5}+\sum_{kl}A_{kl}\left(1-\frac{z}{a}\right)^{k+1}\left(\frac{a}{W}\right)^{l}\right], \qquad \textbf{Eq 5.6}$$

where the coefficients A_{kl} are listed in Table 5.2 as calculated in [23, 25]. W is the total thickness. It is worth of note that whereas in a homogeneous material the stress intensity factor is a function of the crack size and the applied mechanical or thermal

load, the stress intensity factor in graded materials is also dependent on the variation of Young's modulus in the component.

Table 5.2: Coefficients A_{kl} [23].

A_{kl}	$l = 0$	$l = 1$	$l = 2$	$l = 3$	$l = 4$
$k = 0$	0.4980	2.4463	0.0700	1.3187	-3.067
$k = 1$	0.54165	-5.0806	24.3447	-32.7208	18.1214
$k = 2$	-0.19277	2.55863	-12.6415	19.7630	-10.9860

In order to calculate the residual stresses in the laminates, Equation 2.3 and Equation 2.4 have been used.

In the following discussion, symmetrical *N*-layer laminates are studied (*N* being an odd number to fulfill the condition of symmetry). All the layers made of the same material (A or AZ respectively) have the same thickness, so the laminate is well defined by the thicknesses t_A and t_{AZ}, or the total thickness W and $\lambda = t_{AZ}/t_A$. Through the discussion, W will be considered constant and equals to $W = 1.5$ mm, according to a possible design condition.

The corresponding effective R-curves are calculated according to the procedure explained above. The influence of the residual stress field, defined by geometrical and material properties, on the apparent R-curve is examined in detail. The results are expressed for the laminated system $Al_2O_3 - xAl_2O_3/(1-x)ZrO_2$, but the conclusions can be extended for any ceramic multilayer system with ideally strong interfaces.

5.3.1.2. Results and Discussion

As shown by previous authors, the apparent R-curve in multilayers presents an oscillating behavior [3, 4] (see Figure 5.4, where the R-curve is presented for two architectures). The toughness increases in the layers under compression with increasing crack length and reaches a local maximum at the interface. Later, it decreases in the tensile layers reaching a local minimum at the interface, and so on. It can be stated that the compressive stresses shield the material against flaws, while the tensile stresses have a detrimental effect in the effective R-curve.

We caution the reader about the fact that a weight function that applies to a homogeneous material (*E* constant) has been considered. This approximation results in an error of maximal 10% for the calculated stress intensity factor [5]. The A/AZ laminate contains an AZ core that is less stiff than the A. Compared to a situation with

homogeneous stiffness, the A-layers carries more load and the AZ-layers less load, so that the calculated apparent toughness is overestimated in the alumina.
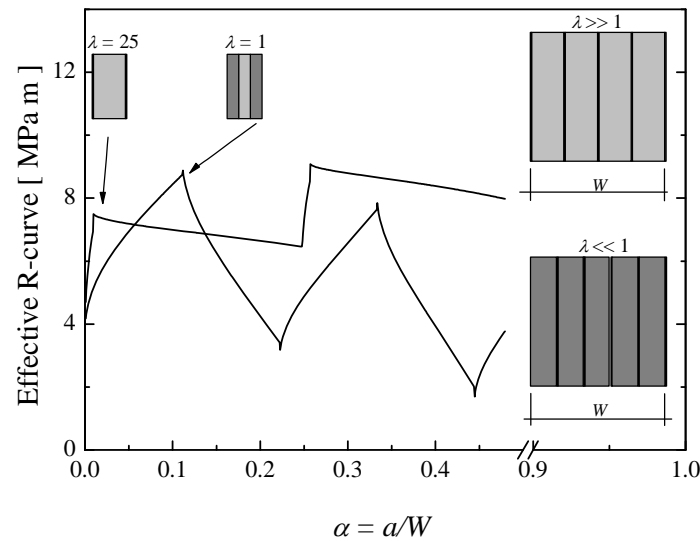

Figure 5.4: Characteristic R-curves of multilayer ceramics: one corresponds to a laminate containing high compressive stresses ($\lambda \gg 1$) and the other one containing high tensile stresses ($\lambda \ll 1$).

Figure 5.4 shows two interesting tendencies that appear in R-curves. For materials with high compressive stresses ($\lambda \gg 1$) the local maximums in the cyclic R-curve are placed in an ascending way, therefore the toughening level - in average - grows with crack length. On the other hand, if the magnitude of the tensile stresses dominates over the compressive, the toughening level decreases with the crack length. Especially for multilayers with a high number of layers, it can happen that the R-curve of a high λ-laminate is greater than one with a small λ for every crack length, and thus the architecture with a small λ should be rejected in terms of toughness.

As it derives from Equation 2.3 and 2.4, the architecture (λ) defines the residual stress field. It was the aim of this investigation to understand how the architecture influences the maximum shielding in the first layer. In Figure 5.5, apparent R-curves (until the crack length a being half of the thickness) are presented for different values of λ in the range from 0.2 to 25. Low values of λ correspond to thin alumina layers t_A in comparison to t_{AZ}, and thus high compressive stresses are present in these layers. That is the reason why the shielding increases so steep in the alumina layers and a high stress intensity factor has to be applied to fail the specimen. For high values of λ, the thickness of alumina layers is much bigger than that of the AZ composite layers and as a result, high tensile stresses arise in the AZ layers, while almost no compressive stress appears in the A-layers. That is the reason that the curves are not so steep in the compressive layers and the effective toughness drops in the AZ layers for these laminates. This kind of multilayers, could even present a lower apparent toughness for

all the crack lengths, so its mechanical performance is not so interesting as compared to laminates with $\lambda < 1$.
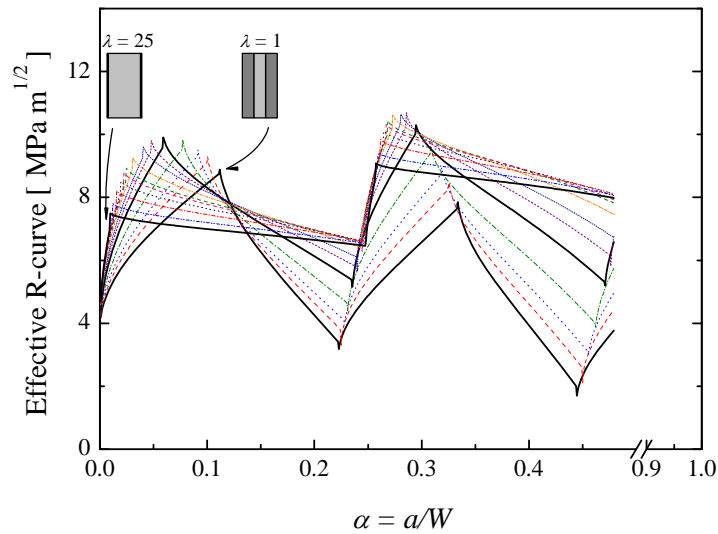

Figure 5.5: Influence of the thickness ratio $\lambda = t_{AZ}/t_A$ on the effective R-curve. The situation $W = 1.5$ mm and $N = 7$ layers has been chosen to present the results.

An interesting conclusion drawn from Figure 5.5 is the existence of an architecture that maximizes the shielding in the first interface. Opposite to what could be expected, the highest surface compressive stress (the highest λ) does not correspond to the highest shielding in the first layer. Since the maximum shielding in the first layer is obtained at a distance equal to the outer layer thickness, the thickness t_A plays an important role. In fact, in effective R-curves some crack growth is necessary for the development of the toughening.

This architecture that maximizes the apparent toughness at the first interlayer is especially interesting when short cracks are expected. Otherwise, for long cracks a laminate with $\lambda \ll 1$ could be more adequate due to the overall increase toughness that is present this type of multilayer.

A second conclusion worth of note concerns the fracture process. It is interesting to note that some *stable crack propagation* can be observed due to the cyclic nature of the effective curve. As shown in Figure 5.4, two clearly different behaviors are observed. In both cases, while the crack is propagating through layers under compression the shielding is increasing, reaching a maximum at the interface, but the overall tendencies are different. There are laminates for which the effective toughness presents an overall increase with crack length, while there are laminates that show an overall decrease.
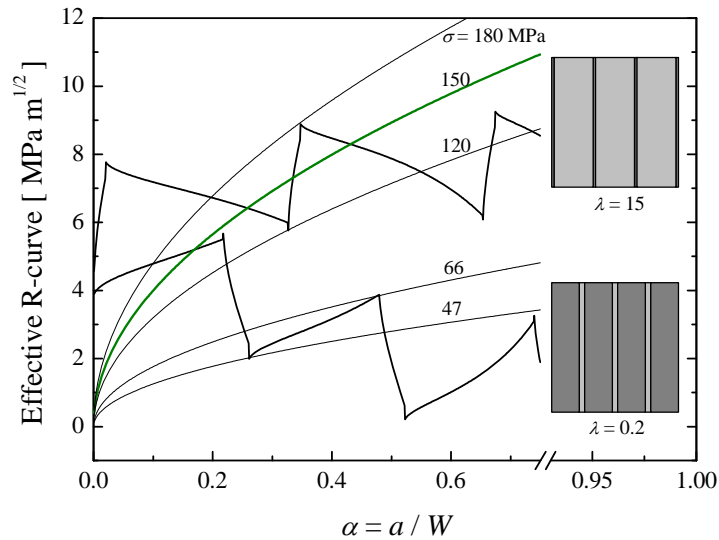
Figure 5.6: Two clear tendencies provoking different fracture process.

To evaluate for which crack lengths stable crack growth can occur, it is necessary to compare the effective toughness of a material for a given crack length (what is the same the effective R-curve) with the applied stress intensity factor. Then a classic failure criterion can be applied to determine if fracture occurs or not ($K > R$). The stress intensity factor K is dependent on $\sqrt{a}$ since its definition is $K = \sigma Y \sqrt{a}$ where σ is the stress and Y a geometric factor that can be found in the literature. Figure 5.6 presents the stress intensity factor for different stress levels.

It is interesting to note that if the slope of the effective R-curve in the compressive layers is smaller than the slope of the applied stress intensity factor stable crack growth can not appear. Therefore, laminates with thick compressive layers ($\lambda \ll 1$), which withstand low compressive stresses, present narrower stable extension range.

Figure 5.7 presents the range of crack length and stresses in which a laminate can present stable crack growth. Differently to classic R-curves which have stable crack growth during certain crack extension, laminates present stable crack growth only for certain initial crack lengths. In the example given in Figure 5.7 crack stability occurs between $a = a_0$ and $a = 2t_A + t_{AZ}$. The minor crack length that presents stable crack growth is a_0, which is calculated by the intersection (point B in Figure 5.7) of the effective R-curve and the stress intensity factor determined for a stress that equals the effective R-curve and the stress intensity factor in the point A (see Figure 5.7). A laminate with an initial flaw of length infinitesimally larger than a_0 would unstably extent after application of a stress of 180 MPa since at this moment the stress intensity factor equals the effective R-curve, but after certain extension $\Delta a = 2t_A + t_{AZ} - a_0$ (or for a crack length $a = 2t_A + t_{AZ}$) where the effective R-curve reaches a local maximum. A crack shorter than a_0 would grow inevitably until failure since it can not meet any

local maximum in the effective R-curve, but the stress necessary to grow it is higher than for larger cracks.
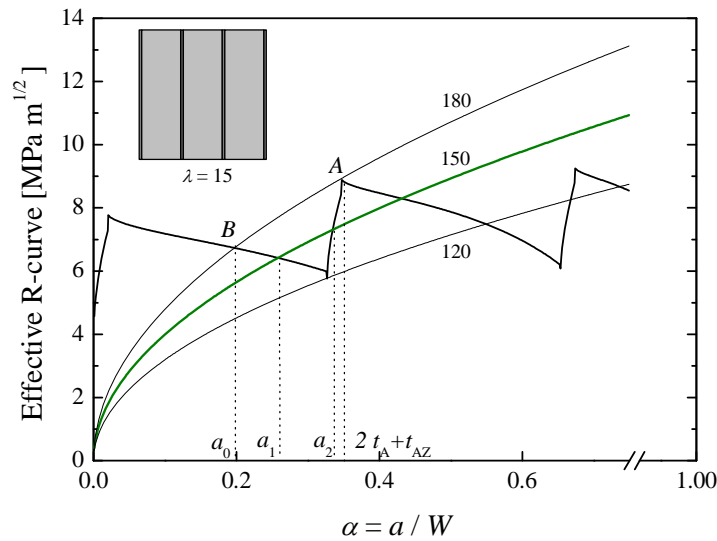

Figure 5.7: Fracture mechanics criterion.

Figure 5.7 presents the case of crack a_1 which under 150 MPa extends unstably to a crack length a_2 and later, in a controlled way until reaching a crack length $a = 2t_A + t_{AZ}$. This is the normal situation in multilayers and it happens not only from the second layer (in tension) to the third layer (in compression) but, in general, it could happen from any layer in compression to another in tension, depending on how the effective R-curve looks like. This unstable/stable behavior has been experimentally observed carrying out 4-point bending tests [26].

The architecture $\lambda = \lambda_{opt}$ that maximizes the shielding in the first interface, also deserves some attention. In Figure 5.8, an envelope with the maximum shielding for each λ is presented. Obviously all the maxima of these envelopes correspond to λ_{opt}. Figure 5.8 also presents the influence of the different architecture parameters (N and W) on shielding. N modifies the residual stress field thus influencing the shielding and W normalizes the crack depth in the effective R-curve. The envelopes can be obtained by evaluating the effective R-curves for each architecture (λ) at the first interface ($z = t_A$). The reader should keep in mind that for this work the stress field considered is given by Equation 2.3 and 2.4 that introduces some error in the outer layer since does not consider free surface. FEM calculations demonstrate that the difference is not significant in our case (see Chapter 4).

As one can appreciate from Figure 5.8 and Figure 5.9 the architecture does not influence the position of the maximum. This means that the optimal architecture λ_{opt} is exclusively defined by the physical constants. It also shows that shielding is more

protective with a low number of layers (keeping W constant) and for thicker specimens (keeping N constant). However, for relatively thick layers the authors expect a non-uniform stress field within the layers (Saint Venant principle) and the stress field considered here (Equation 2.3 and 2.4) would not apply.
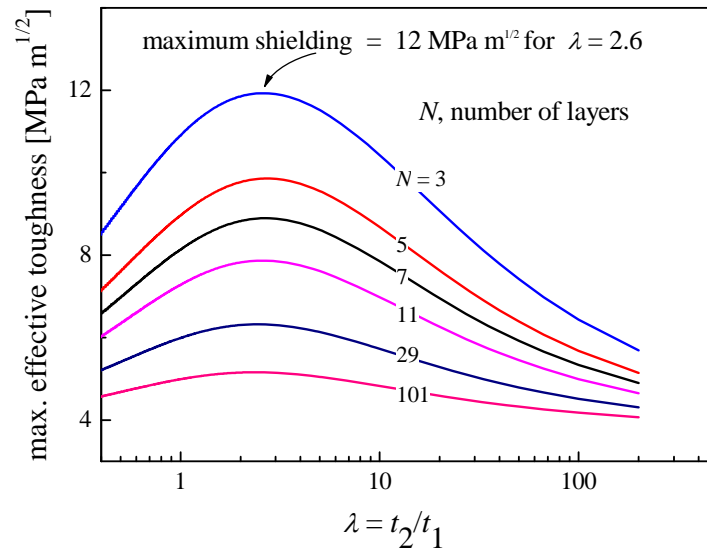
Figure 5.8: Influence of architecture on shielding. N is the number of layers.
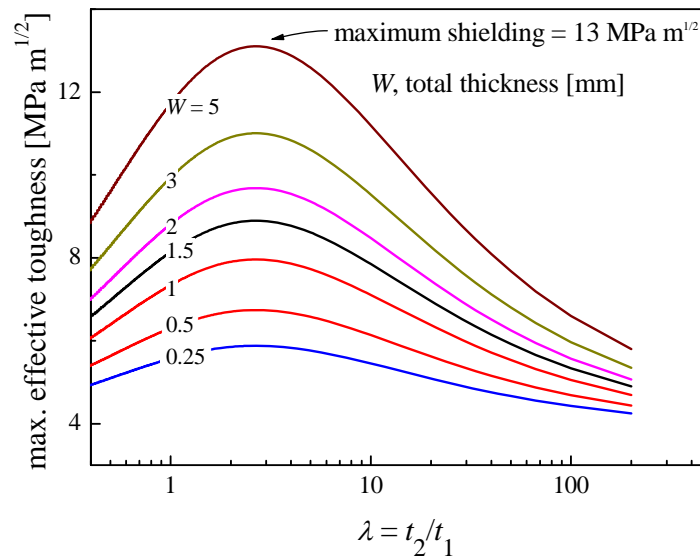
Figure 5.9: Influence of architecture on shielding. W is the total thickness.

The influence of the materials properties on the residual stress field is clear by Equation 2.3 and 2.4. The Figure 5.10 presents the maximum shielding in A/AZ laminates for several compositions of the composite AZ. The composition of the AZ composite cannot be chosen arbitrarily as problems may arise during processing if the thermal expansion mismatch is too high. An limited interval has been chose for this study. As one can observe the maximum for each composition is obtained for a different λ_{opt}. λ_{opt} varies from 2.25 for 95 vol% alumina to 2.7 for 50 vol% alumina.

Properties of the different composites (thermal expansion and elastic modulus) were estimated by applying the rule of mixtures to the values presented in the Annex 2.
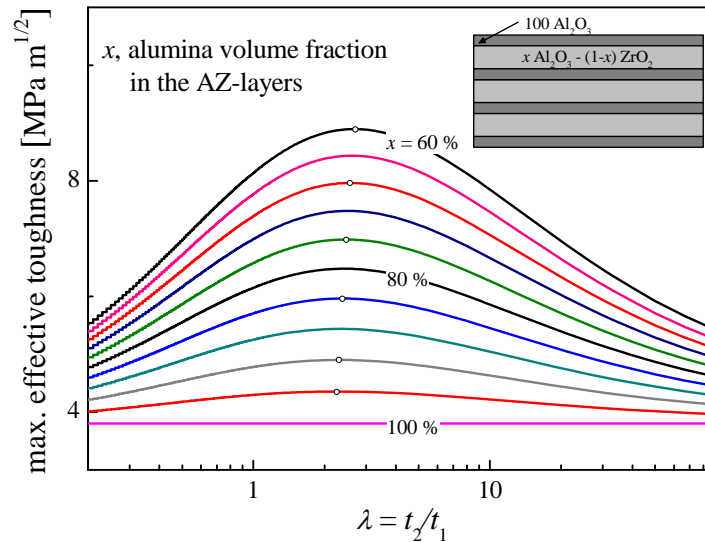
Figure 5.10: Influence of the AZ-composite chemistry on the maximum shielding of the outer A-layer.

Next we consider the influence of the modulus mismatch. Figure 5.11 reveals how a stiffer material than alumina in the outer layer will increase the toughness. In general the larger the elastic ratio (defined as $e'=E_{\text{outerlayer}}/E_{\text{innerlayer}}$) is, the layer the shielding will be. Figure 5.11 also introduces how the optimal architecture depends on the elastic mismatch, the larger the elastic mismatch is, the larger λ_{opt} is.
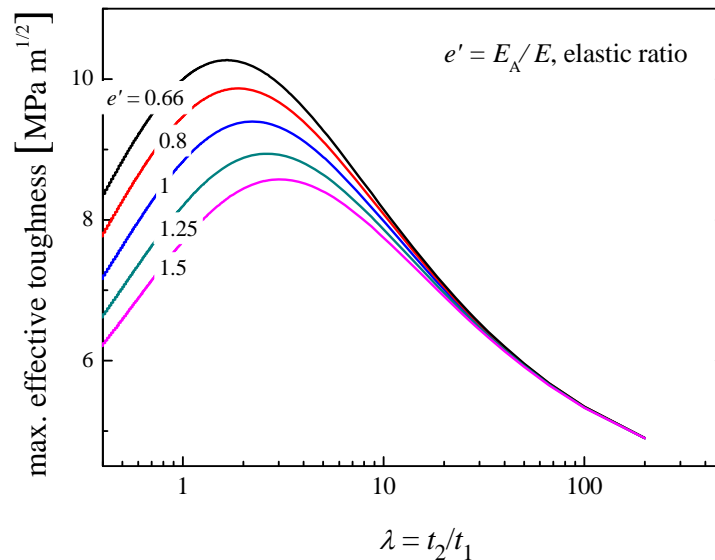
Figure 5.11: Influence of the Young's modulus E on the maximum shielding.

Interestingly, λ_{opt} is not depending on the thermal mismatch (defined as $\Delta\alpha = \alpha_{\text{inner}} - \alpha_{\text{outer}}$) as shown in Figure 5.12. Figure 5.12 shows that the higher the thermal

mismatch is the higher the shielding is. This is of course reasonable since the thermal mismatch is the origin of the stresses. For $\Delta a = 0$ the toughening would be zero.
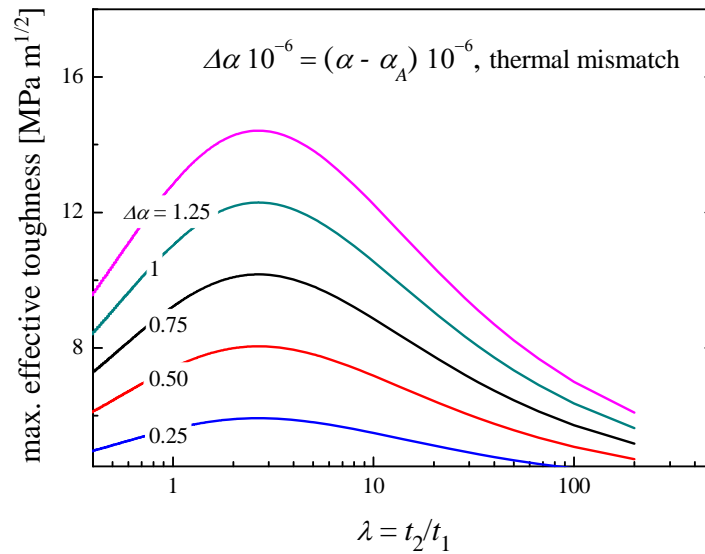
Figure 5.12: Influence of the coefficient of thermal expansion α on the maximum shielding.

5.3.2. Modeling the crack driving force by the configurational forces approach

The finite element simulations presented in the following have been performed by Dr. Chen in the framework of an enjoyable collaboration between ISFK Leoben, Institut für Mechanik and the Erich Schmidt Institute in Leoben. The results have been published in Acta Materialia, vol 55, 409-421, 2007. There exist nomenclature changes between the thesis and the publication.

5.3.2.1. Description of the Model

The global setting is depicted in Figure 5.13. The laminate beam is supported at a distance S_1 of 20 mm and loaded by a pair of loads at a distance S_2 of 10 mm. The laminate lie in planes parallel to the x-y-plane. The stacking arrangement and thickness of the laminate can be taken from the longitudinal section at $z = 0$, Figure 5.13. In this longitudinal section, an integration path Γ is marked surrounding a rectangle Ω_{far} with the area $W \cdot L_x$. The length L_x will be varied to obtain different paths Γ. The six interfaces, numbered from 1 to 6, intersect the integration path Γ at $x = 0$ and $x = L_x$. The normal unit vectors to the interfaces as well as to the integration path Γ are designated $\underline{n}$. The crack with variable length a is located in the plane $x = 0$; the crack front is assumed to be parallel to the line $z = 0$.
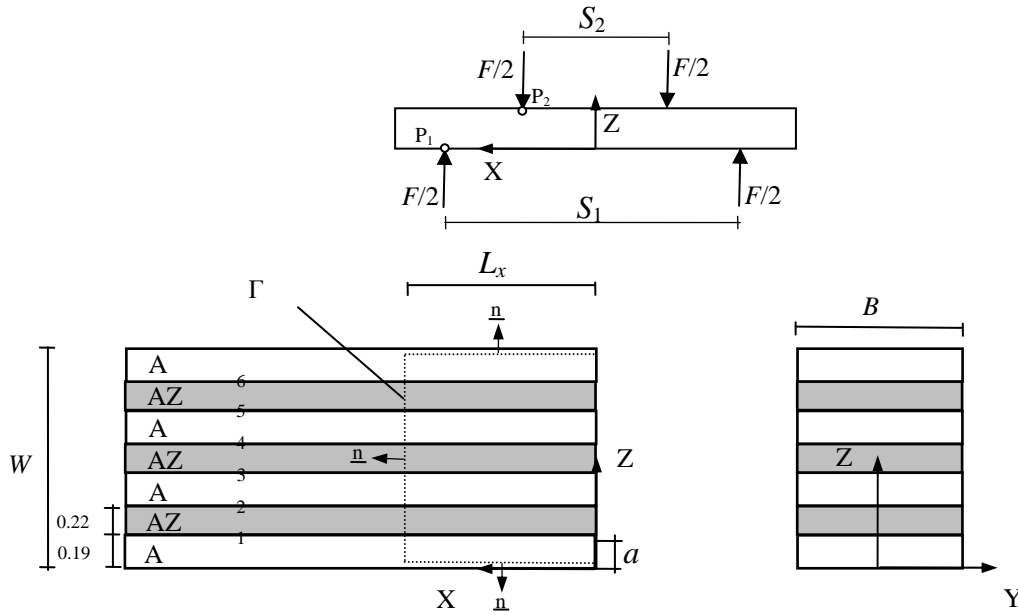
Figure 5.13: Geometry of the four-point-bending test arrangement of the laminate specimen consisting of layers of A- and AZ-material.

The Residual Stress State

In addition to the 3D computation presented in Chapter 4, two simple 2D computations were also performed [22]. The first one uses a plane strain model covering the area $0 \leq z \leq W$, $0 \leq x \leq \delta$ with unit thickness in the y-direction. The plane strain model assumes no displacement in the y-direction, $u_y \equiv 0$. To avoid any stresses due to the global shrinkage of the specimen, we set $\alpha_A^* = 0$ as the substitute CTE in the A-material and $\alpha_{AZ}^* = \alpha_{AZ} - \alpha_A = 0.6 \cdot 10^{-6} \ K^{-1}$ as the substitute CTE in the AZ-material. The second 2D computation uses the corresponding plane stress model. Results are presented in the Annex 2.

Beam Bending

As outlined above, the four-point-bend tests are performed on rather slender beams. The classical beam bending theory could be used to evaluate the stress state in the uncracked composite beam. We leave this task to the reader and refer to the open literature, e.g. [28, 29]. Since we need the stress state in the specimen with a crack of length a, finite element calculations are performed. The beam is replaced by a two-dimensional plane strain model covering the area, $0 \leq z \leq W$ and $x \geq 0$. Note that the plane strain model can be treated as a plane stress model by replacing the Young's modulus E by $E^* = E/(1-v^2)$. Only z-displacements u_z are allowed at $x = 0$. The

specimen is fixed at the point P_1 in z-direction; the load F applies at the point P_2 (see Figure 5.13). The mesh consists of 8-node plane strain elements.

To model a realistic stress state of the fracture mechanics specimens, the following procedure is applied: First, the uncracked and unloaded specimen is subjected to a thermal loading by a temperature difference $\Delta T = -1140°C$ ($T_{sf} = 1160°C$) to calculate the thermal residual stresses. Then in the unloaded specimen the crack of length, a, is introduced by a node release technique. Subsequently, the specimen is loaded by prescribing the load F at the load application point. The final stress and strain distribution within the specimen is used for the evaluation of the crack driving force which is described below.

Calculation of the Crack Driving Force

Simha et al. [7] provide a general model for the effect of inhomogeneities on the crack-driving force. The model will build on the material or configurational forces framework and will be derived without any a priori assumptions about the constitutive behavior of the materials or about the distribution of inhomogeneities. In the configurational forces approach two systems of forces are introduced: the classical deformational forces that act in the current configuration such as gravity and a new system of forces called configurational forces that act in the reference configuration. The configurational forces are responsible for kinematic changes in the reference such as the propagation of phase boundaries or crack growth due to the movement of the crack-tip.

The configurational forces approach has three fundamental advantages:
1. It is not variational and can account for dissipation (viscous, plastic)
2. In addition to crack growth, it can model diffusion, martensitic and diffusional transformations, thin film growth…. Hence, it provides a comprehensive framework for studying the influence of these processes on fracture.
3. It provides a measure that quantifies computational errors due to discretization.

It is well-known that the J-integral is not path-independent when inhomogeneities are present in the vicinity of a growing crack. We show that the inhomogeneity effect on the crack-driving force is precisely the difference between the J-integrals close to the tip and in the far-field.

The concept of configurational forces considers a material inhomogeneity as an additional defect in the material (besides the crack) which induces an additional contribution to the crack-driving force. This contribution has been called the material inhomogeneity term C_{inh}. The thermodynamic force at the crack tip, denominated as the local, near-tip crack driving force J_{tip} is the sum of the nominally applied far-field crack driving force J_{far} and the material inhomogeneity term C_{inh} [21]

$$J_{tip} = J_{far} + C_{inh} \, ,$$ Eq 5.7

where C_{inh} is the effect of inhomogeneities on the crack driving force.

J_{far} is the classical J-integral of fracture mechanics. For a crack growing in z-direction, J_{far} is

$$J_{far} = 2\int_{\Gamma} (\phi n_z - t_i \frac{\partial u_i}{\partial z}) ds \; .$$ Eq 5.8

The components t_i ($t_i = t_x$, t_z) of the traction vector $\underline{t}$ along the contour Γ follow from the stress tensor $\underline{\underline{\sigma}}$ with the relevant components σ_x, σ_z, τ_{xz} as $\underline{t} = \underline{\underline{\sigma}} \cdot \underline{n}$. Note that the stress components are the sum of their contributions due to bending and the residual stress state, e.g. $\sigma_x = \sigma_{x,b} + \sigma_{x,res}$. The components u_i ($u_i = u_x$, u_z) of the displacement vector $\underline{u}$ are differentiated with respect to the crack growth direction, i.e. the z-direction. The quantity ϕ is the elastic strain energy per unit area and n_z the z-component of the unit normal vector $\underline{n}$ to the integration path Γ.

The material inhomogeneity term can be evaluated by [21]

$$C_{inh} = \sum_{i=1}^{I} C_{inh,i} \, , \; C_{inh,i} = -2\int_{0}^{L_x} \left(\left\| \phi_i \right\| - \left\langle \underline{\underline{\sigma}}_i \right\rangle \right) dx \; .$$ Eq 5.9

where ϕ is the bulk (Helmholtz) free energy per unit area. The jump $\left\| b \right\|$ and the average $\left\langle b \right\rangle$ of a quantity b at an interface are defined as

$$\left\| b \right\| = (b_r - b_l), \left\langle b \right\rangle = (b_l + b_r)/2 \, ,$$ Eq 5.10

where b_r and b_l denote the limiting values of the quantity b on the right and left side of the interface, respectively. The index i refers to the individual interface; the integer I denotes the total number of interfaces in the specimen. In our case $I = 6$.

The following comments may be useful:

- The multiplier 2 in Equation 5.8 and Equation 5.9 points to the fact that only the upper half of a symmetric configuration with respect to Γ is considered.
- The material inhomogeneity terms $C_{inh,i}$ can be also found via the J-integral calculation routine provided by the finite element code by evaluating the J-integral around the ith interface $J_{int,i}$ [19]. In ABAQUS, this is done by specifying the set of nodes on the interface as virtual crack tip nodes. Even a contour directly adjacent to the interface yields very accurate results. For the evaluation of the J-integral, the virtual crack growth direction must be specified; it is the (0,0,1)-direction, as for the evaluation of J_{far}.
- Generally, both J_{far} and C_{inh} depend on the crack length a. They also depend on the integration path, L_x, but produce J_{tip}-values which are independent on L_x; for details see Annex 3.

After the finite element stress analysis, the material inhomogeneity term C_{inh} is calculated from Equation 5.9 by a post-processing procedure. The integration along the interface is performed using the trapezoid formula. Hereby, the node values of the stress and strain components and the strain energy density are taken, which are extrapolated values from the Gauss integration points. The far-field J-integral J_{far} is calculated using the virtual crack extension method of ABAQUS. Then the near-tip crack driving force J_{tip} is calculated from Equation 5.7. The numerical results will be presented in the following section.

It should be noted that Sun and Wu [30] have calculated the effective crack driving force by replacing the region Ω_{far} by subregions, each including only one layer, and applying the *J*-integral procedure for each individual layer. The strength of the configurational forces concept lies in its general applicability. The material inhomogeneity can be either a sharp interface with a discrete jump of the material properties or a region where the material properties change continuously. The C_{inh}-evaluation procedure can be applied to any arbitrary spatial distribution of these material inhomogeneities in both elastic and elastic-plastic materials. In general, the evaluation of C_{inh} can be performed very accurately. This enables us to evaluate J_{tip} as the sum J_{far} and C_{inh} more accurately than it would be possible from the calculation of J_{tip} using the conventional *J*-evaluation procedures, especially for cases when the crack tip comes close to an interface. All these points show the advantages of the configurational force concept over the conventional J-integral approach.

5.3.2.2. Results and Discussion

In the following, the results of the numerical analyses for our multilayer composite are presented. Corresponding analytical evaluations which are helpful for the discussion of the results are shown in the Annex 1 and Annex 3. In Annex 1 the strain energy density and the thermal residual stresses are derived for the composite under plane strain conditions. In Annex 3 useful analytical estimates of the crack driving force are given.

Elastically Homogeneous Material with Inhomogeneity in CTE

There are two sources of shielding and anti-shielding effects in our multilayer composite, the spatially varying residual stresses and the different elastic moduli of the laminate. To separate the two effects, we will first present the results for an elastically homogeneous material with spatially varying thermal residual stresses. It is assumed that the whole specimen has the elastic properties of material A. The CTE shows a spatial variation with values of α^* as defined in section 4.2. To get in the elastically homogeneous composite exactly the same residual stresses as they appear in the elastically inhomogeneous composite, $\sigma_{x,\text{res}}^{\text{A}} = -144$ MPa and $\sigma_{x,\text{res}}^{\text{AZ}} = 166$ MPa, the effective temperature difference was set to $\Delta T = -1007.3$ °C.

In Figure 5.14 the crack driving force J_{tip} is plotted against the specific load $\hat{F} = F/(2B)$. Presented are the curves for two specific crack lengths, $a = 0.18$ mm (crack tip 0.01 mm before the first interface) and $a = 0.20$ mm (crack tip 0.01 mm behind of the first interface). For comparison, the curves of the completely homogeneous specimen without residual stresses are also given which exhibit the common quadratic dependency on the load. The residual stresses shift the origin of the curves. Since the residual stress state in the first layer is a compressive one and the bending stresses $\sigma_{x,\text{b}}$ are tensile, the crack will open at a load F_{o} when the bending stresses balance the residual stresses $\sigma_{x,\text{bmax}} = \sigma_{x,\text{res}}^{\text{A}}$, compare Equation A3.6. From this equation, the quadratic dependency of J_{tip} on $(F - F_{\text{o}})$ can be also deduced. In Figure 5.14 the intrinsic fracture toughness values of the A and AZ material are indicated (compare Table A2.1). The fracture load can be estimated as the intersection point of these horizontal lines with the J_{tip} versus $\hat{F}$ -curve. Note that the material is rather brittle; thus it exhibits only a small process zone in front of the crack tip where the microscopic processes of micro-crack formation and growth take place, which lead to brittle fracture. Therefore, it can be assumed that the fracture resistance of the composite is primarily determined by the material in which the process zone is located. Due to the residual stresses, the specific fracture load of the specimen with $a = 0.20$ mm increases from $\hat{F}_{\text{fr}} \approx 12.5$ N/mm to $\hat{F}_{\text{fr}} \approx 20$ N/mm. For the specimen

with $a = 0.18$ mm the shift of the fracture load is even larger, from $\hat{F}_{fr} \approx 10$ N/mm to $\hat{F}_{fr} \approx 22$ N/mm.
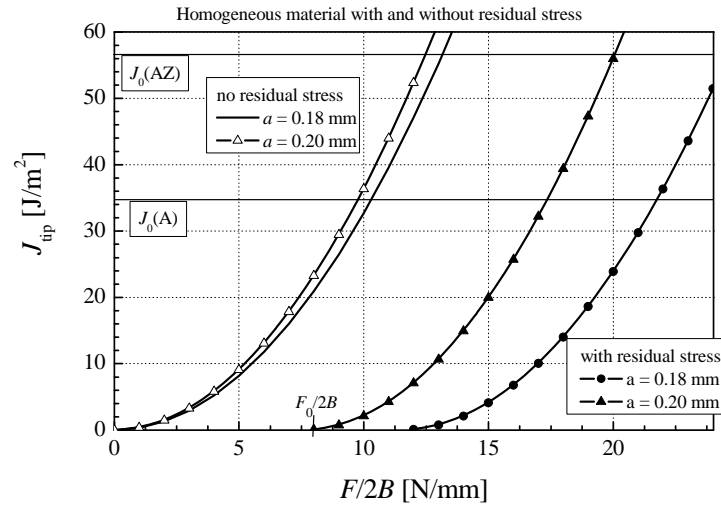
Figure 5.14: Effective crack driving force J_{tip} as a function of the specific loading $F/2B$ for the homogeneous specimen (material A), with and without residual stresses.

The influence of the crack length a on the crack driving force at a constant loading is shown in Figure 5.15a and Figure 5.15b. Plotted are the effective crack driving force J_{tip} and the term $J_{far} - J_{far}(0)$. Hereby J_{far} denotes the far-field J-integral for the composite with crack length a, and the expression $J_{far}(0)$ describes the far-field J-integral for the composite with zero crack length, see Annex 3. Note that for a loaded component which contains residual stresses $J_{far}(0)$ is non-zero and depends on the length of the integration path L_x, see Equation A3.2 and Equation A3.3. For a component with a crack $J_{far}(a)$ depends also on L_x, but the term $J_{far} - J_{far}(0)$ is path-independent, see Equation A3.6.

(a)

(b)
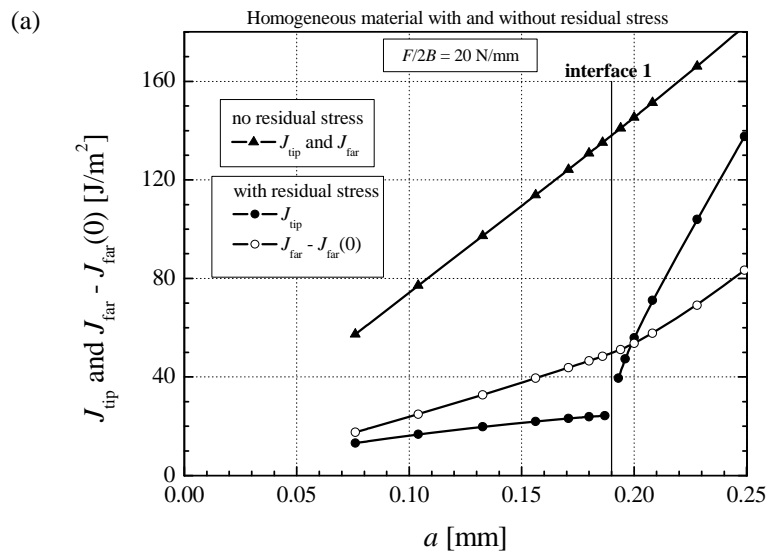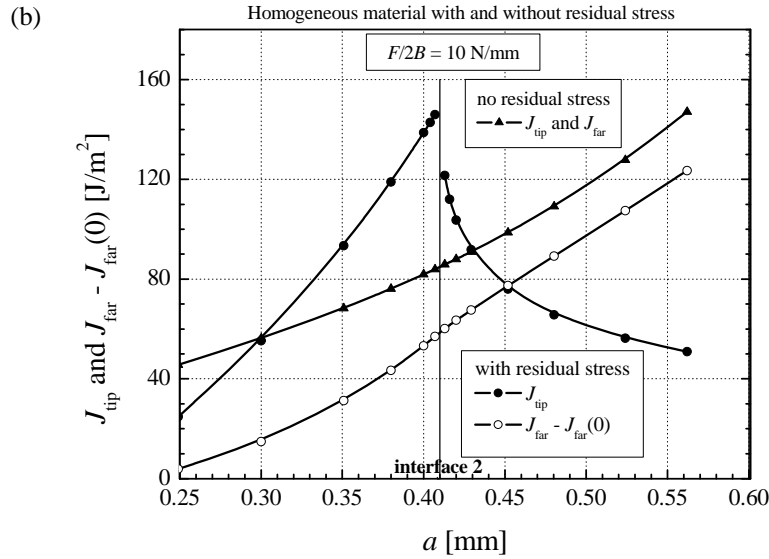
Figure 5.15: J_{tip} and the path independent far field J-integral term J_{far} - $J_{\text{far}}(0)$ as a function of the crack length a for the homogeneous specimen with and without residual stresses. a) for $F/2B = 20$ N/mm, b) for $F/2B = 10$ N/mm.

For comparison, the J_{tip} and J_{far} vs. a curves of the completely homogeneous specimen without residual stresses are also given. Of course, the two curves coincide and $J_{\text{far}}(0) = 0$. Figure 5.15a shows the curves for a crack close to the interface 1 and $\hat{F} = 20$ N/mm; Figure 5.15b shows the curves for a crack close to the interface 2 and $\hat{F} = 10$ N/mm. (The loads were chosen so that J_{tip} has a realistic size, not far from the size of the intrinsic fracture toughness values.) As deduced in Equation A3.7, the effective crack driving force J_{tip} shows approximately a linear dependence on the crack length a. The small deviation from non-linearity appears, since the parameter κ (see Annex 3, Equations A3.7 and A3.12) is slightly dependent on the crack length a. Note that $J_{\text{tip}} = J_{\text{far}} + C_{\text{inh}}$ does not depend on the length of the integration path L_{x} and that for a component with zero crack length $J_{\text{tip}}(0) = 0$, see Equation A3.5. The curves reveal a twofold effect of the residual stresses: The first effect is that, compared to the fully homogeneous material, the term $J_{\text{far}} - J_{\text{far}}(0)$ is generally reduced. This is due to the compressive residual stresses in the outer layer which restrain the opening of the crack. The second effect arises from the shielding or anti-shielding of the crack tip due to the inhomogeneity of the residual stress distribution in the specimen. This makes the effective crack driving force J_{tip} becoming different from the term $J_{\text{far}} - J_{\text{far}}(0)$. Equation 5.7 can be extended to the relation

$$J_{\text{tip}} - \left(J_{\text{far}} - J_{\text{far}}(0) \right) = C_{\text{inh}} - C_{\text{inh}}(0) \ , \qquad\qquad \textbf{Eq 5.11}$$

where $C_{\text{inh}}(0)$ denotes the material inhomogeneity term for a component with zero crack length. Note that the terms $J_{\text{far}}(0)$ and $C_{\text{inh}}(0)$ are used in the figures only to

make the J_{far}- and C_{inh}-values path independent, and that the relation $J_{far}(0) = -C_{inh}(0)$ holds, see Annex 3 and Equation A3.5.

The material inhomogeneity term C_{inh} reaches a local extremum, if the crack is just penetrating an interface. The material inhomogeneity term C_{inh} is negative and crack tip shielding occurs for a crack located at the interface 1; positive C_{inh} and strong anti-shielding occurs for a crack located at the interface 2.

Multilayer Composite with Inhomogeneity in Elastic Modulus and CTE

In this section, the results of the numerical analysis are presented and compared to the experimental results. Besides the spatially varying residual stresses, also the different elastic moduli of the A- and AZ-laminate influence the fracture behavior.

Figure 5.16 shows the J_{tip} vs. $\hat{F}$ curves for specimens with $a = 0.18$ mm and $a = 0.20$ mm. Plotted is the J_{tip} versus the $F/2B$ including the elastic mismatch of the layers. The curves of the elastically inhomogeneous specimen without residual stresses are also given. The comparison with Figure 5.14 delivers the following findings: It is seen that the inhomogeneity of the elastic modulus does not influence the origin of the curves; however, it generally increases the slopes of the curves so that all the fracture loads are decreased by approximately 10%.
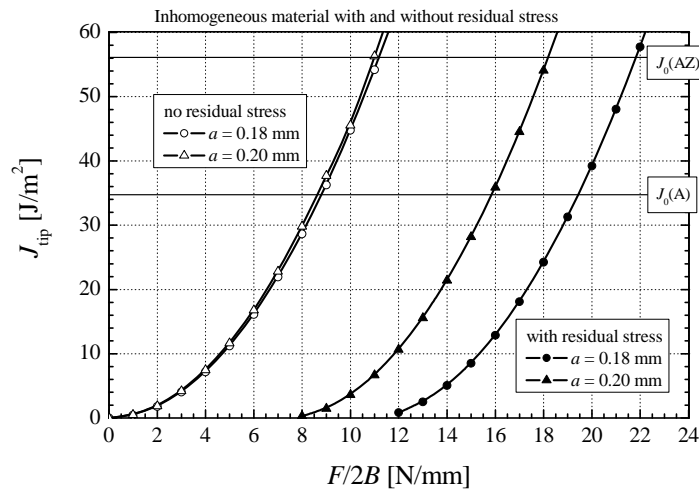
Figure 5.16: Effective crack driving force J_{tip} as function of $F/2B$ for the elastically inhomogeneous composite with and without residual stresses.

The dependency of the effective crack driving force J_{tip} and the term $J_{far} - J_{far}(0)$ on the crack length a at a constant load is presented in Figure 5.17a and Figure 5.17b. Figure 5.17a shows the curves for a crack near to the interface 1 and $\hat{F} = 20$ N/mm; Figure 5.17b shows the curves for a crack near to the interface 2 and $\hat{F} = 10$ N/mm.

The corresponding curves of the elastically inhomogeneous specimen without residual stresses are also plotted. These J_{far} vs. a curves are continuous curves which are only slightly bent. The comparison with Figure 5.15a,b shows that these curves lie above the corresponding curves of the completely homogeneous specimen. The inhomogeneity of the elastic modulus induces a material inhomogeneity term which is positive near the interface 1, since the stiff-compliant transition ($E_A > E_{AZ}$) induces an anti-shielding effect and $J_{tip} > J_{far}$ [19, 21]. For the crack ending directly at the interface, the values become singular: $C_{inh} \to \infty$ and $J_{tip} \to \infty$. Near the interface 2, the shielding effect of the compliant-stiff transition induces a negative material inhomogeneity term. For the crack ending directly at the interface, we get $C_{inh} \to -J_{far}$ and $J_{tip} \to 0$ [19, 31, 32], for a discussion see also [33].
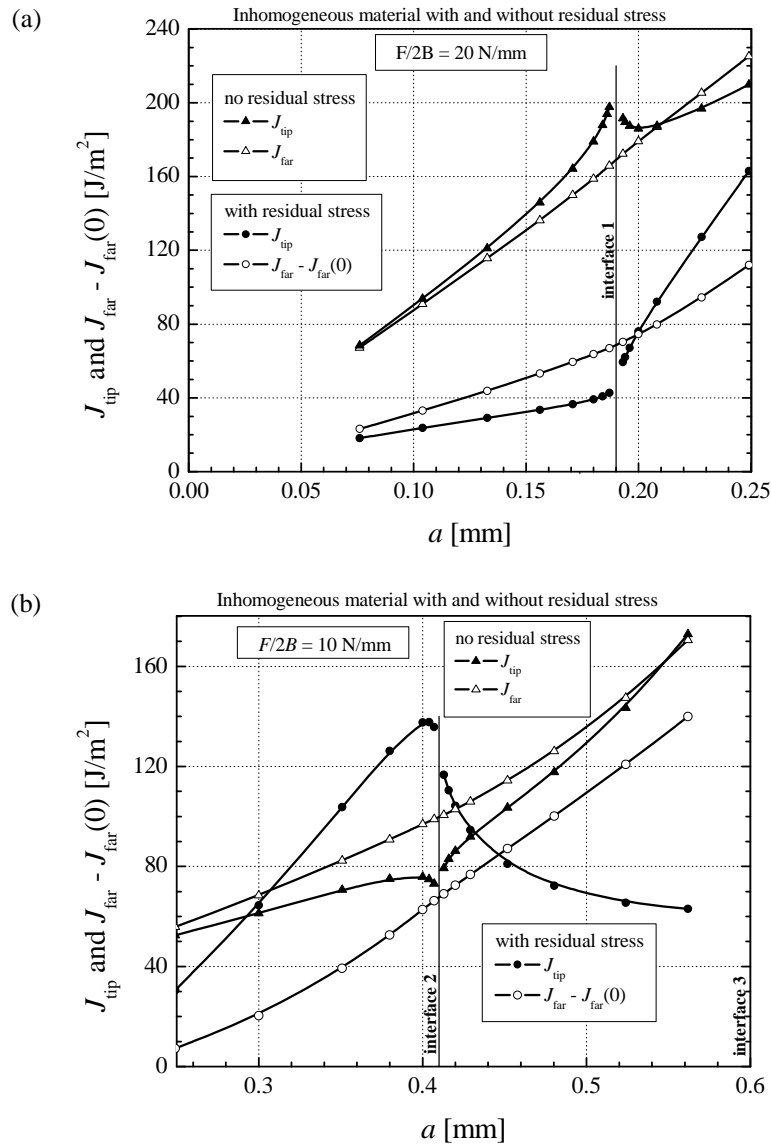
Figure 5.17: J_{tip} and J_{far} - J_{far} (0) as a function of the crack length, a, for the elastically inhomogeneous composite with and without residual stresses. a) for $F/2B$ = 20 N/mm, b) for $F/2B$ = 10 N/mm.

When comparing the curves of the real composite with E- and CTE-inhomogeneity to those with only the E-inhomogenity and, therefore, without residual stresses, it is noticed that the thermal residual stresses provoke a general decrease of the apparent crack driving force. The inhomogeneity of the elastic modulus and the CTE inhomogeneity have opposite effects on the material inhomogeneity term, but obviously the thermal residual stresses have a much stronger influence on the shielding/anti-shielding behavior than the modulus inhomogeneity. A comparison of Figure 5.15 and Figure 5.17 shows that, compared to the elastically homogeneous specimen, the J_{tip} vs. a curves of the real composite are generally shifted to higher J_{tip}-values. In addition the shapes of the curves differ when the crack comes close to the interfaces: Near the interface 1, J_{tip} is enhanced; near the interface 2, J_{tip} is reduced.

As discussed earlier in this section, it can be assumed that the specimen fractures when J_{tip} reaches the value of the intrinsic fracture toughness J_0 of the material where the crack tip is located. With this condition, the fracture loads F_{fr} of specimens with arbitrary crack lengths can be evaluated. Figure 5.18 shows the dependency of the specific fracture load $\hat{F}_{\mathrm{fr}} = F_{\mathrm{fr}}/(2B)$ on the crack length a. For comparison, the corresponding curves of the elastically inhomogeneous specimen without residual stresses are also given. Note that in a homogeneous specimen, F_{fr} should be proportional to $a^{-1/2}$. It is seen that the compressive residual stresses in layer 1 greatly increase F_{fr}. This is so not only when the crack tip is located in the layer 1, but also for some crack length after crossing the interface 1. For the crack tip in layer 2, the tensile residual stresses in the layer make the slope of the F_{fr} vs. a curve distinctly larger than that of the model without the residual stresses. When the crack tip has passed the middle of the layer 2, the fracture load falls below the F_{fr}-value of the model without the residual stresses. After the crack tip has penetrated the interface 2, the compressive residual stresses in the layer 3 quickly enhances F_{fr} over that of the model without the residual stresses. According to this curve, even a stable crack extension should be possible for an initial crack with its tip close to interface 2. For all other initial crack lengths, unstable crack growth will occur and the specimen will fail catastrophically when the crack starts to grow.

In Figure 5.18 also the experimentally measured fracture loads of the specimens 1, 2, and 3 are indicated. The numerically predicted values fit to the experimental data.
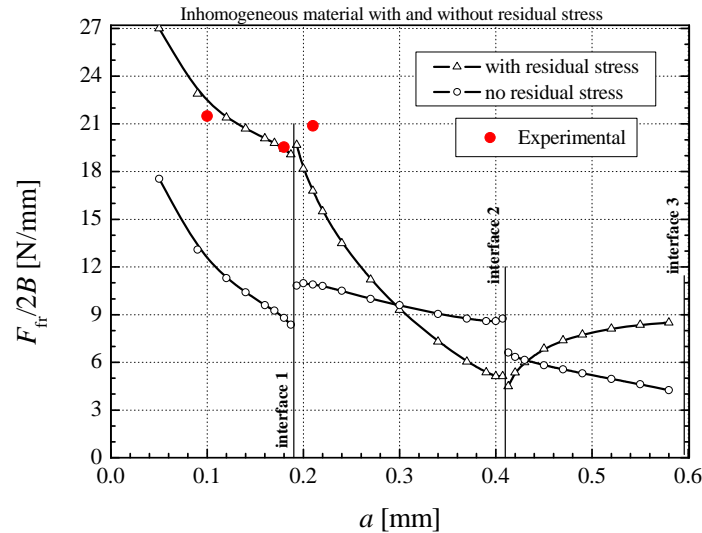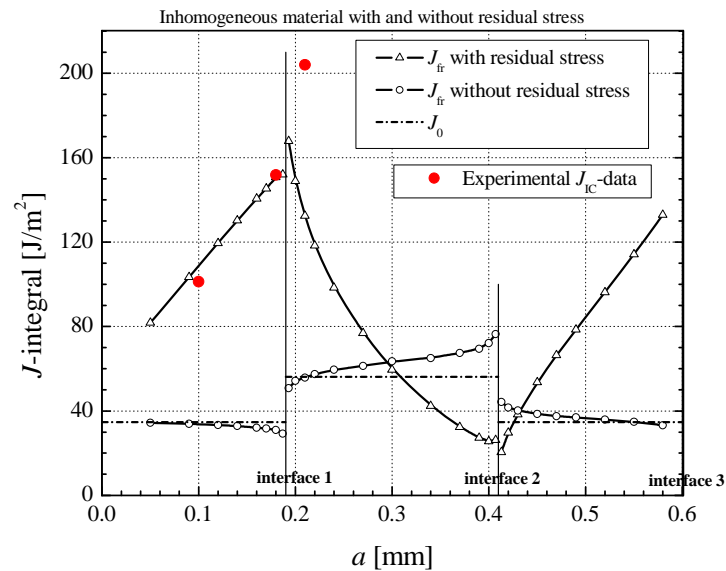
Figure 5.18: Numerically predicted and experimentally measured specific fracture loads $F_{fr}/2B$ which makes J_{tip} equal to the intrinsic fracture toughness J_0 of the individual layers.

For a specimen without residual stresses, the far-field J-integral of the specimen evaluated at the fracture load $F = F_{fr}$ can be taken as the apparent fracture toughness J_{fr} of the specimen which would be measured in the experiment. For an elastically inhomogeneous material without residual stresses, the far-field J-integral of the specimen with zero crack length $J_{far}(0) = 0$ and, therefore, J_{far} is path independent if the path Γ crosses all the interfaces and if L_x is not too small. In the case of a residual stress discontinuity, the size of $J_{far}(0)$ depends on the load F and, therefore, J_{far} becomes strongly path-dependent. This is the reason why the J_{far}-value which corresponds to the critical force F_{fr} cannot be directly taken as the apparent fracture toughness of the specimen. Instead, we use an "apparent far-field J-integral" J_{fr} which is determined as follows: First the fracture load F_{fr} is determined so that for the real composite J_{tip} equals J_0. Then this F_{fr}-value is applied to the model without the thermal residual stresses and, subsequently, the path independent value of J_{far} is evaluated. This J_{far} value represents the apparent fracture toughness J_{fr} of the specimen with the residual stress state.

In Figure 5.19 the apparent J_{fr}-values are plotted as a function of the crack length a. For comparison, the intrinsic fracture toughness values J_0 of the A- and AZ-material and the J_{fr}-values of the elastically inhomogeneous specimen without residual stresses are also inserted. The latter demonstrate the effect of the inhomogeneity of the elastic modulus on the apparent fracture toughness. This effect is rather small compared to the effect of the thermal residual stresses; but still, for a crack approaching interface 2, it leads to a significant increase of the fracture toughness. The largest benefit of the compressive thermal residual stresses in layer 1 occur for a crack approaching interface 1: For the crack tip in the layer 1, J_{fr} increases almost linearly with

122

increasing *a*, reaching finally a value more than 4 times higher than the intrinsic fracture energy. After having penetrated interface 1, the apparent fracture energy sharply decreases, reaching for the crack tip at interface 2 a minimum value which is far below the intrinsic energy. When the crack tip is in the layer 3, J_{fr} increases again with the increase of *a*.

Figure 5.19: Numerically predicted fracture toughness J_{fr}, computed for the composite with and without thermal residual stresses, and experimentally measured J_c-values.

In Figure 5.19 also the experimental values of the fracture toughness are plotted. These values were evaluated from the measured fracture loads of the specimens, using the above mentioned procedure to determine J_{far}. These values fit well to the numerically predicted values.

The difference between experiments and the configurational forces approach solution for the AZ-layer (about 60 J/m², see Figure 5.19) can be explained in several ways:

The crack driving forces calculated here do not consider that the material in each layer can present an R-curve. This hipothesis is true for a material like alumina (A) which has a small grain size [34]. However, for the AZ-composite - which also presents a small grain size - shall be remember that a characteristic of transformation-toughened ZrO_2-composite is their pronounced R-curve behavior due to the transformation $t \longrightarrow m$. This effect is believed to be of a great importance for the measurements and the predictions with the initial crack tip in the AZ layer.

Another possible source of error can be the frozen stress temperature - here considered to be 1160 °C [35] - which is difficult to measure accurately. Other

authors propose T_{sf} to be 1200 °C [36]. This higher value would increase the shielding residual stresses, and therefore a higher effective crack-driving force would be obtained. The increase from 1160 °C to 1200 °C bears an increase in toughness of about 20 J/m^2 that would partially explain the observed differences. But in order to fit the experimental value in the second layer, we shall misfit the experimental values in the first layer.

Concluding Remark.

Earlier was discussed, in the material forces section, that it can be assumed that the specimen fractures when J_{tip} reaches the value of the intrinsic fracture toughness J_0 of the material where the crack tip is located. This condition applies for crack initiation that in brittle ceramics is normally equivalent to fast fracture, but it does not consider the existence of stable crack propagation. We have introduced that some stable crack propagation may occur (see Figure 5.7). Therefore, crack initiation may not correspond directly to fracture.

Figure 5.20 presents the force to failure, F_{fr}, for the laminate with the R-curve presented in Figure 5.19. As expected, for very short cracks a large force is necessary to make fail the specimen. Until a crack length $a = 0.32$ mm, force to failure and force to crack initiation are coincident. Later, the stable-crack-growth regime appears and the force to failure is given by the force to failure at the end of the next compressive layer $a = 0.58$ mm (as introduced in Figure 5.7, the local maximums at the end of the compressive layers may stabilize the fracture process of shorter cracks in a previous layer under tension).
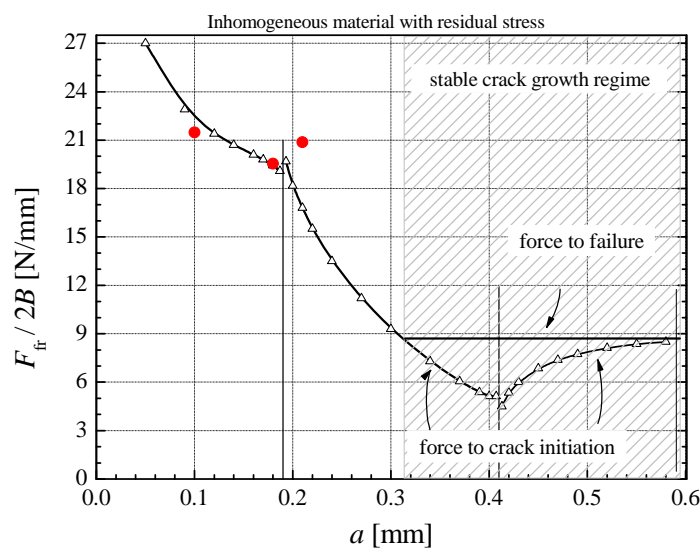
Figure 5.20: Numerically predicted and experimentally measured specific fracture loads $F_{fr}/2B$ which makes J_{tip} equal to the intrinsic fracture toughness J_0 of the individual layers.

5.4. Literature

[1]   Blattner, A., Lakshminarayanan, R., Shetty, D. K., "Toughening of layered ceramic composites with residual surface compression: effects of layer thickness", Engineering Fracture Mechanics, **68**, 1-7, (2001).

[2]   Moon, R. J., Hoffman, M., Hilden, J., Bowman, K. J., Trumble, K. P., Rödel, J., "Weight function analysis on the R-curve behavior of multilayered alumina-zirconia composites", Journal of the American Ceramic Society, **85**, 1505-1511, (2002).

[3]   Lube, T., Pascual, J., Chalvet, F., De Portu, G., "Effective Fracture Toughness in Al_2O_3 – Al_2O_3/ZrO_2 laminates", Journal of the European Ceramic Society, **27**, 1449-1453, (2006).

[4]   Sglavo, V. M., Paternoster, M., Bertoldi, M., "Tailored residual stresses in high reliability alumina-mullite ceramic laminates", Journal of the American Ceramic Society, **88**, 2826-2832, (2005).

[5]   Fett, T., Munz, D., Yang, Y. Y., "Applicability of the extended Petroski-Achenbach weight function procedure to graded materials", Engineering Fracture Mechanics, **65**, 393-403, (2000).

[6]   Fett, T., Munz, D., Yang, Y. Y., "Direct adjustment procedure for weight functions of graded materials", Fatigue and fracture of engineering material structures, **23**, 191-198, (2000).

[7]   Simha, N. K., Fischer, F. D., Kolednik, O., Chen, C. R., "Inhomogeneity effects on the crack driving force in elastic and elastic-plastic materials", Journal of the Mechanics and Physics of Solids, **51**, 209-240, (2003).

[8]   Kübler, J., "Procedure for determining the fracture toughness of ceramics using the single-edge-V-notched beam (SEVNB) method", EMPA, Swiss Federal Laboratories for Materials Testing and Research, (2000).

[9]   Damani, R., Gstrein, R., Danzer, R., "Critical notch-root radius effect in SENB-S fracture toughness testing", Journal of the European Ceramic Society, **16**, 695-702, (1996).

[10]   Anstis, G. R., Chantikul, P., Lawn, B., Marschall, D. B., "A critical evaluation of indentation techniques for measuring fracture toughness: I, Direct crack measurements", Journal of the American Ceramic Society, **64**, 533-538, (1981).

[11]   Toschi, F., Melandri, C., Pinasco, P., Roncari, E., Guicciardi, S., de Portu, G., "Influence of residual stresses on the wear behavior of alumina/alumina-zirconia laminated composites", Journal of the American Ceramic Society, **86**, 1547-1553, (2003).

[12]   Lugovy, M., Slyunyayev, V., Orlovskaya, N., Blugan, G., Kübler, J., Lewis, M., "Apparent fracture toughness of Si_3N_4-based laminates with residual compressive or tensile stresses in surface layers", Acta Materialia, **53**, 289-296, (2005).

[13]   Lugovy, M., Orlovskaya, N., Berroth, K., Kübler, J., "Macrostructural engineering of ceramic-matrix layered composites", Composites Science and Technology, **59**, 1429-1437, (1999).

[14]   Pascual, J., Chalvet, F., Lube, T., de Portu, G., "Strength distributions in ceramic laminates", Materials Science Forum, **492-493**, 581-586, (2005).

[15]   Murakami, "Stress Intensity Factors Handbook", Pergamon Press, (1987).

[16]   Tada, H., Paris, P. C., Irwin, G. R., "The stress analysis of cracks handbook", Del Research Corporation, (1986).

[17]   Fett, T., Munz, D., "Stress Intensity Factor and Weight Functions", Computational Mechanics Publications, (1997).

[18]   Bueckner, "A novel principle for the computation of stress intensity factors", ZAMM, **50**, 529-546, (1970).

[19]   Kolednik, O., Predan, J., Shan, G. X., Simha, N. K., Fischer, F. D., "On the fracture behavior of inhomogeneous materials -a case study for elastically inhomogeneous bimaterials", International Journal of Solids and Structures, **42**, 605-620, (2005).

[20]   Rakin, M., Kolednik, O., Simha, N. K., Fischer, F. D., "Influence of residual stresses on the crack driving force in bimaterials with sharp interface". In: International Conference in Fracture; Turin, (2005).

[21]   Simha, N. K., Fischer, F. D., Kolednik, O., Predan, J., Shan, G. X., "Crack tip shielding or anti-shielding due to smooth and discontinuous material inhomogeneities", International Journal of Fracture, **135**, 73-93, (2005).

[22]   Chen, C. R., Fischer, F. D., Kolednik, O., Pascual, J., Danzer, R., "Prediction of the fracture toughness of a ceramic multilayer composite - Modeling and experiments", Acta Materialia, **55**, 409-421, (2007).

[23]   Fett, T., Munz, D., "Determination of Fracture toughness at High Temperatures after Subcritical Crack Extension", Journal of the American Ceramic Society, **75**, 3133-3136, (1992).

[24]   Sglavo, V. M., Larentis, L., Green, D. J., "Flaw-insensitive ion-exchanged glass: I, Theoretical aspects", Journal of the American Ceramic Society, **84**, 1827-1831, (2001).

[25]   Fett, T., "Stress Intensity Factors and Weight Functions for the Edge Cracked Plate Calculated by the Boundary Collocation Method", Kernforschungszentrum Karlsruhe, (1990).

[26]   Pascual, J., Chalvet, F., Lube, T., De Portu, G., "R-curves in Al_2O_3 - Al_2O_3/ZrO_2 Laminates " in: Dusza, J., Danzer, R., Morrell, R. Key Engineering Materials. Trans Tech Publications Ltd., **290**, 214-221, (2005).

[27]   Shan, G. X., Kolednik, O., Fischer, F. D., Stüwe, H. P., "A 2D model for numerical investigations of stable crack-growh in thick smooth fracture-mechanics specimens", Engineering Fracture Mechanics, **45**, 99-106, (1993).

[28]   Malzbender, J., Steinbrech, R. W., "Mechanical properties of coated materials and multi-layered composites determined using bending methods", Surface and coatings technology, **176**, 165-172, (2004).

[29]   Bermejo, R., Torres Hernández, Y., Sánchez-Herencia, A. J., Baudín, C., Anglada, M., Llanes, L., "Fracture behaviour of an Al_2O_3-ZrO_2 multi-layered ceramic with residual stresses due to phase transformations", Fatigue and Fracture of Engineering Matererial Structures, **29**, 71-78, (2006).

[30]   Sun, C. T., X.X, W., "On the J-integral in periodically layered composites", International Journal of Fracture, **78**, 89-100, (1996).

[31]   Romeo, A., Ballarini, R., "A crack very close to a bimaterial interface", Journal of Applied Mechanics, **62**, (1995).

[32]   Fischer, F. D., Predan, J., Kolednik, O., Simha, N. K., Arch. Appl. Mech. submitted, .

[33]   Joyce, M. R., Reed, P. A. S., Syngellakis, S., "Numerical modelling of crack shielding and deflection in a multi-layered material system", Material Science and Engineering A, **342**, 11-22, (2003).

[34]   Steinbrech, R. W., Reichl, A., Schaarwaechter, W., "R-curve behavior of long cracks in alumina", Journal of the American Ceramic Society, **73**, 2009-2015, (1990).

[35]   Pascual, J., Chalvet, F., Lube, T., De Portu, G., "Strength of unsymmetrical ceramic laminates", SICMAC newsletter, (2004).

[36]   Green, D. J., Cai, P., Messing, G. L., "Residual stresses in alumina-zirconia laminates", Journal of the European Ceramic Society, **19**, 2511-1517, (1999).

Chapter 6. Strength in A/AZ Laminates

Weibull statistics is up to now the backbone in the mechanical design procedure of ceramic components but is not generally valid. Ceramic multilayers are one of those exceptions as they do not always fulfill all requirements to exhibit a Weibull behavior. In this chapter the applicability of this theory is discussed for the different multilayers existing in the literature. Additionally, a realistic strength distribution for multilayers strongly bond with surface compressive stresses is presented and supported by experimental results.

6.1. Introduction to Weibull's statistics

Fracture of brittle materials (e.g. ceramics) usually initiates from flaws [1], which are distributed in the material. Flaws are inhomogeneities in the microstructure, which can result from the processing, the machining or the handling of the specimens. Examples in ceramic materials are inorganic inclusions, hard or hollow agglomerates, badly sintered grain boundaries, large grains or cracks arising from the machining [2]. The material strength depends then on the size of the major flaw, which varies from specimen to specimen. Therefore, the strength of brittle materials is not given by a simple number but described by a probability distribution function [3-6]. Often, the two-parameter Weibull distribution is required, which in its simplest form -for a specimen of volume, V in a homogeneous uniaxial tensile stress state of amplitude σ - is given by:

$$F(\sigma,V)=1-\exp\left[-\frac{V}{V_0}\left(\frac{\sigma}{\sigma_0}\right)^m\right] \; , \qquad\qquad \textbf{Eq 6.1}$$

where F is the probability of failure and V_0 a normalizing volume usually set to $1\,\text{mm}^3$. The Weibull modulus, m, is a measure for the scatter of strength data: the wider the distribution is the smaller m is. Typical values for ceramics are around 5-15. σ_0 is a characteristic strength value (it is the stress at which the probability of failure equals 63% when $V = V_0$).

The Weibull distribution reveals two interesting practical points. The probability of failure, F, increases with the load amplitude and with the size of the specimen [3, 4,

7]. The first observation is trivial. The second observation follows from the fact that it is more likely to find a major flaw in a large specimen than in a small one. Therefore the mean strength of a set of large specimens is smaller than the mean strength of a set of small specimens. This size effect on strength is the most relevant consequence of the statistical treatment of strength in brittle materials.

The design of components made from brittle materials is based on the knowledge of this distribution function, which can be only measured on a large set of test specimens. This is expensive and will be hardly done in the daily design practice.

The mathematical structure of strength distributions has been deduced from physical principles that reduce experimental efforts necessary to find a proper distribution [8, 9]. The premises to derive a probabilistic distribution are listed in the following:

1. The density of defects is low enough so that interaction between flaws can be neglected (defined in a volume element which is large enough to contain several defects).
2. Weakest link hypothesis: the material fails when the weakest defect fails, like a chain breaking when the weakest link fails.
3. A density of critical defects, ρ_c, can be defined for a set of microscopically identical specimens.

After these three initial assumptions, it results that the probability of failure F for a small volume element is defined by [9]

$$F(V) = 1 - \exp\left[-\left\langle N_{c,V}(V)\right\rangle\right] , \qquad\qquad \text{Eq 6.2}$$

where $\left\langle N_{c,V}(V)\right\rangle$ is the mean number of destructive (critical) volume defects in a large volume V. For a small critical flaws density, $\left\langle N_{c,V}(V)\right\rangle \ll 1$, the probability of failure is approximately equal to the mean number of critical defects per specimen, while for a high mean value, $\left\langle N_{c,V}(V)\right\rangle \gg 1$, there is some (small) probability of finding specimens which do not contain any critical defect.

Based on these three initial premises it is possible to derive Equation 6.1 - the Weibull distribution in a homogeneous stress state - by assuming the additional hypotheses:

4. The defects are volume (surface) defects,
5. the defects are homogeneously distributed within the material,
6. the stress state is homogeneous,

7. compressive stress do not damage.

8. the volume (surface) defects behave as flat cracks which can be characterized by a single variable (crack length a),

9. the cracks are oriented perpendicular to the applied stress direction,

10. the frequency distribution density of defect lengths (mean number of defects per volume and defect length) is given by an inverse power law $g(r) = A \cdot a^{-r}$, where A and r are material constants.

11. the Griffith failure criterion applies: $K = \sigma Y \sqrt{a} \geq K_c$, where K is the stress intensity factor, Y the geometry factor for a given defect in a given component, and K_c the fracture toughness.

From these assumptions the Weibull distribution can be mathematically derived [9]. The parameters in the distribution, m and σ_0, yield

$$m = 2(r-1) \quad \text{and}$$

Eq 6.3

$$\sigma_0 = \frac{K_c}{Y}\left(\frac{r-1}{V_0 A}\right)^{1/m},$$

Eq 6.4

where A and r are the coefficients of the inverse power law that defines the frequency distribution density of defect lengths. K_c and Y come from the Griffith criterion, and are the fracture toughness and the geometry factor respectively.

In a similar way, this procedure can be applied to different cases. For instance, an analogous derivation can be done for surface defects, just replacing the volume V by the surface S, the new strength distribution yields

$$F(\sigma, S) = 1 - \exp\left[-\frac{S}{S_0}\left(\frac{\sigma}{\sigma_0}\right)^m\right],$$

Eq 6.5

being the surface submitted to a homogenous stress state σ.

Actually, Weibull proposed a three parameter form [10], where σ in Equation 1 is replaced by the expression $(\sigma - \sigma_{th})$ in which a third parameter appears, σ_{th}. It is usually called threshold stress. The physical meaning of σ_{th}, is that for stresses below the tensile threshold stress, σ_{th}, failure can not occur. Although this threshold stress reflects the wishes of ceramic engineers for reliable components, the two parameter

form of the Weibull distribution seems to reflect the observed behaviour of ceramic materials better than the three parameter form (see for example Lu et al [11]). Besides, it can be seen that using, for example, the Monte Carlo simulation technique [12] - especially in small data sets which contain no more than 30 specimens - σ_{th} is not a stable parameter to fit. It depends to a large extent on the subset of specimens selected to simulate the distribution function and not on its real value. Therefore, this lower bond is often set to be zero, $\sigma_{th} = 0$.

Weibull statistics apply also to describe the reliability of components, which are loaded not only under a uniaxial stress state but also under a complex spatially varying stress field. In the second case the relationships determined for tensile testing remain valid, if the stress σ in Equation 6.1 is replaced by a suitable equivalent stress (to account for the action of a multiaxial stress state) and the volume is replaced by the effective volume. Details can be found elsewhere [3-5].

In summary, Weibull's statistics is the most common tool to calculate probabilities of failure in brittle materials, but as exposed, many premises shall be fulfilled for its proper utilization. Several situations in which Weibull's theory could fail have been treated in the literature [13], for example, multimodal flaw size distribution or materials presenting an R-curve. Ceramic multilayers are also, in general, one of the exceptions to the Weibull's theory even if they are built-up by brittle materials that fulfill the Weibull's hypotheses.

The goal of this chapter is to investigate the applicability of the Weibull model to ceramic laminates by revising carefully its assumptions. A realistic strength distribution is assessed by two alternative ways, giving identical result.

6.2. Experimental

Laminates with a symmetrical stacking sequence (2A/AZ/A/AZ/A/AZ/2A) are investigated in this chapter. The thicknesses of the individual A- and AZ-layers are 190 µm and 220 µm, respectively. Details about processing can be found in Chapter 3. The physical properties necessary in this chapter are listed in Annex 2.

The strength was investigated on 2A/AZ/A/AZ/A/AZ/2A and A/A/A/A/A/A/A laminates. Both have alumina surface layers, one with surface compressive stresses (the first case) and the other one is free of stresses. The strength measurements (4-point bending tests) were performed on specimens with the following geometry $1.7 \times {\sim}2.6 \times {\sim}28$ mm. The interfaces were perpendicular to the applied force F (see

Figure 6.1). The tensile surface was an as-sintered surface. The specimens were chamfered prior to the test. The 4-point bending tests were carried out by means of a Zwick Z010 universal testing machine. The span lengths were 10 and 20 mm, the chosen crosshead speed 2 mm/min. The tests were conducted at laboratory conditions, relative humidity 23% and temperature 20 °C. The fracture surfaces were analyzed by light optic microscopy and scanning electron microscopy. Approximately 30 specimens were tested for each laminate.
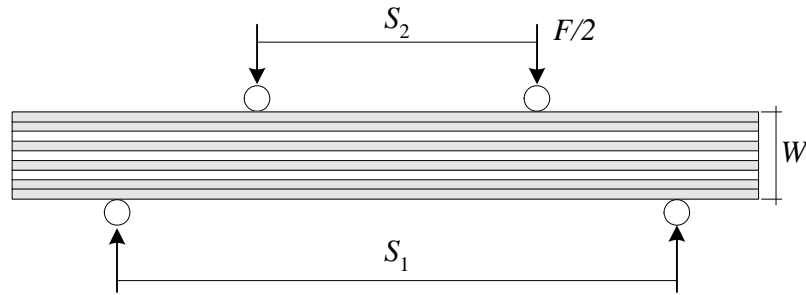
Figure 6.1: 4-point bending strength sketch. Interfaces are normal to the applied force.

For all the laminates the maximal stress at the outer fiber of the component can be calculated through the well-known relation

$$\sigma = \frac{3F(S_1 - S_2)}{2BW} \ ,$$

Eq 6.6

where F is the fracture load, S_1 and S_2 are the span lengths (see Figure 6.1), B is the width and W is the height of the specimen. The maximal stress in the component will be defined to be the strength of the material.

For a layered material with the layers having different elastic moduli, the above expression can only be considered a "nominal" strength, and it no longer represents the true maximum surface stress upon failure. To calculate the maximum stress in four-point bending, one needs invoke the classical laminate stress analysis. The exact solution (considering the elastic mismatch) can be found in the literature [14].

6.3. Results and discussion

After testing, the fracture surfaces of the specimens were examined for fracture origins. The fracture surface for an A/AZ laminate is presented in Figure 6.2. The different grain size between the materials results clear in Figure 6.3. The fracture surfaces were straight and no deflections were observed (deflections are common to

laminates with weak interfaces [15] or strong compressive stresses [16]). A common characteristic to both laminates is the existence of an abnormal grain growth of alumina at the surfaces that is believed to be the cause of failure [17]. As expected, the presence of zirconia impedes the grain growth of alumina at high temperature in the AZ-composite. Figure 6.4 presents the characteristic failure defect for the laminates, the abnormal large grains of alumina (around 20-35 μm) which is supposed to be the unique defect population. Exceptionally, it was observed an alignment of large grains along the surface that act as a "notch" (see Figure 6.4b). Other surface defects could be observed during the examination of the fracture surfaces, but their presence was anecdotic (see Figure 6.4c).

Because the failure occurs at the surface and because the stress is homogeneous at the surface during a 4-point bending test, it will be assumed that Equation 6.5 is valid. In fact, if we assume that the fracture process has nothing to do with the interface,- where the definition of critical defect is unclear - all eleven necessary premises to derive Equation 6.5 are fulfilled. The interface A/AZ has demonstrated to be strong enough by Jimenez-Melendo et al. [18, 19]. Let us remark that this is not the conventional trend in ceramic multilayers as many of them do not present strong interfaces, some contain weak layers that deflect cracks, others contain "tough" layers that arrest cracks, and therefore the two first premises do not apply: no interaction between flaws and weakest link hypothesis.
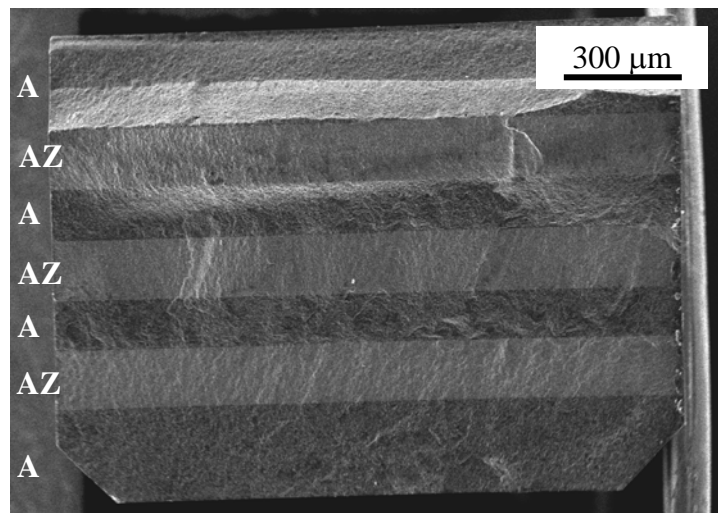

Figure 6.2: Fracture surface of an A/AZ laminate. The failure originated somewhere in the lower surface (the surface in tension during the 4-point bending test). At this surface, large grains of alumina are observable at higher magnification. The compressive curl, characteristic of bending tests, is observable.

The strength results are presented for a 2A/AZ/A/AZ/A/AZ/2A laminate and an A/A/A/A/A/A/A-"laminate" in Figure 6.5. They are calculated with the Equation 6.6. As commented, Equation 6.6 is not strictly valid for the A/AZ-laminate since it does not consider the elastic mismatch. An exact calculation [14] would increase the stress by 4 - 6% for the A/AZ-laminate. The influence is not significant as there are only 3 AZ-layer while 6 A-layers, and the A-layers are located at the surfaces (high stresses area). Besides, the elastic mismatch is relatively important.

The usual Weibull plot is used to present the results. In this plot Equation 6.5 is a straight line where the Weibull's modulus m is given by the slope. The characteristic strength σ_0 is given by the stress that equals $F = 0.63$ (or $\ln(\ln(1/1\text{-}F)) = 0$). As expected, the measurements seem to follow a straight line, so it does not look unreasonable to calculate the Weibull's parameters, m and σ_0. The values were fitted by means of the maximum likelihood method. The fitting results are listed in Table 1.

Table 1: Fitting of m and σ_0 by means of the maximum likelihood method.

laminate	m	σ_0
A/A/A/A/A/A/A	10.4	492
2A/AZ/A/AZ/A/AZ/2A	18.1	650
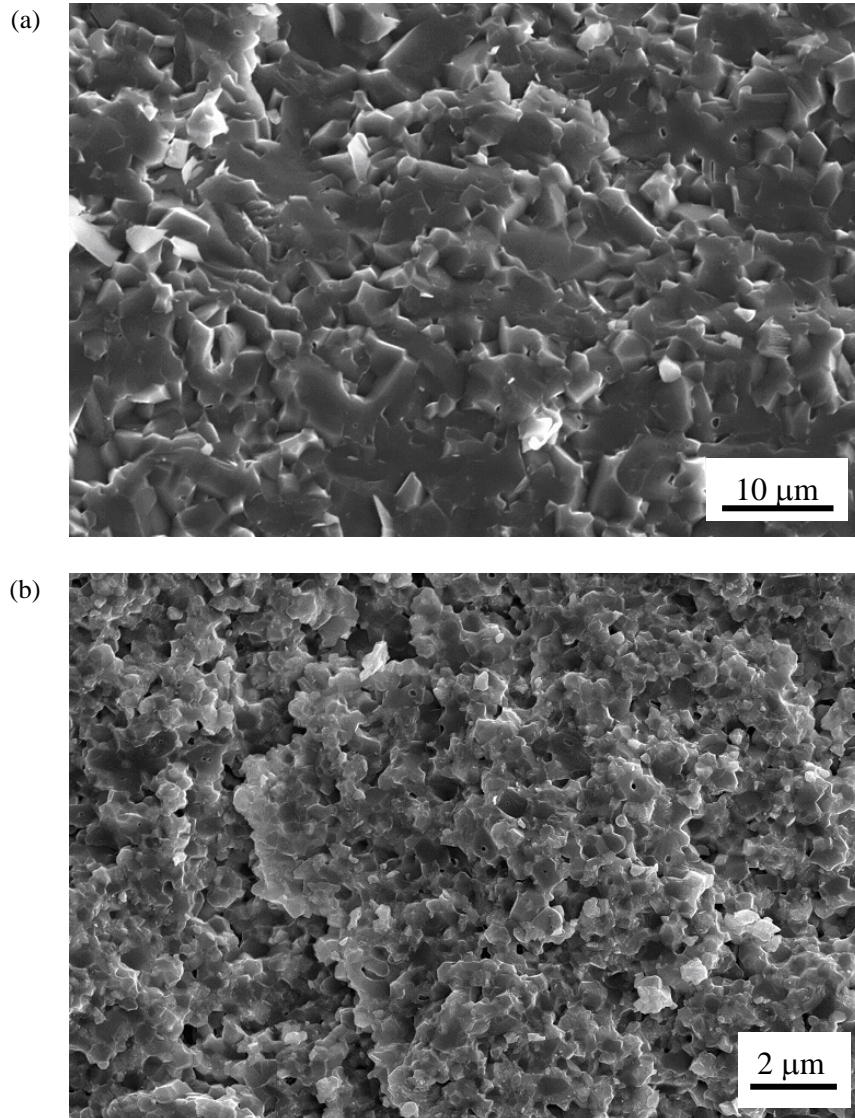
Figure 6.3: Detail of the fracture surface in: (a) an A-layer and (b) in AZ-layer.

(a)

(b)

(c)
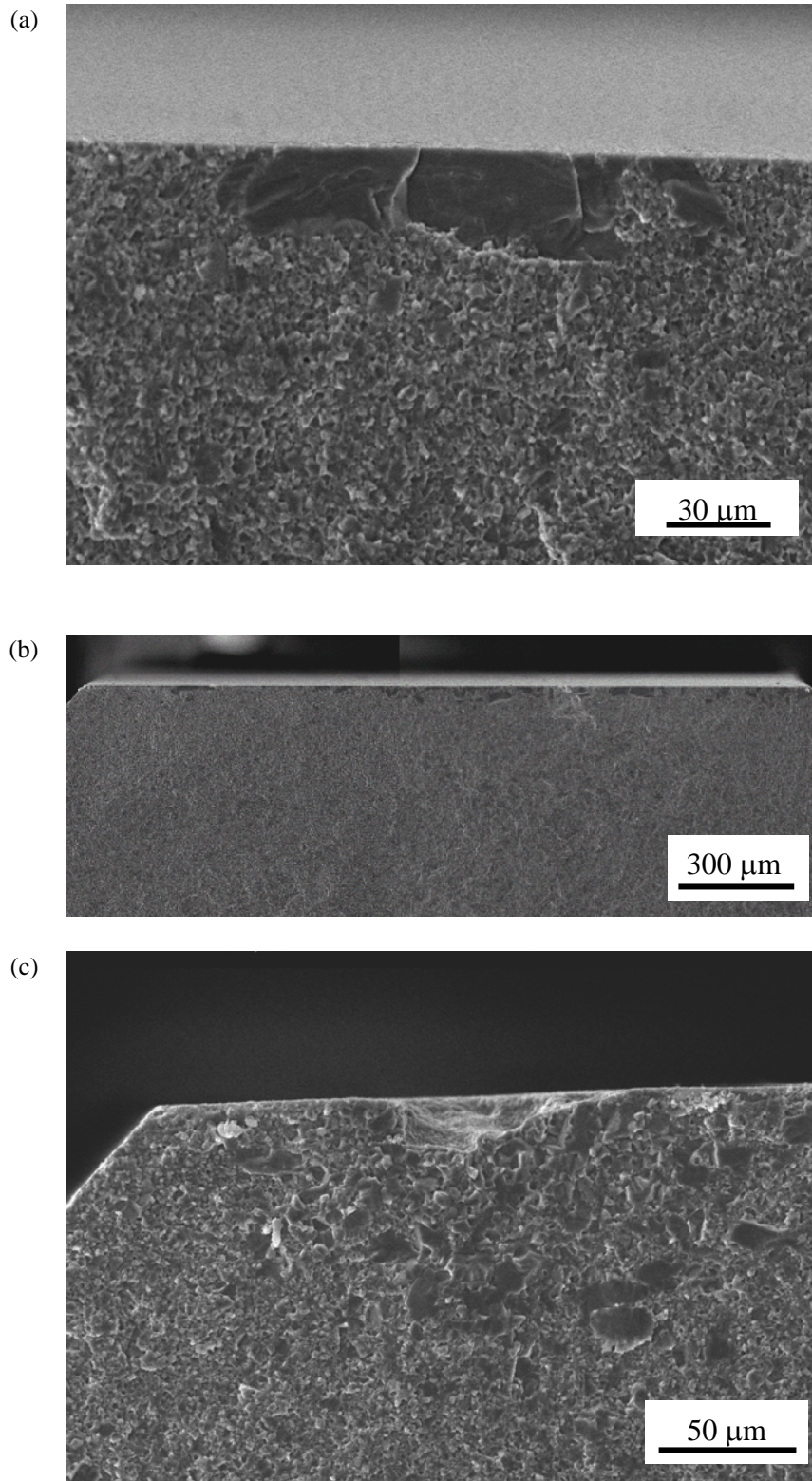
Figure 6.4: Characteristic flaw in the laminates: abnormal large grains of alumina at the surface. This is supposed to be the unique defect population (a) Abnormal large alumina grains. (b) Aligned large grains acting as a "notch". (c) Surface defect most probably due to processing since the surface looks like "as sintered". Large grains are also observable. In the micrographs the chamfers of the bending specimen are observable on both sides.
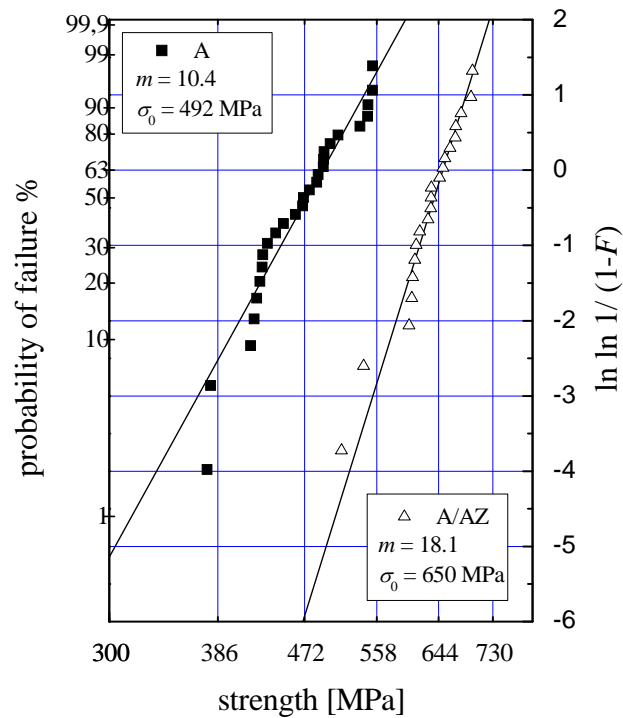
Figure 6.5: Weibull plot for an A-"laminate" and a 2A/AZ/A/AZ/A/AZ/2A laminate. The values are directly comparable since the specimens have the same volume (or same surface area in tension).

The results in Figure 6.5 are directly comparable as all the specimens have the same volume (or surface area under tension). It means, the difference is not attributable to a volume effect. We are measuring the strength in the same material for both laminates (alumina which has been prepared in an identical way and has the same defects in both laminates), therefore the difference in m and σ_0 is only due to the existence of residual stresses in the A/AZ-laminate.

Residual stresses in ceramic laminates have been deeply investigated [20, 21] (see also Chapter 4). They are originated during cooling from the sintering temperature due to the thermal expansion mismatch between the A and AZ-layers [22]. The residual stress was experimentally measured at the surface by an indentation technique [23]. The measurement results in $\sigma_{res} = -150$ MPa (see Figure 4.14). So, it is believed that, in effect, the residual stress σ_{res} shields the material again applied stresses and increases its strength in a quantity equals to σ_{res}.

A way to check that both strength distributions correspond to the same material is to subtract the residual stress, $\sigma_{res,}$ from each measured strength value on the A/AZ

laminate. If the difference is only due to the residual stress both distribution should then look similar. The results are presented in Figure 6.6, the difference between both characteristic strengths σ_0 was considered to be equal to the real residual stress.
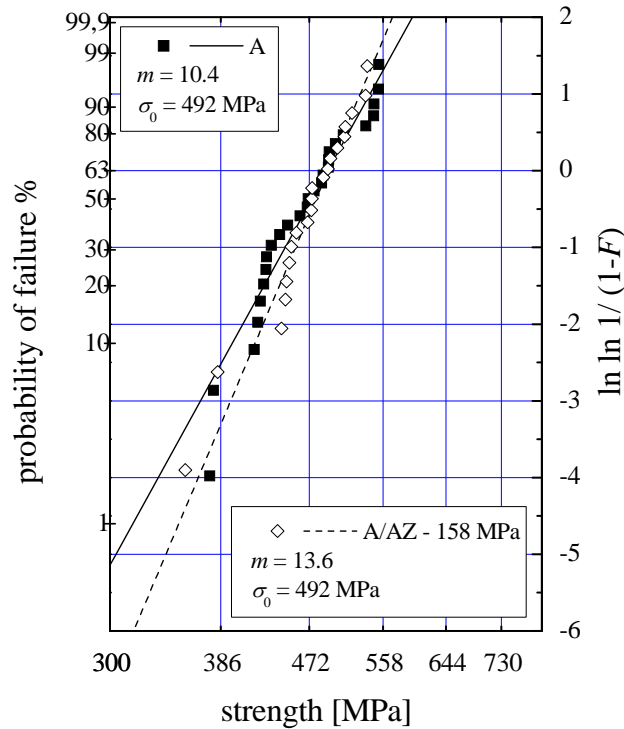
Figure 6.6: Comparison between the strength distribution of the A-laminate and the strength of the A/AZ laminate after subtracting the magnitude of the residual stress (σ_{res} = -158 MPa). σ_{res} was considered the difference in the characteristic strength σ_0.

Figure 6.6 shows that both populations have obviously the same characteristic strength σ_0, and similar Weibull's modulus m. The Weibull's modulus for the A/AZ laminate has dropped from 18.1 to 13.6 which is a notable change for ceramics (note that despite we have subtracted a constant value from all the strength data, the slope, m, changes as the x-axis is logarithmic). Table 6.2 summarizes the results and shows the 90% confidence intervals for the Weibull's modulus. It is clear that the confidence intervals overlap, and therefore it can be assumed that we are testing the same alumina in both cases.

Table 6.2: Fitting of m and σ_0 for the strength distribution presented in Figure 6.6.

laminate	m	σ_0
A/A/A/A/A/A/A	10.4 (7.7 – 12.8)	492
2A/AZ/A/AZ/A/AZ/2A	13.6 (9.5 – 17.2)	492

It is worth of note that the advantage of a surface compressive stress is not only an increase in the strength σ_0 but also an increase in the Weibull modulus.

This is because if we add a compressive stress, σ_{res}, to a material with a given strength distribution $f(\sigma)$, the new strength distribution $f^*(\sigma)$ would suffer a displacement by σ_{res} towards higher stress levels: $f^*(\sigma) = f(\sigma - \sigma_{res})$, see Figure 6.7a. The new strength distribution $f^*(\sigma)$ keeps the same absolute scatter but for a higher level of σ_0 and therefore the relative scatter diminishes, and a higher Weibull's modulus is observed.
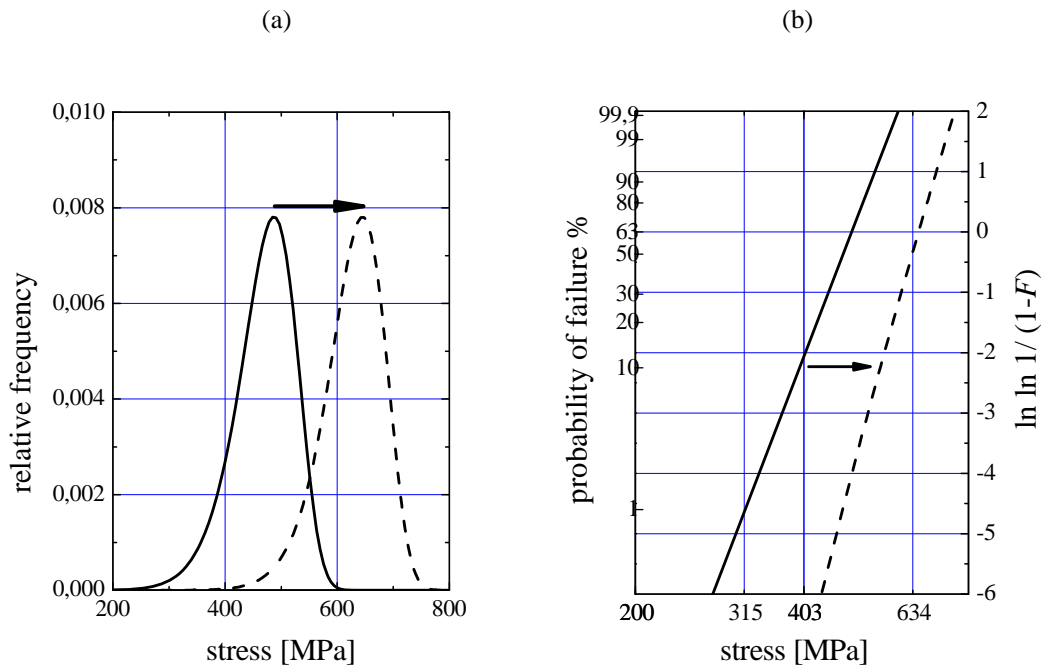
Figure 6.7: (a) Strength distribution for a given material and effect of adding a compressive stress σ_{res} to it. (b) Both distributions represented in a Weibull plot. $f^*(\sigma)$ presents a higher m and σ_0.

An interesting point can be noted in Figure 6.7. So far, we have assumed that the probability of failure follows an expression like Equation 6.5 for both materials. But, as we have shown $f^*(\sigma) = f(\sigma - \sigma_{res})$, and therefore, the real mathematical equation for the probability of failure of an A/AZ-laminate, F^*, has the form, $F^*(\sigma) = F(\sigma - \sigma_{res})$,

$$F^*(\sigma, S) = 1 - \exp\left[-\frac{S}{S_0}\left(\frac{\sigma - \sigma_{res}}{\sigma_0^*}\right)^{m^*} \right].$$ **Eq 6.7**

In general, this expression is valid for any brittle material that fails at the surface, and in which surface is protected by means of a residual stress, σ_{res}. This form is known in the literature as the 3-parameter Weibull's distribution. The physical meaning of the third parameter is clear, it is a threshold strength. The threshold strength must be overcome to fail the material, below σ_{th} the material cannot fail. This is clearly observed in Figure 6.7a. If we assume that σ_{th} is zero for the $f(\sigma)$ distribution (this is normally assumed for monolithic ceramics), then it is clear that $f^{*}(\sigma)$ presents a threshold strength, $\sigma_{th} = \sigma_{res}$. If an external stress is applied, the specimen will not break for $\sigma < \sigma_{th}$ because it is under compression (one of the premises for the derivation of the Weibull distribution is that brittle materials do not break under compressive stresses).

As a conclusion, the strength data for the A/AZ-laminate should have been fitted by a three parameter Weibull distribution because they present a threshold strength; the surface residual stress σ_{res}. As mentioned before, determining the parameters of a 3-parameter Weibull distribution gives unstable results for small (realistic) samples. In our case, we know the value of the 3rd parameter because it is equal $\sigma_{th} = \sigma_{res}$, and thus it can be successfully done.

The strength results for the A/AZ-laminate are presented in Figure 6.8 after being fitted to a 2- and a 3-parameter distribution. In the usual range of a Weibull plot both fits are similar (the range of "measured" failure probabilities). It is important to note that the 3-parameter distribution is not a straight line anymore in the classical Weibull plot but it tends asymptotically to the threshold strength for very low probabilities of failure.

The range of "measured" failure probabilities, F, increases with the sample size [24] and is - for a sample of 30 tests - very limited (between $\sim 1/60$ and $\sim 59/60$). To determine the design stress, the measured data have - in general - to be extrapolated to the "tolerated" failure probability of the components ($\sim 1/10^6$), which often results in a very large extrapolation span [24].

As it can be observed the difference is important at low probabilities of failure, where the fit has more practical importance. Industrial components are designed to offer a probability of failure about $\sim 1/10^4$ or much less depending on their importance. The consequence of using a 2-parameter instead of a 3-parameter distribution for a A/AZ-laminate is clear from Figure 6.8. For a given stress σ the probability of failure will be overestimated by the 2-parameter distribution. The mistake is not so bad from the

mechanical point of view because we are on the "safe-side" of design but it will provoke large costs as the design will be oversized.
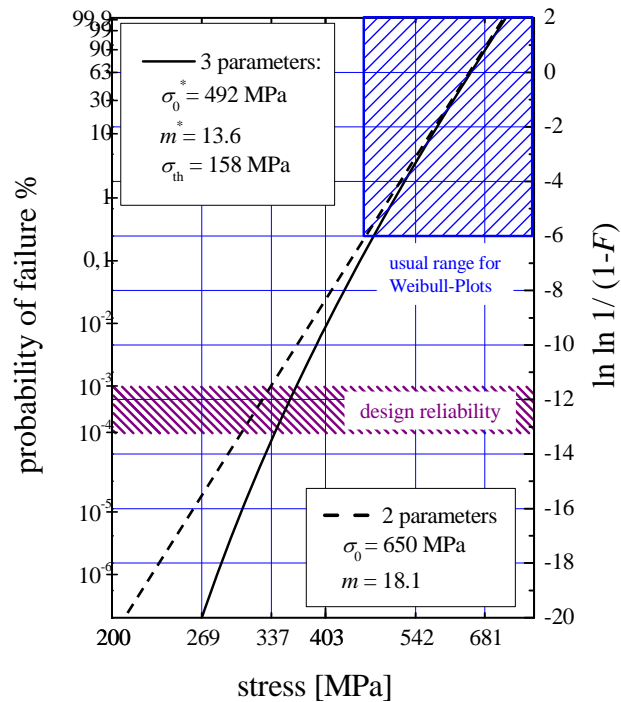
Figure 6.8: Fitting of the A/AZ laminate strength with 2- and 3-parameter Weibull distribution.

Results for the fits presented in Figure 6.8 are listed in Table 6.3. The parameters m and σ_0 are not comparable between the different distributions as they have different meanings for each distribution. It has been demonstrated that m^* is lower than m if a set of strength data is fitted to both distributions (Equation 6.5 and Equation 6.7) [25].

Table 6.3: Fitting of m and σ_0 for the strength distribution presented in Figure 6.8.

2A/AZ/A/AZ/A/AZ/2A	m / m^*	σ_0 / σ_0^*	σ_{th}
2-parameter	18.1	650	-
3-parameter	13.6 (m^*)	492 (σ_0^*)	158

So far, we have demonstrated that the effect of a compressive stress on the strength distribution of an A/AZ-laminate is to introduce a threshold strength that can be modeled with a 3-parameter Weibull distribution. An alternative way to show that A/AZ-laminates deviate from the conventional Weibull behavior is treated in the following.

The Griffith failure criterion (premise 11) is not exactly the same for A-laminates and A/AZ-laminates. The Griffith criterion for an A-laminate follows the classic form $K > K_c^A$, where K_c^A is a constant. On the other hand, for an A/AZ-laminate it has the

form $K > K_c^A(a) = K_R$, where K_c^A depends on the crack length a. As presented in Chapter 5, A/AZ-laminates present an R-curve due to presence of the residual stress, σ_{res}. The R-curve was experimentally measured and analytically investigated in Chapter 5. It was clearly demonstrated that laminates present an oscillatory R-curve that grows in the layers under compression and drops in the layers under tension (see Figure 5.13). However, for our purpose in this section (calculate the strength distribution corresponding to an apparent R-curve), we will give our attention to the R-curve only in the first layer, where the failure will happen *(note that here we are introducing a threshold strength!!)*. The Figure 6.9 presents the R-curve of the studied A/AZ laminate by the weight function method (see Chapter 5). The residual stress in the first layer was considered to be -158 MPa (exactly the difference in the characteristic strength between the studied laminates).
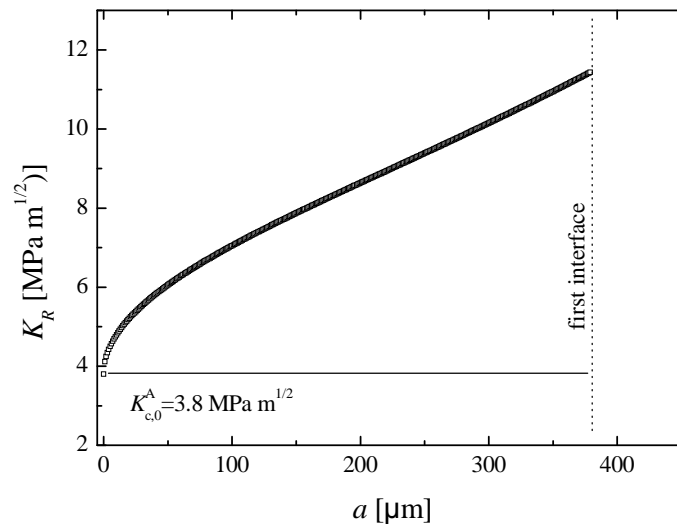
Figure 6.9: Apparent R-curve of the A/AZ-laminate calculated by the weight function method. It was assumed $\sigma_{res} = -158$ MPa and the elastic properties and $K_{c,0}$ listed in Table 1.

As said, A/AZ laminates present an *apparent* R-curve. Some essential differences must be noted between a conventional R-curve and an apparent R-curve. An R-curve is a relation of the type $K_R = K_R (\Delta a)$ where Δa is the crack extension and does not depend on the initial crack length, but an apparent R-curve is defined by $K_R = K_R(a)$, and therefore the toughening depends on the initial crack length. This fact has consequences, for example, in the failure criterion. A material with an *apparent* R-curve will fail if the stress intensity factor is larger than the apparent toughness ($K > K_R$). On the other hand, it is well known [26] that a additional condition is necessary for R-curves: $\partial K/\partial a = \partial K_R/\partial a$ or, in energetic terms, $\partial G/\partial a > \partial J_c/\partial a$ (where G is elastic energy release rate and J_c the fracture energy, $J_c = (1-\nu^2) K_R^2/E$). Because the failure criterion is different for R- and apparent R-curves, their theoretical strength

distributions are different. The failure criterion for an R-curve material is presented in Figure 6.10.
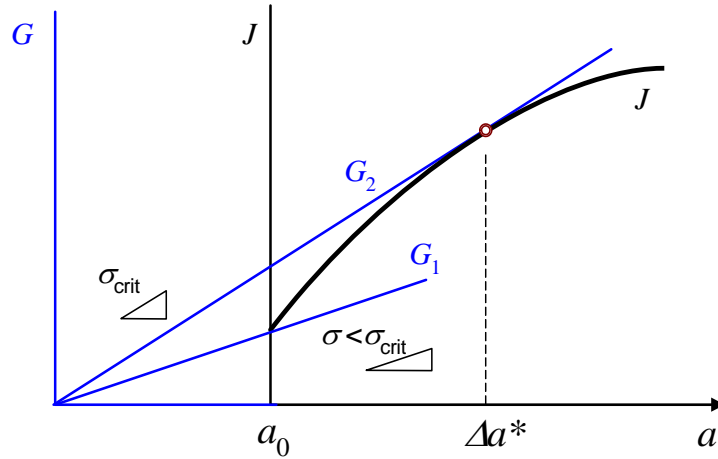
Figure 6.10: Failure criterion for R-curve materials. For a critical defect size ($a_0+\Delta a^*$), failure occurs after some stable crack extension Δa^*, when both failure conditions are fulfilled. Failure takes place for a critical stress σ_{crit} defined by the slope of the straight line G_2.

Two more differences to note are, firstly, that apparent R-curves do not tend asymptotically to a plateau value like some R-curves do [27] and, secondly, that an R-curve is not effective for very short initial cracks ($K = K_{c,0}$) while an apparent R-curve actuates immediately (for every crack length).

The strength distribution of a material presenting an R-curve has been previously discussed in the literature [13]. Figure 6.11 presents the strength distribution for an arbitrary material that increases its toughness from $K_{c,0} = 3$ MPa·m$^{1/2}$ to $K_{c,plateau} = 8$ MPa·m$^{1/2}$ in 400 µm length in a Weibull plot. It is obvious that the distribution deviates from the straight behavior.

For very small flaws (high stresses) the R-curve is not effective ($K = K_{c,0}$) and the material follows a Weibull distribution with slope m. Later the strength distribution deviates from the initial straight line increasing the slope of the strength distribution (m). When approaching the plateau of the R-curve, the distribution tends asymptotically again to a Weibull behavior with the same slope m. It is interesting to note that lines of constant toughness are straight lines with slope m.

The strength distribution for R-curves does not present a threshold strength, σ_{th}, and therefore cannot represent the behavior of an A/AZ laminate (*in fact it does not have an R-curve but an apparent R-curve*). Because apparent R-curves do not tend

asymptotically to a plateau value but increases monotonically with in the crack-length regime of interest (see Figure 6.9), it is expected that the strength distribution of an apparent R-curve deviates more and more from the Weibull straight, thus presenting a threshold strength.
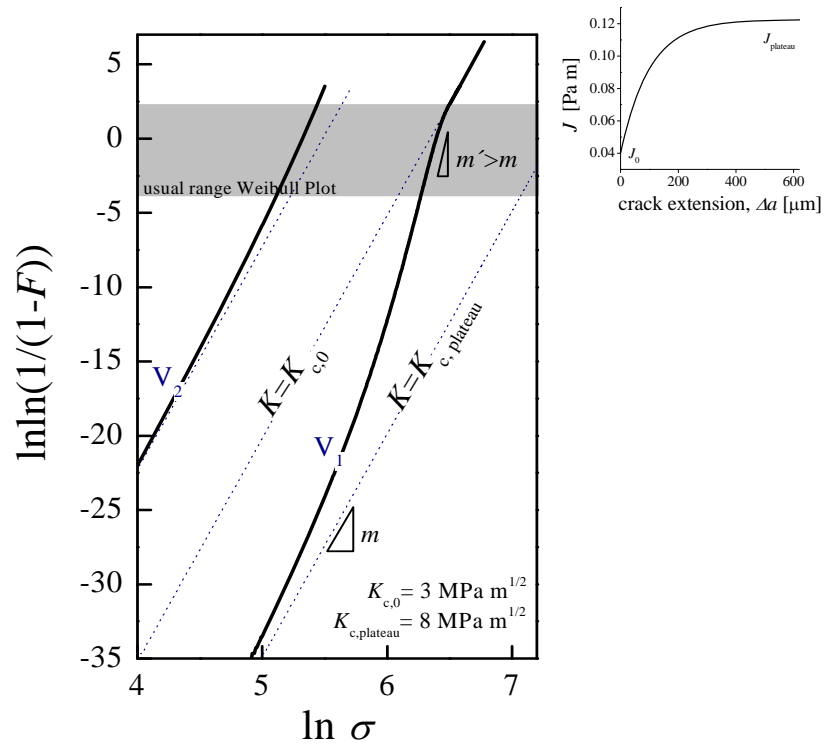
Figure 6.11: Strength distribution for a material with an R-curve [13].

It should also be noted that the Weibull behavior for an R-curve at high stresses (in that range of stresses where the material fails with $K = K_{c,0}$), will not appear for an apparent R-curve since the condition $K = K_{c,0}$ only applies for $a = 0$.

The strength distribution for an apparent R-curved is presented in Figure 6.12. The results are the expected ones and fit well with the experimental values shown in Figure 6.5 and the 3-parameter distribution. This fact validates the weight function method to calculate apparent R-curves. For the calculation it is necessary to know the frequency distribution density of defect lengths (or A and r, see premise 10 in the introduction). The values are known since we have measured m and σ_0 for the A-laminate, and Equation 6.3 and 6.4 relate m and σ_0 with A and r.

Finally, it is recalled that attention has been paid only to one family of laminates: strongly bond laminates with compressive surface stresses. In the literature some others multilayers are of interest. For example, strongly bond laminates with tensile surface stresses have demonstrated that under certain conditions cracks can arrest/deflect cracks in internal compressive layers [16]. For these multilayers, the first two premises to derivate Weibull distributions are not fulfilled. In fact, when the weakest defect fails, it could happen that the crack is later arrested, so it is an interaction of flaws what produces the total failure of the component. Another technologically interesting family of laminates is those laminates that incorporate porous layers (or weak interfaces) to deflect cracks. Of course, in highly porous layers the interaction of flaws inhibits the application of Weibull's theory to these laminates.
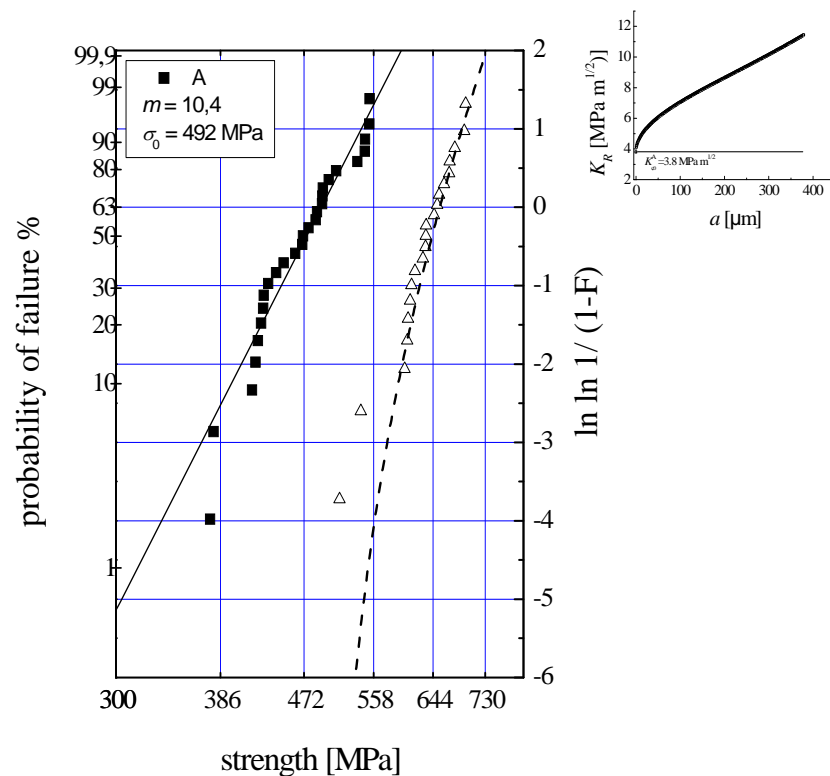
Figure 6.12: Strength distribution for the A/AZ laminate that presents an apparent R-curve.

6.4. Bibliography

[1]   Evans, A. G., "Structural Reliability: A processing-dependent phenomenon", Journal of the American Ceramic Society, **65**, 127-137, (1982).
[2]   Danzer, R., "Mechanical failure of advanced ceramics: The value of fractography", Key Engineering Materials, **223**, 1-18, (2002).
[3]   Davidge, R. W., "Mechanical behaviour of ceramics", Cambridge University Press, (1979).
[4]   Munz, D., Fett, T., "Ceramics. Mechanical properties, failure behaviour, materials selection", Springer, (1999).

[5]   Wachtman, J. B., "Mechanical properties of ceramics", John Wiley, (1996).

[6]   Danzer, R., "Mechanical performance and lifetime prediction" in: Brook, R.J. Concise encyclopedia of advanced ceramic materials. Pergamon Press, 286-299, (1991).

[7]   Danzer, R., Börger, A., Supancic, P., Ruiz Villanueva, M.-A., "Ein einfacher Festigkeitsversuch für Scheiben aus spröden Werkstoffen", Materialwissenschaft und Werkstofftechnik, **34**, 490-498, (2003).

[8]   Freudenthal, A. M., "Statistical Approach to Brittle Fracture" in: Liebowitz, H. Fracture, vol II. Academic Press, 591-619, (1968).

[9]   Danzer, R., "A general strength distribution function for brittle materials", Journal of the European Ceramic Society, **10**, 461-472, (1992).

[10]   Weibull, W., "A statistical theory of strength of materials", Royal Swedish Institute for Engineering Research, 1-45, (1939).

[11]   Lu, C., Danzer, R., Fischer, F. D., "Influence of Threshold Stress on the Estimation of the Weibull Statistics", Journal of the American Ceramic Society, **85**, 1640-1642, (2002).

[12]   Danzer, R., Lube, T., Supancic, P., "Monte-Carlo simulations of strength distributions of brittle materials - Type of distribution, specimen- and sample size", Zeitschrift für Metallkunde, **92**, 773-783, (2001).

[13]   Danzer, R., Supancic, P., Pascual, J., Lube, T., "Fracture statistics of ceramics – Weibull statistics and deviations from Weibull statistics", Engineering Fracture Mechanics, **In Press, Corrected Proof**, (2007).

[14]   Malzbender, J., Steinbrech, R. W., "Mechanical properties of coated materials and multi-layered composites determined using bending methods", Surface and coatings technology, **176**, 165-172, (2004).

[15]   Clegg, W. J., Kendall, K., Alford, N. M., Button, T. W., Birchall, J. D., "A simple way to make tough ceramics", Nature, **347**, 455-457, (1990).

[16]   Rao, M., Sanchez-Herencia, J., Beltz, G., McMeeking, R. M., Lange, F., "Laminar ceramics that exhibit a threshold strength", Science, **286**, 102-105, (1999).

[17]   Bae, I. J., Baik, S., "Abnormal grain growth of alumina", Journal of the American Ceramic Society, **80**, 1149-1156, (1997).

[18]   Dominguez-Rodriguez, A., Gutierrez-Mora, F., Jimenez-Melendo, M., Routbort, J. L., R, C., "Current understanding of superplastic deformation of Y-TZP and its application to joining", Material Science and Engineering A, **302**, 154-161, (2001).

[19]   Jimenez-Melendo, M., F, G.-M., Dominguez-Rodriguez, A., "Effect of layer interfaces on the high-temperature mechanical properties of alumina/zirconia laminate composites", Acta Materialia, **48**, 4715-4720, (2000).

[20]   Chen, C. R., Fischer, F. D., Kolednik, O., Pascual, J., Danzer, R., "Prediction of the fracture toughness of a ceramic multilayer composite - Modeling and experiments", Acta Materialia, **55**, 409-421, (2007).

[21]   Zhang, X. C., Xu, B. S., Wang, H. D., Wu, Y. X., "An analytical model for predicting thermal residual stresses in multilayer coating systems", Thin Solid Films, **488**, 274-282, (2005).

[22]   Chartier, T., Merle, D., Besson, J. L., "Laminar Ceramic Composites", Journal of the European Ceramic Society, **15**, 101-107, (1995).

[23]   Pascual, J., Chalvet, F., Lube, T., De Portu, G., "Strength of unsymmetrical ceramic laminates", SICMAC newsletter, (2004).

[24]   Danzer, R., Lube, T., "Fracture Statistics of Brittle Materials: It Does not always have to be Weibull Statistics" in: Niihara, K. Ceramic Materials, Components for Engines. Japan Fine Ceramics Association, 683-688, (1998).

[25]   Fok, S. L., Mitchell, B. C., Smart, J., Marsden, B. J., "A numerical study on the application of the Weibull theory to brittle materials", Engineeering Fracture Mechanics, **68**, 1171-1179, (2001).

[26]   Broek, D., "Elementary engineering fracture mechanics", Sijthoff & Noordhoff International Publishers, (1978).

[27]   Steinbrech, R. W., Reichl, A., Schaarwaechter, W., "R-curve behavior of long cracks in alumina", Journal of the American Ceramic Society, **73**, 2009-2015, (1990).

Chapter 7. Conclusions and Future Work

This work has focused on a specific family of laminates, which are strongly bond and have surface compressive stresses. Initially, attention has been paid to measure the elastic properties as well as the thermal expansion coefficients. These properties are necessary to analytically estimate the residual stress state.

The residual stresses were experimentally measured. An indentation technique was performed to measure them at the surface. The experiments corroborate the analytical estimations. Also, 3-D simulations by the finite element method were also conducted, results agree the experimental values and show important known localized effects (high tensile stresses) that could lead to failure (edge cracks).

In this thesis, efforts were focused on toughness. Although fracture toughness of a layered composite can be experimentally measured, it is only an apparent or effective value because of the superposition of the residual stress. It has been shown, in fact, that the existence of a residual stress state originates an apparent R-curve. The apparent R-curve has an oscillatory nature, it increases in the layers under compression and decreases in the tensile layers.

Apparent R-curves have been modeled with two different methods: the weight function method and the material forces approach. A simplified two-dimensional problem was solved in both cases. A plane stress situation is considered for the residual stress field because it is similar to the real 3-dimensional solution. For the weight function method, a second simplification is assumed, the laminate has an homogeneous elastic modulus. This brings a quantitative difference with respect to the solution by means of the material forces approach. Despite of that, it is believed that the weight function method - even if presents a quantitative difference with respect the material forces approach - can describe the qualitative behavior of the toughening introduced by a internal stress in a non-homogeneous material.

The results extracted from the weight function analysis have been used to show regions of crack stability in the apparent R-curve. It has been outlined the difference existing between a conventional R-curve (which is function of the crack extension, $K = K_c^A(\Delta a)$) and an effective R-curve (which is function of the crack length, $K_R = K_c^A(a)$). For instances, they present different regions of stable crack propagation.

It has been shown that the apparent R-curve can lead to a high toughening in the first layer. The highest toughening in the first layer is obtained at a depth equals to its thickness. A priori, it could be expected that thin layers (high compressive stresses) could lead to the highest shielding, but because the apparent R-curve needs distance to develop, the maximum toughening is obtained for a compromise thickness, thin enough to sustain compressive stress, and thick enough to develop the apparent R-curve.

A study has been conducted about the influence of different parameters on the architecture that maximizes the toughening. The studied parameters studied are the architecture (total thickness and thickness ratio, t_A/t_{AZ}), the elastic properties and the thermal mismatch. It has been concluded that for the A/AZ laminates here studied, the elastic mismatch has a significant influence while the other parameters almost do not influence the optimal architecture.

Considering the strength of ceramic laminates, it has been shown that a compressive surface stress introduces a threshold in the strength distribution if the material fails at the surface. Therefore, multilayers should be modeled with a 3-parameter Weibull distribution instead of a classical 2-parameter Weibull distribution. The threshold strength (the minimum stress that may fail the multilayer) is exactly the value of the residual stress at the surface.

The classic 2-parameter distribution can be used to rank the strength of laminates, but if a design is done based on this distribution, the designer is cautioned about the mistake that he is introducing at low stresses (or low probabilities of failure). The mistake is a "safe-mistake" since the designer is oversizing the multilayer. This idea can be generalized to any brittle material that, firstly, fails at the surface, and secondly, it holds an internal compressive state. Examples, may be certain coatings, tempered glasses,…

An alternative way has been followed to obtain the real strength distribution of our ceramic multilayers. The strength distribution can be calculated replacing the Griffith criterion ($K > K_c^A$) for a valid failure criterion. In the case of A/AZ laminates, the valid failure criterion concerns the apparent R-curve, $K > K_c^A(a) = K_R$. This solution is coincident with the theoretical distribution, a 3-parameter Weibull distribution. Therefore, because the R-curve was calculated with the weight function method, the weight function method is a valid method to calculate apparent R-curves.

Additionally, the strength distribution corresponding to a material with an R-curve is also presented and compared to that of an apparent R-curve. Differences are commented.

In the author's opinion, future investigations shall be directed on the search of industrial applications once the state-of-the-art is well-based. Most probably cylindrical or spherical applications are easier to put into practice since they will offer a compressed surface against contact damage (plates contain free surface that are interesting to avoid). Recent applications are found in the literature, i. e., SiC nozzles for sand blasting equipments which possess an improved wear resistance due to the effect of the surface compressive stresses. Of course, developments on processing will have a vital importance, especially interesting are those techniques that may allow producing laminated granulates that later can be sintered to any shape.

Concerning mechanical properties, it seems that wear applications are one of the most interesting to be investigated. In general, different authors have found an enhancement in wear resistance but not always significant. More experimental work and modeling is required for a better understanding of the influence of surface compressive stresses on wear.

Chapter 8. List of Papers, Posters and Presentations

8.1. List of Papers

[1] **Pascual, J**., Chalvet, F., Lube, T., De Portu, G., "R-curves in Al_2O_3 - Al_2O_3/ZrO_2 laminates" in: Dusza, J., Danzer, R., Morrell, R. Key Engineering Materials. Trans Tech Publications Ltd., **290**, 214-221, (2005).

This paper introduces the effective R-curve in A/AZ laminates, theoretically and experimentally. The weight function method was used for the theoretical analysis. It was shown that crack arrest can happen in internal compressive layers by means of a bending test. J. Pascual conducted the experimental part and the weight function analysis.

[2] Lube, T., **Pascual, J.**, Chalvet, F., De Portu, G., "Effective fracture toughness in Al_2O_3 – Al_2O_3/ZrO_2 laminates". Journal of the European Ceramic Society, 27, 1449-1453, (2006).

The weight function method is used to show the maximum toughening that a residual stress can propitiate in the first layer of a multilayer. A discussion is given on the influence of different parameters (architecture and physical constants) on the maximum shielding. J. Pascual performed the weight function analysis.

[3] Chen, C. R., Fischer, F. D., Kolednik, O., **Pascual, J.**, Danzer, R., "Prediction of the fracture toughness of a ceramic multilayer composite - Modeling and experiments", Acta Materialia, 55, 409-421, (2007).

This paper predicts the fracture toughness to be measure in an A/AZ multilayer by means of the material forces approach. The method considers the elastic mismatch existing between the layers. Experimental results fit well with the numerical solutions. J. Pascual performed the experimental part.

[4] **Pascual, J.**, Chen, C. R., Kolednik, O., Fischer, F. D., Danzer, R., Lube, T., "Weight function, J-Integral and material forces approach to apparent toughness

of ceramic multilayers" in: Gdoutos, E.E. Fracture of Nano and engineering materials and structures. Springer, 317-318, (2006).

The fracture toughness for a ceramic multilayer as predicted by two techniques, the weight function method and the material forces approach, is presented. Differences between the two approaches are commented. J. Pascual compared and discussed both solutions.

[5]   Bermejo, R., Torres Hernández, Y., Baudín, C., Sánchez-Herencia, A. J., **Pascual, J.**, Anglada, M., Llanes, L., "Threshold strength evaluation on an Al_2O_3-ZrO_2 multilayered system", Journal of the European Ceramic Society, 27, 1443-1448, (2007).

This paper deals with a multilayer that contains tensile stresses at the surface. After failing at the surface, cracks are arrested in inner compressive layers, and thus, a threshold strength is observed. The apparent R-curve for this multilayer is calculated by J. Pascual. Predictions are corroborated by experimental measurements.

[6]   **Pascual, J.**, Chalvet, F., Lube, T., de Portu, G., "Strength distributions in ceramic laminates", Materials Science Forum, 492-493, 581-586, (2005).

Strength measurements are conducted on a stressed alumina (A/AZ laminate) and on a free-of-stresses alumina (A/A laminate). The observable differences are attributed to the residual stress, which is measured by an indentation technique. J. Pascual performed the experimental part and discussed the results.

[7]   Danzer, R., Supancic, P., **Pascual, J.**, Lube, T., "Fracture statistics of ceramics – Weibull statistics and deviations from Weibull statistics", Engineering Fracture Mechanics, **In Press,** (2007).

ISFK (Institute for structural and functional ceramics) reviews the state-of-the-art on deviations from Weibull statistics in this paper. J. Pascual presents the case of an R-curve material.

[8]   Gurauskis, J., **Pascual, J.**, Lube, T., Sánchez-Herencia, A. J., Baudín, C., "Fracture of monoliths fabricated by stacking water processed green ceramic tapes" in: Dusza, J., Danzer, R., Morrell, R. Key Engineering Materials. Trans Tech Publications Ltd., 290, 203-207, (2005).

Different A/AZ laminates were fabricated by gluing the constituent tapes and pressing at room temperature. The quality of the interfaces between the different tapes in sintered specimens was evaluated by means of the fracture behavior during the ball-on-three-ball test. J. Pascual conducted the strength tests at ISFK.

[9]   **Pascual, J.**, Chalvet, F., Lube, T., De Portu, G., "Strain mismatch in ceramic multilayers: Determination by strength measurements", Key Engineering Materials, 333, 251-254, (2006).

The strain mismatch between the layers in A/AZ-laminates was evaluated through the analysis of strength results of non-symmetrical laminates. J. Pascual carried out the experiments and discussed the results

8.2. List of Posters

[1]   **Pascual, J**., Lube, T., <u>Danzer, R.</u>, Bermejo, R. "Rißwiderstand in keramischen Schichtverbunden" in: Symposium Hochleistungskeramik, Stuttgart, Germany, 5-6 April, 2006.

[2]   **Pascual, J**., Lube, T., Danzer, R., Bermejo, R. "Rißwiderstand in keramischen Schichtverbunden" in: ASMET Forum für Metallurgie und Werkstofftechnik. Leoben, Austria, 22-24 May, 2006.

[3]   **Pascual, J**., Lube, T. "Indentation techniques to estimate surface residual stresses" in: SICMAC summer school: Layered, functional gradient ceramics, and thermal barrier coating: Design, fabrication and applications. Maó, Spain, 11-16 June, 2006.

8.2. List of Oral Presentations

[1]   **Pascual, J.**, Lube, T. "The contribution of ISFK. Collaboration project with ISTEC" in: 3rd SICMAC Meeting, Faenza (Italy) 9–10 October, 2003.

[2]   **Pascual, J.**, Lube, T. "On mechanical properties of ceramics laminates" in: 4th SICMAC Meeting, Köln (Germany) 11–12 March, 2004.

[3]   **Pascual, J.**, Chalvet, F., Lube, T., de Portu, G. "Strength distributions in ceramic laminates" in: FGM 2004, Leuven, Belgium, 11–14 July, 2004.

[4]   **Pascual, J.**, Chalvet, F., Lube, T., de Portu, G. "Fracture in $Al_2O_3 - Al_2O_3/ZrO_2$" in: FAC 2004, Stara Lesna, Slovakia, 3–6 October, 2004.

[5]   **Pascual, J.**, Lube, T. "Influence of architecture and materials properties on effective toughness" in: 6th SICMAC Meeting, Madrid (Spain) 3–4 March, 2006.

[6]   Lube, T., **Pascual, J**., Chalvet, F., de Portu, G. "Effective fracture toughness in $Al_2O_3 - Al_2O_3/ZrO_2$ laminates" in: ECERS IX, Portoroz, Slovenia, 19–23 June, 2005.

[7]   **Pascual, J**., Danzer, R. "Failure behavior and strength distribution in laminates" in: 7th SICMAC Meeting, Leuven, Belgium, 11–14 July, 2005.

[8]   **Pascual, J**., Lube, T. "Bending and contact strength in $Al_2O_3 - Al_2O_3/ZrO_2$ multilayer ceramics" " in: ESIS Austria meeting, Steyr, Austria, 4th May, 2006.

[9]   Chen, C.R., **Pascual, J**., Kolednik, O., Fischer, F.D., Danzer, R. "Weight function and material forces approach to toughness in ceramic laminates" in: 52. Metallkunde-Kolloquium. Werkstoffforschung für Wirtschaft und Gesellschaft, Lech am Arlberg, Austria, 19-21 April, 2006.

[10]   **Pascual, J**., Chen, C.R., Kolednik, O., Fischer, F.D., Danzer, R. "Weight function and material forces approach to toughness in ceramic laminates" in: ECF16 – 16th European Conference on Fracture, Alexandroupolis, Greece, 19-21 July, 2006.

[11]   Harrer, W., Danzer, R., Supancic, P., Börger, A., **Pascual, J**. "Biaxial strength testing on mini specimens" in: ECF16 – 16th European Conference on Fracture, Alexandroupolis, Greece, 19-21 July, 2006.

Annex 1. Analytical Prediction of thermal stresses

This annex presents the analytical solution of the residual stress state for a generic multilayer, i.e. a multilayer coating or laminate when the stress state is originate due to a thermal strain mismatch, as presented by different authors.

Firstly, Oël [1] presented a solution of the residual stress state in a symmetrical multilayer made of alternative layers of two materials. The direction of the thickness (*y*-direction) is considerable smaller than the rest of dimensions for the derivation of the solution (Figure A1.1).
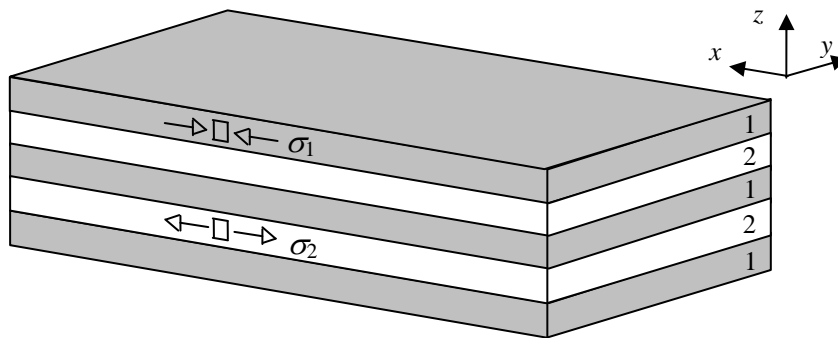
Figure A1.1: Symmetric laminate by alternating two materials ($t << L$)

The general expression for the strain in the *z*-direction reads from the Hookean Law,

$$\varepsilon_x = \frac{\sigma_x}{E} - v\frac{\sigma_y}{E} - v\frac{\sigma_z}{E} \ . \qquad \textbf{Eq A1.1}$$

where σ_i represents the stress in the *i* direction, ε_i the strain in the *i* direction, *E* is the Young's modulus and v is the Poisson's ratio.

In this situation the stress is expected to be very small in the *z*-direction ($\sigma_z = 0$) and the residual stress field is symmetrically biaxial in the *x*- and *y*-directions. This means that far away from the free surfaces, $\sigma_x = \sigma_y = \sigma_{res}$,

$$\varepsilon_x = \frac{\sigma_x}{E} - v\frac{\sigma_y}{E} = \frac{\sigma_{res}}{E} - v\frac{\sigma_{res}}{E} = \frac{\sigma_{res}(1-v)}{E} \ . \qquad \textbf{Eq A1.2}$$

For a symmetrical multilayer built up of n layers (n therefore must be odd), $(n+1)/2$ are made of a material 1, while $(n-1)/2$ are constituted by a material 2. At the interfaces the strain differential is given by the thermal strain mismatch,

$$\Delta\varepsilon = \varepsilon_{x,2} - \varepsilon_{x,1} = \int_{T_{room}}^{T_{sf}} (\alpha_2 - \alpha_1)\,dT = \Delta\alpha\,\Delta T\,,$$

Eq A1.3

where T_{sf} is the temperature below which the residual stresses can not be relaxed and thus start constraining the layers, and T_{room} is the room temperature. α is the thermal expansion coefficient.

Additionally the equilibrium is required since the laminate is balanced. A cross-section balance results in,

$$\sum_{i=1}^{n} F_x = \sum_{i=1}^{n} \sigma_i\,t_i = 0\quad.$$

Eq A1.4

where t_i is the thickness of the i-layer.

Considering Equation A1.3 and A1.4, the following solution holds for the residual stress in the layers of material 1 and 2, respectively.

$$\sigma_1 = -\frac{\Delta\varepsilon\,E_1'}{1 + \dfrac{(n+1)t_1\,E_1'}{(n-1)\,t_2\,E_2'}}$$

Eq A1.5

$$\sigma_2 = -\sigma_1\frac{(n+1)\,t_1}{(n-1)\,t_2}$$

Eq A1.6

where $E_i' = E_i/(1-\nu_i)$.

A more general solution was presented later by Zhang. Zhang assumed an elastic multilayer strip at elevated temperature and under stress-free condition, where n layers with individual thickness, t_i, are bonded sequentially to the substrate (or first layer) with a thickness, t_s, are bonded sequentially to the substrate. The subscript, i, denotes the layer number for the multilayer and ranges from 1 to n. Accordingly, the coefficient of thermal expansions are α_s and α_i. Because of the temperature difference, ΔT, there are constrains in the system. Hence, the thermal strains, $\alpha_s\,\Delta T$ and $\alpha_i\,\Delta T$, are generated in the substrate and ith layer. The Hooke's law defines the relation between the normal stresses in the ith layer

$$\sigma_i = E_i\,\varepsilon_i\,,$$ **Eq A1.7**

where E_i is the elastic moduli of the *ith* layer.

It is well known that the total strain in the individual coating layers is composed of two parts, namely, stress strain and bending strain. Here, a symmetric laminate is assumed thus no bending strain exists. It should be noted that in the model the multilayer system is assumed to be a strip. Only plane stress state is hence discussed. If the system has a planar geometry rather than a strip, i.e. plane strain state, elastic modulus, E, should be replaced by $E/(1-\nu)$. Considering the whole coating system cooled from a stress-free state, a misfit strain due to the temperature difference, ΔT, is created and can be expressed as

$$\Delta\varepsilon = (\alpha_s - \alpha_i)\,\Delta T = \Delta\alpha\,\Delta T\ \ .$$ **Eq A1.8**

Because of the misfit strain, $\Delta\varepsilon$, in-plane forces will be generated in the layers of the multilayer. By a force balance argument in the length direction of the multilayer

$$\Delta\alpha\,\Delta T = \frac{F_i}{E_i t_i} - \frac{F_s}{E_s t_s}\ \ ,$$ **Eq A1.9**

where F_1 and F_i are the in-plane forces in *ith* layer of coating and substrate, respectively.

In order to satisfy the equilibrium condition, the summation of in-plane forces in the whole system should be zero, that is

$$\sum_{i=1}^{n} F_i + F_s = 0\ \ .$$ **Eq A1.10**

Note that the stresses are calculated based on the undeformed cross-section areas and the force, F, is assumed to distribute across each section uniformly. Combining Equation A1.9 and A1.10 is obtained

$$F_i = \frac{E_i t_i \left[E_s t_s \Delta\alpha\Delta T + \sum_{k=1}^{n} E_k t_k (\alpha_k - \alpha_i)\Delta T \right]}{\sum_{k=1}^{n} E_k t_k + E_s t_s} \quad (1 \le k \le n) \quad \text{and,} \qquad \textbf{Eq A1.11}$$

$$F_s = -\frac{E_s t_s \sum_{k=1}^{n} E_k t_k \Delta\alpha \Delta T}{\sum_{k=1}^{n} E_k t_k + E_s t_s}$$

. $\qquad\qquad\qquad\qquad\qquad\qquad\qquad$ **Eq A1.12**

Therefore, the stress strains of *ith* layer and substrate can be expressed as

$$\varepsilon_i = \frac{E_s t_s \Delta\alpha\Delta T + \sum_{k=1}^{n} E_k t_k (\alpha_k - \alpha_i)\Delta T)}{\sum_{k=1}^{n} E_k t_k + E_s t_s} \quad \text{and} \qquad \textbf{Eq A1.13}$$

$$\varepsilon_s = \frac{\sum_{k=1}^{n} E_k t_k \Delta\alpha \Delta T}{\sum_{k=1}^{n} E_k t_k + E_s t_s}, \qquad\qquad\qquad \textbf{Eq A1.14}$$

that can be introduced in the Hooke's law to calculate the residual stresses.

The plain strain solution is exactly the same than that of Oël earlier exposed. An extension to this calculation is done by Zhang for non-symmetrical laminates or coatings that suffer bending [2]. Also by Zhang a residual stresses analysis of functionally graded materials is presented in [3].

A third alternative is given in the following. It concerns the elastic strain energy density. Since the layers in our laminate lie parallel to the *x-y*-plane, very low stresses in the *z* direction σ_z can be expected; therefore, we can assume $\sigma_z \equiv 0$ in the following context. In the case of plane strain, the conditions $\varepsilon_y \equiv 0$ and $\sigma_z \equiv 0$ yield the stresses in *y*-direction:

$$\sigma_y = \nu\sigma_x - E\alpha^*\Delta T. \qquad\qquad\qquad\qquad \textbf{Eq A1.15}$$

Hereby, $\Delta\alpha$ denotes the thermal expansion mismatch. The elastic strain components ε_x^{el} and ε_y^{el} follow as

$$\varepsilon_x^{el} = \frac{(1-\nu^2)}{E}\sigma_x + \nu\alpha^*\Delta T \quad , \quad \varepsilon_y^{el} = -\alpha^*\Delta T \; .$$

Eq A1.16

The elastic strain energy density ϕ can then be calculated as

$$\phi = \frac{1}{2}(\sigma_x\varepsilon_x + \sigma_y\varepsilon_y) = \frac{1}{2}\left(\frac{1-\nu^2}{E}\sigma_x^2 + E(\alpha^*\Delta T)^2\right) \; .$$

Eq A1.17

Equation A1.17 is valid for any material point under thermal and/or mechanical loading, if plane strain conditions prevail and the stresses in z-direction are zero. The strain energy density ϕ consists of two parts, one depending on the stress in x-direction σ_x and another one due to the thermal expansion or contraction. Note that the stresses in x-direction σ_x depend on both the external loading and the thermal expansion/contraction.

If no external loading applies and only the eigenstrain $\Delta\alpha\,\Delta T$ is active, the strain state ε_x is, apart from the end regions, independent of the position vector, say $\varepsilon_{x,\text{res}} = c$ with c being a constant. The stress $\sigma_{x,\text{res}}$ follows as

$$\sigma_{x,\text{res}} = \frac{cE}{1-\nu^2} - \frac{E\alpha^*\Delta T}{1-\nu} \; ,$$

Eq A1.18

and the constant c is found by utilizing the global equilibrium condition, $\int_0^h \sigma_{x,\text{res}}\,dz = 0$. This integral can easily be evaluated, since $E, \alpha^*, \Delta T, \nu$ are constant in the individual layers.

Bibliography

[1]   Oël, H. J., Fréchette, V. D., "Stress distribution in multiphase systems: I, composites with planar interfaces", Journal of the American Ceramic Society, **50**, 542-549, (1967).
[2]   Zhang, X. C., Xu, B. S., Wang, H. D., Wu, Y. X., "An analytical model for predicting thermal residual stresses in multilayer coating systems", Thin Solid Films, **488**, 274-282, (2005).
[3]   Zhang, X. C., Xu, B. S., Wang, H. D., Jiang, Y., Wu, Y. X., "Modeling of thermal residual stressses in multilayer coatings with graded properties and compositions", Thin Solid Films, **497**, 223-231, (2006).

Annex 2. Material Properties Concerning Chapter 5 and 6.

This annex summarizes the properties of the multilayers used in Chapter 5 and 6. The common physical properties are listed in Table A2.1.

Table A2.1: Material properties of each layer.

Material	E [GPa]	ν [-]	α [10^{-6} K^{-1}]	$K_{c,0}$ [MPa$\sqrt{m}$]	$J_{c,0}$ [J/m^2]
Al_2O_3 (A)	392 ± 5	0.24 ± 0.04	8.64 ± 0.03	3.8 ± 0.3	35 ± 2
Al_2O_3-ZrO_2 (AZ)	305 ± 4	0.26 ± 0.03	9.24 ± 0.02	4.3 ± 0.6	57 ± 3

The residual stresses are also exposed, for the laminate studied in Chapter 4 and Chapter 6 with the following geometry, the results are presented in Figure A2.1

Table A2.2: Geometry of the laminate 2A/AZ/A/AZ/A/AZ/A/AZ/2A.

t_A [mm]	t_{AZ} [mm]	B [mm]	L [mm]	W [mm]
0.190	0.220	2.5	28	1.8
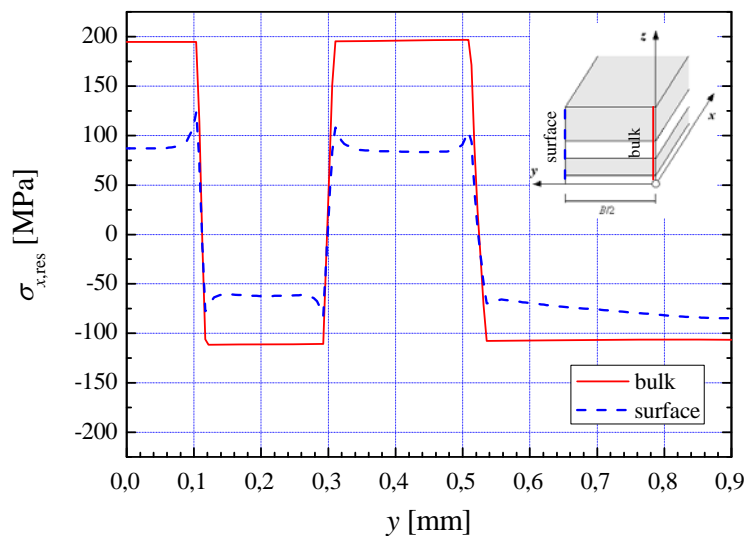
Figure A2.1: Thermal residual stresses $\sigma_{x,res}$ along the z-direction in the bulk ($x = 0$, $y = 0$, solid line) and in the surface ($x = 0$, $y = B/2$, dashed line) for a 2A/AZ/A/AZ/A/AZ/A/AZ/2A. The solution corresponding to a 3-D model is presented.

For the laminate studied in Chapter 5, in Figure A2.2 and Figure A2.3 the results of the 3D and 2D computations are compared. As already experienced in a study by Shan et al., nearly 80% of the cross section measured in the y-direction shows residual stresses $\sigma_{x,res}$ according to the plane strain model. In the side-surface region, say

within $1.0 \leq y \leq 1.25$ mm, the residual stresses can be roughly approximated by the plane stress distribution. Directly at the side-surface the absolute values of $\sigma_{x,\text{res}}$ can, however, become significantly smaller than the plane stress values. It should be mentioned that at the positions where the interfaces 1 to 6 impinge the surface, weak stress singularities for $\sigma_{x,\text{res}}$ occur which can be ignored.
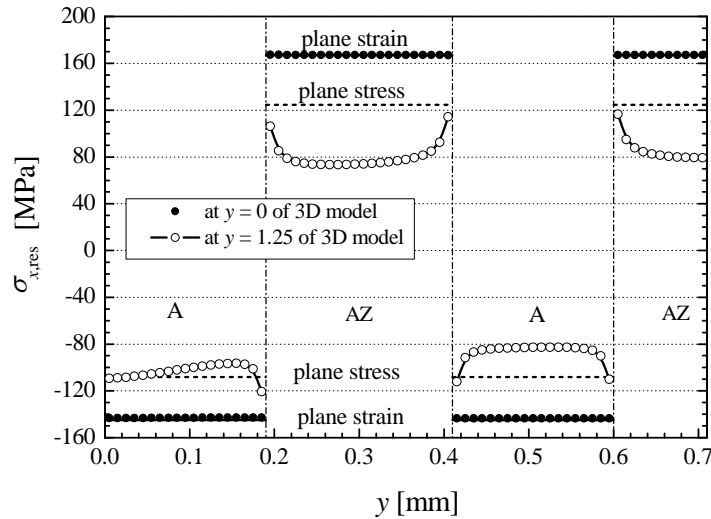
Figure A2.2: Thermal residual stresses $\sigma_{x,\text{res}}$ along the y-direction at $y = 0$ and $y = 1.25$ mm for a plane stress, plane strain, and three-dimensional (3D) model.
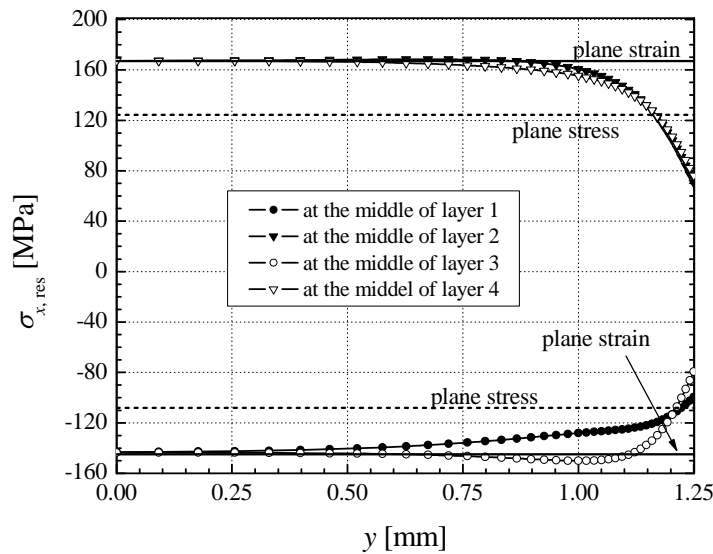
Figure A2.3: Thermal residual stresses $\sigma_{x,\text{res}}$ along the y-direction for various values of x for a plane stress, plane strain, and three-dimensional (3D) model.

Annex 3. Analytical Estimate of the Crack Driving Force

A3.1. Expressions for J_{far} and C_{inh}

To evaluate the crack driving force according to Equation 5.3, both an estimate of the far-field J-integral J_{far} and the material inhomogeneity term C_{inh} are needed. First we consider the line integral along a contour Γ_{far} around the crack tip following Equation 5.4, see Figure 5.3. The following specifications can be made:

- Due to the symmetry condition, the path along $0 \leq z \leq W$, $x = 0$, provides no contribution to J_{far}.

- The *z*-component of the unit normal vector to the integration path n_z is zero along $0 \leq z \leq W$, $x = L_x$; note that we refer here to the (undeformed) reference configuration when calculating material forces. The *z*-component of the traction vector t_z is zero if L_x is so large that both the stress relieved zone in the wake of the crack and the crack tip field have negligible effect on the stress and strain conditions: $L_x \geq \kappa a$ where κ is a positive factor in the order of magnitude 1. The *x*-component of the traction vector t_x is equal to σ_x. Therefore, only the term $t_x \partial u_x / \partial z$ is of relevance.

- The *x*-component of the displacement vector u_x is linearly distributed along the *z*-direction, $\partial u_x / \partial z$ is constant. The integral of the stresses due to bending $\int_0^W \sigma_{x,b} (\partial u_x / \partial z) dz$ is 0, since $\sigma_{x,b}$ has an antimetric distribution with respect to $z = W/2$. The integral of the thermal stresses $\int_0^W \sigma_{x,res} (\partial u_x / \partial z) dz$ is 0, since balance enforces $\int_0^W \sigma_{x,res} \, dz = 0$. Therefore, the integral Equation 5.4 becomes zero for $0 \leq z \leq W$, $x = L_x$.

- The traction vector $\underline{t}$ must be zero at the free surfaces at $z = 0$ and $z = W$.

The consequence is that the far-field J-integral Equation 5.4 depends only on the distribution of the strain energy density along the two surfaces and can be rewritten as

$$J_{far} = 2 \int_0^{L_x} (\phi(x, z = W) - \phi(x, z = 0)) dx \qquad \textbf{Eq A3.1}$$

For a further analysis the specific elastic strain energy density can be inserted from Equation A1.17, $\phi = (\sigma_x^2 / E + E(\alpha^* \Delta T)^2)/2$ with E and α^* belonging either to the A- or AZ-material. Note again that σ_x depends on both the external loading and the thermal expansion/contraction.

Next we consider the material inhomogeneity term C_{inh}, see Equation 5.7 and Figure 5.13. The second term in the integrand of $C_{inh,i}$ becomes zero, since:

- the stress components in z-direction are small and can be neglected;
- the stress components in y-direction do not play a role as the corresponding total strain components are zero.
- the strain components $\left\|\varepsilon_{x,i}\right\| = \left\|\varepsilon_x\right\|\big|_{z=z_i}$ have no jump.

The consequence is that $C_{inh,i}$ can be written as

$$C_{inh,i} = -2\int_0^{L_x} (\phi(x, z = z_{i,r}) - \phi(x, z = z_{i,l}))dx \ ,$$

Eq A3.2

with $z_{i,l}$ and $z_{i,r}$ denoting the position at the right and left side of the ith interface. Generally, both J_{far} and C_{inh} depend on the crack length a. They also depend on L_x, but Equation 5.5 delivers J_{tip}-values which are independent on L_x. In the further context the notation $J_{tip}(a)$ and $J_{far}(a)$ is sometimes used.

A3.2. Crack driving force for zero crack length

In the case of zero crack length the stress state at $z = 0$ is $\sigma_x\big|_{z=0} = \sigma_{x,b\,max} + \sigma_{x,res}^A$ and at $z = W$ is $\sigma_x\big|_{z=0} = -\sigma_{x,b\,max} + \sigma_{x,res}^A$. Hereby $\sigma_{x,b\,max}$ denotes the maximum stresses in x-direction due to the bending and $\sigma_{x,res}^A$ the thermal residual stresses in the A-layers. From Equation A3.1 with $\alpha^* = 0$ in the material A follows

$$J_{far}(0) = -(4L_y / E_A)\sigma_{x,b\,max} \cdot \sigma_{x,res}^A$$

Eq A3.3

Thus, if one of the two stress components is zero, the far-field J-integral for the component without a crack becomes zero. This is the case for an elastically inhomogeneous specimen without residual stresses at arbitrary loading, as well as for an unloaded specimen with residual stresses.

Next we consider the material inhomogeneity term. We introduce a dimensionless coordinate ξ, $0 \le \xi \le 1$ with $\xi = 0$ at $z = W/2$ and with $z = 1$ at $x = W/2$. Then z_1 corresponds to $-\xi_3$, z_2 to $-\xi_2$, z_3 to $-\xi_1$, z_4 to ξ_1, z_5 to ξ_2, and z_6 to ξ_3. Following this notation, the term $-\left[\phi(x, z = z_{i,r}) - \phi(x, z = z_{i,l}) \right] = \left\| \phi(x, z_i) \right\|$ with $i = 1, 2, ..., 6$ transforms to $-\left\| \phi(x, \xi_i) \right\|$ or $-\left\| \phi(x, -\xi_i) \right\|$ with $j = 1, 2, 3$. Inserting the stresses due to bending and thermal misfit, we can get the jump of the strain energy density at the interfaces [1].

For an even number of interfaces *I*, ensuring compressive residual stresses in the surface A-layers, the sum of the jumps above yields with Equation 5.7 and Equation A3.2)

$$C_{\text{inh}}(0)/2L_{\text{x}} = -2\sigma_{x,b\,\text{max}}(\sigma_{x,\text{res}}^{\text{A}} - \sigma_{x,\text{res}}^{\text{AZ}})/E_{\text{A}} \cdot \sum_{j=1}^{I/2}(-1)^j \xi_j \ . \qquad \textbf{Eq A3.4}$$

The alternating sign in the sum corresponds to the fact that material A on the right and AZ on the left side of the interface switches to AZ on the right and A on the left side. It is seen from Equation A3.4 that the material inhomogeneity term of the component without a crack is zero for an elastically inhomogeneous specimen without residual stresses at arbitrary loading, as well as for a specimen with residual stresses if no external loading applies.

If we add to Equation A3.4 the corresponding term $J_{\text{far}}/2L_x$ from Equation A3.3, we find

$$J_{\text{tip}}(0)/2L_{\text{x}} = -(2\sigma_{x,b\,\text{max}}/E_{\text{A}}) \cdot \left[\sigma_{x,\text{res}}^{\text{A}} + (\sigma_{x,\text{res}}^{\text{A}} - \sigma_{x,\text{res}}^{\text{AZ}}) \cdot \sum_{j=1}^{I/2}(-1)^j \xi_j \right] \ .$$

The expression in the brackets $[\ ]$, however, is the global equilibrium expression for the thermal stresses $\sigma_{x,\text{res}}$ in the interval $0 \le \xi \le 1$, enforcing that $[\ ]$ must be 0. Therefore, the following relations hold:

$$J_{\text{tip}}(0) \equiv 0, \qquad J_{\text{far}}(0) \equiv -C_{\text{inh}}(0) \equiv -\sum_{i=1}^{I} C_{\text{inh,i}} \ . \qquad \textbf{Eq A3.5}$$

It is interesting to note that a significant thermodynamical force C_{inh} acts on each interface which would probably provoke an interface motion for interfaces with certain mobility. However, the total driving force on the crack tip is zero.

A3.3. Crack driving force for non-zero crack length

If we introduce now a crack with length a, only a region $0 \le z \le W$ and $0 \le x \le \kappa a$ is affected; the original stress state remains undisturbed for $x \ge \kappa a$. According to the proof above, this undisturbed part of the specimen does not influence J_{tip}. The further conclusion is that $J_{\text{tip}}(a)$ is path-independent for $L_x \ge \kappa a$ (and provided that the path does not cross an interface).

If the crack is very small, its length a being only a small fraction of the thickness of the first lamina, it can be assumed that the stress state of the uncracked specimen can be used as an approximation for regions not influenced by the crack. For a rough estimate of J_{far}, we assume that due to the interruption of the stress flow in x-direction by the crack mouth the stresses are reduced to zero in the influence zone of the crack $-\kappa a \le x \le \kappa a$ and for $z = 0$. Then J_{far} becomes (compare section A3.1)

$$J_{\text{far}} \approx J_{\text{far}}(0) + 2\kappa a(-\sigma_{x,b\max} + \sigma_{x,\text{res}}^{\text{A}})/(2E_{\text{A}}) \ . \qquad \textbf{Eq A3.6}$$

We can further assume that the material inhomogeneity term will be not affected by the short crack: $C_{\text{inh}} \approx C_{\text{inh}}(0)$. From Equation 5.5 and the condition $J_{\text{far}}(0) + C_{\text{inh}}(0) = 0$ then follows

$$J_{\text{tip}} \approx 2\kappa a(-\sigma_{x,b\max} + \sigma_{x,\text{res}}^{\text{A}})^2/(2E_{\text{A}}) \ . \qquad \textbf{Eq A3.7}$$

We can compare this solution with the stress intensity factor for a small surface crack $K = 1.12(-\sigma_{x,b\max} + \sigma_{x,\text{res}}^{\text{A}})^2/(2E_{\text{A}})$, utilizing the well known relation $J = K^2/E$. This comparison yields $\kappa \approx 3.94$. Since $\sigma_{x,b\max}$ depends linearly on the load F and $\sigma_{x,\text{res}}^{\text{A}}$ linearly on $\tilde{E}\,\Delta\tilde{\alpha}^*\,\Delta T$, where $\tilde{E}$ and $\Delta\tilde{\alpha}^*$ are weighted averages, J_{tip} can be considered as a quadratic form in the variables F and. $\tilde{E}\,\Delta\tilde{\alpha}^*\,\Delta T$.

For a large crack one may assume that the stress state, now denominated as $\sigma_{x,a}$, exists only in the region $0 \le z \le W$ and $0 \le x \le \kappa a$. In other words, the transfer of the stresses is interrupted in the region $0 \le z \le a$, and the rather "distorted" stress distribution is now approximated by a stress distribution $\sigma_{x,a}$ which shall be linearly distributed in $0 \le z \le W$ and independent of x for $0 \le x \le \kappa a$. These assumptions yield

$$\varepsilon_{y,a} = \beta_1 z/(W - a) + \beta_2 \ , \qquad \textbf{Eq A3.8}$$

$$\sigma_{y,a} = E^*(\beta_1 z /(W-a) + \beta_2 - \alpha^* \Delta T) \;, \qquad\qquad \text{Eq A3.9}$$

with α^*, E^* belonging either to the A- or AZ-material and β_1, β_2 as two constants. The equilibrium conditions require that the integration of $\sigma_{x,a}$ over z in the interval $0 \le z \le a$ must be zero and the integration of $z\sigma_{x,a}$ must yield the moment per unit thickness $M / B = F \cdot (S_1 - S_2)/2B$. This task is left to the reader and can easily be performed by any finite element program. The coefficients β_1, β_2 are linearly dependent on $\Delta\tilde{\alpha}^* \Delta T$ (with $\tilde{E}, \Delta\tilde{\alpha}^*$ being weighted averages over $0 \le z \le a$) and the dimension-free moment term $\tilde{M}$,

$$\beta_1 = \beta_{11}\Delta\tilde{\alpha}^* \Delta T + \beta_{12}\tilde{M} \;\; \text{and} \;\; \beta_2 = \beta_{21}\Delta\tilde{\alpha}^* \Delta T + \beta_{22}\tilde{M} \;. \qquad\qquad \text{Eq A3.10}$$

The coefficients $\beta_{11}, \beta_{12}, \beta_{21}, \beta_{22}$ are rational functions in a, W and the interface coordinates z_i, and $\tilde{M} = M /(\tilde{E}^*(W-a)^2 B)$. The strain energy density ϕ_a follows from Equation A3.3 with Equation A3.9 as

$$\phi_a(z) = E^*(\beta_1 z /(W-a) + \beta_2 - \alpha^* \Delta T)^2 / 2 + E^*(\alpha^* \Delta T)^2 / 2 \;. \qquad\qquad \text{Eq A3.11}$$

Finally, $\phi_a(z)$ becomes a quadratic form in $\tilde{E}\,\Delta\tilde{\alpha}^*\Delta T$ and $\tilde{M}$. The coefficients of this form are rather complicated rational expressions including also weighted averages of the material data. These are very lengthy expressions and not listed in this paper. However, they can be calculated by any mathematics processor, e.g. MAPLE (http://www.maple.com). With the strain energy density known, J_{far} and C_{inh} can be evaluated from Equation A3.1 and Equation A3.2. With Equation 5.5 then follows the crack driving force J_{tip} which will appear in the form

$$J_{tip} \approx 2\kappa a \left[\phi_a(W) - \sum_{i=i_s}^{I} (\phi_a(z = z_{i,r}) - \phi_a(z = z_{i,l})) \right] \;. \qquad\qquad \text{Eq A3.12}$$

The summation in Equation A3.11 starts from $i = i_s$, which is the number of the first interface not intersected by the crack. It should be noted that J_{tip} estimated by Equation A4.12 reflects only the global effect of a crack in a layered bending specimen. The very local effect of the crack tip field, specifically when it approaches an interface, cannot be reproduced. In this case J_{tip} may tend to infinity or zero depending whether the crack is propagating from material A to AZ or from material AZ to A [2-4], for a discussion see also [5].

Bibliography

[1]   Chen, C. R., Fischer, F. D., Kolednik, O., Pascual, J., Danzer, R., "Prediction of the fracture toughness of a ceramic multilayer composite - Modeling and experiments", Acta Materialia, **55**, 409-421, (2007).

[2]   Kolednik, O., Predan, J., Shan, G. X., Simha, N. K., Fischer, F. D., "On the fracture behavior of inhomogeneous materials -a case study for elastically inhomogeneous bimaterials", International Journal of Solids and Structures, **42**, 605-620, (2005).

[3]   Fischer, F. D., Predan, J., Kolednik, O., Simha, N. K., Arch. Appl. Mech. submitted, .

[4]   Romeo, A., Ballarini, R., "A crack very close to a bimaterial interface", Journal of Applied Mechanics, **62**, (1995).

[5]   Joyce, M. R., Reed, P. A. S., Syngellakis, S., "Numerical modelling of crack shielding and deflection in a multi-layered material system", Material Science and Engineering A, **342**, 11-22, (2003).

ISFK

Javier Pascual   A4. Weight function Method vs. Material Forces Approach

MONTAN**UNIVERSITÄT**
LEOBEN

Annex 4. Comparison between the Weight Function Method and the Material Forces Approach

A comparison between both methodologies is interesting to be investigated. The results show how both techniques predict a similar behavior of the effective R-curve, however quantitatively they are different (see Figure A4.1).

Figure A4.1 presents both solutions for a same laminate, the results are presented in terms of the crack driving force which has units of J/m^2. Since the solution is presented in energetic terms, the weight function solution is calculated from the relation $J = \left(1 - \bar{v}^2\right) K^2 / \bar{E}$, using volume-averaged values of the Poisson's ratio, $\bar{v} = 0.25$, and the Young's modulus, $\bar{E} = 375$ GPa.
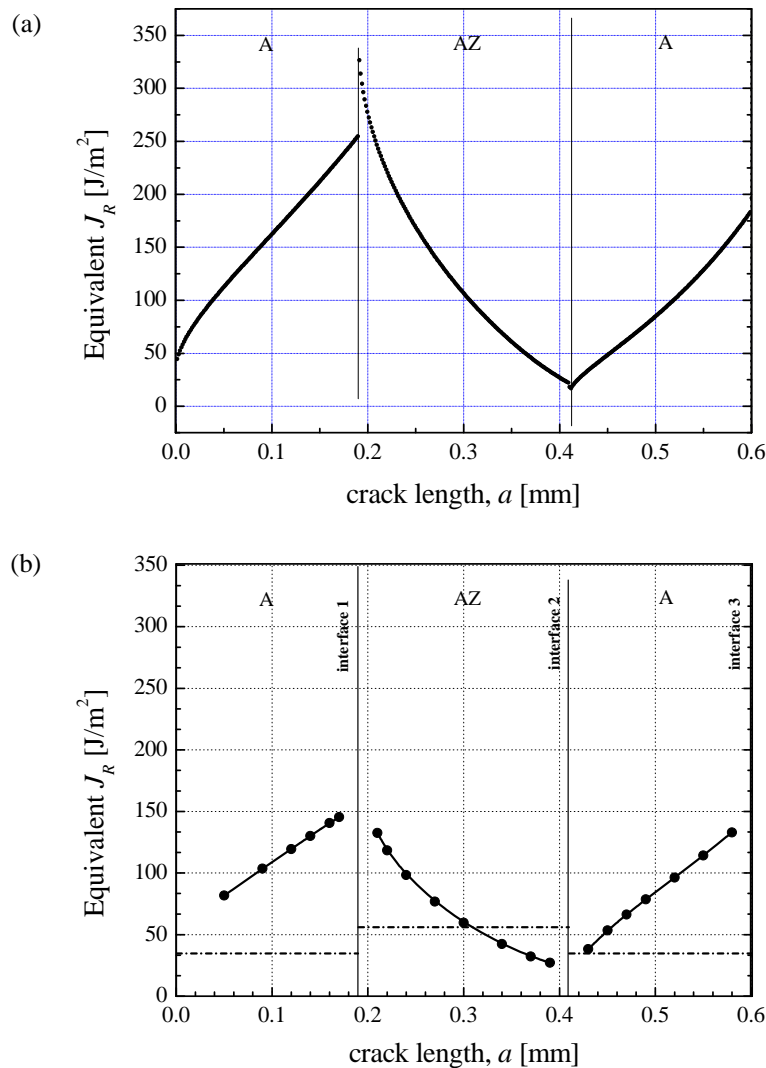
Figure A4.1: Effective crack driving force calculated through (a) the weight function method and, (b) the configurational forces approach.

ISFK

Javier Pascual   A4. Weight function Method vs. Material Forces Approach

It turned out that - in this particular case - the weight function method overestimated the calculated toughness curve by a factor of approx. $\sqrt{2}$, whereas experimental data fitted well to the results obtained with the material forces method (see Figure A4.1). Even though these differences seem to be not negligible it is believed that the tendencies for the apparent R-curves and the implications for laminate design will remain valid.

The appreciable difference between them can be due to the simplifications done with the weight function method, i.e. the elastic mismatch is not considered in the derivation of the weight function $h(z,a)$. A constant residual stress state within each layer has been also assumed that could lead to overestimate the shielding as the residual stress decay at the edges.

For the laminate studied in this paper, the effects of the compressive residual stress on the crack driving force and on the fracture toughness of the laminate specimen are much stronger than the effects of elastic inhomogeneity. In open circles, Figure A4.1b presents the effective crack driving force only considering the elastic mismatch neglecting the existence of residual stresses on the material.

It is clear that the AZ-layer attracts cracks in the A-layer since the crack driving force slightly decays in the first layer. Therefore if the weight function is calculated with a homogeneous elastic modulus we are neglecting the elastic attraction and overestimating the effective R-curve.